PROCESSING-DEPENDENT BROADBAND DIELECTRIC PROPERTIES OF $KTaO_3$ CERAMICS, FILMS AND $KTa_{0.6}Nb_{0.4}O_3$ FILMS

Sebastjan Glinšek

Doctoral Dissertation
Jožef Stefan International Postgraduate School
Ljubljana, Slovenia, April 2012

Evaluation Board:

Prof. Barbara Malič, Jožef Stefan Institute, Jamova cesta 39, 1000 Ljubljana, Slovenia

Prof. Angus I. Kingon, School of Engineering, Brown University, Providence, Rhode Island 02912, USA

Dr. Jan Petzelt, Institute of Physics, Academy of Sciences of the Czech Republic, Na Slovance 2, 182 21 Prague 8, Czech Republic

MEDNARODNA PODIPLOMSKA ŠOLA JOŽEFA STEFANA
JOŽEF STEFAN INTERNATIONAL POSTGRADUATE SCHOOL

Sebastjan Glinšek

PROCESSING-DEPENDENT BROADBAND DIELECTRIC PROPERTIES OF $KTaO_3$ CERAMICS, FILMS AND $KTa_{0.6}Nb_{0.4}O_3$ FILMS

Doctoral Dissertation

DIELEKTRIČNE LASTNOSTI KERAMIKE IN PLASTI $KTaO_3$ TER PLASTI $KTa_{0,6}Nb_{0,4}O_3$, MERJENE V ŠIROKEM FREKVENČNEM OBMOČJU

Doktorska disertacija

Supervisor: Prof. Marija Kosec

Co-Supervisor: Prof. Zdravko Kutnjak

Ljubljana, Slovenia, April 2012

Index

Abstract ..... **IX**

Povzetek ..... **XI**

Abbreviations ..... **XIII**

1 Introduction **17**

1.1 Ferroelectrics and Related Materials 17

1.1.1 Ferroelectrics and Relaxors 17

1.1.2 Ferroelectrics in Microwave Devices 19

1.1.3 Incipient Ferroelectrics 22

1.1.3.1 $KTaO_3$ 23

1.1.3.2 Dielectric Grain Size Effect in Incipient Ferroelectric Ceramics 24

1.1.3.3 Strain-Induced Ferroelectricity in Thin Films of Incipient Ferroelectrics 25

1.1.4 Solid Solutions of Incipient Ferroelectrics with the Ferroelectrics 28

1.1.4.1 $K(Ta,Nb)O_3$ 28

1.2 Processing and Dielectric Properties of $KTaO_3$-Based Ceramics and Thin Films 31

1.2.1 $KTaO_3$ Ceramics 31

1.2.2 $K(Ta,Nb)O_3$ Ceramics 33

1.2.3 Processing of Thin Films 35

1.2.3.1 Chemical Solution Deposition 36

1.2.3.1.1 Alkoxide-Based Chemical Solution Deposition 37

1.2.3.2 $KTaO_3$ and $K(Ta,Nb)O_3$ 39

1.2.3.3 $K(Ta,Nb)O_3$ Thin Films Prepared by Other Methods 42

2 Aims and Hypothesis **43**

3 Materials and Methods **45**

3.1 Preparation of the Samples 45

3.1.1 $KTaO_3$ Ceramics 45

3.1.1.1 High-Energy Milling 46

3.1.1.2 Calcination and Sintering 46

3.1.2 $KTaO_3$ and $KTa_{0.6}Nb_{0.4}O_3$ Thin Films 46

3.1.2.1 Synthesis of the Sols 47

3.1.2.2 Substrates 48

3.1.2.3 Preparation of the Films 48

3.2 Characterization Methods 48
3.2.1 Thermal Analysis 48
3.2.2 Mid-Infrared Spectroscopy 49
3.2.3 Extended X-Ray-Absorption Fine-Structure Spectroscopy 49
3.2.4 Laser Granulometry 49
3.2.5 Inductively Coupled Plasma Spectroscopy 49
3.2.6 X-Ray Diffraction 50
3.2.7 Density Measurements 50
3.2.8 Scanning Electron Microscopy 50
3.2.9 Transmission Electron Microscopy 50
3.2.10 Broadband Dielectric Spectroscopy 51
3.2.10.1 Radio-Frequency Measurements 51
3.2.10.2 Quasi-Static Measurements 53
3.2.10.3 Microwave Measurements 54
3.2.10.4 Terahertz Spectroscopy 55
3.2.10.5 Infrared Spectroscopy 56
3.2.10.6 Raman Spectroscopy 56

4 Results and Discussion 57

4.1 $KTaO_3$ Ceramics 57
4.1.1 Synthesis of the Powders 57
4.1.1.1 Mechanochemical Activation 57
4.1.1.2 Phase Composition and Microstructure 59
4.1.2 Sintering, Phase Composition and Microstructure of the Ceramics 62
4.1.3 Radio-Frequency Dielectric Properties 67
4.1.3.1 Discussion 68
4.1.4 Broadband Dielectric Properties 69
4.1.4.1 Microwave Properties 69
4.1.4.2 Terahertz and Infrared Properties 70
4.1.4.3 Analysis of the Broadband Dielectric Properties 73
4.1.4.4 Raman Measurements 75
4.1.5 Summary 77
4.2 $KTaO_3$ Thin Films 79
4.2.1 Preparation of the Films 79
4.2.1.1 Thermal Decomposition of the Sols 79
4.2.1.2 Phase Composition and Microstructure of the Films 81
4.2.2 Broadband Dielectric Properties 87
4.2.2.1 Radio-Frequency and Quasi-Static Properties 87
4.2.2.2 Microwave, Terahertz and Infrared Properties 90
4.2.3 Summary 96
4.3 Single Crystals – Ceramics – Polycrystalline Thin Films Relations in $KTaO_3$ 99
4.3.1 Grain Boundaries and Pores 100
4.3.2 Biaxial Stress 101
4.4 $KTa_{0.6}Nb_{0.4}O_3$ Thin Films 103

4.4.1 Preparation of the Films 103
4.4.1.1 Synthesis of the Sols 103
4.4.1.1.1 EXAFS Spectra of the $KTa_{0.6}Nb_{0.4}O_3$ Sols 103
4.4.1.1.2 Ta and Nb Local Environments 106
4.4.1.1.3 Local Structure and Reactions in the Sols upon Refluxing 107
4.4.1.2 Thermal Decomposition of the Dried Sols 109
4.4.1.3 Phase Composition and Microstructure of the Films 111
4.4.2 Radio-Frequency and Microwave Dielectric Properties 115
4.4.2.1 Discussion on Processing – Dielectric Properties Relations in $KTa_{0.6}Nb_{0.4}O_3$ Films 118
4.4.3 Summary 119

5 Summary, Conclusions and Future Prospects 121
5.1 $KTaO_3$ Ceramics and Thin Films 121
5.2 $KTa_{0.6}Nb_{0.4}O_3$ Thin Films 124

6 Acknowledgements 125

7 References 127

8 Index of Figures 145

9 Index of Tables 155

10 Appendix 157
10.1 High-Frequency Spectroscopic Properties and Lattice Dynamics of Perovskite Ferroelectrics and Related Materials 157

11 Personal Bibliography 165
11.1 Scientific Articles from the Thesis 165
11.2 Other Scientific Articles 165
11.3 Chapters in Monographs 166
11.4 Conference Contributions 166
11.4.1 Published Scientific Conference Contributions 166
11.4.2 Published Scientific Conference Contributions – Invited Talks 166
11.4.3 Published Scientific Conference Contributions – Abstracts 167
11.4.4 Unpublished Scientific Conference Contributions 169

Abstract

$KTaO_3$ belongs to the group of incipient ferroelectrics, which are materials important from the fundamental, as well as from the applications, point of view. It is well known in its single-crystal form; however, the processing of technologically interesting ceramics and thin films is a challenging task and knowledge of their dielectric properties is still at a basic level.

In the frame of the thesis we have prepared $KTaO_3$ powder from mechanochemically activated K_2CO_3-Ta_2O_5 powder mixtures by heating at 800°C. The powders were found to be heterogeneous at the microscopic level; therefore, additional heating at the same temperature was performed. Single-phase $KTaO_3$ ceramics with relative densities above 95 % were obtained by hot pressing the powder compacts at 1250°C for 2 h. The ceramics have a bimodal grain size distribution in the μm range. The dielectric permittivity of the hot pressed ceramic, prepared from the double-calcined powder, measured at 5 K and 1 kHz is 4080, which is almost twice the value obtained for the ceramic prepared from the single-calcined powder. In fact it is comparable to the value reported for single crystals, i.e., 4500.

The lattice dynamics of the $KTaO_3$ ceramics with enhanced dielectric properties were evaluated for the first time. Three polar modes expected for the cubic structure were observed. As in single crystals, the lowest-frequency TO1 mode (soft mode) strongly softens on cooling, while the TO2 and TO4 mode frequencies do not change with temperature. The permittivity does not show any significant dispersion below the soft-mode frequency and its value in the kHz and GHz ranges is mainly given by the intrinsic polar lattice mode contribution. The soft-mode frequency agrees with the values found in single crystals; this indicates a negligible influence of the grain boundaries on the dielectric response in $KTaO_3$, unlike in other ferroelectric or incipient ferroelectric perovskite ceramics.

Furthermore, we prepared solution-derived polycrystalline $KTaO_3$ thin films on polycrystalline alumina and (0001) sapphire substrates. The 200-nm-thick phase-pure perovskite films were obtained after heating at 900°C by adding 30 at.% excess of potassium to the sols.

Broadband dielectric spectroscopy was employed to evaluate the properties of the films. In contrast to the single crystals and ceramics, a peak was observed in the temperature-dependent dielectric permittivity measured in a radio-frequency and microwave ranges. The low-temperature ferroelectric state was fingerprinted by the quasi-static polarization measurements. Analyses of the lattice dynamics of the $KTaO_3$ films on sapphire revealed that the soft mode softens on cooling, with a minimum frequency at ~60 K. It was found to be linearly coupled to a central mode, which is silent in the paraelectric phase, and becomes coupled to the polarization below ~60 K. The result

gives strong evidence for the paraelectric-ferroelectric phase transition, which was not observed before in polycrystalline $KTaO_3$ thin films.

We also studied the processing and properties of the solution-derived $KTa_{0.6}Nb_{0.4}O_3$. It is a composition in the solid solution of $KTaO_3$ with the ferroelectric $KNbO_3$ ($K(Ta,Nb)O_3$), and is a candidate material for microwave applications.

We have employed extended X-ray-absorption fine-structure spectroscopy to follow the structural evolution of the potassium acetate and transition-metal alkoxide-based sols upon refluxing. While the monomeric Ta-species were found to be rather inert, the dimeric Nb-alkoxide started to form oligomers upon prolonged refluxing. The K-O-transition-metal correlations were detected in all the sols and the number of K neighbors around Nb increased upon refluxing, saturating at 24 h.

The formation of bimetallic species between K and both transition metals strongly affects the crystallization behavior of the films on polycrystalline alumina substrates. We obtained single-phase perovskite films after heating at 900°C only from the 24-h-refluxed solutions, while the films prepared from the 1-h-refluxed solutions had a multi-phase composition and heterogeneous microstructures. The dielectric properties were strongly enhanced as well. The room-temperature tunability, measured at 1 MHz and an applied field of 92 kV/cm, has the value of 3.8.

The room-temperature permittivity decreases from 2430 at 10 kHz to 590 at 14.5 GHz and the relaxor-like behavior was confirmed by a fit to the Vogel-Fulcher law. Even though this frequency dependence and the rather high dielectric losses represent a challenge for the applicability of the solution-derived $K(Ta,Nb)O_3$ thin films in microwave devices, the observed formation of nanoscale heterogeneities in the sols provides a hint for further improvements to the functional properties.

Povzetek

$KTaO_3$ je značilni predstavnik feroelektrikov v zametku, ki so pomembni materiali tako iz vidika temeljnih kot tudi aplikativnih raziskav. Kljub temu, da je zelo dobro poznan kot monokristal, je podatkov o tehnološko zanimivi keramiki ter tankih plasti zelo malo, predvsem zaradi zahtevnega procesiranja. Prav tako so slabo poznane tudi njihove dielektrične lastnosti.

V okviru doktorske disertacije smo pripravili perovskitne prahove $KTaO_3$ s segrevanjem mehanokemijsko aktiviranih mešanic prahov K_2CO_3-Ta_2O_5 pri 800°C. Ker smo opazili strukturno heterogenost na nanometrskem nivoju, smo jih dodatno segrevali pri isti temperaturi. Enofazno perovskitno keramiko, z relativnimi gostotami višjimi od 95 %, smo uspešno pripravili s sintranjem pod pritiskom pri 1250°C. Keramika je imela bimodalno razporeditev velikosti zrn na mikrometrskem nivoju. Dielektričnost, izmerjena pri 5 K in 1 kHz, keramike pripravljene iz dvakrat kalciniranih prahov, je dosegla vrednost 4080, kar je skoraj dvakrat toliko kot v primeru keramike iz enkrat kalciniranih prahov. Za primerjavo, monokristal ima pri isti pogojih merjenja vrednost dielektričnosti približno 4500.

V disertaciji je bila prvič analizirana dinamika kristalne mreže v keramiki $KTaO_3$. V infrardečih spektrih smo opazili pasove, ki pripadajo trem različnim resonancam značilnih za perovskitne materiale s kubično strukturo. Frekvenca prvega nihanja, označenega s TO1 (mehki način nihanja), ki je večinoma posledica nihanja Ta^{5+} ionov v O_6 oktaedrih, se drastično znižuje z nižanjem temperature. Pri frekvencah nižjih od mehkega načina nihanja dodatnih disperzij nismo opazili in dielektričnost, izmerjeno v radio ter mikrovalovnem frekvenčnem območju, lahko opišemo zgolj z intrinzičnim prispevkom dinamike kristalne mreže. Obnašanje je zelo podobno kot v monokristalu, vrednosti frekvenc mehkega načina nihanja, ki so primerljive z vrednostmi pri monokristalu, pa nakazujejo na zanemarljiv vpliv meja med zrni na dielektrični odziv keramike $KTaO_3$.

Za primerjavo smo s sintezo iz raztopin pripravili tudi 200 nm debele polikristalinične tanke plasti $KTaO_3$. Enofazne perovskitne plasti smo pripravili z nanosom solov, ki so vsebovali 30 at.% prebitka kalija, na korundne oziroma (0001) safirne podlage, ter segrevanjem pri 900°C.

Dielektrične lastnosti plasti $KTaO_3$ smo analizirali s široko-frekvenčno dielektrično spektroskopijo. Opazili smo vrh v temperaturni odvisnosti dielektričnosti, ki smo jo izmerili v radio in mikrovalovnem frekvenčnem območju, kar je v nasprotju z opažanji na monokristalih in keramiki. Prisotnost nizko-temperaturne feroelektrične faze smo zaznali tudi z meritvijo kvazi-statične polarizacije.

Analiza dinamike kristalne mreže plasti na safirnih podlagah je pokazala, da se frekvenca mehkega načina nihanja znižuje z nižanjem temperature zgolj do ~60 K. V teraherčnih spektrih smo zaznali dodatno relaksacijo, tako imenovani centralni način

nihanja, ki nad ~60 K ni aktivna, pod to temperaturo pa postane neposredno sklopljena s polarizacijo. Opisano obnašanje nakazuje na induciran prehod iz paraelektrične v feroelektrično fazo, ki je bil v polikristaliničnih tankih plasteh $KTaO_3$ opažen prvič.

Z metodo iz raztopin smo pripravili tudi tanke plasti $KTa_{0,6}Nb_{0,4}O_3$, sestave v trdni raztopini $KTaO_3$ s feroelektrikom $KNbO_3$. Material se v literaturi omenja kot kandidat za uporabo v mikrovalovnih elektronskih aplikacijah.

Plasti smo pripravili z refluksom kalijevega acetata in etoksidov obeh kovin prehoda v 2-metoksietanolu. S spektroskopijo podaljšane fine strukture rentgenske absorpcije smo spremljali strukturo solov po različnih časih refluksa. Ugotovili smo, da se struktura monomernih molekul Ta alkoksida ne spreminja, medtem ko dimerne molekule Nb alkoksida s časom preraščajo v oligomerne oblike. Povezavo med K in obema kovinama prehoda preko kisika smo zaznali v vseh solih, vendar število K sosedov v Nb okolici narašča s časom refluksa ter se ustali šele po 24 h refluksa.

Nastanek povezav med kalijem ter obema kovinama prehoda ugodno vpliva na kristalizacijo plasti $KTa_{0,6}Nb_{0,4}O_3$ na korundnih podlagah. Enofazne perovskitne plasti smo uspešno pripravili z nanosom solov po 24 h refluksu ter segrevanjem pri 900°C, medtem ko so bile plasti, pripravljene iz solov refluktiranih 1 h, vedno večfazne in so imele heterogeno mikrostrukturo. Prav tako so se z daljšim časom refluksa izboljšale tudi dielektrične lastnosti. Napetostna prilagodljivost plasti pripravljenih iz solov refluktiranih 24 h, izmerjena pri sobni temperaturi, 1 MHz in polju 92 kV/cm, ima vrednost 3.8.

Ugotovili smo, da je dielektričnost $KTa_{0,6}Nb_{0,4}O_3$ plasti pripravljenih iz solov refluktiranih 24 h, močno frekvenčno odvisna in se zniža iz 2430 pri 10 kHz na 590 pri 14.5 GHz. Relaksorsko obnašanje smo potrdili z opisom eksperimentalnih podatkov s pomočjo Vogel-Fulcherjevega zakona. Kljub temu da omenjeno obnašanje in z njim povezanim visoke dielektrične izgube omejujejo uporabnost plasti $KTa_{0.6}Nb_{0.4}O_3$ pripravljenih iz raztopin v mikrovalovnih komponentah, bi lahko nadaljnje raziskave lastnosti plasti v povezavi z opaženimi nano-metrskimi heterogenostmi v solih, pripeljale do izboljšanja funkcijskih karakteristik.

Abbreviations

A	=	constant in Cochran law
a	=	cubic lattice parameter
C	=	Curie-Weiss constant
C	=	capacitance
D	=	diffusion coefficient
d_{50}	=	median particle size
E	=	Young's modulus
E	=	electric field
E_c	=	coercive field
E_a	=	activation energy
F_0	=	resonant frequency
f	=	technical frequency
f	=	oscillator strength
$f_{(l00)}$	=	Lotgering factor
g	=	strength of the central mode
h	=	thickness
I	=	integral intensity of the peak in the XRD pattern
k	=	wave vector
k	=	Boltzmann constant
m	=	mass
N	=	complex index of refraction
n	=	real part of the index of refraction
N	=	average number of the atomic species
n	=	tunability
P	=	polarization
P_r	=	remanent polarization
P_s	=	spontaneous polarization
P_0	=	ratio between the sum of the integral intensities corresponding to the (l00) family and the sum of the integral intensities of all the peaks in the XRD pattern of the non-oriented sample.
$P_{(l00)}$	=	ratio between the sum of the integral intensities corresponding to the (l00) family and the sum of the integral intensities of all the peaks in the XRD pattern of the oriented sample.
p	=	porosity
Q	=	quality factor
q	=	charge
R	=	normal reflectivity

r = distance
S_0^2 = amplitude-reduction factor
s = gap
T = temperature
T_C = Curie point
T_f = freezing temperature
T_{max} = temperature of the permittivity maximum
T_0 = Curie-Weiss temperature
T_1 = temperature when the quantum fluctuations become important
t = complex transmission function
$\tan\delta$ = dielectric losses
U = voltage
u = strain

α = linear thermal expansion coefficient
β = coefficient of the dielectric non-linearity
Γ_{CM} = frequency of the central mode
γ_{LOj} = damping of the j-th longitudinal optic mode
γ_{TOj} = damping of the j-th transverse optic mode
ΔE_0 = energy shift
$\Delta\varepsilon_j$ = dielectric strength of the j-th optic mode
ΔG^*_{hetero} = energy needed for heterogeneous nucleation
ΔG^*_{homo} = energy needed for homogeneous nucleation
δ = standard deviation
ε^* = complex dielectric permittivity
ε_b = temperature independent part of the permittivity
ε' = real part of the dielectric permittivity
ε'' = imaginary part of the dielectric permittivity
ε_0 = vacuum permittivity
ε_∞ = high-frequency permittivity
θ = diffraction angle
θ = contact angle
κ = imaginary part of the index of refraction
ν = Poisson's ratio
ρ = density
ρ_{rel} = relative density
ρ_{teo} = theoretical density
ω = radial frequency
ω_{LOj} = frequency of the longitudinal optic mode
ω_{TOj} = frequency of the transverse optic mode
σ = stress
σ^2 = Debye-Waller factor
Ω_i = mode-plasma frequency

Ω_{TOT}	=	overall plasma frequency
ω_0	=	attempt frequency
AC	=	alternating current
BST	=	$(Ba,Sr)TiO_3$
CM	=	central mode
CSD	=	chemical solution deposition
DC	=	direct current
DR	=	dielectric resonator
DTG	=	differential thermogravimetry
DTA	=	differential thermal analysis
EDXS	=	energy-dispersive-X-ray spectroscopy
EELS	=	electron-energy-loss spectroscopy
EGA	=	evolved-gas analysis
EXAFS	=	extended X-ray-absorption fine-structure spectroscopy
IR	=	infrared
KTN	=	$K(Ta,Nb)O_3$
KNN	=	$(K,Na)NbO_3$
LO_j	=	*j*-th longitudinal optic mode
MBE	=	molecular beam epitaxy
MOCVD	=	metal organic chemical vapor deposition
MW	=	microwave
PLD	=	pulsed-laser deposition
PLZT	=	$(Pb,La)(Zr,Ti)O_3$
PMN	=	$Pb(Mg_{1/3}Nb_{2/3})O_3$
PMN-PT	=	$Pb(Mg_{1/3}Nb_{2/3})O_3$-$PbTiO_3$
PNR	=	polar nanoregions
PZT	=	$Pb(Zr,Ti)O_3$
RF	=	radio frequency
SM	=	soft mode
TEM	=	transmission electron microscope
TG	=	thermogravimetry
TO_j	=	*j*-th transverse optic mode
XRD	=	X-ray diffraction

1 Introduction

The first chapter of the thesis is divided into two parts. In the first, the physical aspects of the ferroelectrics and related materials are presented, including their applicability in microwave devices. In the second part, the processing-related issues of the $KTaO_3$ and $K(Ta,Nb)O_3$ ceramics and thin films are described.

1.1 Ferroelectrics and Related Materials

1.1.1 Ferroelectrics and Relaxors

Ferroelectrics are polar materials with at least two equilibrium orientations of the spontaneous polarization P_s in the absence of an external electric field at given temperature. Direction of the spontaneous polarization can be switched between these states by an external electric field E. They are distinguished by the strong nonlinear electric field dependence of the polarization, i.e., ferroelectric hysteresis loop, shown in Figure 1.1a. The zero-field polarization is called the remanent polarization P_r, and the field necessary to bring the polarization to the zero value is called the coercive field E_c.

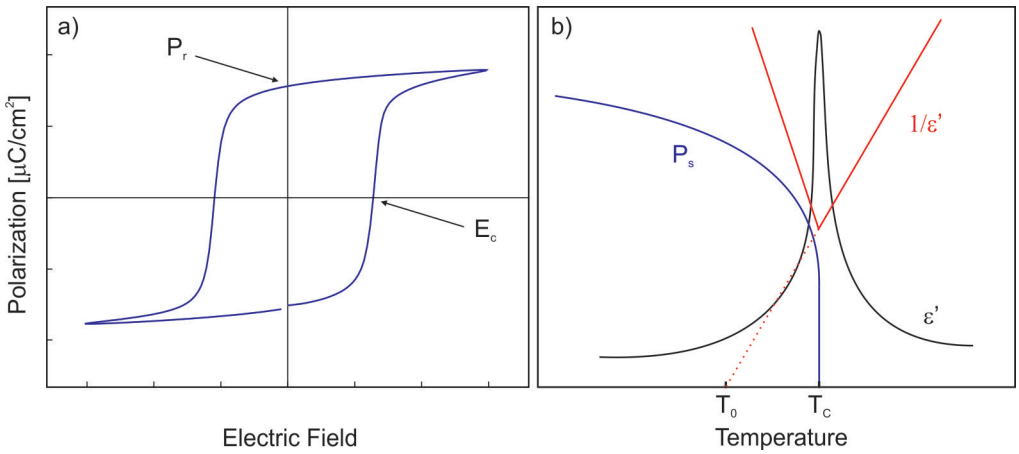

Figure 1.1: a) Typical ferroelectric (P-E) hysteresis loop. Remanent polarization P_r and coercive field E_c are marked. b) Schematic temperature dependence of the dielectric permittivity ε', inverse permittivity $1/\varepsilon'$ and spontaneous polarization P_s of a first-order ferroelectric. The T_0 and T_C are the Curie-Weiss temperature and Curie point, respectively.

The majority of ferroelectrics undergo a structural phase transition from the high-temperature paraelectric phase into a lower-symmetry, low-temperature, ferroelectric phase, which is associated with the peak in dielectric permittivity ε'.[i] The temperature of the phase transition is called the Curie point T_C. Above the Curie point the permittivity

[i] Strictly valid below ~100 GHz.

increases with decreasing temperature according to the Curie-Weiss law, as shown in Figure 1.1b:

$$\varepsilon' = \varepsilon_b + \frac{C}{T - T_0}, \tag{1.1}$$

where ε_b is the temperature-independent part of the permittivity, C is the Curie constant and T_0 is the extrapolated Curie-Weiss temperature ($T_0 \leq T_C$). Ferroelectrics are characterized by an exceptionally high permittivity, especially in the vicinity of T_c, which can reach values of ~10^5.

The paraelectric-ferroelectric phase transition can be classified into:

- first-order, in which the spontaneous polarization vanishes to zero discontinuously (e.g., $BaTiO_3$),
- second-order, in which the spontaneous polarization vanishes continuously (e.g., $LiNbO_3$).

In terms of the phase-transition character the ferroelectrics can be divided into:

- displacive, in which permanent dipole moment and spontaneous polarization appear when the material is cooled through the Curie point (e.g., $BaTiO_3$),
- order-disorder, where the permanent dipole moments exist in the unit cells already above the Curie point but because of their random orientation the spontaneous polarization is zero; on cooling through the Curie point they become more ordered and the spontaneous polarization appears (e.g., KH_2PO_4).

Most of the ferroelectric materials of practical interest, such as $BaTiO_3$, $Pb(Zr,Ti)O_3$ (PZT), $(K,Na)NbO_3$ (KNN), etc., are of the displacive type. However, as discussed in the Appendix, these are only the limiting cases and real materials often exhibit elements of both [1,2].

Many of the useful ferroelectric materials are in fact solid solutions. Some of them, such as $Pb(Mg_{1/3}Nb_{2/3})O_3$ (PMN), $(Pb,La)(Zr,Ti)O_3$ (PLZT), $(K,Na,Sr)(Nb,Ti)O_3$ etc. are characterized by a broad and strongly frequency-dependent peak of dielectric permittivity ε' (Figure 1.2a). These are called relaxors. The common feature of all oxide relaxors is compositional disorder, i.e., a heterogeneous distribution of the ions on the crystalographically equivalent sites. Relaxor behavior was observed in the perovskites with a B-site disorder of the heterovalent ions (PMN), in non-stoichometric solid solutions with A-site vacancies (PLZT), as well as in homovalent solid solutions, such as $Ba(Ti,Zr)O_3$. In their paraelectric state the permittivity increases with decreasing temperature according to the Curie-Weiss law (Equation (1.1), Figure 1.2a). At the Burns temperature T_B, the inverse permittivity $1/\varepsilon'$ starts to deviate from the linear temperature dependence and the ergodic relaxor state appears. The source of this peculiar behavior are the polar nanoregions (PNRs), whose relaxation dynamics are mainly governed by dipole reversal (flipping) and a fluctuation of their volume (breathing), both with a wide distribution of the relaxation times [3]. On further cooling, the dynamics of the polar PNRs slows down tremendously and the distribution becomes extremely wide. At the freezing temperature T_f the longest relaxation time diverges and the non-ergodic relaxor state appears [4,5]. The size of the PNRs below T_f is typically of the order of 5–10 nm.

Even though the presence of the compositional disorder seems to be a universal property of relaxors, its correlation to the PNRs is still not completely understood [6].

Slowing down of the PNRs dynamics is associated with the appearance of the frequency-dependent permittivity maximum, which in contrast to the ferroelectrics is not associated with the structural phase transition. However, the long-range ferroelectric order can be induced by the application of an electric field (e.g., PMN), or in some cases the spontaneous transition to the ferroelectric state takes place (e.g., PMN-PT) [6,7].

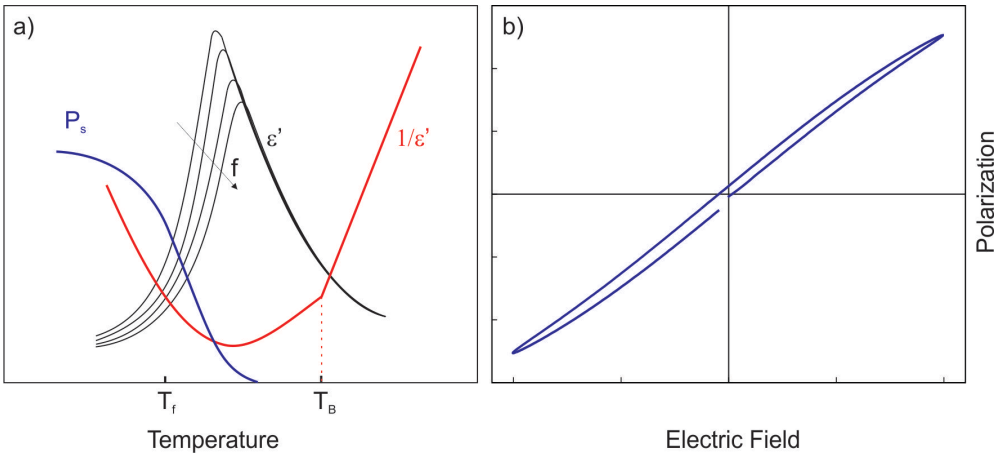

Figure 1.2: a) Schematic temperature dependence of the permittivity *ε'*, inverse permittivity *1/ε'* and spontaneous polarization P_s of the relaxor. An arrow is indicating the increase of the frequency. b) Slim relaxor *P-E* hysteresis loop.

Slim *P-E* loops are distinctive for relaxors and the spontaneous polarization P_s may persist far above the temperature of the permittivity maximum T_{max} (Figure 1.2). The T_{max} is connected to the frequency through the Vogel-Fulcher law [8]:

$$\omega = \omega_0 \exp\left(-\frac{E_a}{k(T_{max} - T_f)}\right), \tag{1.2}$$

where E_a is the activation energy, k is the Boltzmann constant[i] and T_f is the freezing temperature.

Different properties of ferroelectric and relaxor materials have been exploited in a wide range of devices, such as sensors, actuators, micro-electro-mechanical systems (MEMS), storage devices, etc. In addition to the already-established technologies, new devices are emerging in which ferroelectrics-based materials are expected to play an important role in the near future, for instance electro-caloric cooling and electronically tunable devices for wireless communication systems [9-11].

1.1.2 Ferroelectrics in Microwave Devices

Ferroelectric materials are gaining importance in the field of microwave (MW) devices and ferroelectric varactors have been realized in a number of components, such as phase shifters, tunable filters, impedance matching networks, etc. [12]. In comparison with the semiconductor and MEMS varactors, the ferroelectrics are characterized by a high tuning

[i] $k = 8.617 \times 10^{-5}$ eV / K

speed, relatively low dielectric losses (especially compared to semiconductors at higher frequencies), good reliability and low costs [13]. Displacive ferroelectrics are mainly considered for the purpose.

Their main functional property is a strong electric field dependence of the dielectric permittivity. It is characterized by the tunability n, defined as the ratio between the permittivity at zero applied field $\varepsilon'(0)$ and the permittivity at non-zero field $\varepsilon'(E)$:

$$n = \frac{\varepsilon'(0)}{\varepsilon'(E)}, \tag{1.3}$$

and the relative tunability is defined as:

$$n_r = \frac{\varepsilon'(0) - \varepsilon'(E)}{\varepsilon'(0)} = 1 - \frac{1}{n} \tag{1.4}$$

In the vicinity of the Curie point T_C the dielectric response of ferroelectrics can be described in terms of the Landau phenomenological theory, which is based upon a series expansion of the Helmholtz free energy with respect to the macroscopic polarization P. In the paraelectric phase, taking the first two terms of this expansion, the electric-field-dependent permittivity $\varepsilon'(E)$ has the form of [14]:

$$\varepsilon'(E) = \varepsilon'(0)\frac{1}{1 + 3\beta\varepsilon'(0)\varepsilon_0 P^2}, \tag{1.5}$$

where β is the phenomenological coefficient of the dielectric non-linearity and ε_0 is the vacuum permittivity.[i] Combining Equations (1.3) and (1.5) the tunability n reads as:

$$n = 1 + 3\beta\varepsilon'(0)\varepsilon_0 P^2 \approx 1 + 3\beta(\varepsilon'(0)\varepsilon_0)^3 E^2. \tag{1.6}$$

The above equation is valid in the limit of small fields ($n_r << 1$). In the case of higher fields, when $n >> 1$, it is modified to [14]:

$$n \approx 3\beta^{1/3}\varepsilon'(0)\varepsilon_0 E^{2/3}. \tag{1.7}$$

In any case, the above two equations indicate that in order to obtain high tunability values the material should possess high zero-field permittivity $\varepsilon'(0)$ and high coefficient of the dielectric non-linearity β. The respective values of typical microwave ferroelectrics are given in Table 1.1. As a rule of thumb for the applicability the material should have the tunability values above ~1.5 ($n_r \geq 0.3$) [14].

Another important property of the ferroelectric material is the dielectric losses $\tan\delta$, defined as the ratio between the imaginary ε'' and real ε' parts of the frequency-dependent complex dielectric permittivity $\varepsilon^*(\omega) = \varepsilon'(\omega) - i\varepsilon''(\omega)$:

$$\tan\delta = \frac{\varepsilon''}{\varepsilon'}, \tag{1.8}$$

which are often expressed as a quality factor $Q = 1/\tan\delta$. To avoid the hysteresis and

[i] $\varepsilon_0 = 8.85 \times 10^{-12}$ F/m

dielectric losses associated with the absorption of the domain walls, the ferroelectrics are usually considered in their paraelectric phase [14].

Table 1.1: Permittivity ε', dielectric losses $\tan\delta$, and non-linear coefficient β of typical microwave ferroelectrics in their single-crystal form.

Material	T [K]	ε'	$\tan\delta$	β [J C^{-4} m^5]	Ref.
$SrTiO_3$	5.4	~25,000$^+$	3.4 x 10^{-3} (3 GHz)	8 x 10^9	[14,15]
$Ba_{0.65}Sr_{0.35}O_3$	300	~3100	0.02 (10 GHz)	2.8 x 10^9	[14,16]
$KTaO_3$	5.4	~4500$^+$	4.2 x 10^{-5} (3 GHz)	9 x 10^9	[15,17]

$^+$Low-temperature plateau value

The microwave dielectric losses of a displacive ferroelectric in the paraelectric state are the sum of the intrinsic and extrinsic contributions. The main mechanisms of the intrinsic losses are:

- the three-quantum contribution (interaction of one photon with two phonons),
- the four-quantum contribution (interaction of one photon with three phonons).

The presence of the external electric field breaks the symmetry of the material and additional loss-mechanisms appear:

- the quasi-Debye contribution (relaxation of the phonon distribution function),
- the transformation of the microwave signal into an acoustic wave.

The intrinsic mechanisms fix the lower-losses threshold for the specific ferroelectric material. However, with the exception of high-quality single crystals, the losses are usually governed by the extrinsic contributions:

- the losses due to charged defects (dielectric activation of acoustic waves due to the defects motion)
- the losses due to local polar regions (quasi-Debye mechanism in the polar regions surrounding defects),
- the Curie-von-Schweidler relaxation.

Even though there are several theoretical attempts to describe the extrinsic losses in paraelectric materials, more research is needed to completely understand the microwave loss-phenomena in ferroelectric materials [12-14].

Ferroelectrics can be employed in microwave devices as single crystals, ceramics, thick films, or thin films. While the first usually have excellent dielectric properties, their production is expensive, and ceramics represent a cost-efficient technological alternative. However, the application of relatively thick bulk materials requires high tuning voltages of the order of kV.

In recent years the main driving force for the development of the field has been thin-film technology, which enables easier integration, the use of lower bias voltages and substantial miniaturization of the microwave components. The desired properties of the thin-film varactors are a high tunability ($n \geq 1.5$), low dielectric losses ($\tan\delta \leq 0.01$) and low fabrication costs on an inexpensive substrate. To achieve high performance the substrate should have a low permittivity and low microwave dielectric losses. Alternatives include single crystals of MgO, $LaAlO_3$, different cuts of sapphire and the low-cost polycrystalline alumina (Table 1.2).

Table 1.2: Room-temperature dielectric properties of the substrates typically used in thin films for microwave devices [12,13].

Substrate	ε'	$\tan\delta$ (10 GHz)
MgO	9.8	$< 2 \times 10^{-5}$
$LaAlO_3$	24	3×10^{-4}
(0001) sapphire	11.5	$< 5 \times 10^{-5}$
alumina	9.8	$\sim 10^{-4}$

1.1.3 Incipient Ferroelectrics

An important group of materials that has been considered for microwave applications is the incipient ferroelectrics, especially $SrTiO_3$ and $KTaO_3$. They are characterized by an increasing permittivity with decreasing temperature (Figure 1.3), which at higher temperatures obeys the Curie-Weiss law (Equation (1.1). However, the ferroelectric phase does not appear, either because the extrapolated Curie-Weiss temperature T_0 lies below 0 K, or quantum fluctuations suppress the long-range ordering. The latter materials are a subgroup of the incipient ferroelectrics, called quantum paraelectrics [18]. In any case, the permittivity saturates at low temperatures according to the Barrett equation [19]:

$$\varepsilon' = \varepsilon_b + \frac{C}{\frac{T_1}{2}\coth\left(\frac{T_1}{2T}\right) - T_0}, \tag{1.9}$$

where, T_1 denotes the temperature where the quantum fluctuations start to play a role and ε_b is the temperature-independent part of the permittivity. Note that the above equation becomes the Curie-Weiss law in the $T >> T_1$ limit. Typical values of the low-temperature permittivity are between 10^2 and 10^4 (Table 1.1).

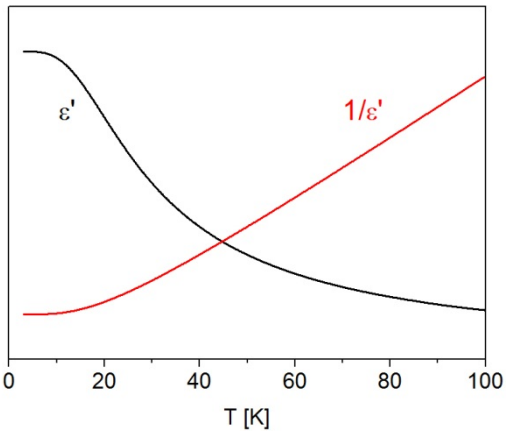

Figure 1.3: Schematic temperature dependence of the permittivity ε' and inverse permittivity $1/\varepsilon'$ of the incipient ferroelectrics.

Dielectric permittivity of the incipient ferroelectrics is completely described by the contribution of the polar optic phonons. Their behavior is purely displacive and the permittivity ε' increase is driven by the softening (decrease of frequency) of the lowest-frequency polar optic mode (soft mode, SM) only (see Appendix). No dielectric relaxation is present below the soft-mode frequency ω_{SM}, lying in the THz frequency

range, and in the absence of defects their microwave dielectric losses tanδ are very low, primarily caused by the intrinsic multi-phonon mechanisms.

1.1.3.1 $KTaO_3$

$KTaO_3$ is one of the prototype incipient ferroelectrics. It stays in the cubic structure with the space group $Pm\bar{3}m$ at all temperatures and the permittivity reaches a low-temperature value of ~4500 [20]. The typical parameters of the Barrett equation (Equation (1.9)) are collected in Table 1.3.[i]

Table 1.3: Parameters of the Barrett equation for the $KTaO_3$ single crystal ((100) direction) [21].

C	T_1	T_0	ε_b
54500 K	57 K	13.1 K	47.5

$KTaO_3$ has a slightly larger non-linear factor β than $SrTiO_3$; still it is less tunable because of the lower permittivity value (Table 1.1). Its advantage lies in the very low intrinsic microwave dielectric losses tanδ. Geyer et al. [15] measured the $KTaO_3$ single crystal at 3 GHz and obtained tanδ values of 4.2 x 10^{-5}, 8.9 x 10^{-5} and 1.4 x 10^{-4}, measured at 5.4 K, 77 K and 300 K, respectively (Figure 1.4).

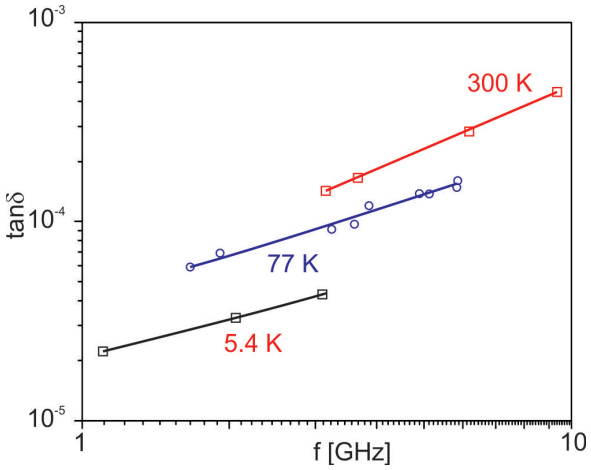

Figure 1.4: Frequency dependence of the dielectric losses tanδ of the $KTaO_3$ single crystal measured at different temperatures. After Geyer et al. [15].

$KTaO_3$ has also been studied as a model ABO_3-type ferroelectric compound, whose crystal lattice is highly polarizable. Even extremely small amounts of impurities or lattice defects, forming re-orientable dipolar entities inside the $KTaO_3$ crystal lattice, have a profound effect on its dielectric properties [22]. In the limit of small concentrations (of the order of 0.01 at. %) the PNRs formed around the polar entities do not interact with each other. The corresponding dielectric relaxations are observed in the radio-frequency (RF) and MW ranges as the peaks in the dielectric losses tanδ, whose frequency-dependent maximum temperature obeys the Arrhenius law:

[i] Parameters slightly vary in different reports.

$$\omega = \omega_0 \exp\left(-\frac{E_a}{kT_{max}}\right). \quad (1.10)$$

In fact, low-temperature relaxation was observed even in the "nominally pure" $KTaO_3$ single crystals, with the $\tan\delta$ peak at ~45 K and 1 kHz (Table 1.4) [20]. Its exact origin is difficult to determine; however, it is most probably related to the presence of Li-impurities [22-25]. The parameters of the Arrhenius-type relaxations of the $KTaO_3$ single crystals doped with several transition-metal ions are collected in Table 1.4.

Table 1.4: Temperature of the $\tan\delta$ maximum measured at 1 kHz, Arrhenius activation energy E_a and attempt frequency ω_0, of the $KTaO_3$ single crystals doped with various ions. The concentration of all the dopants is between 0.01 at.% and 0.1 at.%.

Dopant	T_{max} (1kHz) [K]	E_a [meV]	ω_0 [s^{-1}]	Ref.
"pure"	48	86*	4.7×10^{13}	[23]
Mn^{2+}	55	110	5×10^{13}	[23]
Fe^{3+}	185	340	3.3×10^{13}	[23]
Fe^{2+}	150	300	1×10^{14}	[23]
Co^{2+}	186	360	4×10^{13}	[26]
Ni^{3+}	193	400	1.5×10^{13}	[26]

*Values vary in different reports from ~70 meV – 90 meV and it was even suggested that the peak is composed of two individual peaks.

If the concentration of the polar entities inside the crystal lattice is increased the PNRs may start to interact, and the relaxor-like features are observed in the dielectric spectra. Typical examples of such behavior are $KTaO_3$ single crystals doped with 0.3 at.% of Mn^{2+} or with 1 at.% of Li^+. In the case of Nb^{5+} doping, even the long-range ferroelectric order is established above ~2 at.%. The exact behavior depends on the type of the dopant [22,27].

1.1.3.2 Dielectric Grain Size Effect in Incipient Ferroelectric Ceramics

Because of the absence of ferroelectric domains, the incipient ferroelectric ceramics are convenient for studies of the grain-size effect on the intrinsic dielectric permittivity value. In ferroelectrics and similar materials[i] the effect can be rather important, and takes place when the grain size is below ~1–10 μm. Its explanation is far from being trivial, mainly because different sintering techniques are employed, such as conventional sintering, pressure-assisted sintering, two-step sintering and spark-plasma sintering, resulting in a different defect-state of the investigated ceramics. Nevertheless, the effect has been mainly attributed to the presence of the low-permittivity layer at/near the grain boundary [28].

In fact the most profound grain size effect of all the ferroelectrics-based ceramics was observed in $SrTiO_3$. The low-temperature permittivity ε' value has never exceeded ~10,000, which is more than half the value of the averaged response of the $SrTiO_3$ single crystals (~25,000) [29-31]. The plateau value strongly decreases with decreasing grain

[i]The materials exhibiting so-called colossal permittivity, such as $CaCu_3Ti_4O_{12}$, are not considered here because the origin of high ε' values is not intrinsic (of lattice contribution), but it arises from the Maxwell-Wagner-type contributions.

size, reaching 700 in the case of spark-plasma-sintered ceramics, with a grain size of ~80 nm. Petzelt and co-workers [29,30,32] analyzed $SrTiO_3$ ceramics with different grain sizes using THz, IR and Raman spectroscopies and combined the data with the literature results on high-resolution and analytical TEM investigations of ceramics and bi-crystals, as well as with the first-principle calculations of the grain-boundary structure [33-35]. They explained the remarkable effect by the universal 3-layer structure of the $SrTiO_3$ grains. The grain boundary is ~1 nm thick, has a permittivity ε' value of ~10, and is charged due to the O-deficiency. The middle layer has an ε' value of ~500 and is polarized with the local dipole moment normal to the grain boundary, which gradually decreases towards the center of the grain. Its thickness increases from ~3 nm to ~6 nm in the temperature range from 300 K to 5 K. The appearance of this layer was explained by the migration of different charged defects during the high-temperature processing in order to compensate for the charge of the grain boundary. The core of the grains was assumed to be the same as in single crystals. Further investigations on other incipient ferroelectric ceramics are needed.

1.1.3.3 Strain-Induced Ferroelectricity in Thin Films of Incipient Ferroelectrics

Even though the incipient ferroelectrics stay in their paraelectric phase at all temperatures, they are very sensitive to any perturbations of the crystal lattice and the ferroelectric phase was experimentally induced by:

- doping [22,36],
- external electric field (proven for $SrTiO_3$ only) [37],
- isotope exchange of ^{16}O with ^{18}O (proven for $SrTiO_3$ only) [38],
- uniaxial stress [39,40],
- or, in the case of thin films, by biaxial strain [41,42].

There are also theoretical predictions of the ferroelectricity in nanosized incipient ferroelectrics. Using a first-principles-based calculation, Akbarzadeh et al. [43] predicted that the ultrathin 2.8-nm-thick (100) oriented $KTaO_3$ films are ferroelectric. Additionally, using the Landau-Ginsburg-Devonshire phenomenological approach, Morozovska and co-workers[44] observed that the ferroelectric phase could be stable in the $KTaO_3$ nanorods with a diameter less than 5–20 nm, even at room temperature.

The residual stresses in thin films of incipient ferroelectrics can have different origins, such as defects, lattice mismatch between the film and the substrate, the mismatch in thermal expansion coefficients, etc. [45].[i] The last two contributions arise from the presence of the substrate and distinguish thin films from bulk materials. Usually, they prevail and the total in-plane stress σ_{tot} can be expressed as:

$$\sigma_{tot} = \sigma_{epi} + \sigma_{therm}, \tag{1.11}$$

where the epitaxial σ_{epi} and thermal σ_{them} stresses are defined as:

[i] In polycrystalline thin films the so-called “growth stress” may also arise during the crystallization. It might be tensile or compressive, however, it is difficult to evaluate it, and the films are often considered to be in the zero-stress state before cooling from the crystallization temperature.

$$\sigma_{epi} = \frac{E}{1-\nu} \cdot u_{epi} = \frac{E}{1-\nu} \cdot \left(\frac{a_s - a_f}{a_f} \right), \tag{1.12}$$

$$\sigma_{therm} = \frac{E}{1-\nu} \cdot u_{therm} = \frac{E}{1-\nu} \cdot \left((\alpha_f - \alpha_s) \cdot (T_{cry} - T) \right). \tag{1.13}$$

In the above equations, E is the Young's modulus and ν is the Poisson's ratio of the film, a_s and a_f are the in-plane lattice parameters of the substrate[i] and of the unstrained film, while α_f and α_s are their respective thermal expansion coefficients. The u_{epi} and u_{therm} are the epitaxial and thermal strains, respectively. The T_{cry} is the crystallization temperature. The in-plane biaxial stress in thin films is usually isotropic [46].

The influence of the biaxial epitaxial strain [47][ii] u on the (100) oriented single-domain epitaxial $SrTiO_3$ thin films was theoretically addressed by Pertsev at al. [48,49] using the Landau-Ginsburg-Devonshire theory. They showed that a large enough tensile or compressive strain should induce ferroelectricity, with the polarization lying in-plane and out-of-plane, respectively, with the Curie point depending on the strain magnitude (Figure 1.5). A very similar result was obtained later, also by first-principles studies and the thus obtained theoretical strain interval, in which the film should still be paraelectric, is -0.22 % ≤ u ≤ 0.16 % [50].[iii]

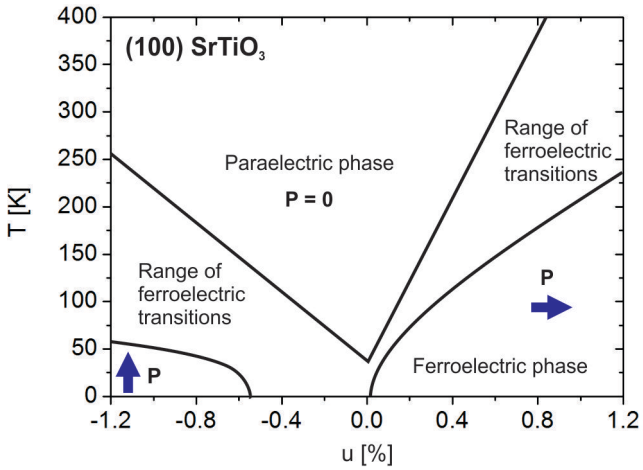

Figure 1.5: Schematic presentation of the temperature – in-plane biaxial strain u phase diagram of the epitaxial single-domain (100) $SrTiO_3$ thin films obtained from the thermodynamic analysis. The arrows indicate the expected direction of the polarization: in-plane and out-of-plane for the tensile and compressive strains, respectively. The ranges of the ferroelectric transitions are due to the spread of the reported coefficients used in the calculation [48,51].

Strain-induced ferroelectricity was experimentally confirmed in molecular-beam-epitaxy-derived (MBE) (100) $SrTiO_3$ films on (110) $DyScO_3$ substrates by Haeni et al. [51]. The XRD analysis showed that the 50-nm-thick films were under 0.8 % tensile epitaxial strain. The authors observed the maximum of the in-plane dielectric permittivity

[i] Cubic crystal structure (or pseudo-cubic) of the film and the substrate are assumed.

[ii] In epitaxial thin films strain is often considered because it can be evaluated directly from the XRD measurements. Besides, in the case of very high strains the Hook's law might not be completely valid anymore.

[iii] The convention is that the tensile and compressive strains (stresses) are denoted with positive and negative signs, respectively.

ε' at ~293 K, measured at 10 GHz. Employing broadband dielectric spectroscopy, including the soft-mode analysis, the in-plane ferroelectricity was also confirmed by other groups in ~100-nm-thick films on $DyScO_3$, grown by pulsed-laser deposition (PLD) [52,53]. Interestingly, Wördenweber and co-workers [52] showed that the ferroelectricity can be induced in the (100) $SrTiO_3$ films deposited on a CeO_2-buffered $(1\bar{1}02)$ (r-cut) sapphire substrate, which do not show an epitaxial relationship with the substrate. Instead, they explained it with the tensile thermal strain arising from the thermal expansion coefficients' mismatch. The films with thicknesses in the range from 8 nm to 710 nm had a thickness-independent transition temperature at ~210 K.

Despite the theoretical and experimental evidence, the nature of the strain-induced ferroelectricity in $SrTiO_3$ thin films is still unclear. Biegalski et al. [54] prepared 50-nm-thick 1 % tensile strained (100) $SrTiO_3$ films on (101) $DyScO_3$ substrates using MBE. The ferroelectric-like polarization loops were obtained; however, the in-plane dielectric properties, measured from 500 Hz to 10 GHz, showed strong relaxor-like frequency dispersion. In addition, the diffusion of the Sc into the film, and thus the unintentional doping of the films, was observed.

Concerning the compressively strained $SrTiO_3$ films, the ferroelectricity was determined by means of piezo force microscopy (PFM) in ultrathin 3-nm-thick ~ -1.7 % strained film on (100) Si substrates, grown by the MBE method [55]. The question arises from the recent report of Nuzhnyy et al. [56], who analyzed 1.1 % compressively strained 17-nm-thick MBE-derived $SrTiO_3$ films on (110) $NdGaO_3$ substrate. Neither XRD, nor polarized IR spectroscopy provided evidence for the out-of-plane ferroelectric phase transition, which should appear according to the theory (Figure 1.5). The result is in agreement with Ref. [57] in which only relaxor-like behavior of the 60-nm-thick films with the T_{max} value ~150 K and slim polarization loops below 50 K was observed. Only a strongly stiffened soft mode was observed also in the case of PLD-derived (100) $SrTiO_3$ films on the (100) $La_{0.18}Sr_{0.82}Al_{0.59}Ta_{0.41}O_3$ substrates (0.9 % compressively strained) [58].

Surprisingly, room-temperature ferroelectricity was observed in the 100-nm-thick PLD-derived homoepitaxial (100) $SrTiO_3$ films with a $SrRuO_3$ top and bottom electrode [59,60]. The tetragonality[i] of the films increased with decreasing partial oxygen pressure during the deposition and the authors attributed the induced ferroelectricity to the presence of the vacancy-related defects. Recent papers report on studies of MBE-derived homo-epitaxial (100) $Sr_{1+x}TiO_{3+\delta}$ films, with x ranging from -0.2 to 0.25 [57,61]. A-site-deficient films showed strong first-order Raman scattering peaks on cooling below ~350°C, which is forbidden in the cubic paraelectric state. Importantly, the first-order Raman peaks were observed also at 10 K in the nominally stoichiometric $SrTiO_3$ films. The general conclusion is that all Sr-deficient and nominally stoichiometric $SrTiO_3$ thin films (authors claim that also single crystals) are to some extent relaxors. The polar nanoregions, with short-range correlation lengths, arise from the A-site non-stoichiometry. The role of the biaxial strain in the induced ferroelectricity observed in $SrTiO_3$ films is the stabilization of the long-range correlation between the pre-existing nanopolar regions.

[i]Defined as $c/a - 1$, where c and a are the out-of-plane and in-plane lattice constants of the film.

Much less data is available regarding the strain-induced ferroelectricity in epitaxial $KTaO_3$ thin films. Recently, Tyunina et al. [42] prepared by PLD 2.1 % compressively strained 9-nm-thick (100) $KTaO_3$ films on conductive (100) Nb-doped $SrTiO_3$ substrates. A ferroelectric phase transition as high as ~700 K was determined from the out-of-plane RF dielectric measurements and the optical index of refraction n. The epitaxial $KTaO_3$ films did not show any relaxor-like dielectric behavior. The result is in agreement with their first-principle analysis, which predicted that the paraelectric strain gap is -1.0 % ≤ $u_{epi} \leq 0.5$ %.

Despite the fact that the majority of the literature data on induced ferroelectricity in incipient ferroelectrics is focused on epitaxial films, it has been observed before also in polycrystalline $SrTiO_3$ thin films. Galt and co-workers [62] analyzed 550-nm-thick PLD-derived films on $LaAlO_3$ substrates. These films, with an in-plane grain size of ~50 nm, had the ferroelectric phase transition at ~160 K, as determined from the in-plane polarization-loop measurements. No explanation of its origin was given. Ostapchuk et al. [63] performed high-resolution soft-mode spectroscopy of three polycrystalline $SrTiO_3$ thin films prepared by metal organic chemical vapor deposition (MOCVD) and chemical solution deposition (CSD) on a c-sapphire substrate. All the films had an ~100 nm in-plane grain size and were under tensile strain. The MOCVD-derived film was fully (111) oriented, while the CSD-derived films showed a weak preferential (100) orientation. Their respective thicknesses were 290 nm and 360 nm (or 720 nm). The onset of the ferroelectric phase at ~125 K was unambiguously confirmed for the MOCVD film, while only strong soft-mode stiffening was observed in the CSD-derived films. The latter effect was more pronounced in thicker films, which was interpreted with the influence of the percolated and crack-type porosity along the grain boundaries (normal to the probe field direction).

1.1.4 Solid Solutions of Incipient Ferroelectrics with the Ferroelectrics

The applicability of incipient ferroelectrics in microwave devices is limited to cryogenic temperatures, where the permittivity is large enough to be efficiently tuned. To enhance the tunability at higher temperatures, the solid solutions of incipient ferroelectrics with ferroelectrics have been intensively studied. The most well-known is the solid solution of $BaTiO_3$ and $SrTiO_3$ (BST), whose Curie point, and consequently the permittivity and dielectric losses, can be tuned through the composition from 390 K down to 0 K [16]. Even though the dielectric losses $\tan\delta$ increase and the non-linearity β decrease with increasing Ba concentrations (Table 1.1), the BST films, for instance $Ba_{0.6}Sr_{0.4}TiO_3$, have already been employed in different room-temperature microwave devices. However, the search for alternative materials continues [13,14].

1.1.4.1 K(Ta,Nb)O_3

K(Ta,Nb)O_3 ($KTa_xNb_{1-x}O_3$, KTN) is a solid solution of $KTaO_3$ with $KNbO_3$ and is expected to show complete solubility in the whole compositional range [64-66]. Its Curie point can be varied by the Ta/Nb ratio from 708 K to 0 K; therefore, it represents a direct analogue to BST. The solid solution has four structural phases, i.e., cubic, tetragonal, orthorhombic and rhomobohedral. The Curie point and the temperature stability ranges of

the polar phases decrease with increasing Ta content (Figure 1.6), until $x \approx 0.9$, where only a single phase transition from cubic to rhombohedral phase is present. At $x \geq 0.992$ the ferroelectric phase transition is no longer observed [27]. Because of Nb off-center dynamics in [111] direction KTN is considered as a mixed displacive- and order-disorder ferroelectric [67,68]. The temperature dependence of the dielectric permittivity of the $KTa_xNb_{1-x}O_3$ single crystals of various compositions is shown in Figure 1.7 [66].

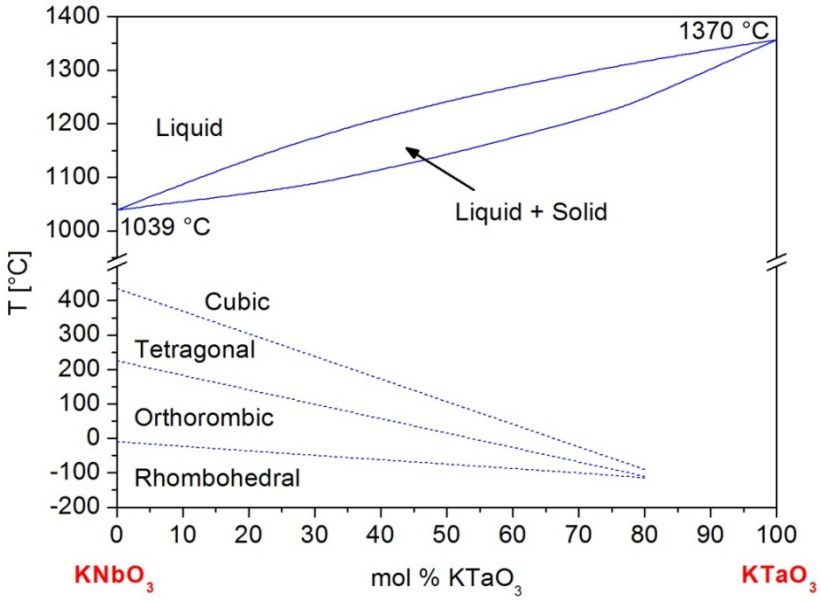

Figure 1.6: $KNbO_3$-$KTaO_3$ phase diagram. Dashed lines indicate transitions between the cubic, tetragonal, orthorhombic and rhomobohedral phases. After Reisman et al. [65] and Triebwasser et al. [64,66].

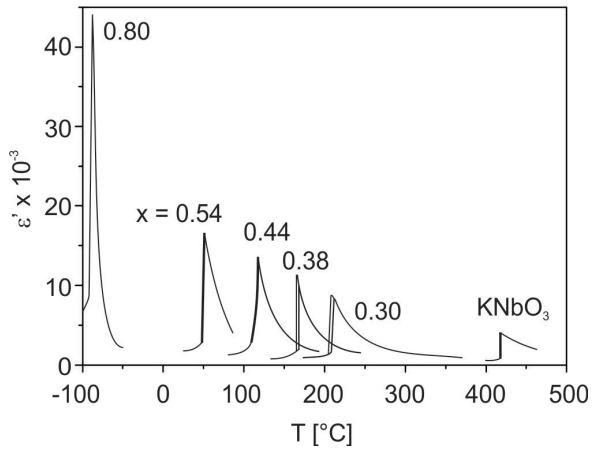

Figure 1.7: Temperature dependence of the dielectric permittivity ε' for the $KTa_xNb_{1-x}O_3$ solid solution for different compositions measured at 10 kHz. After Triebwasser [66].

Venkatesh et al. [23] evaluated the 1-MHz tunable properties of $KTa_{0.6}Nb_{0.4}O_3$ ceramics. The room-temperature tunability n of the hot pressed ceramics, which were in the cubic phase at room temperature, was 1.7 at 20 kV/cm, while the evaluated β factor was 3×10^9 J C^{-4} m^5. For comparison, the $Ba_{0.6}Sr_{0.4}TiO_3$ ceramics exhibit a tunability of 1.8 at the same applied field, and have a β factor of 3.2×10^9 J C^{-4} m^5 [8,24]. However, the permittivity value of the $KTa_{0.6}Nb_{0.4}O_3$ ceramics was strongly frequency dependent

(see Chapter 1.2.2).

1.2 Processing and Dielectric Properties of $KTaO_3$-Based Ceramics and Thin Films

1.2.1 $KTaO_3$ Ceramics

The phase diagram of Ta_2O_5-K_2O (K_2CO_3) in the whole compositional range was published by Reisman and co-workers (Figure 1.8) [69]. Four compounds with different K/Ta ratios were determined: KTa_5O_{13}, $K_2Ta_4O_{11}$, $KTaO_3$ and K_3TaO_4. The perovskite $KTaO_3$ phase melts at 1370°C. The temperature of the eutectic melting between $KTaO_3$ and K_3TaO_4 is 1090°C.

In a later study by Roth et al. [70] part of the diagram between Ta_2O_5 and $KTaO_3$ was found to be much more complicated, consisting of KTa_5O_{13}, $K_4Ta_{10}O_{27}$, $K_2Ta_4O_{11}$, two hexagonal phases, as well as four high-temperature tungsten-bronze-type compounds, whose composition may vary (Figure 1.9).

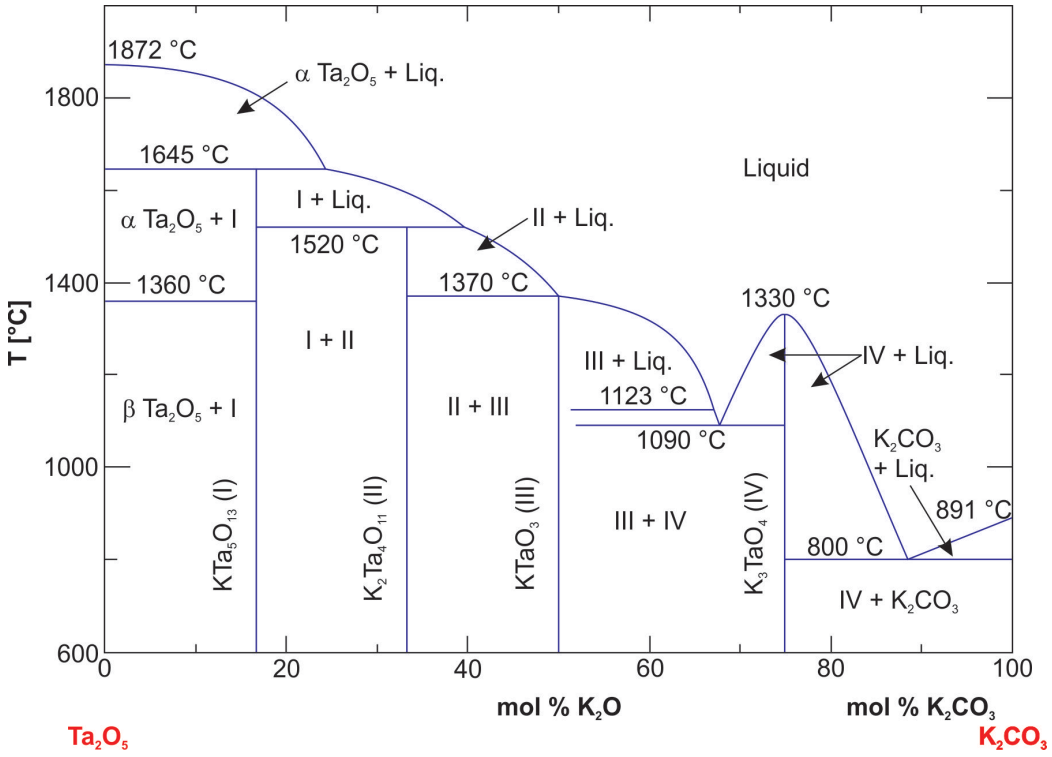

Figure 1.8: Ta_2O_5-K_2O (K_2CO_3) phase diagram. After Reisman et al. [69].

Even though $KTaO_3$ single crystals have been intensively studied since the 1960s the reports on ceramics have only recently started to emerge. The reasons for this scarcity of experimental data lie in the extremely demanding processing, often resulting in ceramics with secondary phases and low densities. Difficulties arise from:

- the hygroscopicity of the starting carbonate compound,
- the sublimation of potassium species at high processing temperatures [71],
- the very covalent character of the Ta–O bond, which inhibits the diffusion process (see Table 1.6).

While the first two are characteristic for all potassium- (alkaline-)based ferroelectric

materials, the high degree of the covalent bonding is specific to those containing Ta. It originates from the significant radial extension of the Ta *5d* orbitals, which then spatially overlap with the O *2p* orbitals [72,73].

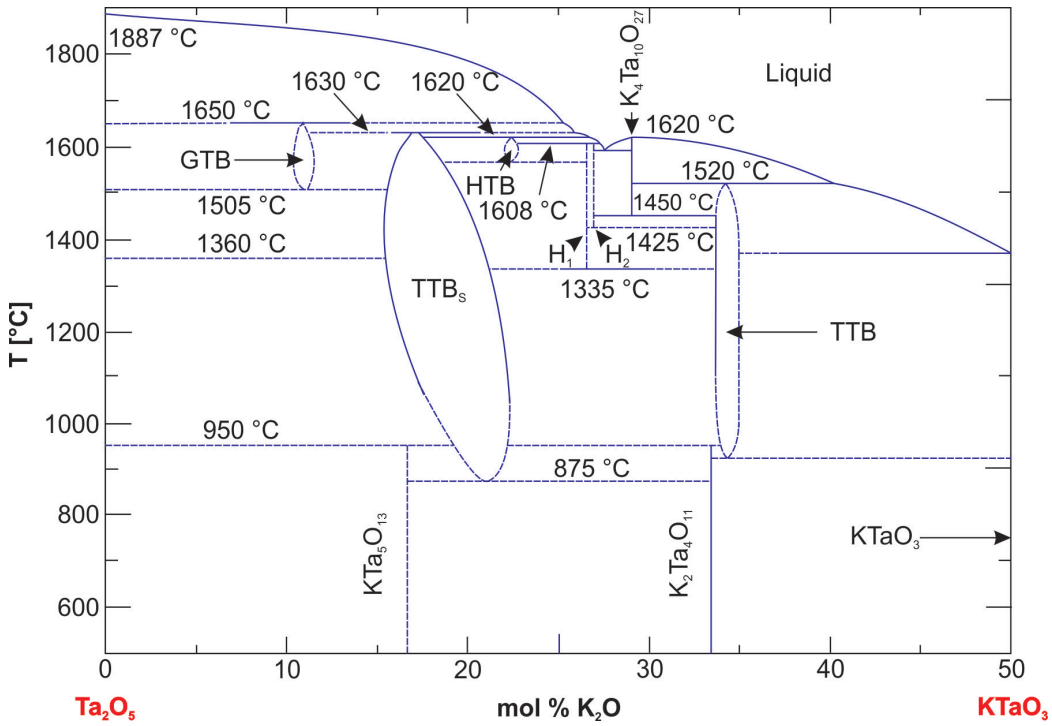

Figure 1.9: Ta_2O_5-$KTaO_3$ phase diagram. GTB – Gatehouse tungsten bronze at 89 % of Ta_2O_5; TTBs – tetragonal tungsten bronze with superstructure between 83.3 % and 80 % of Ta_2O_5; HTB – hexagonal tungsten bronze at 77.3 % of Ta_2O_5; H_1 – hexagonal phase at 73.85 % of Ta_2O_5; H_2 – hexagonal phase at 73.5 % of Ta_2O_5. TTB – tetragonal tungsten bronze near 66 % of Ta_2O_5 ($K_6Ta_{10.8}O_{30}$). After Roth et al. [70].

According to Axelsson and co-workers [71] the reaction between the K_2CO_3 and the Ta_2O_5 to a perovskite phase is a two-step process through an intermediate $K_2Ta_4O_{11}$ compound, which is achieved at ~900°C:

$$K_2CO_3 + 2Ta_2O_5 \xrightarrow{\sim 620°C} K_2Ta_4O_{11} + CO_2 \tag{1.14}$$

$$K_2Ta_4O_{11} + K_2CO_3 \rightarrow 4KTaO_3 + CO_2. \tag{1.15}$$

When they sintered the stoichiometric powder compacts at 1340°C in air, the obtained relative densities were ~77 %. The relative density was increased to 85 % by the addition of the K_2CO_3 excess into the pre-reacted $KTaO_3$ powder. The effect was attributed to the appearance of the liquid phase due to eutectic melting (Figure 1.8). Higher densities, i.e., 87 % and 90 %, were obtained by Chen et al. [74] and Tkach et al. [75], respectively, by sintering the stoichiometric powders at 1330°C and 1350°C. However, with the exception of Chen et al. [74] the presence of the kinetically stabilized $K_6Ta_{10.8}O_{30}$ phase (Figure 1.9) after the sintering of stoichiometric powder compacts was always observed. The XRD phase-pure perovskite ceramics were successfully prepared with the addition of the 5 % excess of K_2CO_3 [71,75].

The densification process was successfully enhanced with the addition of MnO_2[76,77] or Mn_2O_3[76]. Using 3 wt.% of the latter compound a relative density of 95 % was obtained after sintering at 1280°C [76]. The effect can be explained by the aliovalent substitution of the Mn^{2+}, Mn^{3+}, or Mn^{4+} on either the A- or B-site and the formation of vacancies on the A- or oxygen-site, respectively, resulting in the enhanced lattice diffusion. However, A- and B-site substitutions result in strongly modified dielectric properties (Chapter 1.1.3.1) [77-79].

The density of the single-phase ceramics was successfully increased to 92 % by Chen et al. [74], who employed isostatic hot pressing at 1310°C.

The dielectric properties of the $KTaO_3$ ceramics collected from the literature are shown in Table 1.5. The dielectric permittivity ε' of the $KTaO_3$ ceramics shows typical incipient ferroelectric behavior, as expected from single crystals. To the best of our knowledge broadband dielectric characterization, which would confirm the intrinsic nature of the permittivity behavior, has not been performed yet.

The values of the dielectric losses, which are higher than in the single crystals, are indicating some extrinsic mechanisms associated with the defects. Additional dispersion regions were observed in the $\tan\delta$ spectra of the ceramics and their intensity was found to be strongly processing dependent. They were attributed to the presence of impurities [74]. potassium deficiency [71,75], charged defects at the grain boundaries [71,74], or secondary phases [71,74,75].

Table 1.5: Low-temperature permittivity ε', dielectric losses $\tan\delta$, and measured frequency f of the $KTaO_3$ ceramics taken from the literature. Reported relative density ρ_{rel} and grain size are also given.

Grain size	$\rho_{rel.}$	ε'	$\tan\delta$	T	f	Ref.
1–8 μm	92 %	2000	0.01	5 K	100 kHz	[74]
~1 μm	85 %	3100	0.003	15 K	~1 GHz	[71]
6.5 μm	88 %	4000	0.008	10 K	100 Hz	[75]

1.2.2 $K(Ta,Nb)O_3$ Ceramics

Even though the KTN solid solution was reported to show complete solubility across the whole compositional range (Figure 1.6), Hill et al. [80] additionally studied the subsolidus phase relations. On the basis of the high 2θ angle XRD analysis of the samples prepared by the conventional solid-state and hydrothermal synthesis, they concluded that a significant immiscibility gap exists in the $K(Ta,Nb)O_3$ phase diagram and care should be taken during the processing (Figure 1.10).

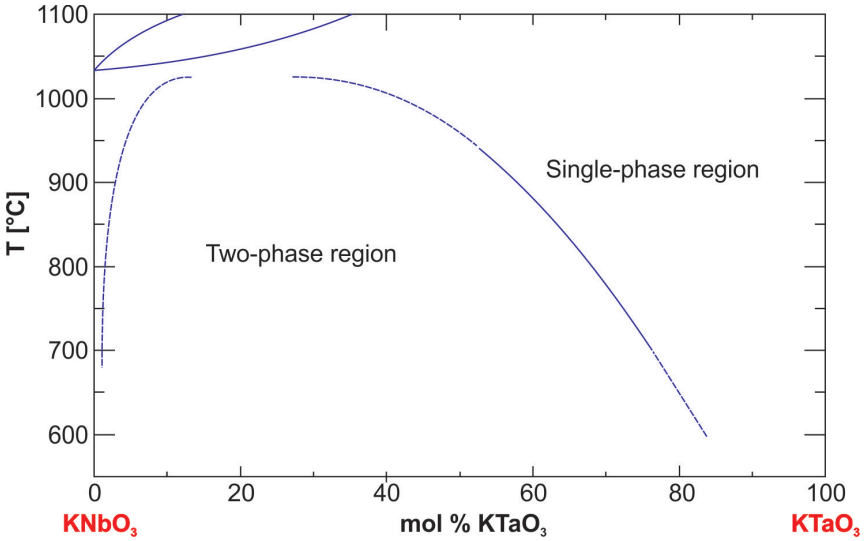

Figure 1.10: Subsolidus phase relations in the $KNbO_3$-$KTaO_3$ phase diagram. After Hill et al. [80].

Additional obstacles during the processing of $KTa_{0.6}Nb_{0.4}O_3$ may arise from the kinetic factors. As can be observed from Table 1.6, Ta is the slowest diffusional species in the course of the processing of $K(Ta,Nb)O_3$ ceramics. Furthermore, the extrapolated diffusion coefficient of Ta at 800°C is 7 orders of magnitude smaller than that of Nb.[i]

Table 1.6: Maximum diffusion coefficient D_0, activation energy E_a *and* the value of the diffusion coefficient extrapolated to 800°C $D_{800°C}$ of the K, Ta, Nb and O species [81-84].

	K[$]	Ta[*]	Nb[§]	O[#]
D_0 [m²/s]	3.7 x 10^{-7}	677	3.6 x 10^{-7}	12
Q [kJ/mol]	100	590	263	85
$D_{800°C}$ [m²/s]	~ 5 x 10^{-12}	~10^{-26}	~10^{-19}	~10^{-3}

[$]Diffusion of potassium ions in alkali silicate glass.
[*]Diffusion of tantalum in β-Ta_2O_5.
[§]Diffusion of niobium in different niobium silicides.
[#]Diffusion of oxygen ions in $Pb(Zr,Ti)O_3$.

Xu et al. [85] employed extended X-ray-absorption fine-structure spectroscopy (EXAFS) to investigate the B-site compositional homogeneity of KTN powders prepared by an alkoxide-based hydrolytic sol-gel route and conventional solid-state synthesis. While the former method yielded powders with a uniform Ta/Nb distribution already after heating at 700°C, it was impossible to prepare homogeneous powders via solid-state synthesis. Furthermore, deliberately introduced heterogeneities in the sol-gel processed powders could not be eliminated even after heating as high as 1000°C.

An additional method to improve the processing of $KTaO_3$-based ceramics might be the mechanochemical activation of the starting-powder mixtures. It contributes to the increased reactivity, improved homogeneity and decreased diffusion paths in various perovksite powders [86]. Recently, it has been used for the preparation of $(K,Na,Li)(Ta,Nb)O_3$ ceramics with very good properties. It was shown that the method is efficient in distributing the low-reactive Ta_2O_5 in the mixture [87,88].

[i]Ta^{5+} and Nb^{5+} with the coordination number VI have the same ionic radius (0.61 Å), however, the Nb–O bond is less covalent.

The main characteristics of the literature reports on $K(Ta,Nb)O_3$ ceramics are collected in Table 1.7 The most striking feature is the large discrepancy in the dielectric properties of the KTN ceramics within the same composition reported by different authors. For instance, the kHz-range room-temperature permittivity ε' and dielectric losses $\tan\delta$ of the $KTa_{0.6}Nb_{0.4}O_3$ ceramics vary from 1300 to 6790 and from 0.02 to 0.06, respectively. The temperature of the permittivity maximum T_{max} varies in the range from 358 K to 245 K. Note that the Curie point of this composition expected from the single crystals is ~300 K (Figure 1.6), and that the $KTa_{0.6}Nb_{0.4}O_3$ ceramics with the highest room-temperature permittivity value of 6790 and the T_{max} very close to the single-crystals value of 300 K were prepared from powders obtained through the sol-gel method [89].

A significant frequency dependence of the dielectric properties was often observed and a broad relaxor-like permittivity maximum was reported [90,91]. Venkatesh et al. [90] measured the dielectric properties of the $KTa_{0.6}Nb_{0.4}O_3$ ceramics up to the MW frequency range. The hot pressed ceramics showed high MW losses, reaching 0.17 at 2.5 GHz. The described features were ascribed to the heterogeneous Ta/Nb [90,91], charged defects arising from the K-deficiency [90], or to the presence of the secondary phase at the grain boundaries [92].

Table 1.7: Overview of the literature reports on $KTa_xNb_{1-x}O_3$ ceramics. T_{calc} – calcination temperature; T_{sint} – sintering temperature; SM – sintering method: CS – conventional sintering, HP – hot pressing, UHP – uniaxial hot pressing; ρ_{rel} – relative density; T_{max} – temperature of the permittivity ε' maximum; f – measurement frequency; Room-temperature permittivity ε' and dielectric losses $\tan\delta$ values are given.

x	T_{calc} [°C]	T_{sint} [°C]	SM	Grain Size [μm]	ρ_{rel} [%]	ε'	$\tan\delta$	T_{max} [K]	f	Ref.
0.6	950	1105	CS*	0.7 – 4	96	~1300	~0.04	358	1 kHz	[93]
0.6	800	1200	CS	~ 1	92.5	1985	0.02	245	1 MHz	[90]
						1100	0.09	/	4.8 GHz	
0.6	800	1100	UHP	~ 1	93.4	2880	0.048	258	1 MHz	
						2295	0.17	/	2.5 GHz	
0.6	850	1150	CS+	~ μm	~90	~2800	~0.06	~290	1 kHz	[94]
0.6	700	1200	HP$	~ 3 μm	97.8	6790	–	307	1 kHz	[89]
0.65	830	1230	HP	~ 1	99.5	~3000	–	228	1.6 kHz	[95]
0.65	850	1300	CS	3–5	92	~1700	~0.01	242	1 kHz	[91]
0.7	950	1120	CS*	0.5 – 2	91.5	~1700	~0.04	310	1 kHz	[92]
0.8	850	1300	CS	3–5	89	~500	>0.01	121	1 kHz	[91]

*1 wt. % of LiF was used as a sintering additive.
+8 mol % of potassium excess was used.
$Powders were prepared by the alkoxide-based sol-gel route.

1.2.3 Processing of Thin Films

Thin-film deposition methods can be divided into physical and chemical methods. The first group comprises pulsed-laser deposition, evaporation, which includes also molecular beam epitaxy and sputtering. The chemical deposition methods can be further divided into

chemical vapor deposition, in which the film arises from the adjacent gas phase, and chemical solution deposition, in which the film arises from the adjacent liquid phase.

1.2.3.1 Chemical Solution Deposition

CSD has been employed for the deposition of electronic oxide thin films since the 1980s. Its advantages are:

- preparation of the films with high chemical homogeneity at low heating temperatures,
- good control of the film stoichiometry through the solution composition,
- low capital investment (especially when compared to the physical deposition methods),
- large area coverage.

On the other hand, CSD is not very convenient for the preparation of epitaxial films, the step coverage of the 3D structures is rather poor and thickness of the final films is limited in the range from a few tens of nm up to a few μm [96].

The method is schematically presented in Figure 1.11. It begins with the dissolution of the starting compounds, such as metal alkoxides, carboxylates, oxides, or nitrates in the solvent, which are most often simple or complex alcohols. To promote the reactions the sols are often refluxed and distilled afterwards to remove the by-products. The exact sol preparation route depends on the type of starting compounds. The main characteristics of the alkoxide-based synthesis, usually in the literature referred to as the sol-gel route, will be presented in the following chapter.

The sol can be deposited on the substrate either by spin-, dip-, or spray-coating. The formation of the gel film already during the deposition is driven by the solvent evaporation and consequent physical and chemical interactions between the precursor species. The film is then dried and pyrolyzed (~150°C to ~450°C), usually on a hot plate, during which chemical reactions proceed, until all the remaining solvent and the majority of the organic species are removed. In some cases densification also takes place.

In the final step the film is heated to high temperatures (up to ~1000°C). The heating can be performed in conventional tube furnaces, though, in the recent years rapid thermal annealing (RTA) furnaces, which enable controlled heating rates of more than 100 K/s, are frequently used. The main processes during this step are densification and crystallization. To increase the thickness of the final films the deposition-heating steps can be repeated several times.

Chemical solution deposition is a highly versatile film-deposition method. The above description is generalized, and each of the stages during the preparation can be modified or even skipped. In addition, some of the described processes may overlap, depending on the specific route employed [97,98].

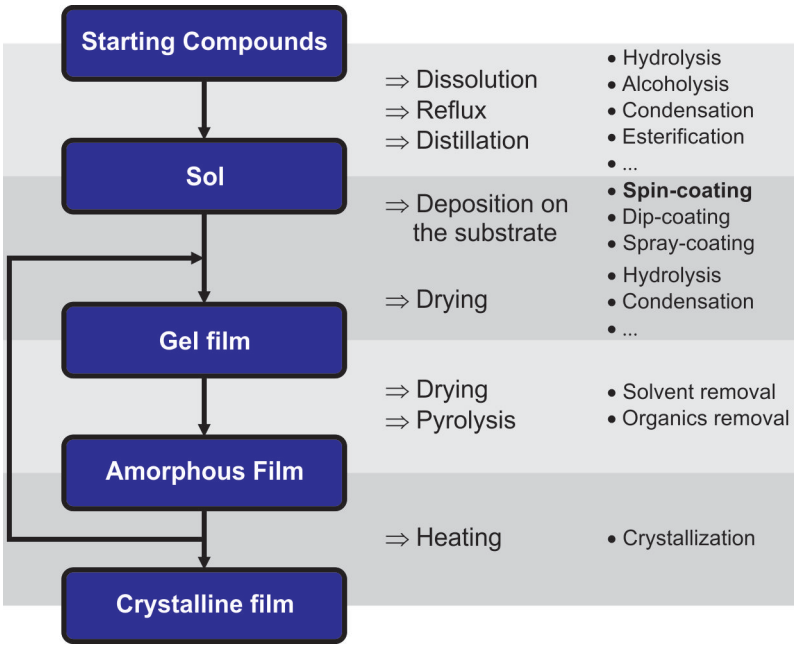

Figure 1.11: Schematic presentation of the chemical solution deposition process.

1.2.3.1.1 Alkoxide-Based Chemical Solution Deposition

The general formula of the metal alkoxides is $M(OR)_n$, where *M* is the metal atom, *-OR* is the alkoxide group and *n* is the oxidation state of the metal. The alkoxide derivatives are known for almost all the elements of the Periodic Table and are frequently used as the metal sources in the solution deposition of electronic thin films.

Highly electronegative OR groups stabilize the metals in their highest oxidation state and this makes them highly susceptible toward any nucleophilic reagent. The reactivity is especially high in the case of the transition metals (TMs) due to:

- their low electronegativity,
- their ability to expand the coordination.

The TM can increase its coordination number by accepting the lone electron pairs from the nucleophilic ligands. As a consequence, the TM alkoxides have a tendency to form oligomers. The number of molecules in the oligomer (molecular complexity) depends on the metal atom, the nature of the alkoxy groups and the type of the solvent. The dimeric structure of the Ta- and Nb-methoxides and ethoxides in their parent alcohols is shown in Figure 1.12. A dimeric mixed alkoxide was observed when the Ta- and Nb-methoxides were dissolved together in octane, toluene, or acetonitrile [99].

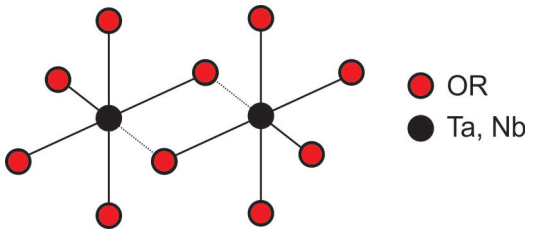

Figure 1.12: Scheme of the dimeric structure of the $[M(OR)_5]_2$ (M - Ta, Nb; R - CH_3, CH_2–CH_3). Adopted from Bradley et al. [100].

Several reactions[i] are characteristic for the alkoxide-based CSD. Hydrolysis takes place if water is present in the system:

$$M(OR)_n + xHOH \rightarrow M(OR)_{n-x}(OH) + xROH, \tag{1.16}$$

and is followed by a condensation through the elimination of the water (oxolation) or alcohol (alcoxolation):

$$\begin{aligned} {}_{x-1}(RO)M\text{–}OH + HO - M'(OR)_{x-1} \\ \rightarrow {}_{x-1}(RO)M - O - M'(OR)_{x-1} + H_2O \end{aligned} \tag{1.17}$$

$$\begin{aligned} {}_{x-1}(RO)M - OR + HO - M'(OR)_{x-1} \\ \rightarrow {}_{x-1}(RO)M - O - M'(OR)_{x-1} + ROH. \end{aligned} \tag{1.18}$$

When the full coordination of the metal alkoxide is not satisfied the condensation can proceed also through olation. While the oxolation and alcoxolation result in the two metals connected by the bridging oxo (–O–) group, the result of olation are metals connected by the bridging hydroxo (–OH) group [101].

The rates of the hydrolysis and condensation reactions depend on several factors:

- length and branching of the alkyl groups,
- molecular complexity of the alkoxides,
- acid or base catalyst possibly used,
- concentration, temperature,
- solvent.

The solvent plays a very important role. If the protic[ii] solvents are used the solvent molecule can donate the lone electron pair to the metal to expand its coordination number. In addition, the alkoxide groups can be exchanged with the groups from the solvent through the transalcoholysis reaction:

$$M(OR)_n + xR'OH \rightarrow M(OR)_{n-x}(OR')_x + xROH, \tag{1.19}$$

resulting in a decreased reactivity of the heteroleptic alkoxide. Due to Le Chatelier's principle, significant exchange of the alcohol groups can be expected already after dissolution at room temperature.

A very popular solvent in the CSD processing is 2-methoxyethanol, $CH_3OCH_2CH_2OH$, a representative of the glycol ethers. It can interact with the metal atom through both types of the above-described reactions by forming a chelate cycle, showed in Figure 1.13. The formed alkoxide is much less reactive towards the hydrolysis.

[i] All the reactions are shown for the monomeric species only.

[ii] All solvents that contain dissociable hydrogen atom, usually bounded to oxygen or nitrogen atom.

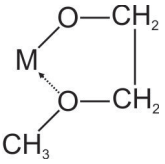

Figure 1.13: Structure of the chelate cycle formed by 2-methoxyethanol. M – metal. From Turova et al. [102].

Despite the many possibilities for the modification of TM alkoxides, the hydrolysis and condensation reactions are often still difficult to control when the water is intentionally added to the system. In such cases, the non-hydrolytic routes are employed. During the reflux or prolonged storage the condensation can proceed via ether elimination reaction:

$$_{x-1}(RO)M - OR + RO - M'(OR)_{x-1} \rightarrow {}_{x-1}(RO)M - O - M'(OR)_{x-1} + ROR. \quad (1.20)$$

During the synthesis of the sol the formation of the oxygen bridges M–O–M' between different metal atoms is desired. This has two advantages: first, the precursor is homogenous on the atomic level; second, if the precursor structure is similar to the final oxide, the crystallization temperature can be strongly reduced. However, in reality the competition between the homocondensation, resulting in M–O–M bridges, and heterocondensation, resulting in M–O–M' bridges, defines the structure of the precursor [100-102].

1.2.3.2 $KTaO_3$ and $K(Ta,Nb)O_3$

To the best of our knowledge the first two groups who initiated the processing of KTN powders and thin films through chemical solution deposition were the groups of Hirano [103-105] and Kahn [106,107]. Both were using the transition-metal ethoxides and potassium ethoxide or acetate, while ethanol was used as a solvent. Crystallization of the perovskite powders with Ta-rich compositions proceeds through the intermediate pyrochlore phase:

$$Amorphous \xrightarrow{\sim 450°C - 650°C} Pyrochlore \xrightarrow{\sim 700°C} Perovskite. \quad (1.21)$$

The transformation temperatures are only approximate and depend strongly on the composition, as well as on the potassium precursor. In the $KTaO_3$ powders this temperature can be as high as 850°C, while in the case of the powders with Nb-rich compositions, the perovskite phase can appear already below 650°C [103]. The pyrolysis and crystallization processes seem to be well separated for the acetate potassium precursor, while the traces of the crystalline phases were observed in the air-gelled samples already at room-temperature, when the potassium ethoxide precursor was used. In any case, single-phase KTN powders are difficult to prepare because of the non-stoichiometry arising from the sublimation of potassium species upon high-temperature heating [106].

Both groups were preparing the sols by refluxing the starting compounds in the solvent

for at least 24 h. This is most probably related to the results on $LiNbO_3$ system, prepared from the ethoxide precursors in ethanol, in which the phase-pure ilmenite powders and films were prepared at low temperatures (below 400°C) from the sols being refluxed for at least 22 h [108,109]. As was shown by Eichorst and Payne [110], the bimetallic alkoxide $LiNb(OEt)_6$ is formed during the reflux, which serves as the "molecular building block" for the crystallization. On the basis of the ^{1}H, ^{13}C and, ^{93}Nb NMR analyses, the alkoxide-based KTN sols after prolonged refluxing were considered to consist of the $KNb(OEt)_6$ and $KTa(OEt)_6$ species, uniformly distributed on the molecular level [104].

The majority of the CSD-derived thin-film activities have been focused on the $KTa_{0.65}Nb_{0.45}O_3$ composition. Hirano and Kahn reported that the pyrochlore phase is usually the major phase in the films prepared at low heating temperatures, and at least 750°C is needed to prepare phase-pure perovskite films. Hirano et al. [103] successfully decreased the temperature to 675°C by pyrolyzing the films in a H_2O–O_2 atmosphere, which enhances the crystallization of the perovskite phase through the promoted organics removal.

An important factor influencing the crystallization is also the heating rate. If slow rates are used the pyrochlore phase is formed at lower temperatures, which slowly transforms to the perovskite at higher temperatures. However, pyrochlore formation could be kinetically "over jumped" by using RTA processing and the perovskite can crystallize directly from the amorphous phase. [107]

By far the most important parameter for the crystallization of KTN films was found to be the substrate. When the substrates with little crystallographic relationship, such as glass, (100) Si and (0001) sapphire (c-cut), were used, the pyrochlore phase was the major phase in the films after the heating. When substrates with a crystal structure and lattice parameters similar to KTN were used, such as (100) and (110) $SrTiO_3$, (100) MgO and (100) Pt / (100) MgO, phase-pure (100) oriented perovskite films were obtained after heating at 750°C [103,104,106,107].

The above-described findings were confirmed later also by other groups [111-114] and the main results are summarized in Table 1.8. Buršik and co-workers [115,116] successfully prepared the perovskite KTN thin films in the whole range of compositions on glass and (100) Si substrates. They used the metal isobutoxides as the starting compounds and isobutanol as the solvent. To reduce the losses of the potassium species through the reaction with the substrate, Al_2O_3 was used as the buffer layer, while $KNbO_3$ was used as the seeding layer for the crystallization of the perovskite KTN phase.

Not many reports on the CSD processing of $KTaO_3$ exist. Perovskite films were prepared on c-sapphire, (100) MgO, (100) $SrTiO_3$ and (100) $LaAlO_3$ substrates, while only the pyrochlore phase was observed in the case of the polycrystalline alumina. To obtain perovskite films on (100) Si and glass substrates, the Al_2O_3 buffer and $KNbO_3$ seeding layers were employed. It is important to note that the addition of a potassium excess in the sols is inevitable for the phase-purity of $KTaO_3$ films [115,117].

Table 1.8: Overview of the important literature reports on the CSD-processing of the $KTa_xNb_{1-x}O_3$ thin films. T_{cry} – crystallization temperature; P – perovskite phase; Py – pyrochlore phase.

Substrate	*x*	T_{cry} [°C]	Phase Composition	Route	Remarks	Ref.
Glass	0.65	750	Py + P	Ethoxide	–	[113,114]
	0–1	800	(100) P^+	Isobutoxide	K-excess, RTA	[115,116]
(100) Si	0.65	750	Py + P	Ethoxide	–	[111]
	0–1	800	(100) P^+	Isobutoxide	K-excess, RTA	[115,116]
(111) Si	0.65, 0.80	750	Py	Ethoxide	–	[106,113]
Pt / (111) Si	0.65	750	Py	Ethoxide	–	[114]
$(01\bar{1}0)$ SiO_2	0.65	675	Py	Ethoxide	H_2O pyr.[$]	[103]
c-sapphire	0.65, 0.80	750	P + Py	Ethoxide	–	[106]
r-sapphire	0.65	750	(100) P + Py	Ethoxide	–	[111,114]
Pt	0.65, 0.80	750	P	Ethoxide	RTA	[118]
(100) YSZ	0.65	750	P + Py	Ethoxide	–	[114]
(100) $LaAlO_3$[#]	0.65	750	(100) P + Py	Ethoxide	–	[114]
(100) MgO	0.65, 0.80	675 750	(100) P	Ethoxide	H_2O pyr.[$] –	[103] [106,107,113]
(100) Pt / (100) MgO	0.35, 0.50, 0.65	700	(100) P	Ethoxide	H_2O pyr.[$]	[104,105]
(100) $SrTiO_3$	0.65	650	(100) P	Ethoxide	–	[111]
	0.65, 0.80	750				[106,113,114]
	0.65			Ethoxide[*]		[112]
(110) $SrTiO_3$	0.65, 0.80	750	(110) P	Ethoxide		[106,114]
Corundum	1	750	Py	Pechini[§]	25 mol% K-excess	[117]
C-sapphire	1	800	P^+	Isobutoxide	K excess, RTA	[116]
(100) MgO	1	800	(100) P^+	Isobutoxide	K excess, RTA	[116]
(100) $SrTiO_3$	1	750	(100) P	Pechini[§]	25 mol% K-excess	[117]
(100) $LaAlO_3$[#]	1	750	(100) P	Pechini[§]	25 mol% K-excess	[117]

[*]Acetate was used as the potassium source.
[+]$KNbO_3$ and Al_2O_3 were used as a seeding and buffer layers, respectively.
[$]Pyrolysis was performed in the presence of the H_2O vapors.
[#]Pseudo-cubic structure is assumed.
[§]Potassium carbonate and TM ethoxides were used as the metal sources.

The dielectric properties of CSD-derived $KTa_xNb_{1-x}O_3$ films have not often been reported. The permittivity ε' of 1-μm-thick (100) oriented films deposited on (100) Pt / (100) MgO substrates was measured in the 1 kHz to 1 MHz frequency range. A broad permittivity maximum was observed, with 1 kHz T_{max} values of 373 K, 273 K and 213 K for the films with x (at. concentration of Ta) equal to 0.35, 0.5 and 0.65, respectively, which is lower than the Curie point expected from the single crystals (Figure 1.6). Only slim and unsaturated *P-E* hysteresis loops were obtained at 93 K [105].

Železný et al. [119,120] performed a far-infrared characterization of 1.2 μm $KTaO_3$ films on (100) Si substrates. Three bands, corresponding to the TO1, TO2 and TO4 modes (see Appendix), were observed in the transmission spectra, and their room-temperature positions were in agreement with the single-crystal data. The phonon contribution to the permittivity ε' at 5 K was evaluated to be 611, much lower than the single-crystal value of ~4500 [121,122]. The KTN films of various compositions showed infrared behavior similar to the bulk counterparts; however, no quantitative analysis was reported. To the best of our knowledge no dielectric data measured in a broad frequency range that would correlate the intrinsic (of the lattice origin) properties of these films to low-frequency dielectric data has been previously reported.

1.2.3.3 $K(Ta,Nb)O_3$ Thin Films Prepared by Other Methods

$K(Ta,Nb)O_3$ thin films of various compositions were also prepared using other deposition methods, such as magnetron sputtering [123], liquid-phase epitaxy (LPE)[124], metal organic chemical vapor deposition (MOCVD) [125,126] and PLD [127-132]. The common processing challenge for all the techniques is control of the stoichiometry due to losses of potassium species during processing.

Guilloux-Viry et al. [133,134] studied the influence of the substrate on the GHz-range dielectric properties of the ~500-nm-thick PLD-grown $KTa_{0.6}Nb_{0.4}O_3$ thin films. Among the chosen substrates, i.e., (100) MgO, (100) $LaAlO_3$, alumina, c-sapphire and r-sapphire, the highest value of the relative capacitance tunability n_r of 7.2 % at 15 kV/cm and 1 GHz was reported for the (100) oriented film on the latter substrate. In contrast to the ceramics, the room-temperature permittivity ε' was constant in the 6–40 GHz range, with values of 1180 and 280 for the films on (100) $LaAlO_3$ and (100) MgO, respectively. The Raman investigation of the 30-nm-thick epitaxial $KTa_{0.65}Nb_{0.35}O_3$ and $KTa_{0.50}Nb_{0.50}O_3$ thin films on these substrates revealed that the cubic-to-tetragonal phase transition is 50 K higher than expected from the single-crystal data (Figure 1.6). The shift was attributed to the influence of thermal strain [135].

2 Aims and Hypothesis

Incipient ferroelectrics exhibit a richness of different phenomena, important from the fundamental as well as from the technological point of view. As an archetypal representative, $KTaO_3$ is well known in its single-crystal form, but knowledge about the properties of the ceramics and thin films is still at a very basic level.

In the first part of the thesis we prepared $KTaO_3$ ceramics by solid-state synthesis from K_2CO_3 and Ta_2O_5 starting compounds. The principal aims of this part of the thesis were:

- To activate the starting-powders mixtures by implementing high-energy milling.
- To prepare perovskite $KTaO_3$ powders and to evaluate their structural and chemical homogeneity.
- To prepare highly dense and single-phase perovskite $KTaO_3$ ceramics.
- To measure the dielectric properties of the ceramics and establish correlations with the processing parameters.
- To evaluate the properties in a broader frequency range and analyze the lattice dynamics, as well as the extent of the intrinsic and extrinsic contributions to the dielectric response.

In the next step we investigated the synthesis and dielectric properties of CSD-derived $KTaO_3$ thin films on polycrystalline alumina and (0001) sapphire substrates. The foremost goals of this part of the thesis were:

- To prepare phase-pure perovskite $KTaO_3$ thin films on substrates that exhibit no structural matching, without use of seeding layers, which could influence their dielectric response.
- To evaluate the broadband dielectric properties and lattice dynamics of the polycrystalline $KTaO_3$ thin films.

The above-stressed points of the thesis gave us a unique opportunity to directly compare the dielectric properties of $KTaO_3$ in the single crystal (large amount of literature data), ceramic and polycrystalline thin-film forms. Our hypothesis was that the defects, grain-boundaries and strain have a profound influence on the dielectric properties and their contribution should be evaluated by a comparison of the broadband dielectric measurements. The possibility of induced ferroelectricity in CSD-derived $KTaO_3$ (and incipient ferroelectrics in general) thin films was considered.

In the third part of the thesis we have focused on $KTa_{0.6}Nb_{0.4}O_3$ thin films on alumina substrates. Even though the $K(Ta,Nb)O_3$ solid solution has been quoted as having potential in microwave applications, a very limited amount of data on microwave properties can be found in the literature, especially on the solution-derived thin films. In addition, several issues, which seem to be processing related, exist. The main points of this part of the thesis were:

- To follow the structural evolution of the sols based on potassium acetate and transition-metal ethoxides upon refluxing in 2-methoxyethanol by extended X-ray-absorption fine-structure spectroscopy.
- The films were prepared from sols refluxed for different times. The aim was to study the influence of the structure of the sol on the crystallization behavior and to prepare single-phase $KTa_{0.6}Nb_{0.4}O_3$ thin films.
- To measure the dielectric properties, including tunability, of the films in the radio- and microwave-frequency ranges and correlate them with the reflux time.
- To analyze the unexpected dielectric properties of single-phase films, prepared from 24 h-refluxed sols.

Our main hypothesis for this part was that the phase composition, microstructure and dielectric properties of the $KTa_{0.6}Nb_{0.4}O_3$ thin films are controllable through the sol's synthesis parameters.

3 Materials and Methods

3.1 Preparation of the Samples

3.1.1 $KTaO_3$ Ceramics

$KTaO_3$ ceramics were prepared by solid-state synthesis implemented by the mechanochemical activation of K_2CO_3 and Ta_2O_5. The general scheme of the processing route is shown in Figure 3.1.

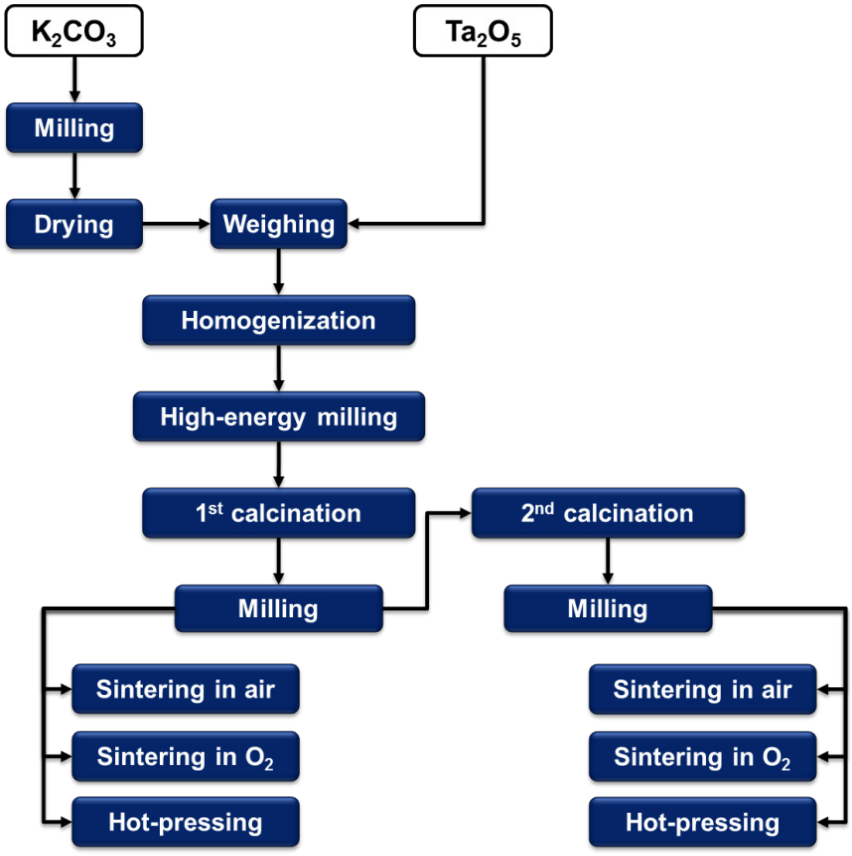

Figure 3.1: Schematic presentation of the $KTaO_3$ ceramics' processing.

The starting K_2CO_3 was milled for 5 h in an acetone medium using a 200-ml polyethylene vial and yttria-stabilized zirconia (YSZ) milling balls with diameters of 3 mm and 10 mm. After the milling its median particle size d_{50} was approximately 5 μm. The Ta_2O_5 had d_{50} 0.5 μm and was used as-received. The exact quantities of the metal components inside the powders were determined gravimetrically. Prior to weighing the K_2CO_3 powder was dried at 200°C to a constant mass. The characteristics of the chemicals used during the processing are collected in Table 3.1.

Table 3.1: Chemicals used during the synthesis of the $KTaO_3$ ceramics.

Chemical Formula	Name	Purity [%]	Supplier
K_2CO_3	Potassium carbonate, A.C.S. reagent	99+	Aldrich
Ta_2O_5	Tantalum (V) oxide (metals basis)	99	Alfa Aesar
$(CH_3)_2CO$	Acetone, p. A.	99.5	AppliChem

3.1.1.1 High-Energy Milling

The high-energy milling was performed with a vidia (WC-Co, ρ = 15.1 g/cm^3) vial and milling balls. After weighing the starting compounds in a glove box with a dry atmosphere in a stoichiometric ratio (50 g batch), homogenization of the mixture was performed in acetone at 200 min^{-1} for 4 h using a planetary mill (Fritsch Pulverisette 4 Vario-Mill). Before the high-energy milling, the slurry was dried at 60°C. The high-energy milling was performed for 10 h, with intermediate sampling of ~1 g of the powder after 5 h. The milling parameters were selected on the basis of Ref. [88] and are given in Table 3.2.

Table 3.2: High-energy milling parameters.

Milling balls		Milling vial		Operation		
Diameter	Number	Diameter	Height	Disk rotational frequency	Vial rotational frequency*	Ball impact energy§
15 mm	16	7.5 cm	5.7 cm	350 min^{-1}	-700 min^{-1}	500 mJ/hit

*Negative sign denotes opposite rotational movement of the disk and the vial. The distance between the rotational axes was 12.5 cm.

§Calculated according to the Ref. [136].

3.1.1.2 Calcination and Sintering

The mechanochemically activated mixtures were pressed into pellets and heated once or twice at 800°C for 4 h in a chamber furnace. After each calcination step the powder was milled in the planetary mill at 175 min^{-1} for 4 h in acetone using a polyethylene vial and YSZ milling balls with diameters of 3 mm and 10 mm. The powder compacts were first pressed uniaxially at 100 MPa and then isostatically at 200 MPa. The pellets were placed on a Pt foil and sintered in a closed corundum crucible at 1325°C for 2 h in a tube furnace in air or in an O_2 atmosphere. For the pressure-assisted sintering the powder compacts were packed in coarse MgO powder in an alumina die and hot pressed at 1250°C and 25 MPa for 2 h. The heating and the cooling rates for the calcination and sintering were 5 K/min.

3.1.2 $KTaO_3$ and $KTa_{0.6}Nb_{0.4}O_3$ Thin Films

Potassium acetate and transition-metal ethoxides were used as the metal sources and 2-methoxyethanol was used as a solvent. The compounds were transported as-received into

the glove-box with a dry atmosphere, where they were stored and manipulated. Characteristics of all the chemicals used during the processing are in Table 3.3.

Table 3.3: Chemicals used during the processing of thin films.

Chemical Formula	Name	Purity [%]	Supplier
$KOOCCH_3$	Potassium acetate, A.C.S. reagent	99+	Sigma-Aldrich
$Ta(OCH_2CH_3)_5$	Tantalum ethoxide, HP	99.99	H. C. Starck
$Nb(OCH_2CH_3)_5$	Niobium ethoxide, HP	99.99	H. C. Starck
$CH_3OCH_2CH_2OH$	2-methoxyethanol, ACS	99.3+	Sigma-Aldrich
$(CH_3)_2CO$	Acetone, p. A.	99.5	AppliChem
$(CH_3)_2CHO$	Isopropanol	99.8	Sigma-Aldrich

3.1.2.1 Synthesis of the Sols

The general scheme of the $KTaO_3$ and the $KTa_{0.6}Nb_{0.4}O_3$ sols synthesis is shown in Figure 3.2. The process began with dissolution of 15 mmol of potassium acetate and the corresponding stoichiometric amounts of transition-metal ethoxides in 40 ml of 2-methoxyethanol. A flask with reagents was connected to a modified Schlenk apparatus [137,138] and purged with dry nitrogen for 15 min under constant stirring with the magnetic stirrer. During purging all the potassium acetate dissolved. The sols were heated to temperatures between 105°C and 115°C and were refluxed for 1 h, 4 h, 24 h or 48 h. After the reflux, the temperature was raised to ~124°C and ~15 ml were distilled off to remove the by-products. The sols were cooled to room temperature and their concentration was adjusted to 0.5 M with 2-methoxyethanol. The sols were stored in a refrigerator and remained clear for months.

Potassium acetate was dissolved in 2-methoxyethanol and different excess amounts were added to the sols. Their concentration used for the deposition of the films was 0.4 M.

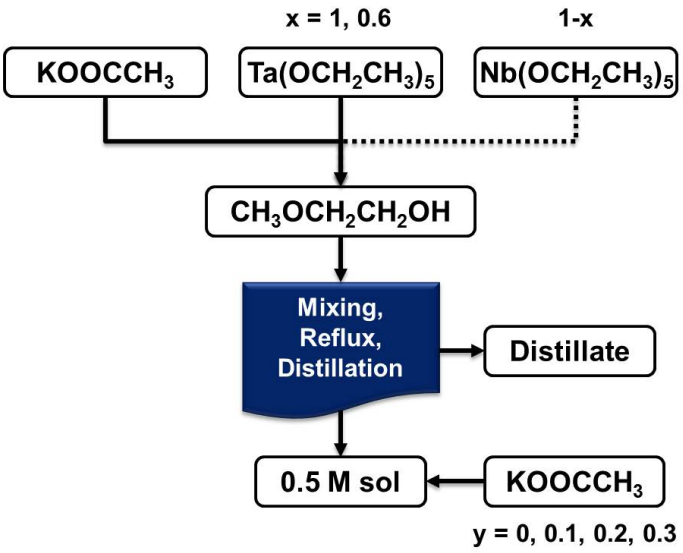

Figure 3.2: Schematic presentation of the synthesis of the $KTaO_3$ and $KTa_{0.6}Nb_{0.4}O_3$ sols.

3.1.2.2 Substrates

Two types of substrates were used. Optically polished polycrystalline alumina with a relative density above 97 % and a grain size below 1 μm was obtained from the CoorsTek supplier [139], while the optically polished, (0001)-oriented, single-crystal, sapphire substrates were supplied by TBL Kelpin.

Prior to the deposition the substrates were ultrasonically cleaned in acetone, isopropanol and deionized water and were dried by blowing N_2.

3.1.2.3 Preparation of the Films

The 0.4-M sols were passed through 0.2 μm filters and spin coated on the substrates for 30 s at 3000 rpm using the Headway Research 1-EC101D-R485 photoresist spinner. The as-deposited films were heated at 180°C or 350°C for 2 min on a hot plate to remove the solvent and partially also the organics. Final heating was performed in an LPT Industries Europe TM 100-BT RTA furnace with a heating rate of 15 K/s and a cooling time ~10 min in a constant flow of N_2 and O_2 in a 4 : 1 ratio. To increase the thickness of the films the deposition step was repeated either after heating on a hot plate or after heating in the RTA furnace, as shown in Figure 3.3.

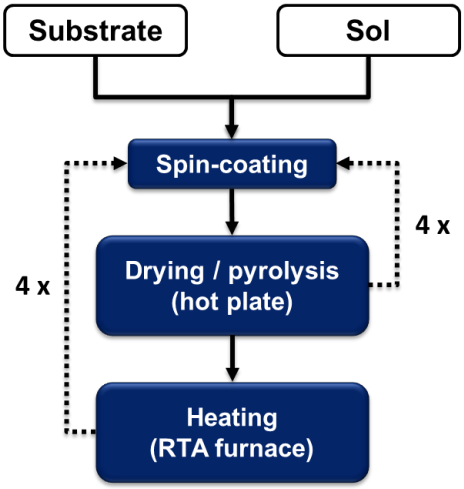

Figure 3.3: Schematic presentation of the $KTaO_3$ and $KTa_{0.6}Nb_{0.4}O_3$ thin films' preparation route.

3.2 Characterization Methods

3.2.1 Thermal Analysis

The thermogravimetry (TG), derivative thermogravimetry (DTG) and differential thermal analysis (DTA) were simultaneously performed with an instrument for thermal analysis (Netzsch STA 409). Evolved gases were concurrently monitored with a mass spectrometer Balzers Thermostar GSD 300 T. The samples were analyzed in Pt crucibles in the temperature range from 25°C to 755°C with a heating rate of 10°C/min and a flowing air atmosphere. The mass of the powder samples was ~25 mg.

The sols were dried, prior the analysis, at 60°C for at least 12 h.

3.2.2 Mid-Infrared Spectroscopy

Infrared spectra were recorded using a Perkin Elmer Fourier-transform infrared (FT-IR) spectrometer in the 4000 cm^{-1} to 600 cm^{-1} range with a resolution of 2 cm^{-1} and 3 superposed scans. The powder samples were recorded in an attenuated total reflectance mode (ATR) with a Specac Golden Gate Diamond ATR as a sample support. The sols were recorded in a transmission mode using a cell with the path length of 25 μm.

3.2.3 Extended X-Ray-Absorption Fine-Structure Spectroscopy

The absorption spectra of the sols were measured at the C station of HASYLAB in transmission detection mode, using a (111) Si double-crystal monochromator with ~1.5 eV resolution at the Ta L_3-edge (9881 eV) and 2 eV resolution at the Nb K-edge (18986 eV). Higher-order harmonics were efficiently eliminated by detuning the monochromator crystals to 60 % of the rocking-curve maximum using a stabilization feedback control. The intensity of the X-ray beam was measured by three consecutive 10-cm-long ionization detectors, filled with 140 mbar of Ar, 530 mbar of Kr and 930 mbar of Kr, respectively, for Ta L_3-edge EXAFS, while for Nb K-edge EXAFs the cells were filled with 940 mbar of Ar, 420 mbar of Kr and 930 mbar of Kr, respectively. The samples were placed between the first two detectors. The exact energy calibration was obtained by a simultaneous absorption measurement on Ta or Nb foil, inserted between the second and the third ionization detectors.

The sols were sealed in thin, vacuum-tight plastic bags in a dry atmosphere to avoid a possible reaction with the atmospheric humidity. The thickness of the liquid bags was adjusted for an absorption thickness (μd) of about 2 above the investigated absorption edge. The absorption spectra were measured within the interval from -250 eV to 1100 eV, relative to the absorption edge. In the X-ray absorption near edge structure region the equidistant energy steps of 0.5 eV were used, while for the EXAFS region the equidistant k-steps ($\Delta k \approx 0.03$ $Å^{-1}$) were used with an integration time of 1 s/step. To improve the signal-to-noise ratio and to check the stability, as well as the reproducibility of the detection system, the data of two identical runs were superposed.

3.2.4 Laser Granulometry

The particle size distribution of the powders was determined by the static light scattering technique using a Microtrack S3500 Series Particle Size Analyzer. Prior to the analysis the powders were dispersed in isopropanol using an ultrasonic bath. All the results were derived from the area particle size distribution.

3.2.5 Inductively Coupled Plasma Spectroscopy

Quantitative elemental analyses of the powders were performed with inductively coupled plasma mass spectroscopy (ICP-MS) using a quadropole-based 7500 CE spectrometer. The measurements were made without a reference. Instead, an additional technique was used to verify the results, i.e., inductively coupled plasma atomic emission spectroscopy

(ICP-AES) using a Thermo Jarrel Ash Atomscan 25 spectrometer.

The ceramic samples were prepared by crushing the pellets in an agate mortar. The sols were dried at 60°C for 3 h and heated in a tube furnace at 900°C for 15 min with heating and cooling rates of 5 K/min.

3.2.6 X-Ray Diffraction

The phase composition of the samples was analyzed at room temperature using a PANalytical X'Pert PRO diffractometer, employing Cu $K_{\alpha 1}$ radiation (λ=1.540598 Å). The diffractograms were recorded in θ-2θ geometry in the range from 5° to 60° and from 10° to 70° for thin films and powders, respectively, with the step 0.017° and a count time of 100 s. The phases were identified with the program X'Pert HighScore [140] using the PDF-2 database [141].

3.2.7 Density Measurements

The densities ρ of the sintered ceramic pellets were determined either geometrically or with Archimedes' method by immersing the pellet into water:

$$\rho = \frac{m_{dry} \cdot \rho_{water}}{m_{dry} - m_{wet}}, \tag{3.1}$$

where m_{dry} and m_{wet} are the masses of the pellet measured in air and in water, respectively, while ρ_{water} is the density of water at the measured temperature. Relative density $\rho_{rel} = \rho / \rho_{teor}$ was calculated using 7.012 g/cm^3 as the theoretical density of $KTaO_3$ [142].

3.2.8 Scanning Electron Microscopy

The microstructures of the samples were investigated with the field-emission scanning electron microscopes (FE-SEM) Carl Zeiss Supra 35 VP and Jeol JSM-7600F.

The powders were dispersed in acetone or isopropanol using an ultrasonic bath. A few drops were spread on the highly oriented pyrolytic graphite. The ceramic samples were mounted in epoxy, ground and polished using standard metallographic techniques. For the plane-view analysis of thin films, the samples were mounted with graphite paste on top of the brass holders, while for the cross-sectional analysis the fracture surfaces were positioned in parallel with the surface of the holder. Approximately 3-5 nm of lacey carbon was deposited on the top of the prepared ceramic and thin-film samples using Gatan Precision Etching Coating System (PECS) Model 682A.

3.2.9 Transmission Electron Microscopy

Transmission electron microscope (TEM) analyses of the powder, ceramic and thin-film samples were performed with a Jeol JEM-2010F TEM instrument equipped with a field-emission electron source, Oxford Instruments Link ISIS 300 energy-dispersive X-ray spectrometer (EDXS) and Gatan DigiPEELS 766 electron-energy-loss spectrometer (EELS). A liquid-N_2 contamination trap was used to reduce the specimen contamination

during the analysis. The thin-film sample was analyzed in the scanning TEM (STEM) mode.

Powder samples were crushed in an agate mortar, transferred onto the TEM Ni-grid and coated with lacey carbon using Gatan PECS Model 682. Ceramic samples were ultrasonically cut to a disk shape and mounted in brass rings with epoxy, followed by conventional grinding, polishing and dimpling. Final Ar^+ milling was performed in Bal-Tec RES 010 ion mill until perforation, using liquid N_2 for cooling. To perform the cross-sectional analysis the thin-film samples were cut with a diamond saw, glued face-to-face and mounted in the brass rings with epoxy. Further preparation was the same as for the ceramic samples. $KTaO_3$ single crystals, obtained from the F.EE GmbH supplier, were used as the standards for the quantification of the EDXS and EELS results. The crystals were prepared either by crushing or by an ion-milling procedure.

EDX spectra were obtained from the electron-transparent areas with thicknesses in the range from 50 nm to 180 nm. Channeling effects were avoided by the off-zone axis orientation of the investigated grain. For each EDX measurement point the EEL low-loss spectrum was simultaneously acquired to obtain the specimen thickness *d* in terms of the mean relative thickness, defined as the ratio between the sample thickness and the inelastic mean free path (IMFP) [143]. The IMFP value of $KTaO_3$ under given experimental conditions was 100 nm [143]. The EDX spectra were quantified using the experimental Cliff-Lorimer factor, obtained from the $KTaO_3$ single crystal by an absorption-corrected, zero-thickness, extrapolation procedure [144].

For the EEL spectra acquisition, the microscope was operated at 200 keV in diffraction mode, the convergence and collection angles were 10 mrad and 7 mrad, respectively. K $L_{2,3}$- and O K-edges were recorded simultaneously with 0.5 eV dispersion and 1.5 eV (full width at half maximum) energy resolution and were corrected for dark current and gain variations. For the quantification, the background was subtracted from all the spectra using a power-law approximation and the contribution from multiple scattering was removed with the Fourier ratio technique. The spectra revealing C K-edge from C-contamination were excluded from the quantitative analysis. To avoid electron-beam-induced degradation the electron doses were measured on the electrically isolated observation screen inside the microscope viewing chamber. The electron dose used for the quantitative analysis was ~1 A/cm^2 or lower. This value does not influence the specimen composition during the chosen acquisition time (up to 5 min), i.e., the K/Ta remains within ±2δ error determined on a single-crystal specimen [145].

3.2.10 Broadband Dielectric Spectroscopy

3.2.10.1 Radio-Frequency Measurements

The complex dielectric permittivity $\varepsilon^*(\omega) = \varepsilon'(\omega) - i\varepsilon''(\omega)$ of the ceramic samples was measured in the frequency range from 1 Hz to 1 MHz using a Novocontrol Technologies Alpha High-resolution Dielectric Analyzer, with the amplitude of the AC probing field being 1 V/mm. The dielectric response was measured in the 300 K to 5 K temperature interval with the cooling rate of 1 K/min. The temperature was stabilized to within ±0.1 K using an Oxford Instruments continuous flow cryostat. The disk-shaped ceramic samples

were polished to an approximate thickness of 0.3 mm and Cr/Au electrodes were deposited at room temperature by a 5Pascal magnetron sputtering device on both sides.

Thin-film samples were measured in the same temperature interval in the frequency range from 3 kHz to 1 MHz using an HP4284A LCR meter or Agilent Technologies E4980A Precision LCR meter. The planar capacitor structures shown in Figure 3.4 were patterned by lift-off photolithography. The 150-nm-thick Cr/Au (30 nm / 120 nm) electrodes were deposited at room temperature by magnetron sputtering. The gap between the electrodes *s* was 2-3 μm.

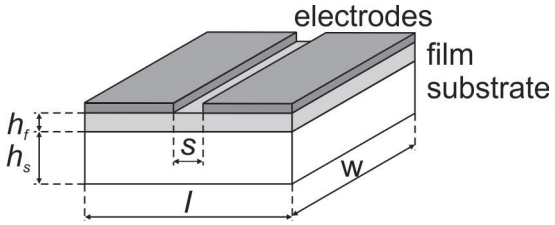

Figure 3.4: Schematic presentation of the planar thin film capacitor. h_f and h_s – thickness of the film and the substrate, respectively; s – gap between the electrodes (2-3 μm); l – length of the electrodes (1.5 mm); w – width of the electrodes (750 μm).

To evaluate the dielectric properties of the films the so-called Vendik's model of partial capacitances was employed [146]. The distribution of the electric field E in the planar capacitor shown above is non-uniform and is approximated with:

$$E = \frac{U}{s}, \tag{3.2}$$

where U and s are the applied voltage and the gap between the electrodes, respectively. To transform this geometry into a classical parallel-plate capacitor a mathematical treatment using the conformal mapping based on the Christoffel-Schwarz transformation is performed. The measured capacitance C_{tot} is separated into discrete contributions of the surrounding medium C_m, thin film C_f and of the substrate C_s connected in parallel:

$$C_{tot} = C_m + C_f + C_s, \tag{3.3}$$

and can be calculated as:

$$C_m = w\varepsilon_0 \frac{2}{\pi} \ln\left(4\frac{l}{s}\right) \tag{3.4}$$

$$C_f = w\frac{\varepsilon_0(\varepsilon_f' - \varepsilon_s')}{\frac{s}{h_f} + \frac{4}{\pi} ln2} \tag{3.5}$$

$$C_s = w\varepsilon_0(\varepsilon_s' - 1)\frac{1}{\pi} ln\left(16\frac{h_f + h_s}{\pi s}\right) \tag{3.6}$$

In the above equations s, l and w are the gap, length and width of the electrodes, respectively, h_f is thickness of the film, h_s and ε'_s are the thickness and permittivity of the

substrate, while ε_0 is the vacuum permittivity. The dielectric permittivity of the film ε'_f is then calculated from the measured capacitance C_{tot} as:

$$\varepsilon'_f = \varepsilon'_s + \left(\frac{s}{h_f} + \frac{4}{\pi}\ln 2\right)\left[\frac{C_{tot}}{\varepsilon_0 w} - \frac{2}{\pi}\ln\left(4\frac{l}{s}\right) - \frac{\varepsilon'_s - 1}{\pi}\ln\left(16\frac{h_f + h_s}{\pi s}\right)\right]. \quad (3.7)$$

All the above equations are strictly valid in the case when the following inequalities are satisfied: $s \leq 0.25 \cdot l$, $s \leq 0.5 \cdot h_s$, $h_f \leq s \leq 10 \cdot h_f$ and $\varepsilon'_f/\varepsilon'_s > 100$. The last two conditions were sometimes not completely fulfilled. In those cases we also performed a more rigorous calculation based on the improved model by Vukadinović et al. [147], which is valid with inequalities relaxed to: $s << h_f + h_s < l$ and $\varepsilon'_m < \varepsilon'_s < \varepsilon'_f$. The ε'_m is the permittivity of the surrounding medium (~1). The difference between the permittivities of the film calculated from both models was always smaller than 10 %. The main experimental uncertainties are the determination of the film thickness (± 5nm) and the optical measurement, as well as the uniformity of the gap between the electrodes (± 0.25 μm). These lead to an approximate relative error of the ε'_f calculation of 10 %.

Because of the low and frequency-independent dielectric losses of the alumina substrates (1–2 x 10^{-4} in the 1 MHz – 10 GHz frequency range)[139] the measured tanδ were assumed to arise from the film only.

3.2.10.2 Quasi-Static Measurements

The quasi-static polarization P of the $KTaO_3$ thin films was measured using a Keithley 617 programmable electrometer. A schematic diagram of the experimental setup is presented in Figure 3.5 [148].

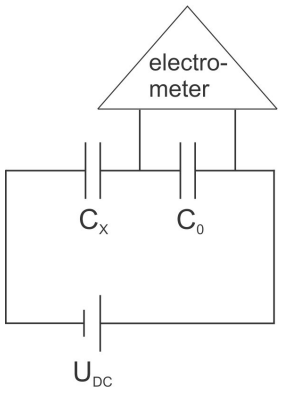

Figure 3.5: Schematic diagram of the experimental setup for the quasistatic measurements.

The C_0 and C_x are the capacitances of the reference and the sample, respectively, and U_{DC} is the applied voltage. During the measurement, the voltage on the reference capacitor U_0 is measured with the electrometer. For two capacitors in series the following relation is valid:

$$U_{DC} = U_0 + U_X, \quad (3.8)$$

where and U_x is the voltage on the sample. Because the charge on the two capacitors is the same $q_0 = q_x = q$ it follows:

$$q = U_0 C_0 = U_x C_x. \tag{3.9}$$

Combining the above equations we get the expression for the voltage on the sample:

$$U_x = \frac{U_{DC} C_0}{C_0 + C_x}. \tag{3.10}$$

From $C_o >> C_x$ we find that approximately all of the applied voltage is on the sample $U_{DC} \approx U_x$.

The partial capacitance model was employed to calculate the in-plane polarization of the film P [149]:

$$P = \frac{1}{w h_f}(q - (C_m + C_s)U_{DC}), \tag{3.11}$$

where w and h_f are the width of the electrodes and the thickness of the film, respectively (Figure 3.4), q is the measured charge, while C_m and C_s are the partial capacitances of the surrounding medium and the substrate, respectively, calculated from the Equations (3.4) and (3.6).

Two types of measurements were performed. In the zero-field-cooled (ZFC) regime the sample was cooled to 5 K, there the electric field E_{DC} was applied, and the corresponding polarization charge was measured on slow heating (1 K/min). In the field-cooled-regime (FC) the sample was cooled in the external electric field to 5 K, after which the polarization charge was measured on heating under the same conditions.

In an additional measurement the sample was cooled from 300 K to 5 K in the ZFC-regime and at selected temperatures an external field of 40 kV/cm was applied. After the induced charge was measured, the field was switched off and the sample was cooled to the next temperature, where the procedure was repeated. The quasi-static permittivity ε_s was calculated from the polarization of the film as:

$$\varepsilon_s = \frac{P}{\varepsilon_0 E_{DC}}. \tag{3.12}$$

Note that the quasi-static permittivity ε_s fundamentally differs from the permittivity $\varepsilon'(\omega)$ measured in different frequency domains, where it can be expressed as a derivative of the polarization P with respect to an applied electric field E. They correspond to each other only in the systems where the polarization is linear in the measured electric field range.

3.2.10.3 Microwave Measurements

The $TE_{01\delta}$ dielectric resonator (DR) method was employed for the microwave (MW) characterization of the ceramic samples. A typical structure, consisting of the base DR and the cylindrical sample with the approximate thickness and diameter of 70 μm and 6 mm, respectively, was used. The measurements were performed on heating from 10 K to 300 K with a heating rate of ~1 K/min in a transmission setup using an Agilent E8364B Network Analyzer and Janis closed-cycle He cryostat. The measurement procedure consisted of two steps: first, the resonator with DR only was measured; in the second step,

the measurement with the resonator with DR and the sample was performed. The dielectric permittivity ε' and dielectric losses $\tan\delta$ of the ceramics were evaluated from the resonant frequency F_0 and quality factor Q by numerical calculations based on electrodynamic analysis [150]. All the measurements were performed with weak coupling between the resonator and the external circuit to diminish parasitic losses. Because of the large change of the permittivity value in the measured temperature interval, which strongly influences the resonant frequency value, the properties were determined at the single frequency of resonance for each temperature, i.e., in the range 2–6 GHz.

The above-described resonator structure was modified for the measurement of the $KTaO_3$ thin films. To increase its sensitivity, DR was removed from the structure, and instead, polycrystalline alumina or c-sapphire substrates were used [151]. Again, individual measurements of the resonator with the substrate and of the resonator with the substrate and the film were performed. Similar calculations as in the case of the ceramic samples were performed to evaluate the dielectric properties of the films. The dielectric properties were evaluated at 14.5 GHz and 16.2 GHz in the case of the alumina and c-sapphire substrates, respectively.

QWED split-post dielectric resonators were used to analyze the dielectric properties of the $KTa_{0.6}Nb_{0.4}O_3$ thin films at 7.3 GHz, 9.9 GHz and 14.5 GHz. The resonators were connected to a Hewlett Packard HP8720ES Network Analyzer with weak coupling and the measurements were performed from 358 K to 238 K in the Artisan Scientific Delta 9023 temperature controlled chamber. First, resonators with bare polycrystalline Al_2O_3 substrates were measured, followed by a measurement of the resonators with the film deposited on the substrate. The resonators were kept at the measurement temperature for at least 10 min before the F_0 and Q values were recorded. Dielectric properties of the films were evaluated by numerical computation as described in Ref. [152,153] using software provided by the resonator's supplier.

3.2.10.4 Terahertz Spectroscopy

Time-domain terahertz (THz) transmission spectroscopy was employed for the measurements of the $KTaO_3$ films on c-sapphire substrates and ceramics with a thickness of 73 μm in the 100 GHz to 2.5 THz (~4–80 cm^{-1}) frequency[i] range. The THz pulses were generated in an interdigitated photoconducting GaAs switch, which was illuminated by a pulse train of a femtosecond laser oscillator, and detected in a 1-mm-thick [110] ZnTe crystal. A more detailed description of the experimental setup can be found in Ref. [154] Measurements were performed from 300 K to ~10 K using an Oxford Instruments Optistat continuous-flow He cryostat equipped with mylar windows.

Two signals are measured at each temperature: a reference waveform $E_r(t)$ with an empty diaphragm or a bare substrate in the case of the ceramics and thin films, respectively, and a signal waveform $E_s(t)$ with a sample attached to the diaphragm. A typical result is shown in Figure 3.6. The ratio of the fast Fourier transforms of both signals is a complex transmission function of the sample:

[i]Term "frequency" is interchangeably used with the term "wavenumber".

$$t(\omega) = \frac{E_s(\omega)}{E_r(\omega)}. \tag{3.13}$$

$t(\omega)$ is correlated to the complex index of refraction $N(\omega) = n(\omega) + i\kappa(\omega)$, from which the complex permittivity function is calculated as $\varepsilon^*(\omega) = N^2$. Detailed calculations are described in Ref. [155-157].

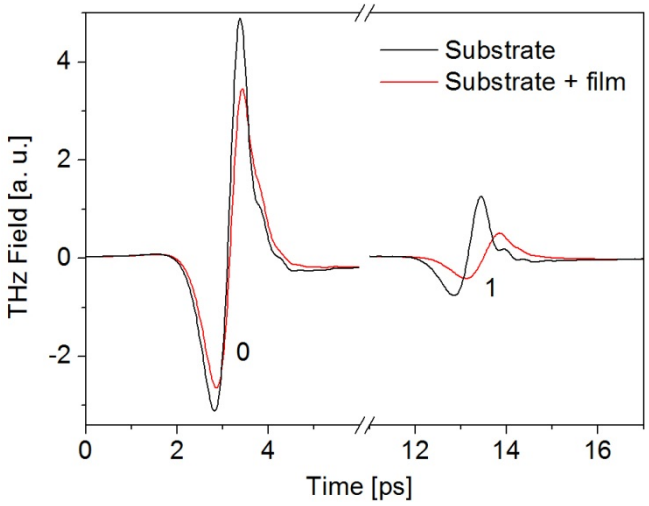

Figure 3.6: THz time-domain waveforms of the bare c-sapphire substrate and substrate with the 200-nm-thick $KTaO_3$ thin film, both measured at 20 K. 0 - direct pass; 1 – first internal Fabry-Pérot reflection.

3.2.10.5 Infrared Spectroscopy

The Fourier-transform infrared (FT-IR) measurements were performed using a Bruker IFS 113v spectrometer. At room temperature the spectra were collected with pyroelectric deuterated triglycine sulfate (DTGS) detector in the 25–3000 cm^{-1} (0.75–90 THz) frequency range. Temperature-dependent measurements were performed from 300 K to ~ 5 K using an Oxford Instruments Optistat continuous-flow He cryostat with polyethylene windows. These spectra were collected in the 20–625 cm^{-1} (0.75–19 THz) range with a highly sensitive helium-cooled Si bolometer detector operating at 1.5 K.

One-side-polished ceramics were measured in a near-normal specular reflectance mode with a resolution of 2 cm^{-1}. In addition to the reflectance mode, thin films were also measured in a transmission mode with a resolution of 0.5 cm^{-1}.

3.2.10.6 Raman Spectroscopy

The unpolarized Raman spectra were measured in a back-scattering configuration using a Renishaw RM 1000 Raman Micro-spectrometer equipped with a grating Rayleigh filter allowing the measurement of Raman shifts down to ~20 cm^{-1} and with a CCD detector. The spectra were excited with the 514.5 nm line of an Ar laser at ~20 mW. The laser beam was focused to a spot of ~5 μm in diameter on the sample surface using a long-working distance x20 microscope objective. The one-side-polished ceramic sample was placed in an Oxford Instruments Optistat continuous-flow He cryostat, equipped with optical windows, operating in the 4–300 K temperature range.

4 Results and Discussion

4.1 $KTaO_3$ Ceramics

In the first part of this chapter the processing and characterization of the $KTaO_3$ powders are described. The mechanochemically activated K_2CO_3-Ta_2O_5 powder mixtures were analyzed using XRD and IR spectroscopy. The phase composition, microstructure, chemical and structural homogeneity of the $KTaO_3$ powders after single- and double-heating at 800°C were analyzed in terms of FE-SEM and analytical TEM.

The conventional and the pressure-assisted sintering of the $KTaO_3$ powder compacts are presented in the second part. The phase composition, microstructure and homogeneity of the ceramics were investigated. The RF dielectric properties of the highly dense ceramics are also shown and discussed in relation to the processing.

In the last part the MW, THz and IR dielectric properties of the hot pressed $KTaO_3$ ceramics, prepared from the double-heated powders, are described. In addition, Raman spectra are also presented. The chapter concludes with an evaluation of the intrinsic dielectric behavior of the $KTaO_3$ ceramics.

4.1.1 Synthesis of the Powders

4.1.1.1 Mechanochemical Activation

The stoichiometric K_2CO_3-Ta_2O_5 starting-powder mixtures were homogenized for 4 h in the planetary mill (Chapter 3.1.1.2). According to the XRD analysis (Figure 4.1), the mixtures consist of the hydrated form of monoclinic K_2CO_3, i.e., $K_2CO_3 \cdot 1.5\ H_2O$ and orthorhombic Ta_2O_5. After 5 h of the high-energy milling the K_2CO_3 could not be detected anymore, instead, small peaks corresponding to the $K_4H_2(CO_3)_3 \cdot 1.5\ H_2O$ phase are present in the pattern. These peaks are hardly observable after 10 h of milling. The intensity of the peaks corresponding to the Ta_2O_5 phase decreased after the high-energy milling. The increased background of the patterns after the milling indicates the presence of the amorphous phase. A small amount of the pyrochlore $K_2Ta_2O_6$ phase was also formed. Note that the formation of the hydrogencarbonate phase upon high-energy milling was also observed in the Na_2CO_3-Nb_2O_5 system [158].

The IR spectra of the powder mixtures are shown in Figure 4.2. The spectrum of the homogenized mixture in the 900–1800 cm^{-1} range reveals absorption bands characteristic of the free carbonate ions: 1) the C–O asymmetrical stretching vibration (ν_3) at 1390 cm^{-1}, with two shoulders at 1445 cm^{-1} and 1365 cm^{-1}; 2) the C–O symmetrical stretching (ν_1) at 1060 cm^{-1}; and 3) a band at 1750 cm^{-1}, which corresponds to a combination of the ν_1 mode and the CO_3^{2-} in-plane deformation (ν_4). Even though the ν_1 vibration is IR inactive in many simple carbonates, it is activated in the hydrated form of K_2CO_3 because of the

slight distortion from original D_{3h} structure of the CO_3^{2-} ion (Figure 4.3) due to K^+ ions and water molecules [159,160].

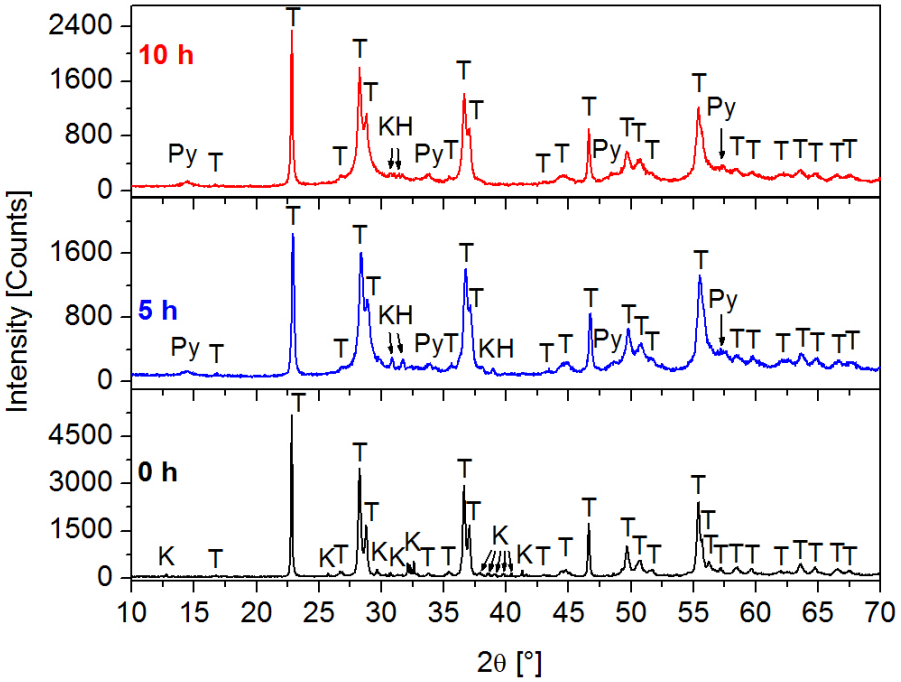

Figure 4.1: XRD patterns of the K_2CO_3-Ta_2O_5 powder mixtures after the homogenization (0 h) and after 5 h and 10 h of the mechanochemical treatment. Note the change of the scale for different patterns. T – Ta_2O_5[161]; K – $K_2CO_3 \cdot 1.5\ H_2O$ [162]; KH – $K_4H_2(CO_3)_3 \cdot 1.5\ H_2O$ [163]; Py – pyrochlore $K_2Ta_2O_6$ [164].

With increasing time of the high-energy milling, the intensity of the ν_3 band becomes progressively smaller and shifts to larger wavenumbers, reaching 1410 cm^{-1} after 10 h. In addition, new broad bands appear at 1625 cm^{-1}, 1550 cm^{-1} and 1320 cm^{-1}, indicating a gradual splitting of the ν_3 vibration into several bands. The ν_1 band broadens and shifts to 1040 cm^{-1}.

The change of the shape and the position of the ν_1 band, as well as the intensive splitting of the ν_3 band upon milling, is a consequence of the strong deformation of the CO_3^{2-} ion structure because of the carbonato complex formation. Splitting of the ν_3 mode ($\Delta\nu_3$) is sensitive to the type of the coordination and in principle increases from the unidentate ($\Delta\nu_3 < 100$ cm^{-1}) to the bridging type ($\Delta\nu_3 > 100$ cm^{-1}) of the coordination (Figure 4.3). In our case, the splitting is rather large, i.e., $\Delta\nu_3 = 1625–1320$ $cm^{-1} = 305$ cm^{-1}, indicating either the bidentate or bridging type. However, the splitting is also sensitive to the polarizing power of the central cation; therefore, the exact type of coordination is difficult to determine [165]. Furthermore, eventual overlapping of the band at 1625 cm^{-1} with the band characteristic for the hydrogencarbonate cannot be completely excluded [166].

To lower its symmetry the CO_3^{2-} ion has to reconstruct and the formed complex is amorphous, or at least nanocrystalline (Figure 4.1). An amorphous structure of the carbonato complex was reported by Rojac et al. [158,167], who performed high-energy milling studies on the Na_2CO_2-Nb_2O_5 and K_2CO_3-Nb_2O_5 systems. Importantly, the

formation of the carbonato complex in the precursor-powder mixtures was proved to strongly facilitate the homogeneity of the (K,Na,Li)(Nb,Ta)O_3 ceramics, resulting in excellent dielectric and piezoelectric properties [87,88].

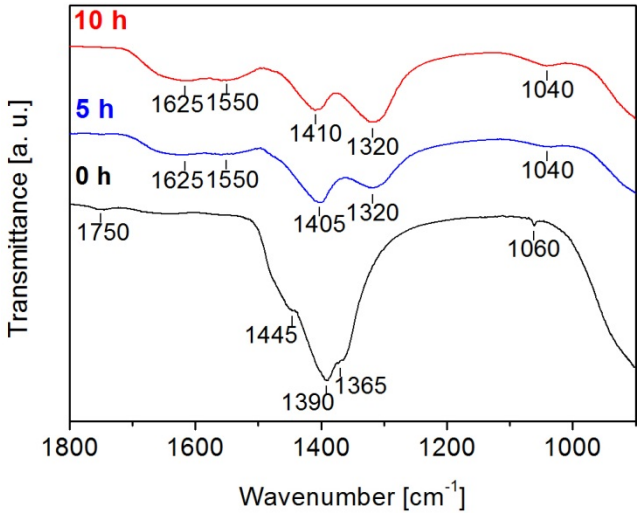

Figure 4.2: IR spectra of the K_2CO_3-Ta_2O_5 powder mixtures after the homogenization (0 h), and after 5 h and 10 h of the mechanochemical treatment.

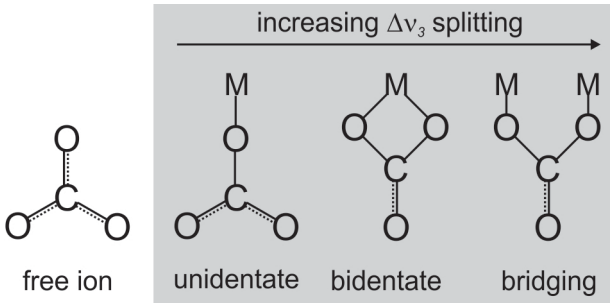

Figure 4.3: Structure of the carbonate CO_3^{2-} ion and its common coordination types. M – metal.

4.1.1.2 Phase Composition and Microstructure

The 10 h mechanochemically activated powder mixtures were single or double heated at 800°C for 4 h, and are subsequently denoted as the 1C and 2C powders, respectively. According to the XRD analysis, both powders are single-phase perovskites (Figure 4.4), without any significant difference between the two patterns.

The particle size distribution is shown in Figure 4.5. The median size d_{50} increases from 290 nm for the 1C powder to 410 nm for the 2C powder, which is related to the particle coarsening during the second calcination. The result is in agreement with the FE-SEM analysis shown in Figure 4.6a and b, in which cuboidal particles with sizes ranging from ~100 nm to ~500 nm can be observed. However, a careful inspection of the 1C powder micrograph reveals the presence of very small particles. The 5–20 nm large nanoparticles can be crystalline or amorphous, as evident from the high-resolution TEM micrograph (Figure 4.6c), and are attached to larger particles with rough and amorphous edges. No such nanoparticles were revealed in the case of the 2C powders.

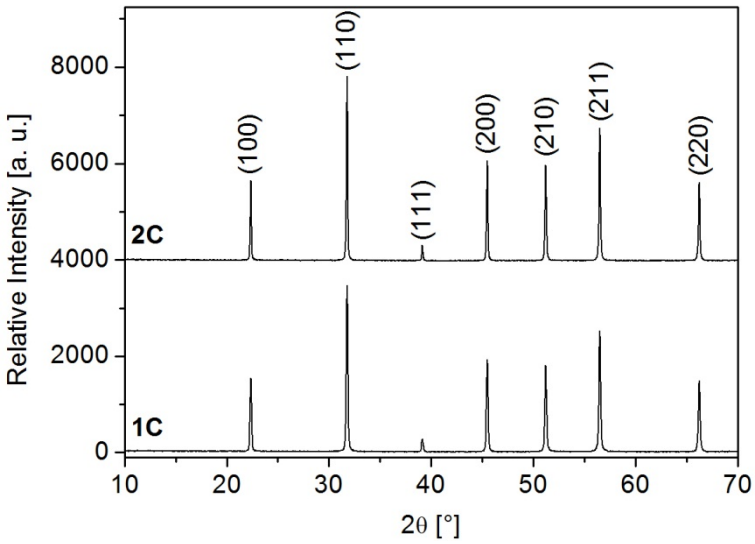

Figure 4.4: XRD patterns of the $KTaO_3$ powders after the first (1C) and the second (2C) heating at 800°C for 4 h. All peaks correspond to the perovskite $KTaO_3$ phase [142].

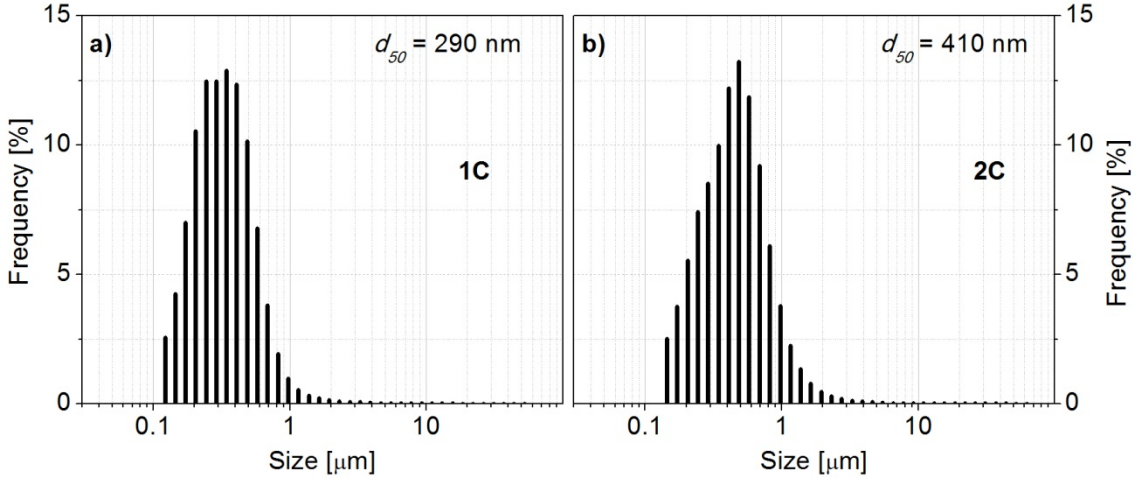

Figure 4.5: Particle size distribution with the median particle size d_{50} of the $KTaO_3$ powders after a) the first (1C) and b) the second (2C) heating at 800°C for 4 h.

The chemical composition of the 1C powders was determined by a combination of the quantitative EDXS analysis in terms of the K and Ta concentration and the quantitative EELS analysis in terms of the K and O concentration. Grains with thicknesses above 100 nm were studied with the EDXS only. The complete analysis is summarized in Figure 4.7. The well-crystallized large particles (area 1) have stoichiometric compositions with a K/Ta ratio of 1. The particles continuously show a slight excess of K, which could be caused artificially because the measurements were performed at the thinner, electron-transparent, parts of the particles. Some of the large particles have amorphized edges (area 2) and their composition is close to the stoichiometric value. They are chemically less homogeneous than the well-crystallized particles. The composition of area 3 strongly varies from K- to Ta-rich, having K/Ta ratios from 1.29 to 0.65. It corresponds to the poorly crystalline or amorphous nanoparticles.

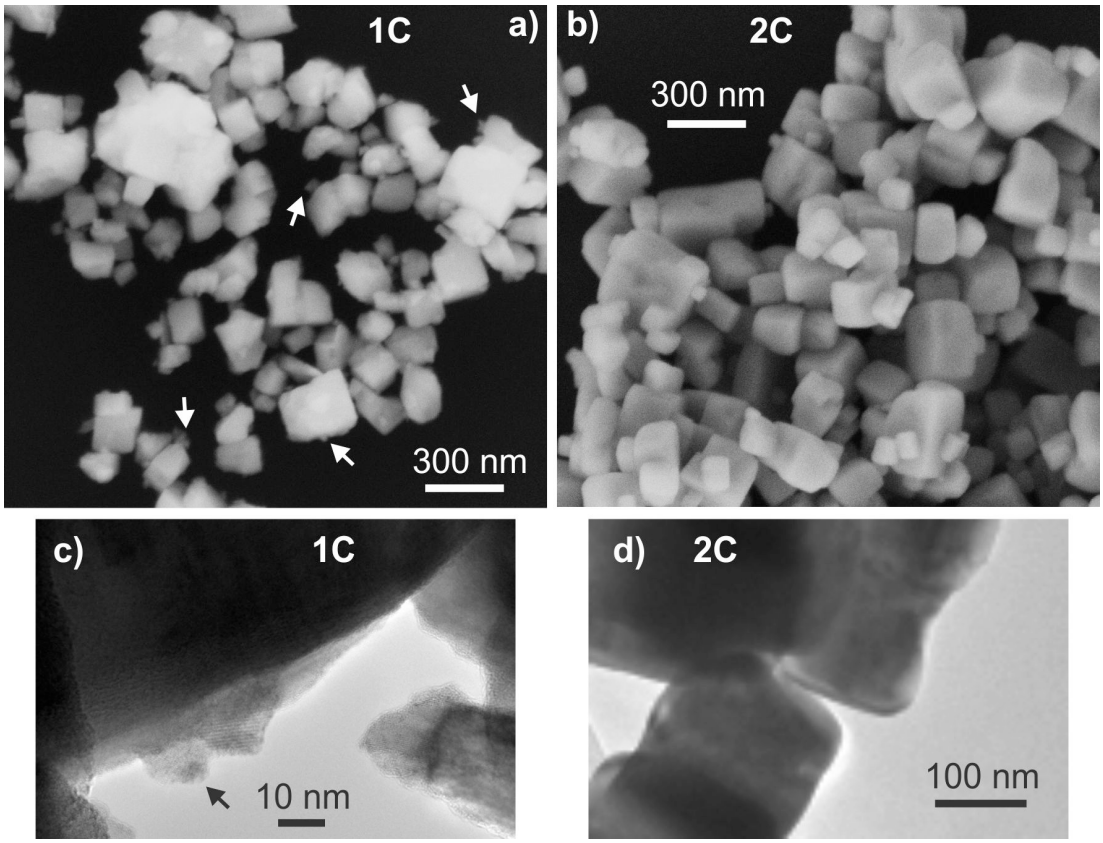

Figure 4.6: a) and b) FE-SEM, c) and d) TEM micrographs of the single (1C) and double (2C) heated $KTaO_3$ powders. Both heatings were performed at 800°C for 4 h. In a) the arrows indicate nanoparticles attached to the larger particles.

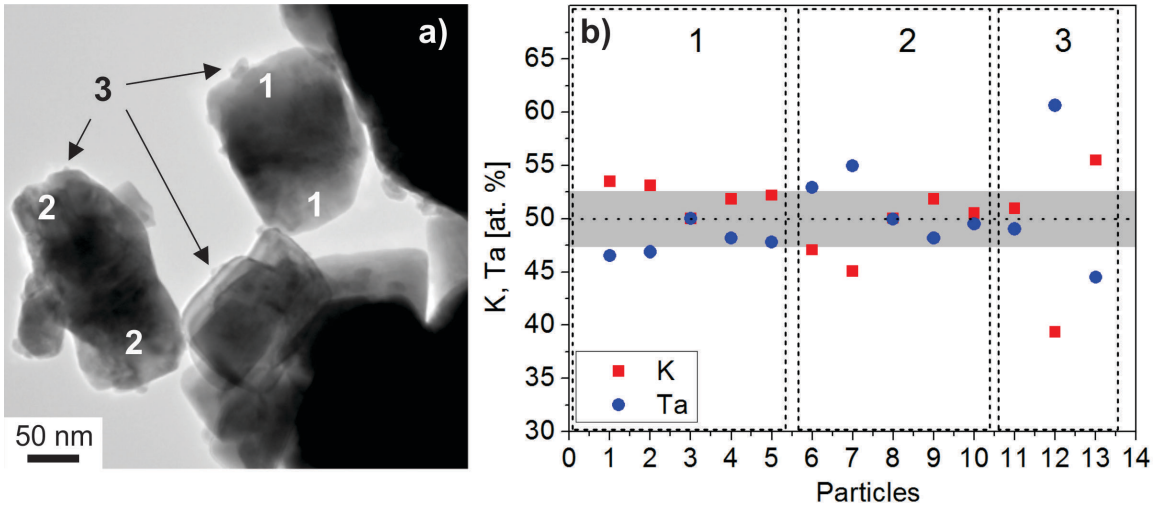

Figure 4.7: a) TEM micrograph of the 1C $KTaO_3$ powder, single heated at 800°C for 4h. Numbers denote the areas from which the composition shown in b) was obtained by the EDXS analysis. The area 1 represents well-crystallized cubic-shaped particles; the area 2 represents the particles with disturbed edges; while the area 3 represents poorly crystalline or amorphous nanoparticles attached to larger ones. In b) the dotted horizontal line denotes the nominal compositions, while grey areas correspond to the standard deviation ± 2δ (± 2.6 at.%). For the concentration of O obtained by EELS see Ref. [145].

Even though the XRD analysis indicated a phase-pure composition the above-

described morphological and compositional investigations revealed rather heterogeneous $KTaO_3$ powders after one heating at 800°C. The partially amorphous nanoparticles with a strongly varying composition could be the residuals of the partially amorphous mechanochemically activated powders. Apparently, at least two heatings at 800°C are necessary for the preparation of $KTaO_3$ powders with enhanced homogeneity.

4.1.2 Sintering, Phase Composition and Microstructure of the Ceramics

The 1C powder compacts were sintered in air at 1325°C for 1 h and the obtained relative density of the ceramic (1C-Air) was 81 %. According to the XRD, the ceramic consisted of the perovskite phase (Figure 4.8a); however, weak reflections assigned to the $K_6Ta_{10.8}O_{30}$ phase [168] are present in the detailed view of the pattern shown in Figure 4.8b. According to the Ta_2O_5-$KTaO_3$ phase diagram [70] (Figure 1.9) this is the high-temperature phase, which was formed because of the losses of potassium oxide during the sintering and was kinetically stabilized upon cooling. To reduce the losses of the potassium species [169] and to enhance the densification [170] the powder compacts were also sintered in an oxygen flow. The 1C-O_2 ceramic had a higher relative density than the 1C-Air ceramic, i.e., 85 %; however, traces of the $K_6Ta_{10.8}O_{30}$ phase were still present. Qualitatively, the same sintering behavior was also observed for the 2C powder compacts.

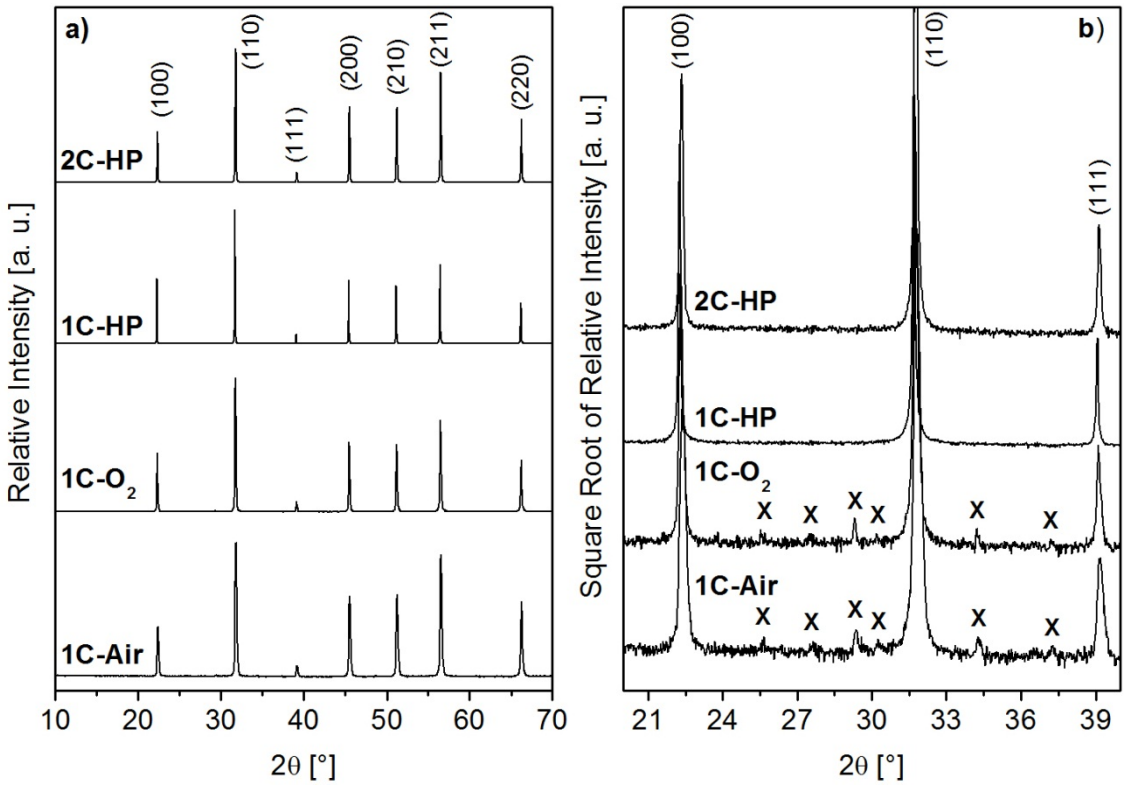

Figure 4.8: XRD patterns of the 1C-Air, 1C-O_2, 1C-HP and 2C-HP $KTaO_3$ ceramics. In b) detailed view of the square rooted XRD patterns in the 20–40° 2θ range is shown. Peaks denoted with the Miller indices correspond to the perovskite $KTaO_3$ phase [142]. X – $K_6Ta_{10.8}O_{30}$ phase [168].

External pressure increases the driving force for the densification of the powder compacts upon sintering [171]. Hot pressing of the 1C and 2C powder compacts was

performed at 1250°C for 2h. The obtained 1C-HP and 2C-HP ceramics had relative densities equal to 98 % and 95 %, respectively, and no peaks corresponding to secondary phases could be detected in the XRD patterns (Figure 4.8).

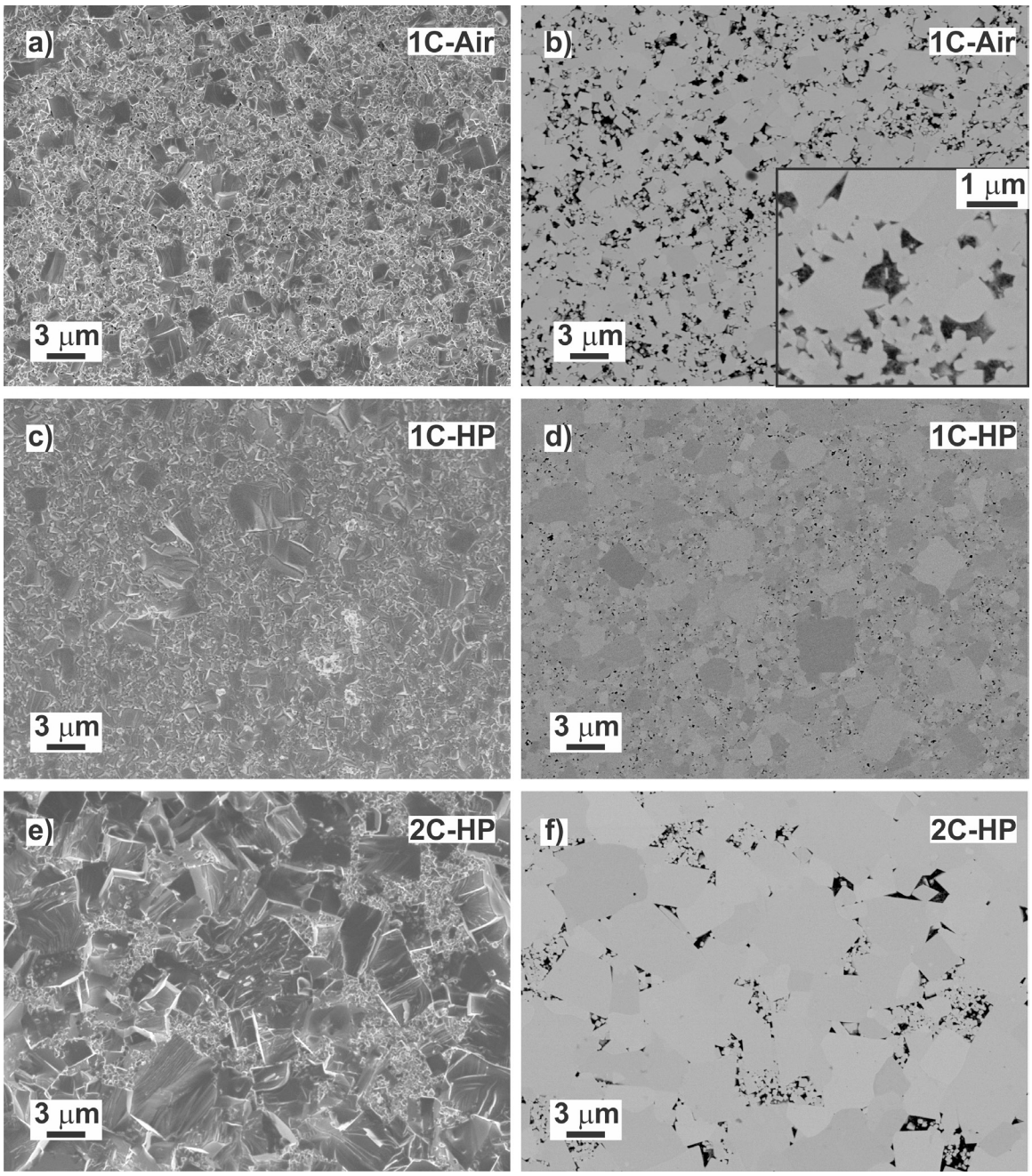

Figure 4.9: FE-SEM micrographs of the fractured (a, c, e) and polished (b, d, f) surfaces of the $KTaO_3$ ceramics prepared by sintering in air at 1325°C (1C-Air) and by hot pressing at 1250°C (1C-HP, 2C-HP). The images of the fractured and polished surfaces were obtained by the secondary- and back-scattered-electron imaging modes, respectively.

FE-SEM micrographs of the fractured and polished surfaces of the 1C-Air ceramics, sintered in air at 1325°C, are shown in Figure 4.9a and b, respectively. A bimodal grain size distribution is observed, with smaller grains below ~500 nm and larger grains reaching a size of 1-2 μm. Approximately 10-μm-large inclusions of the secondary $K_6Ta_{10.8}O_{30}$ phase were observed at the edge of the sample only (not shown here),

indicating that the losses of the potassium species appear mainly from the surface.

A bimodal grain size distribution can also be observed in the micrographs of the 1C-HP and 2C-HP ceramics that were prepared by the hot pressing at 1250°C of single- and double-heated powder compacts, respectively (Figure 4.9c, d, e and f). Compared to the 1C-Air ceramics, the large grains are bigger and can exceed a size of 3 μm. Smaller grains are present inside the porous regions. The grain size distribution is more uniform in the 2C-HP ceramic, though the distribution is still bimodal, with larger grains reaching a size of 5 μm. A relatively intensive contrast between the individual grains is observed in the back-scattered (BE) micrograph of the polished surface of the 1C-HP ceramic shown in Figure 4.9d. It could be a consequence of the different relative orientations of the individual grains and/or a heterogeneous chemical composition of the ceramic, which was confirmed by the TEM analysis (see discussion below).

The poor densification of the $KTaO_3$ ceramics upon atmospheric sintering has been attributed to the covalent character of the Ta–O bond [72]. In a sintering study of covalent materials, such as Si and β-SiC, Greskovich and Rosolowski observed that the low-energy surface diffusion and gas-phase transport, prevailing at low heating temperatures, were much more pronounced than the high-energy material-transport mechanisms, i.e., lattice and grain-boundary diffusion, resulting in localized grain and pore coarsening with only negligible macroscopic densification [172]. In our case the hot pressing enhanced the densification; however, the external pressure during sintering does not influence the grain growth [171] and the broad grain size distribution observed in the atmosphere-sintered ceramics was also retained in the hot pressed ceramics.

The compositional TEM analysis results of the 1C-HP ceramic are summarized in Figure 4.10. Similar to the 1C powder, the sample can be roughly divided into three areas. The majority of the large grains, with a stoichiometric composition within the $\pm 2\delta$ relative error, represent area 1. Area 2 corresponds to the large and small grains in their vicinity, having Ta-rich compositions with a K/Ta ratio in the range from 0.55 to 0.90. Some of the grains also had K-rich compositions and are marked with area 3. Their K/Ta ratio reached values up to 1.30. The deviation interval of the K/Ta ratio observed in the 1C-HP ceramic is very similar to the deviation observed in the 1C powder, i.e., 0.65–1.29 (Figure 4.7). Heating at 1250°C for 2h did not remove the compositional heterogeneities present in the powders prepared at 800°C.

Further TEM analyses at higher magnifications revealed presence of a small amount of the amorphous or partially crystalline triple pockets, situated between the large grains (Figure 4.11). The pockets are strongly K-deficient, with a K/Ta ratio of 0.55, while the adjacent grains have a ratio of 0.8, as determined by the combined EDXS/EELS analysis. In both cases the K/O ratio has a value of 0.28 (Table 4.1), which is less than the stoichiometric value of 0.33. The presence of the amorphous triple pockets could be connected to the appearance of the intergranular liquid phase upon sintering. According to the Ta_2O_5-K_2CO_3 phase diagram (Figure 1.8) the temperature of the eutectic melting between $KTaO_3$ and K_2TaO_4 is at 1090°C. [69] Note that the nanoparticles present in the 1C powder had K-rich and K-deficient compositions (Figure 4.7).

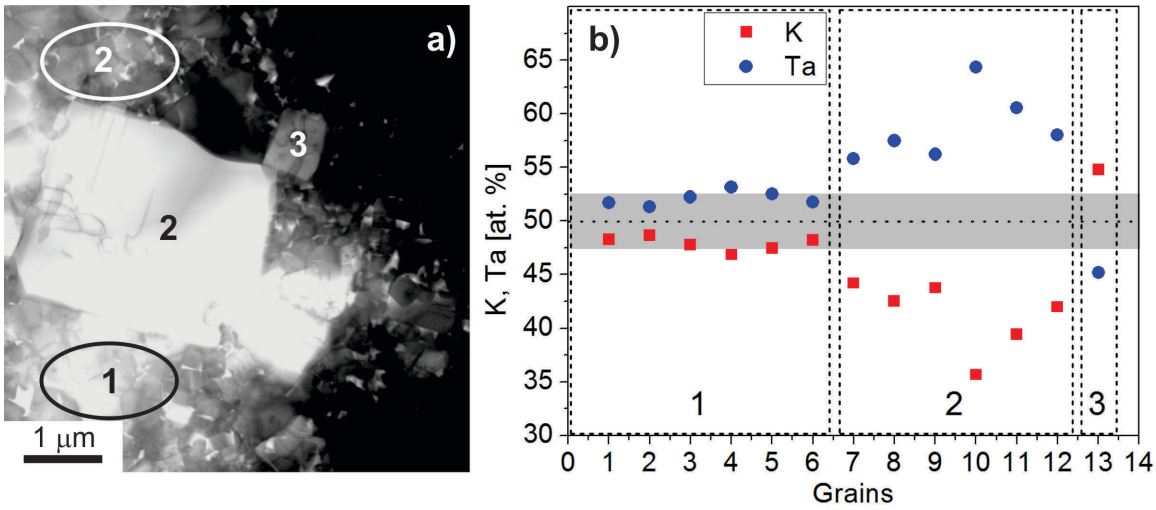

Figure 4.10: a) TEM micrograph of the 1C-HP $KTaO_3$ ceramic prepared from the single-heated powders by hot pressing at 1250°C. Numbers denote the areas from which the composition shown in b) was obtained by the EDXS analysis. The area 1 represents small grains with the perovskite composition and a slightly Ta-rich tendency. The area 2 represents large grains and small grains in their vicinity, both with a similar Ta-rich composition. The number 3 correspond to either small or large grains with a K-rich composition. In b) the dotted horizontal line denotes the nominal compositions, while grey areas correspond to the standard deviation ± 2δ (± 2.6 at.%). For the concentration of O obtained by EELS see Ref. [145].

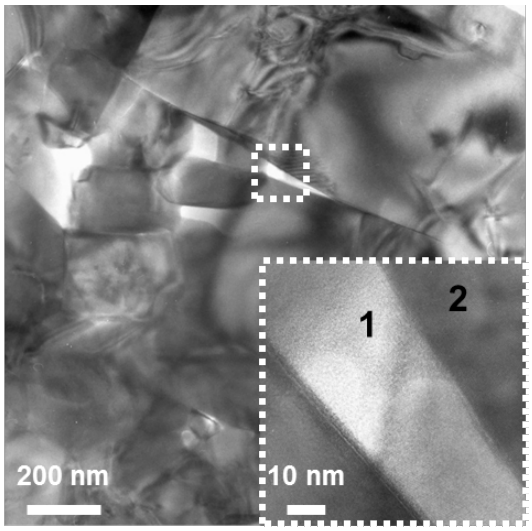

Figure 4.11: TEM micrograph of the 1C-HP $KTaO_3$ ceramic. The amorphous triple pocket (1) between the two grains (2) is shown in the inset. Numbers represent the areas where the combined EDXS/EELS analyses were performed.

Table 4.1: Composition of the amorphous triple pocket and the adjacent grain observed in the 1C-HP ceramic obtained by the combined EDXS and EELS analysis. The nominal values in the perovskite $KTaO_3$ phase are also given.

Atom	Triple Pocket (1)	Grain (2)	Nominal
K [at. %]	15.8 ± 0.8	17.0 ± 0.9	20
Ta [at. %]	28.5 ± 0.8	21.5 ± 0.6	20
O [at. %]	55.7 ± 0.9	61.5 ± 1.1	60

A TEM micrograph of the 2C-HP $KTaO_3$ ceramics, prepared from the double-heated powders, is shown in Figure 4.12. Again, compositional deviations were revealed by the EDXS analysis. Smaller grains are either stoichiometric within the $\pm 2\delta$ error, or they show a K-rich tendency with a K/Ta ratio even up to 1.6 (Figure 4.12b). On the other hand, larger grains can be either stoichiometric, Ta-rich with a K/Ta ratio reaching 0.8, or K-rich with a K/Ta ratio up to 1.6 (Figure 4.12c). In some of the grains the compositional variations within the grains were determined. The examples are shown in the insets of Figure 4.12b and c. A thorough investigation of the sample revealed that the amorphous triple pockets, determined in the 1C-HP ceramic, are not present. In this respect the structural homogeneity of the 2C-HP ceramic is enhanced.

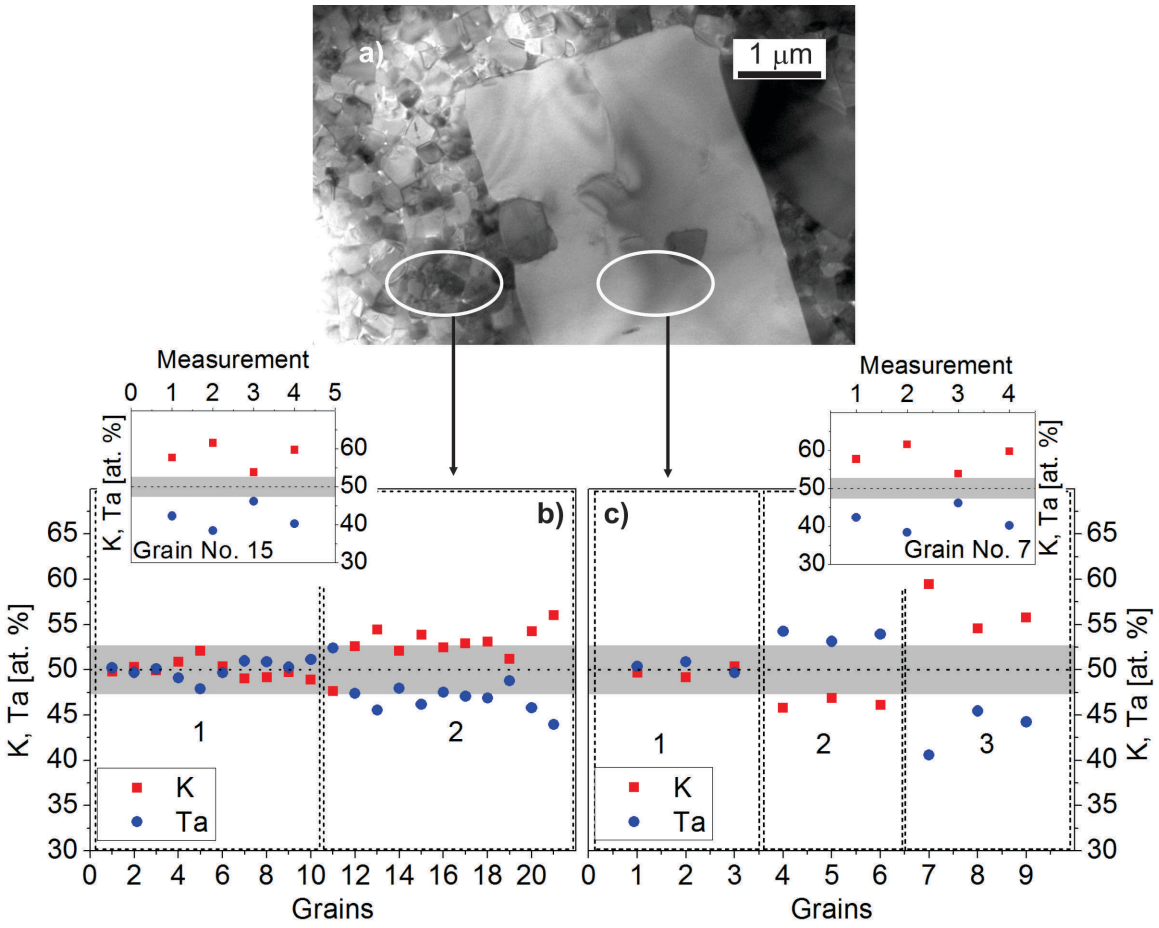

Figure 4.12: a) TEM micrograph of the 2C-HP $KTaO_3$ ceramic prepared from the double-heated powders by hot pressing at 1250°C. The areas from which the compositions shown in b) and c) were obtained by the EDXS analyses are marked. In b) area 1 represents small grains with the perovskite composition, while area 2 represents small grains with the K-rich compositions. In c) area 1 represents large grains with a perovskite composition, area 2 represents large grains with Ta-rich compositions and area 3 represents the grains with K-rich compositions. Some of the grains showed large compositional variations. Examples are shown in the insets of b) and c). The dotted horizontal line denotes the nominal compositions, while the grey areas correspond to the standard deviation $\pm 2\delta$ ($\pm$ 2.6 at.%) for each element.

The global chemical composition of the 1C-HP and 2C-HP ceramics was determined by a quantitative chemical analysis (Table 4.2). The K/Ta molar ratio in both ceramics is equal to 0.98; however, the deviation from the stoichiometric value is within the

measurement uncertainty. Small amounts of Co and W are present in both ceramics. This is a consequence of the wear of the milling vial and the balls during the high-energy milling. The slight difference in the amounts of impurities in the two samples is a consequence of the different milling vials and balls used for individual batches.

Table 4.2: Chemical composition of the 1C-HP and 2C-HP $KTaO_3$ ceramics determined by the ICP spectrometry. The nominal values for K and Ta in the perovskite phase are also given.

Atom	1C-HP	2C-HP	Nominal
K [w. %]	14.3 ± 0.4	14.4 ± 0.4	14.6
Ta [w. %]	67.9 ± 2.0	68.2 ± 2.0	67.5
K [at. %]	19.7 ± 0.6	20.1 ± 0.6	20
T [at. %]	20.2 ± 0.6	20.6 ± 0.6	20
Co [ppm]	77 ± 2	71 ± 2	/
W [ppm]	600 ± 20	900 ± 30	/

4.1.3 Radio-Frequency Dielectric Properties

The RF dielectric properties of the 1C-HP and 2C-HP $KTaO_3$ ceramics were measured upon cooling from 300 K to 5 K and the 1-kHz values of dielectric permittivity ε' and dielectric losses tanδ are compared in Figure 4.13. The permittivity ε' of the 1C-HP ceramic increases from 240 at 298 K to 2450 at 5 K, while a much larger increase is observed in the 2C-HP ceramic, with the permittivity reaching 4090 at 5 K. The losses of the 1C-HP ceramic are 0.053 at 298 K and reach 0.0066 at 5K. On the other hand, the losses of the 2C-HP ceramic are 0.0024 and 0.0048, at 298 K and 5 K, respectively. A strong peak in the spectrum of the 2C-HP ceramic is observed at 46 K, while only a shoulder is present at the same temperature in the spectrum of the 1C-HP ceramic. Several relaxation peaks are observed in the temperature range from 200 K to 70 K in both the loss spectra.

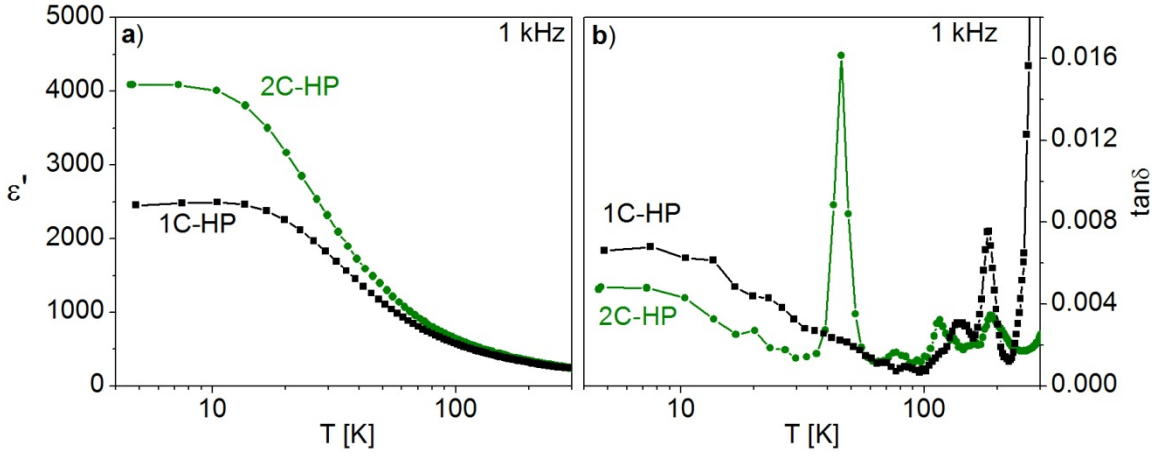

Figure 4.13: a) Temperature dependence of dielectric permittivity ε' and b) dielectric losses tanδ of the 1C-HP and 2C-HP $KTaO_3$ ceramics measured at 1 kHz. Note the logarithmic scale in both cases. Lines between the experimental points are guides to the eye.

The frequency dependence of the losses tanδ of the 2C-HP ceramic in the temperature

range from 250 K to 5 K is shown in Figure 4.14a. The maxima, appearing in the three temperature ranges marked with numbers, follow the Arrhenius law (Equation (1.10), Figure 4.14b) and their attempt frequencies ω_0 and activation energies E_a are given in Table 4.3.

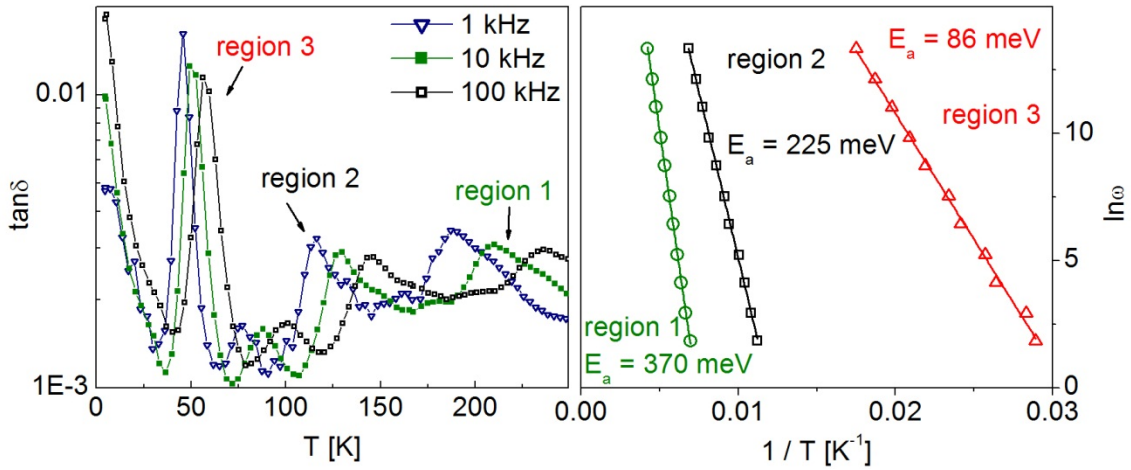

Figure 4.14: a) Temperature dependence of dielectric losses tanδ of the 2C-HP ceramic measured at 1 kHz, 10 kHz and 100 kHz. Different frequency-dispersion regions are marked. b) Arrhenius plots of the three dispersion regions in the frequency range from 100 Hz to 100 kHz. Calculated activation energies E_a are also given.

Table 4.3: Arrhenius activation energy E_a and attempt frequency ω_0 of the three frequency-dispersion regions observed in the loss spectra of the 2C-HP ceramic (Figure 4.14).

Arrhenius Parameter	Region 1	Region 2	Region 3
E_a [meV]	370	225	86
ω_0 [s^{-1}]	5.4 x 10^{13}	3.6 x 10^{13}	2.0 x 10^{13}

4.1.3.1 Discussion

The 2C-HP ceramics, prepared from the double-heated powders, exhibit an almost doubled 1-kHz permittivity ε' (4080) and lower dielectric losses tanδ, both measured at 5 K, as compared to the 1C-HP ceramics, prepared from the single-heated powders. The enhancement of the dielectric properties is attributed to the enhanced structural homogeneity and changed grain size distribution. Compared to the literature, this is one of the highest ε' values reported for $KTaO_3$ ceramics (Table 1.5), and is comparable to the single-crystal value of 4500 [20,75].

Several relaxations are observed as the frequency-dependent peaks in the tanδ spectra of both ceramics, and these were analyzed in detail for the 2C-HP ceramics (Figure 4.14 and Table 4.3). The relaxations indicate the presence of re-orientable dipolar entities inside the perovskite crystal lattice. Their concentration is small, as indicated by the Arrhenius behavior [22]. The presence of these relaxations, which were not observed in the single crystals, was previously reported for $KTaO_3$ ceramics; however, no detailed analysis was made [71,74,75]. However, the intensity of the corresponding tanδ-peaks was found to be strongly processing dependent.

The activation energy E_a and the attempt frequency ω_0 obtained for region 1 are very close to the characteristic values for the Co^{2+}-doped $KTaO_3$ (Table 1.4) [26]. Note that 77 ppm and 71 ppm of Co were detected in the 1C-HP and 2C-HP ceramics, respectively (Table 4.2).

The presence of W was also detected in the ceramics by chemical analysis. The appearance of the dispersion region 2 could be associated with this W; however, no data on the dielectric properties of W-doped $KTaO_3$ could be found. The relaxation feature marked as region 3, with the activation energy of 86 meV, is the typical relaxation observed in $KTaO_3$ ceramics as well as in single crystals as the 1 kHz-tanδ peak at ~45 K (Table 1.4), which appears to be related to Li-impurities [20,24,25].

4.1.4 Broadband Dielectric Properties

Because of the enhanced properties, the 2C-HP $KTaO_3$ ceramics, prepared by hot pressing double-heated powder compacts at 1250°C, were selected for the MW, THz and IR dielectric characterization and lattice-dynamics evaluation. The Raman spectra were also analysed.

4.1.4.1 Microwave Properties

The temperature dependence of the dielectric permittivity ε' and the dielectric losses tanδ, measured in the MW frequency range (2–6 GHz) is shown in Figure 4.15. Similar to the RF-range (Figure 4.13a), the permittivity increases with a decreasing temperature from ~220 at room temperature to 3420 at 20 K. The values of the losses at the respective temperatures have the values 9.5 x 10^{-3} and 5.2.x 10^{-3}, which is higher than in single crystals, where one finds at 3 GHz: 1.4 x 10^{-4} at 300 K and 4.2 x 10^{-5} at 5.4 K (Figure 1.4) [15].

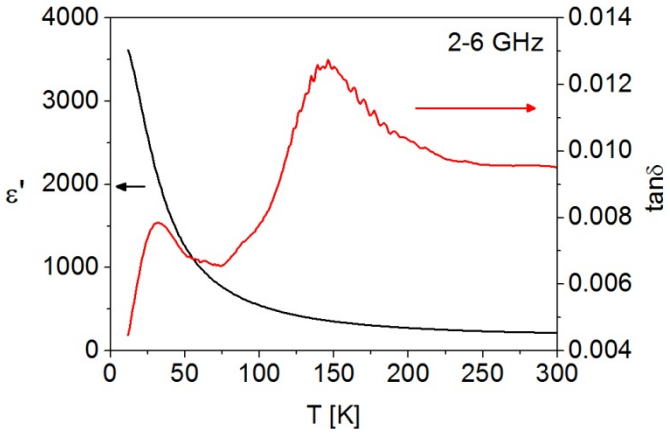

Figure 4.15: Temperature dependence of the permittivity ε' and dielectric losses tanδ of the 2C-HP ceramic measured in the 2–6 GHz frequency range.

Two loss peaks are observed at ~145 K and 32 K. The first was measured at a frequency of 4.76 GHz and assuming an Arrhenius-type temperature dependence of the relaxation frequency it corresponds to the relaxation region 3, observed in the RF-losses spectrum (Figure 4.14). The origin of the second maximum is more unclear. Axelsson and

co-workers [71] measured $KTaO_3$ ceramics at ~1 GHz and observed a peak in tanδ at ~20 K. Based on the work of Breeze et al. [173], who reported that in the low-permittivity oxide ceramics ($\varepsilon' < 10$) a peak in tanδ at ~45 K (9.37 GHz) is associated with the presence of grain boundaries, the authors assigned it to the vacancies-induced dipoles at the grain boundaries. However, the low-temperature maximum MW loss-spectrum is in the same temperature range as reported before for single crystals by Ivanov et al. [174,175]. Here it was ascribed to the interaction between the transverse optic and longitudinal acoustic modes, partially driven by the defects.

4.1.4.2 Terahertz and Infrared Properties

The IR reflectivity spectrum of $KTaO_3$ ceramics measured at room temperature is shown in Figure 4.16a. For comparison we also plot the reflectivity spectrum calculated from the measured THz transmission data.

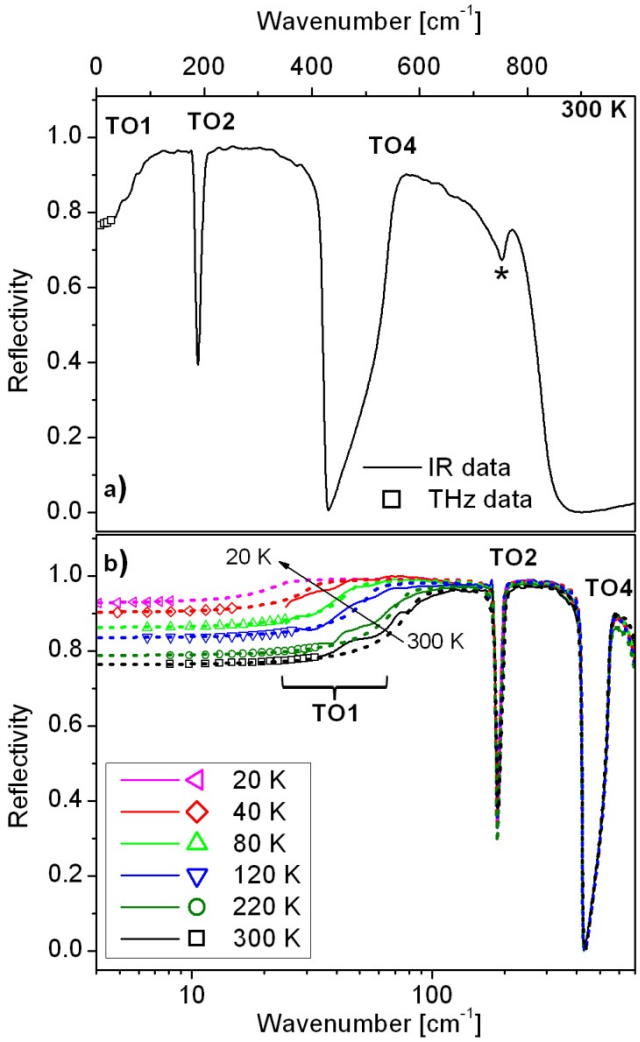

Figure 4.16: IR reflectivity spectra (lines), together with the reflectivity calculated from THz transmission data (symbols), of 2C-HP $KTaO_3$ ceramics measured at a) 300 K and b) at selected temperatures in the 300–20 K range. In b) note the logarithmic wavenumber scale. Approximate positions of the TO1, TO2 and TO4 polar modes are marked. In b) the experimental data are compared to the fits (dashed lines).* – two-phonon combination band.

The measured normal reflectivity $R(\omega)$ is related to the complex dielectric permittivity $\varepsilon^*(\omega)$ by Equation (10.1). We performed a simultaneous fit of the IR reflectivity spectra and the complex permittivity spectra obtained from THz measurements. For this we used the so-called generalized 4-parameter oscillator model with the factorized form of the complex permittivity (Equation (10.3). A temperature-independent value of 4.3[176] was taken for the high-frequency electronic polarization ε_∞.

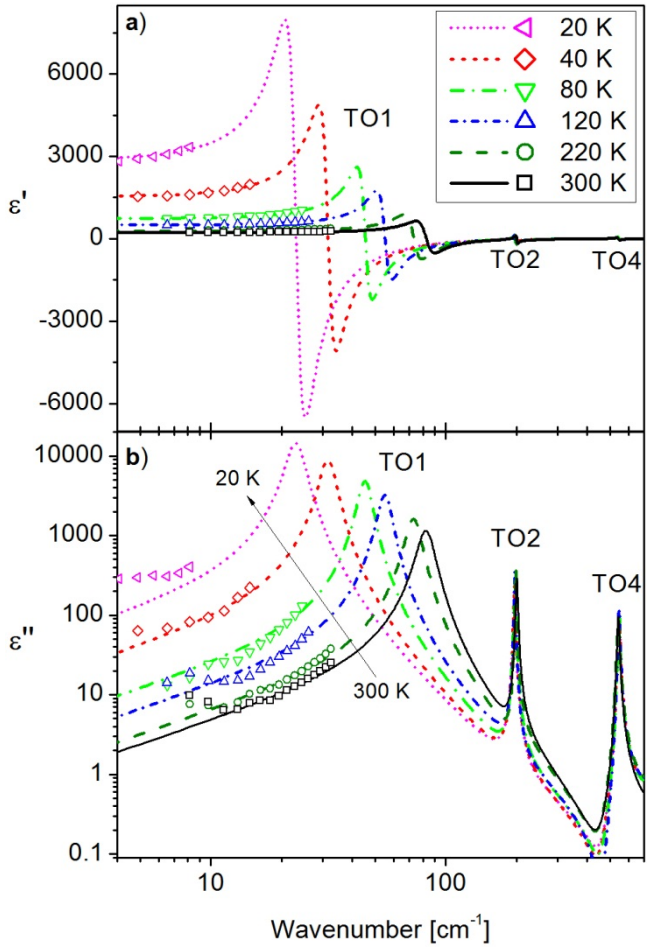

Figure 4.17: a) Real $\varepsilon'(\omega)$ and b) imaginary $\varepsilon''(\omega)$ parts of the complex dielectric permittivity $\varepsilon^*(\omega)$ of the 2C-HP $KTaO_3$ ceramics calculated from the simultaneous fits of the IR and THz data (the latter shown as the symbols) measured at different temperatures.

A good agreement between the experimental data and the fits is seen in Figure 4.16b. The values of the fit parameters were used to calculate the ε' and ε'' spectra, which are plotted in Figure 4.17 along with the permittivity spectra directly calculated form the THz transmission data. The three polar phonons, which are allowed in the cubic $Pm\bar{3}m$ structure, are observed as distinct resonances in the complex permittivity spectra and correspond to the three most pronounced reflection bands in Figure 2 (TO1, TO2 and TO4). An additional band is present in the reflectivity spectrum at 761 cm^{-1}; it is a combination band of the TO2 + TO4 modes, which does not correspond to any fundamental vibrational mode. The room-temperature positions of the TO1, TO2 and TO4 modes are 83 cm^{-1}, 201 cm^{-1} and 543 cm^{-1}, respectively, and are in agreement with the IR literature data on $KTaO_3$ single crystals [176,177]. The temperature dependence of

the frequencies ω_{TOj} obtained by fitting is shown in Figure 4.18.

The resonance corresponding to the TO1 mode is the most pronounced one in the spectra and its dielectric strength strongly increases with decreasing temperature. The TO1 mode strongly softens, and its ω_{TO1} value reaches 23 cm^{-1} at 20 K. The TO1 mode is called the soft mode (SM), and the ω_{TO1} temperature dependence is comparable to that found in single crystals by hyper-Raman scattering [122]. The damping constant γ_{TO1} of the TO1 mode (shown in the inset of Figure 4.18) is also in qualitative agreement with the hyper-Raman data; it continuously decreases from a room temperature value of 15.1 cm^{-1} to 4.6 cm^{-1} at 20 K.

Ichikawa et al. [178] investigated a single crystal using time-domain THz spectroscopy; above 100 K they report slightly lower values of ω_{TO1} and γ_{TO1} compared to our results and the hyper-Raman scattering data. However, in Ref. [178] the data were obtained only in a narrow frequency range below ω_{TO1} and we believe that within the accuracy of the experiments their results correspond well to our data on ceramics.

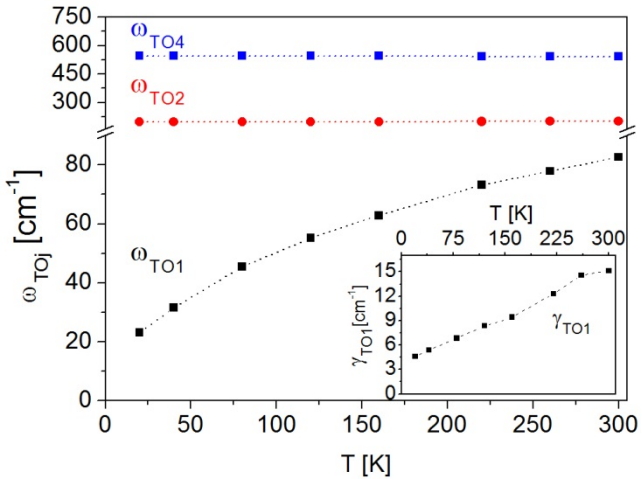

Figure 4.18: Temperature dependences of the ω_{TO1}, ω_{TO2} and ω_{TO4} polar phonon frequencies. The lines are guides to the eye. Inset: Temperature dependence of the TO1 mode damping constant γ_{TO1}.

To analyze further the polar phonons dynamics in $KTaO_3$ ceramics, the mode-plasma frequencies Ω_{TOj} (Equation (10.7)) and the total plasma frequency Ω_{TOT} were calculated at each measured temperature (Figure 4.19). In agreement with the general sum rule (Equation (10.8)), Ω_{TOT} is not temperature dependent. The room-temperature values of the mode-plasma frequencies are: Ω_{TO1} = 1197 cm^{-1}, Ω_{TO2} = 492 cm^{-1} and Ω_{TO4} = 823 cm^{-1}. Ω_{TO4} does not change with the temperature, while Ω_{TO1} and Ω_{TO2} show slight temperature dependences: Ω_{TO1} = 1236 cm^{-1} and Ω_{TO2} = 403 cm^{-1} at 20 K. These dependences indicate a rather small, but detectable, coupling of the two low-frequency modes.

The mode-plasma frequencies are proportional to the effective charges of the modes and may be used for the assignment of the dielectric response function to the atomic displacements in the crystal lattice. A comparison of the Ω_{TOj} values of the $KTaO_3$ ceramics to the literature data on typical cubic ABO_3 perovskites [179] (Table 10.1)

indicates that the TO1 mode primarily corresponds to the vibration of Ta^{5+} ions against rigid O_6 octahedra (Slater mode). The TO2 mode is mainly related to the vibration of K^{1+} ions against a rigid TaO_6 structure (Last mode), while the TO4 mode corresponds to a bending of the O_6 octahedra (Axe mode) (Figure 10.1). The result is also in agreement with the theoretical calculations [180].

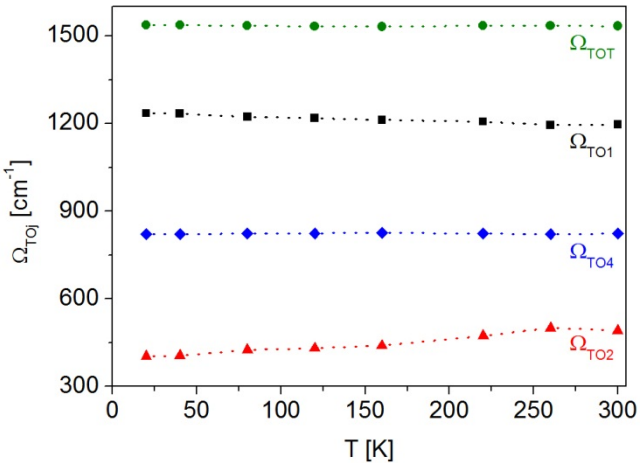

Figure 4.19: Temperature dependences of the Ω_{TO1} Ω_{TO2} and Ω_{TO4} mode-plasma frequencies, together with the overall plasma frequency Ω_{TOT}. Lines between the points are guides to the eye.

4.1.4.3 Analysis of the Broadband Dielectric Properties

As presented in Figure 4.20, the increase of the 1-kHz permittivity ε' with decreasing temperature from 300 K to 30 K follows the Curie-Weiss law (Equation (1.1)), and the obtained fitting parameters (Table 4.4) are in good agreement with the single-crystal data of Wemple et al. [181] Because the quantum fluctuations become important, the permittivity ε' starts to deviate strongly from the Curie-Weiss behavior below ~30 K. Thus, the data can be fitted by the Barrett equation (Equation (1.8)). The obtained fitting parameters correspond well to those previously reported for single crystals, though a slightly lower value of C is found in our ceramic samples (Table 4.4, Table 1.3) [21,121].

On the other hand, softening of the TO1 (SM) mode obeys the Cochran law (Equation (10.9), Figure 4.20). The extrapolated critical temperature can be estimated only roughly because we have only a small number of data points: $T_{cr} = -4 \pm 2$ K; it is somewhat less than that obtained from the Barrett fit of the permittivity. The constant A, obtained from the Cochran fit, and the Curie-Weiss constant are related through: $C = \Omega^2_{SM} / A$. By taking the room-temperature value $\Omega_{SM} = 1197$ cm^{-1}, the calculated Curie-Weiss constant is 62,300 K, which is in reasonable agreement with the value obtained from the Curie-Weiss fit, i.e., 59,400. A deviation of the soft-mode dynamics from the Cochran law is not observed because the sample became too opaque for the THz transmission measurements below ~20 K.

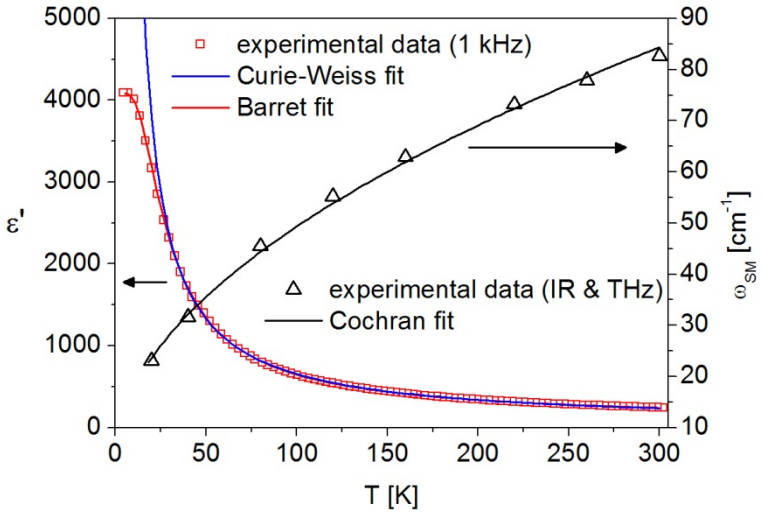

Figure 4.20: Temperature dependence of the 1-kHz permittivity ε' and soft-mode frequency ω_{SM}. Blue line: Curie-Weiss fit from 300 K to 30 K. Red line: Barret fit from 300 K to 5 K; Black line: Cochran fit from 300 K to 20 K.

Table 4.4: Curie-Weiss, Barret and Cochran fit parameters of the 2C-HP $KTaO_3$ ceramics (Figure 4.20).

Curie-Weiss Fit			**Barret Fit**				**Cochran Fit**	
C	***T_0***	***ε_b***	***C***	***T_1***	***T_0***	***ε_b***	***A***	***T_0***
59400 K	4 K	35	51000 K	56 K	15 K	64	23 $K^{-1}cm^{-2}$	-4 K

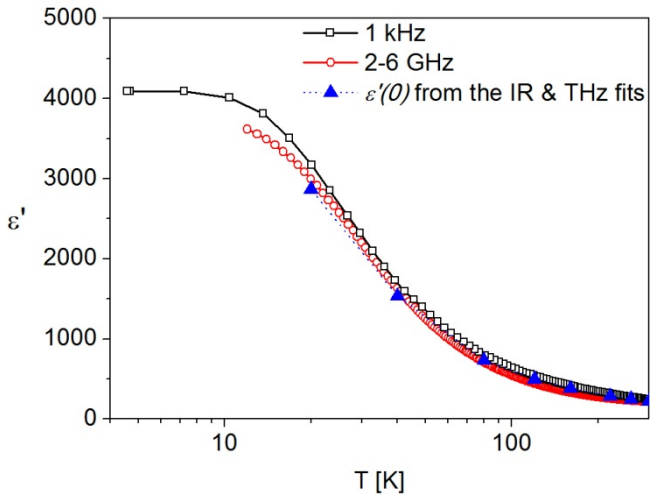

Figure 4.21: Temperature dependence of the RF (1 kHz) and MW (26 GHz) dielectric permittivity ε' compared to the phonon contribution calculated from the IR and THz data fits. Lines between the experimental points are guides to the eye.

The 1-kHz dielectric permittivity ε' is compared in Figure 4.21 to the one measured in the MW range and the phonon contribution $\varepsilon'(0)$, obtained from the IR and THz fits. The small differences at low temperatures are within the uncertainty of the MW experiment and of the IR fit. Slightly different microstructures of individual samples can also

contribute to this difference.[i] Nevertheless, the analysis shows that the low-frequency permittivity ε' in $KTaO_3$ ceramics is mainly of intrinsic origin, i.e., arising from the contribution of the polar phonons.

4.1.4.4 Raman Measurements

Raman spectra of the ceramics measured at selected temperatures are presented in Figure 4.22. At higher temperatures the spectra are dominated by the second-order features with broad room-temperature maxima at 119 cm^{-1}, 159 cm^{-1}, 280 cm^{-1}, 461 cm^{-1}, 584 cm^{-1}, 691 cm^{-1} and 746 cm^{-1}, which are in good agreement with the single-crystal data [182]. At temperatures below ~150 K sharp bands, corresponding to the IR active modes, start to emerge and their intensity increases with decreasing temperature. Similar Raman-forbidden first-order scattering was also observed at low temperatures in the "nominally pure" $KTaO_3$ single crystals. It was ascribed to the local polar nanoregions, which can either dynamic – in this case they could be of intrinsic (anharmonic) origin – or static, induced by some unavoidable symmetry-breaking defects [183,184]. The cluster dynamics is usually relaxational and it appears as a so-called central peak in the microwave spectra. No such feature was observed in our experiments. We can thus conclude that the most plausible origin of the first-order Raman scattering would be defects due to the presence of Co (and W) detected by the chemical analysis (Table 4.2) and non-stoichiometry (A-site deficiency) detected in some of the grains by the EDXS analysis (Figure 4.12).

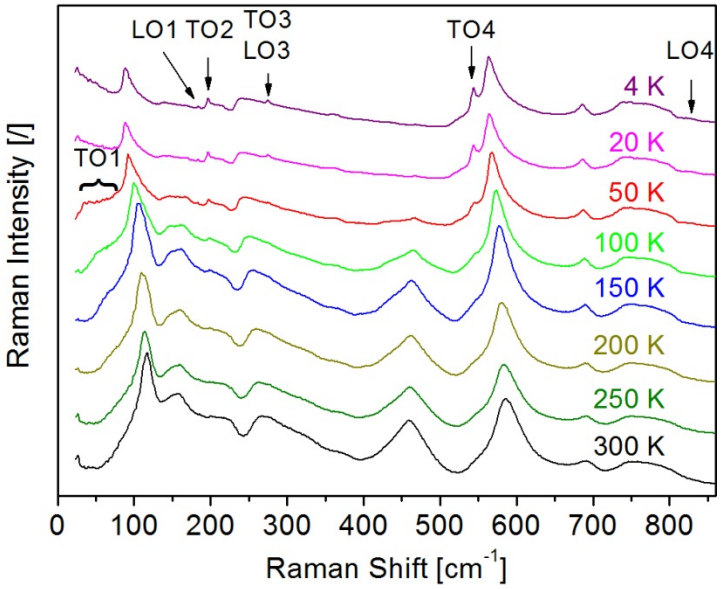

Figure 4.22: Raman spectra of the 2C-HP $KTaO_3$ ceramics measured at selected temperatures. The spectra are displaced vertically for clarity. The positions of the Raman-forbidden one-phonon features are marked.

The details of the fitting procedure of the Raman spectrum measured at 50 K are presented in Figure 4.23. The spectra were fitted in the range from 22 cm^{-1} to 860 cm^{-1} by the sum of the harmonic oscillators multiplied by the corresponding Stokes' temperature

[i]The 2C-HP ceramics used for the MW, THz, IR, and Raman analysis had the relative density of 98 %.

factor. The Rayleigh scattering tail at low frequencies was modeled by a temperature-independent zero-centered mixed Gaussian-Lorentzian peak with a fixed width. The same function was also used for the artifact peak at ~26 cm^{-1}. The harmonic oscillators used for the fits of the second-order features do not have a straightforward physical interpretation. They just represent a phenomenological description of the broad background scattering. The frequencies of the one-phonon modes at selected temperatures are collected and compared to those obtained from the IR and THz fits as well as from hyper-Raman data on single crystals in Table 4.5. The frequency of the TO1 mode decreases with decreasing temperature and falls outside our spectral range below 20 K. The rest of the modes do not show significant temperature dependence, and their frequencies are in good agreement with the room-temperature values for the single crystals [121].

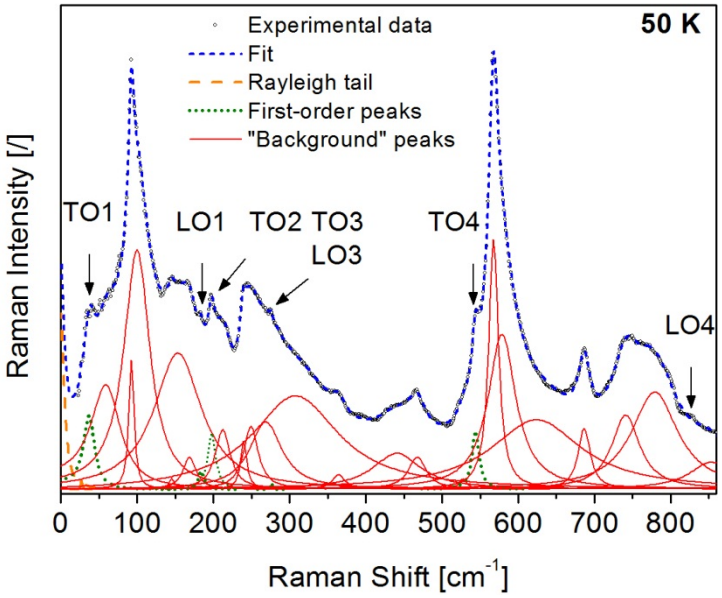

Figure 4.23: Fit of the Raman spectrum measured at 50 K. Positions of the one-phonon peaks are marked.

Table 4.5: Phonon mode frequencies (in cm^{-1}) of the $KTaO_3$ ceramics obtained by the Raman and combined THz and IR spectroscopies at selected temperatures. For comparison, the room-temperature single-crystal values (SC) obtained from the hyper-Raman measurements are added [121].

Phonon Mode	20 K		50 K	40 K	150 K	160 K	300 K	
	Raman	IR	Raman	IR	Raman	IR	IR	SC
TO1	–	23	39	32	66	63	83	81
LO1	184	185	182	185	–	186	187	185
TO2	197	196	198	196	203	198	201	199
TO3 (LO3)	274	–	275	–	–	–	–	279
LO2	–	420	–	420	–	420	422	422
TO4	544	546	544	546	547	546	543	546
LO4	828	825	828	825	–	825	825	826

4.1.5 Summary

According to the XRD analysis, single-phase perovskite $KTaO_3$ powder was obtained after calcination of the mechanochemically activated powder at 800°C; however, chemical and structural heterogeneities were revealed by the analytical transmission microscopy. Another calcination at 800°C was implemented to enhance the homogeneity of the powder.

Sintering of the single-calcined powder compacts at 1325°C in an oxygen atmosphere resulted in a ceramic with an 85 % relative density. However, the sublimation of potassium oxide led to the formation of a potassium-deficient secondary phase. Phase-pure ceramics with relative densities above 95 % were obtained by hot pressing the single- and the double-calcined powder compacts at 1250°C. The hot pressing at a 75°C lower temperature, as compared to the atmospheric sintering, effectively contributed to the enhanced densification of the $KTaO_3$ ceramic and simultaneously also to the reduced sublimation of potassium oxide. All the ceramics have a bimodal grain size distribution in the μm range.

A higher level of homogeneity of the $KTaO_3$ powders after double heating at 800°C contributed also to a doubled 1-kHz dielectric permittivity and lower dielectric losses of the 2C-HP $KTaO_3$ ceramics, with respective values of 4090 and 0.0048, measured at 5 K and 1 kHz. The permittivity is comparable to the values reported for single crystals.

The 2C-HP $KTaO_3$ ceramics were further analyzed with broadband dielectric spectroscopy. The three polar optic phonons, TO1 (Slater mode), TO2 (Last mode) and TO4 (Axe mode), known from single crystals, were observed by the THz and IR spectroscopies, and a weak coupling of the Slater and Last modes was revealed by the mode-plasma frequencies analysis. The increase of the low-frequency permittivity with decreasing temperature is directly related to the strong softening of the TO1 mode (soft mode). The permittivity ε' value in $KTaO_3$ ceramics is mainly of intrinsic origin, i.e., arising from the polar phonons. However, higher MW losses than in single crystals, associated with the extrinsic contributions, and the appearance of the forbidden first-order peaks in the low-temperature Raman spectra, indicate the presence of defects inside the ceramics. According to the chemical analysis and analytical TEM studies, the most plausible origin of these symmetry-breaking defects are Co (and W) and the non-stoichiometric composition of some of the grains.

Despite these defects, the $KTaO_3$ ceramics show typical incipient ferroelectric dielectric behavior, comparable to the one in single crystals.

4.2 $KTaO_3$ Thin Films

In the previous chapter we have shown that through control of the processing the incipient ferroelectric $KTaO_3$ ceramics, with a permittivity comparable to the one found in single crystals, can be prepared. The question arises, can similar behavior also be expected in polycrystalline $KTaO_3$ thin films, in which the grain size is usually much smaller and the substrate induces non-negligible strain?

To answer this question we have prepared and analyzed polycrystalline CSD-derived $KTaO_3$ thin films. The present chapter begins with a description of the processing-related issues of the films on polycrystalline and c-sapphire substrates. In the second part, the broadband dielectric properties of the perovskite films, including quasi-static measurements, are presented. Analyses and a discussion on the evaluated lattice dynamics bring the chapter to the end.

4.2.1 Preparation of the Films

4.2.1.1 Thermal Decomposition of the Sols

Stoichiometric $KTaO_3$ sols were prepared through a 24-h reflux of potassium acetate and tantalum ethoxide in 2-methoxyethanol (Chapter 3.1.2.1). Prior to the thermal analyses the sols were dried at 60°C for at least 12 h. The analysis was performed in the temperature range from 25°C to 755°C in a flowing air atmosphere and the simultaneous thermoanalytical curves are shown in Figure 4.24.

In total the sample loses 19.6 % of the starting mass and we divided the loss into three intervals: 25–200°C, 200–570°C and 570–755°C in which it loses 4.2 %, 12.2 % and 3.2 %, respectively. Three intensive minima are distinguished in the DTG curve at 108°C; 260°C (the strongest), which is followed by a broad shoulder from ~300°C to ~450°C; and at 638°C. Note that the mass loss process is not completely finished even at 755°C.

The unpronounced endothermic peak in the DTA curve at ~105°C is accompanied by a maximum in the EGA curve corresponding to H_2O (mass fragment 18). Evolution of the H_2O and CO_2 (mass fragment 44) also accompanies the asymmetric strong exothermic DTA peak at 264°C. A pronounced exo-DTA peak is present at 642°C, together with EGA-maxima corresponding to H_2O and CO_2. After the analysis the XRD pattern of the powder revealed the presence of the pyrochlore phase only (Figure 4.25).

Up to 200°C the mass loss is mainly the consequence of the evaporation of the adsorbed H_2O and probably also of the residual 2-methoxyethanol, both being endothermic events. In the second interval between 200°C and 570°C, the dominant process is thermal decomposition of the organic, mainly alkoxide, groups. In an inert atmosphere decomposition of the metal alkoxides in general occurs via oxo-alkoxides to oxides, with the simultaneous release of alkenes, ethers and alcohols (Equation (4.1)). In the oxidizing atmosphere the alkoxide groups completely oxidize to H_2O and CO_2 (Equation (4.2)), which is a strongly exothermic process [102].

$$Ta(OR)_5 \xrightarrow{T} Ta_2O_5 + C_nH_{2n} \uparrow + R_2O \uparrow + ROH \uparrow + \cdots \quad (4.1)$$

$$Ta(OR)_5 \xrightarrow{T,O_2} Ta_2O_5 + CO_2 \uparrow + H_2O \uparrow \quad (4.2)$$

In the above equations *R* denotes alkoxide groups, in our case either ethoxide and/or 2-methoxyethoxide. The above equations are also valid for the Nb alkoxides.

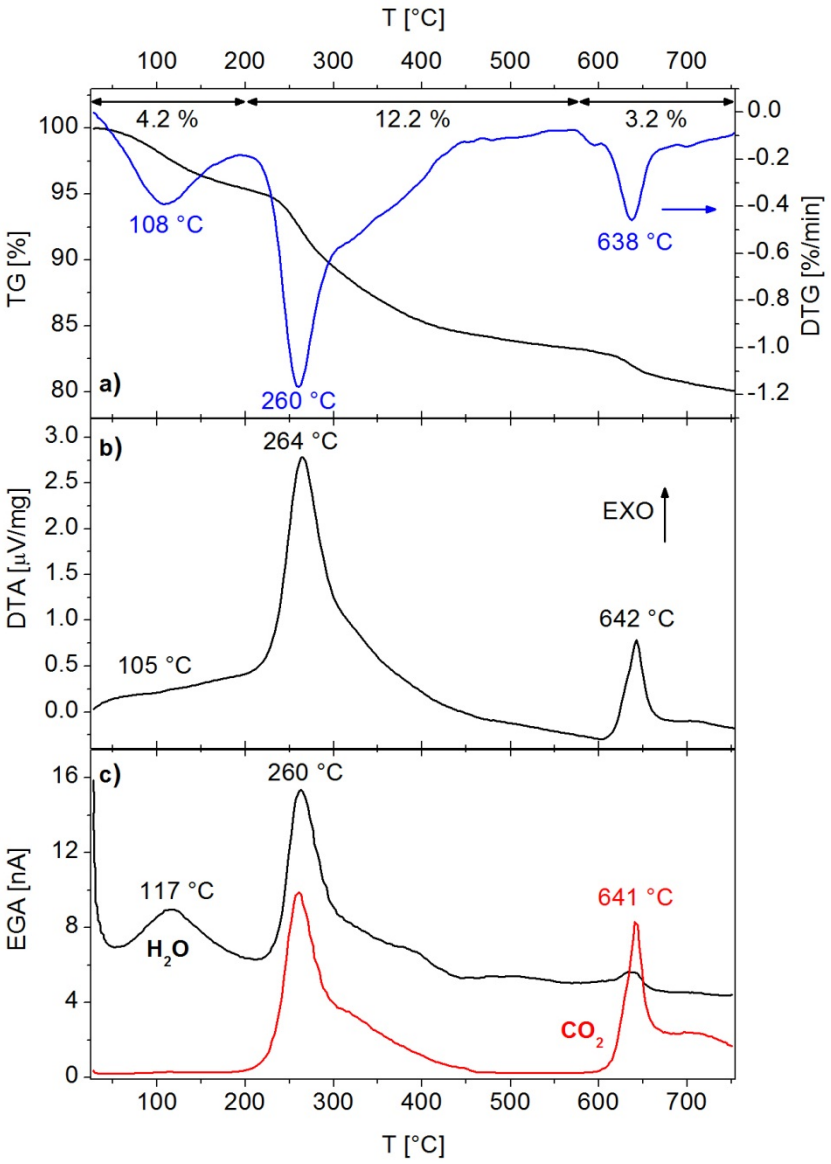

Figure 4.24 a) TG and DTG, b) DTA and c) EGA curves of the stoichiometric $KTaO_3$ sol after drying at 60°C. Positions of the strongest maxima and minima of the curves are denoted.

If the acetate groups are still present in the sols (see the Chapter 4.4.1.1.3) their decomposition through the intermediate carbonate phase (Equation (4.3)) could take place as well. The thermal decomposition of sodium acetate in an inert atmosphere is known to start at ~400°C and similar behavior is also expected for the potassium acetate [185]:

$$NaOOCCH_3 \xrightarrow{T} Na_2CO_3 + CH_3COCH_3. \quad (4.3)$$

Decomposition of the Pb-acetate via the carbonate phase was observed in the 2-methoxyethanol-based PZT sols [186].

The exothermic DTA peak at 642°C most probably corresponds to the crystallization of the pyrochlore phase (Figure 4.25). The accompanying mass loss and the evolving CO_2 and H_2O indicate the simultaneous decomposition of the organic and carbon residues [187].

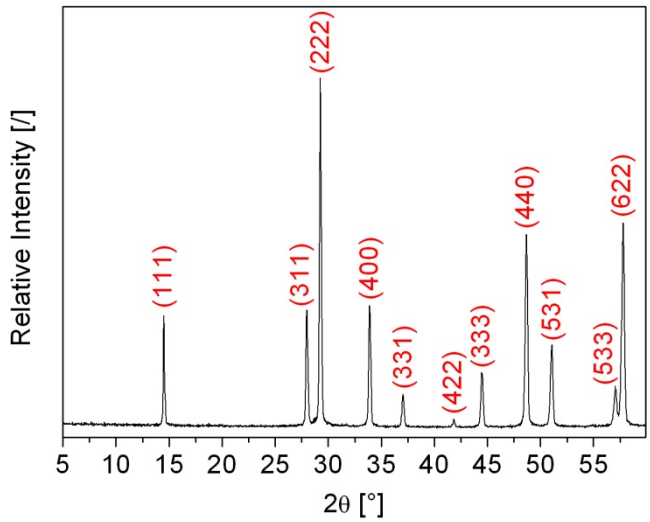

Figure 4.25: XRD pattern of the $KTaO_3$ powder after the thermal analysis. All the peaks denoted with Miller indices correspond to the pyrochlore $K_2Ta_2O_6$ [164].

The amount of impurities in the sols was determined by a quantitative chemical analysis (Table 4.6). The analysis was performed on powders, prepared by drying the sols at 60°C and subsequent heating at 900°C for 15 min. Small amounts of Na and Mg with concentrations of 53 ppm and 13 ppm, respectively, were detected. The amount of Li, Fe and Pb impurities is below 5 ppm.

Table 4.6: Typical amounts of the impurities present in the powders prepared by heating the sol with 30 % excess of potassium acetate to 900°C. The analysis was performed with ICP spectrometry.

Impurity	Concentration [ppm]
Na	53
Mg	13
Li	< 5
Fe	< 5
Pb	< 5

4.2.1.2 Phase Composition and Microstructure of the Films

After spin coating the sols on alumina substrates, the as-deposited films were pyrolyzed at 350°C. To increase the thickness, the procedure was repeated four times. Final annealing was performed at 900°C for 15 min in the RTA furnace (Chapter 3.1.2.3). These films are subsequently denoted as the 1C films.

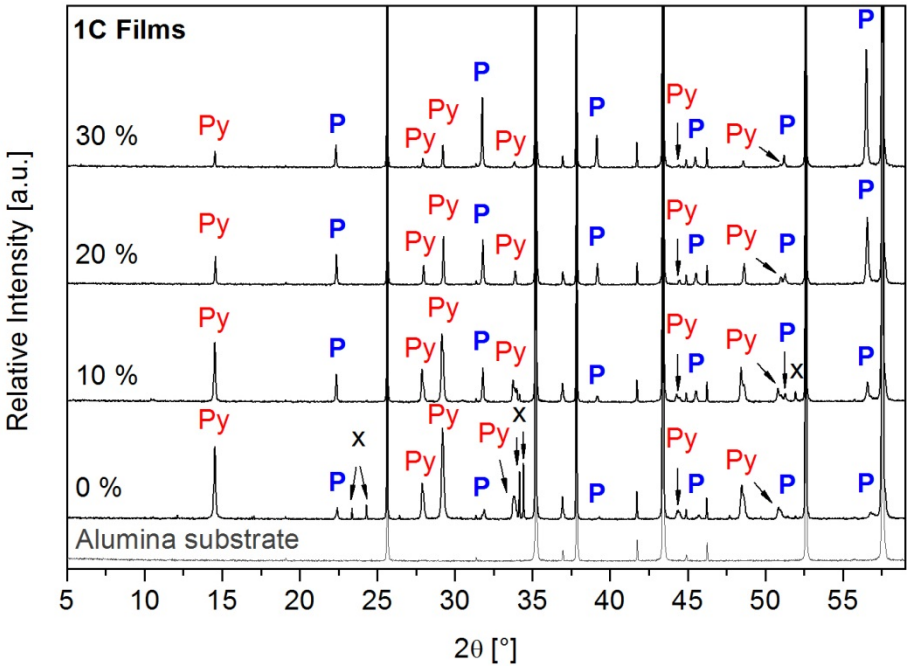

Figure 4.26: XRD patterns of the 1C $KTaO_3$ films on alumina substrates prepared from the stoichiometric sol (0 %) and sols with 10 %, 20 % and 30 % excess of potassium acetate. The films were pyrolyzed at 350°C. After 4 depositions the final annealing was performed at 900°C for 15 min. The pattern of the alumina substrate is also shown. P – perovskite phase [142]; Py – pyrochlore phase [164]; X – unidentified peaks.

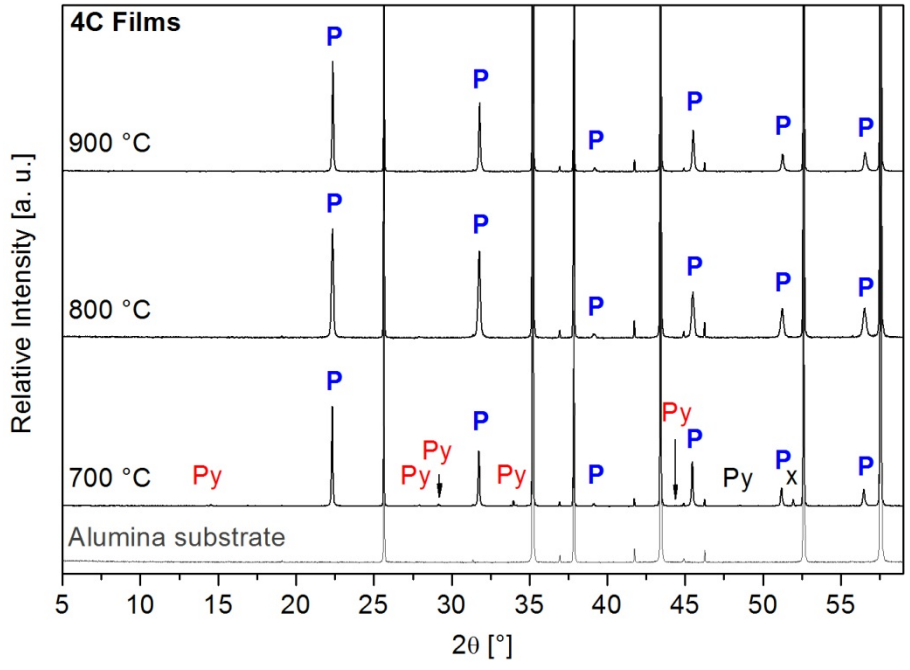

Figure 4.27: XRD patterns of the 4C $KTaO_3$ thin films on alumina substrates prepared from the sols with 30 % excess of potassium acetate. Films were dried at 180°C and annealed after each deposition at 700°C, 800°C and 900°C, respectively. The procedure was repeated 4 times. The pattern of the alumina substrate is also shown. P – perovskite phase [142]; Py – pyrochlore phase [164]; X – unidentified peak.

According to the XRD analysis the films consist primarily of pyrochlore phase, when prepared from the stoichiometric solutions (Figure 4.26). Small peaks corresponding to

the perovskite and also some unidentified phase are also present in the pattern. The relative intensity of the perovskite peaks gradually increases with the increasing amount of the excess of the potassium acetate in the sols. However, the pyrochlore phase is still present, even in the films prepared from the sols containing 30 % potassium excess.

The formation of the pyrochlore phase in the solution-derived $KTaO_3$ powders and thin films has been frequently reported [103,115,117]. Usually it is stable after lower heating temperatures and should in principle be transformed into a thermodynamically stable perovskite phase by increasing the crystallization temperature. However, a strong increase of the partial pressure with increasing temperature causes the sublimation of the potassium species from the sample. The pyrochlore phase is then stabilized again, because it withstands much larger off-stoichiometric deviations than the perovskite phase [188,189].

The films were also prepared from the sols with 30 % excess of potassium acetate by a modified route. After each deposition, the films were dried at 180°C and annealed in the RTA furnace for 5 min. The procedure was repeated four times with final annealing for 15 min. These films are subsequently denoted as the 4C films and their XRD patterns are shown in Figure 4.27. After heating at 700°C the films are composed of the perovskite phase and some traces of pyrochlore, while only the perovskite phase can be detected in the patterns of the films after heating at 800°C and 900°C.

The 4C $KTaO_3$ films were also prepared on the c-sapphire substrates. Detailed XRD patterns of the 4C films on both substrates after heating at 900°C are shown in Figure 4.28. A small unidentified peak occasionally appeared in the pattern of the film on c-sapphire substrate (inset of the Figure 4.28b).

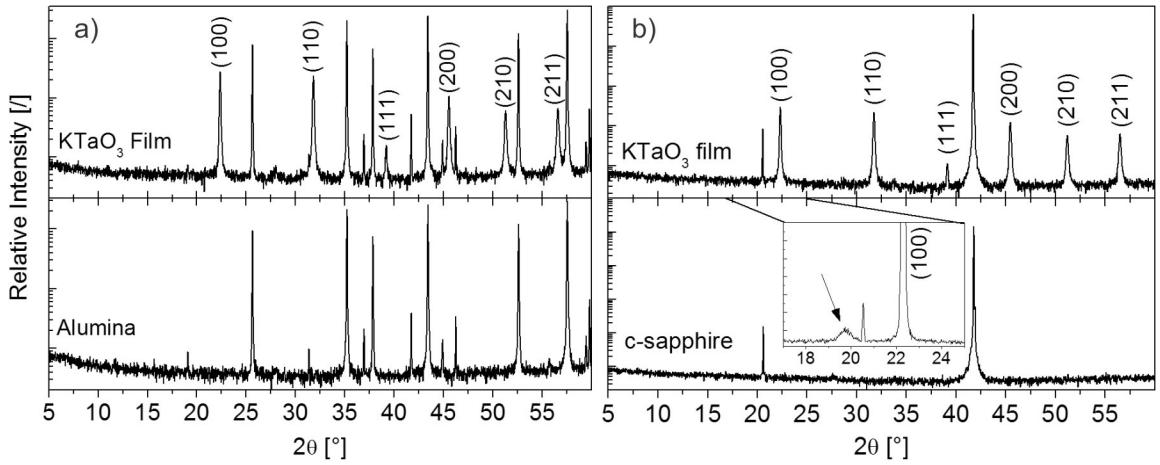

Figure 4.28: XRD patterns of the 4C $KTaO_3$ thin films prepared on a) alumina and b) c-sapphire substrates. The films were dried at 180°C and annealed after each deposition at 900°C. The procedure was repeated 4 times. Patterns of the substrates are also shown. Peaks corresponding to the perovskite phase [142] are denoted with the Miller indices. In the inset of (b), unknown peak, which occasionally appeared in the patterns of the films on the c-sapphire, is shown. Note the logarithmic intensity scale in both patterns.

A comparison of the relative intensities of the perovskite phase in the patterns of the films and the powders (Figure 4.4) reveals that the films have a tendency to crystallize in a slightly (100)-oriented perovskite phase. The preferential orientation can be quantified

using the Lotgering factor $f_{(l00)}$ [190]:

$$f_{(l00)} = \frac{P_{l00} - P_0}{1 - P_0}, \tag{4.4}$$

where P_{l00} is the ratio between the sum of the integral intensities $\sum I_{l00}$ of the peaks corresponding to the (l00) family and the sum of the integral intensities of all the peaks in the pattern of the sample $\sum I_{hkl}$. The P_0 is defined in a similar fashion for the non-oriented sample:

$$P_{l00} = \frac{\sum I_{l00}}{\sum I_{hkl}}, \tag{4.5}$$

$$P_0 = \frac{\sum I^0_{l00}}{\sum I^0_{hkl}}. \tag{4.6}$$

The Lotgering factor $f_{(l00)}$ takes values between 0 and 1 for the non-oriented and perfectly oriented sample, respectively. We performed the calculation for the peaks in the 5–60° 2θ range of at least 5 samples using the data from Ref. [142] as the reference. Rather large scattering between the different samples was observed; nevertheless, the calculated values are in the range between 0–0.3 and 0–0.4 for the films on corundum and c-sapphire substrates, respectively.

The plane-view FE-SEM micrographs of the 4C films after heating at 900°C reveal dense microstructures (Figure 4.29). In the case of the alumina substrate, some regions of changed grain structure can be observed, with voids located in their centers (marked with the arrow in Figure 4.29a). They are most probably related to the "imperfect" porous surface of the polycrystalline substrate (see inset of the Figure). Pores are present in between the grains in the micrographs of the film on c-sapphire (Figure 4.29b and d). Both films have an average in-plane grain size of ~160 nm, estimated from a lineal analysis of the micrographs. The cross-sectional views (Figure 4.29e and f) reveal 200-nm-thick films with columnar-like microstructure.

The STEM analysis results of the 4C film on the alumina substrate are summarized in Figure 4.30. The revealed cross-sectional microstructure is more porous than observed in the FE-SEM micrograph. The STEM-EDXS line-scan was performed across the film thickness in the direction from the substrate to the film surface on the cross-sectional TEM specimen. Within the measurement uncertainty, the composition corresponds to the perovskite phase through the whole thickness.

The 4C $KTaO_3$ films on corundum and c-sapphire substrates have a columnar-like microstructure and show a tendency to crystallize in a (100)-oriented perovskite phase. The rhomobohedral crystal structure of Al_2O_3 (space group $R\bar{3}c$) is crystallographically very different from the cubic crystal structure of the $KTaO_3$ (space group $Pm\bar{3}m$) and epitaxial nucleation cannot be expected. The tendency for the crystallization in a (100) preferentially oriented perovskite phase was also observed in the polycrystalline $K_{0.5}Na_{0.5}NbO_3$ (KNN) thin films [191-194]. Both $KTaO_3$ and KNN are $A^{1+}B^{5+}O_3^{2-}$-type

perovskites, whose surface energies of the crystallographic faces[i] are very anisotropic. A simplified estimation of the interplane binding energies, by taking into account the occupation of the planes, their charge and the interplane distances, reveals that the (100) plane is the lowest surface-energy face in KNN as well as in $KTaO_3$ [195].

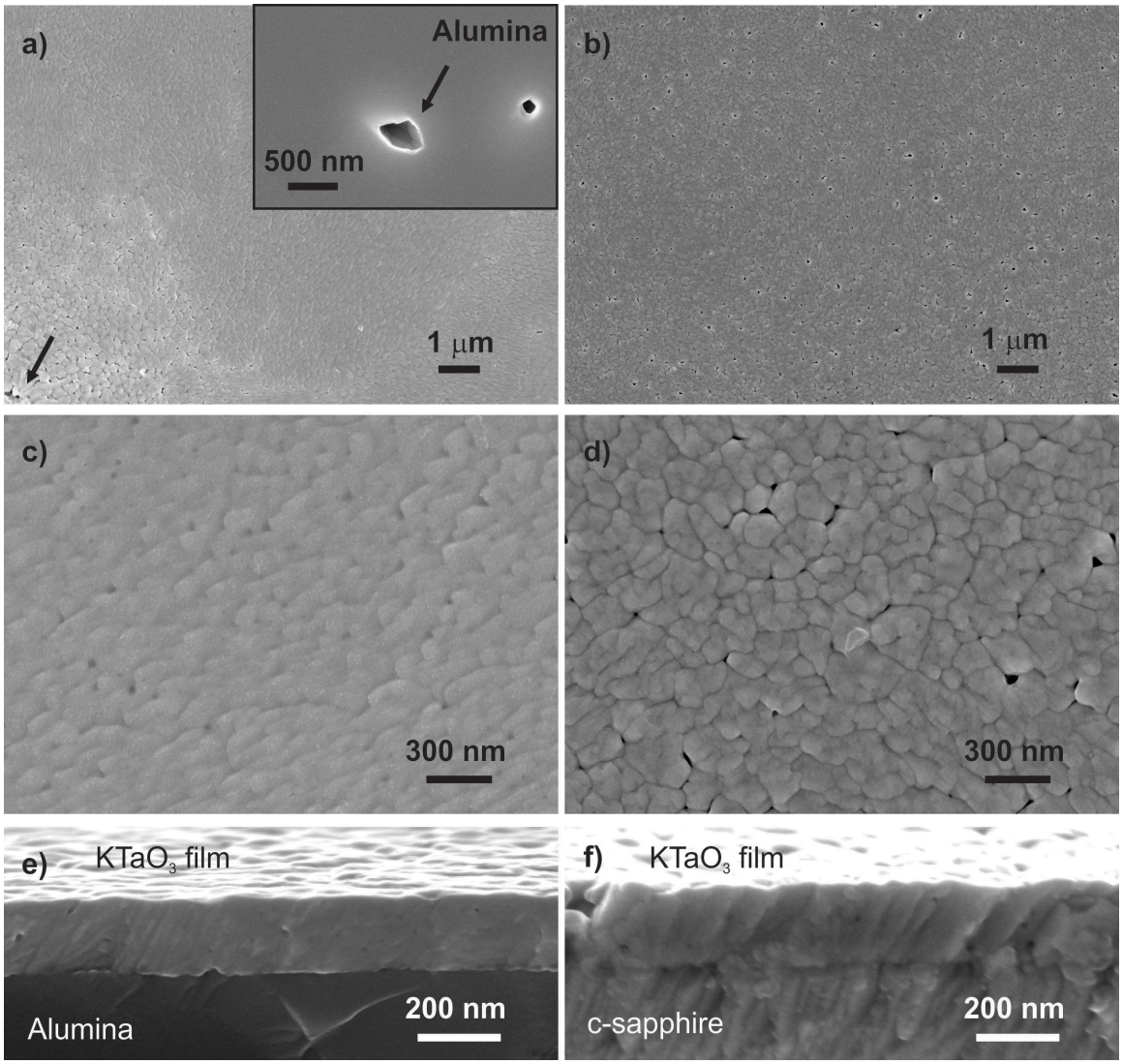

Figure 4.29: a), b), c), d) plane-view and e), f) cross-section view FE-SEM micrographs of the 4C $KTaO_3$ thin films on corundum (a), c), e)) and on c-sapphire (b), d), f)) substrates. In a) surface of the polycrystalline alumina is shown.

From the standard nucleation theory it follows that the energies needed for the heterogeneous nucleation ΔG^*_{hetero} and homogeneous nucleation ΔG^*_{homo} are related through:

$$\Delta G^*_{hetero} = \Delta G^*_{homo} \cdot f(\theta). \qquad (4.7)$$

The function $f(\phi)$ depends on the geometry of the nucleus and takes values between 0 and 1 when θ is between 0° and 180°, respectively. From Equation (4.7) it follows that the lower the contact angle, the more favorable is the heterogeneous nucleation, which is

[i]Energy of bonds between the planes cut perpendicularly to the surface normal.

often the case for the film on the substrate [196].[i] In thin films both nucleation mechanisms compete, as shown in Figure 4.31a.

In very thin layers the interface-to-volume ratio is high; therefore, heterogeneous nucleation prevails. Two different scenarios, both leading to preferential orientation of the film, are presented in Figure 4.31. In the first one, mainly the crystallites with the lowest-energy faces, oriented in-plane[ii], nucleate and grow (Figure 4.31b). In the second case, the nuclei may have different orientations, but the in-plane grain growth is governed by the criterion of the lowest surface energy (Figure 4.31c) [196,197]. The as-crystallized film acts as a seeding layer for the crystallization of additionally deposited layers of the sol.

Furthermore, the high interface-to-volume ratio of the crystallizing layer also favors the formation of the perovskite over the pyrochlore phase; compare the phase composition of the 1C and 4C $KTaO_3$ films (Figure 4.26 and Figure 4.27). Similar enhancement of the crystallization of the perovskite phase was also observed for the CSD-derived PZT thin films on platinized silicon substrates [198].

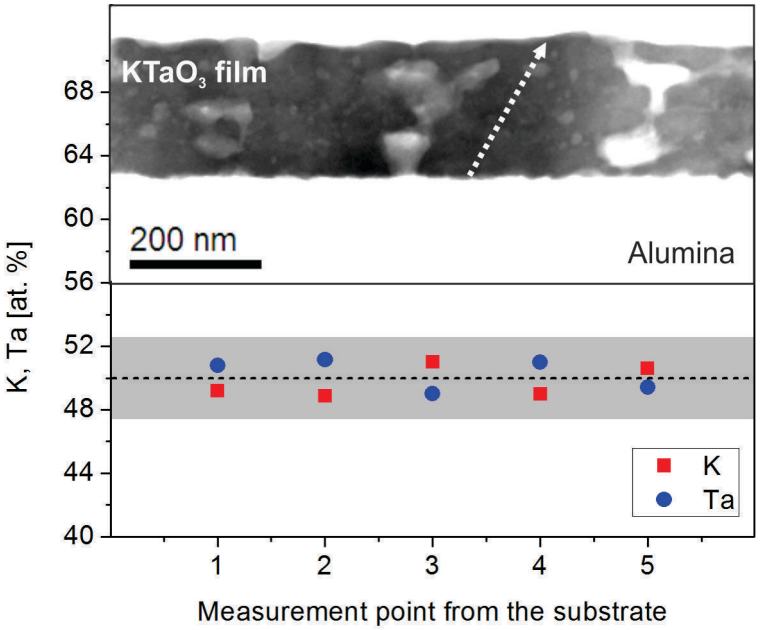

Figure 4.30: Cross-section STEM bright-field micrograph (above) and compositional STEM-EDXS line scan over the cross-section of the 4C $KTaO_3$ thin film on the alumina substrate. The position of the line scan is denoted with the arrow. The error bars represent $\pm 2\delta$ standard deviation. The dotted horizontal line denotes the nominal compositions, while the grey areas correspond to the standard deviation $\pm 2\delta$ ($\pm$ 2.6 at.%) for each element.

The above-described crystallization behavior was demonstrated by Hoffmann and co-workers [199,200] for the solution-derived $BaTiO_3$ thin films on platinized silicon substrates. By decreasing the concentration of the deposited sol, they were able to decrease the thickness of the as-deposited crystallizing layer. The cross-sectional microstructure of the films gradually changed from equiaxed with a random orientation to columnar with a preferential (100) orientation of the perovskite phase.

[i] In fact similar is valid also for the surface between the film and the surrounding atmosphere. Nevertheless, our films were heated in an RTA furnace, in which the sample is heated indirectly via the SiC susceptor which is exposed to an IR radiation. The substrate is heated first and the temperature gradient promotes nucleation at the film/substrate interface.

[ii] Parallel to the substrate.

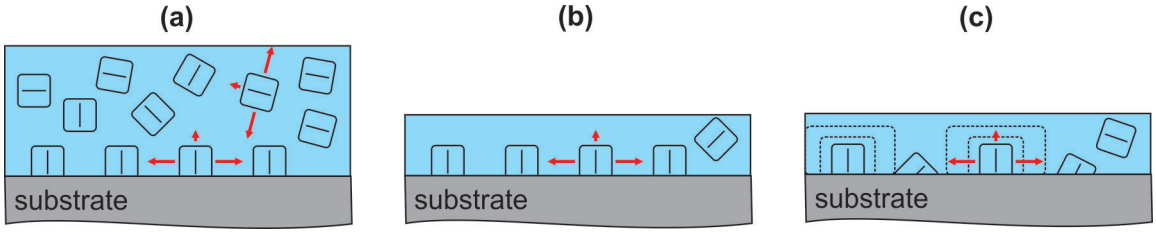

Figure 4.31: Schematic presentation of the crystallization process in the solution-derived thin films. a) Thick crystallizing layer, where both, heterogeneous and homogeneous, nucleation mechanisms compete. b) Thin crystallizing layer where mainly the crystallites with the lowest-energy faces, oriented in-plane, nucleate and grow. c) Thin crystallizing layer, where mainly heterogeneous nucleation of the randomly oriented nuclei takes place. The in-plane grain growth is governed by the criterion of the lowest surface energy. Crystallization of only one phase, i.e., perovskite, is assumed.

4.2.2 Broadband Dielectric Properties

The 200-nm-thick 4C $KTaO_3$ thin films after heating at 900°C were selected for the broadband dielectric characterization. The films on alumina substrates were investigated in the RF and MW frequency ranges, including the quasi-static measurements. The films on c-sapphire substrates were measured in the MW, THz and IR frequency ranges and their lattice dynamics were evaluated. The results are analyzed and discussed in the following chapter.

4.2.2.1 Radio-Frequency and Quasi-Static Properties

The RF and quasi-static dielectric properties were evaluated in a planar geometry (Figure 3.4). The temperature dependence of the dielectric permittivity ε' of the film on alumina substrate measured in the 3 kHz to 1 MHz frequency range is shown in Figure 4.32. The permittivity increases with decreasing temperature from 300 K to ~125 K according to the Curie-Weiss law, with the extrapolated temperature $T_0 \approx 50$ K. The value is close to the temperature of the permittivity maximum $T_{max} = 40.4$ K measured at 10 kHz (Figure 4.32b). However, the fit is only tentative, due to rounding of the data in the vicinity of the peak because of the finite-size effects and other issues with the structural inhomogeneities.

The permittivity ε' shows some frequency dispersion. The exact value of T_{max} can be described with the Vogel-Fulcher law (Equation (1.2), (Figure 4.32c), with the activation energy E_a and freezing temperature T_f of 1.6 meV and 38.6 K, respectively. The fit was obtained from a narrow frequency range and does not necessarily indicate the relaxor nature of the $KTaO_3$ film. It is most probably associated with the experimental error arising from temperature deviations of the LCR-meter calibration factors. Furthermore, the temperature of the permittivity maximum T_{max} increases with increasing DC electric field E_{DC} (Figure 4.32d), which is typical dependence around the paraelectric-to-ferroelectric phase transition.

The E_{DC} dependence of the normalized dielectric permittivity $\varepsilon'(E_{DC})/\varepsilon'(0)$ is shown in Figure 4.33. At room temperature the permittivity is only slightly electric-field-dependent, while this dependence is strongly enhanced at 100 K. The tunability n

(Equation (1.3)) at 100 K and applied field of 150 kV/cm is 2.8 (n_r = 65 %). By using Equation (1.7) and taking the ε' value of 640 (at 100 K) and β value of 9 x 10^9 J C^{-4} m^5, one gets the estimated single-crystal tunability value n at the same applied field 2.2.

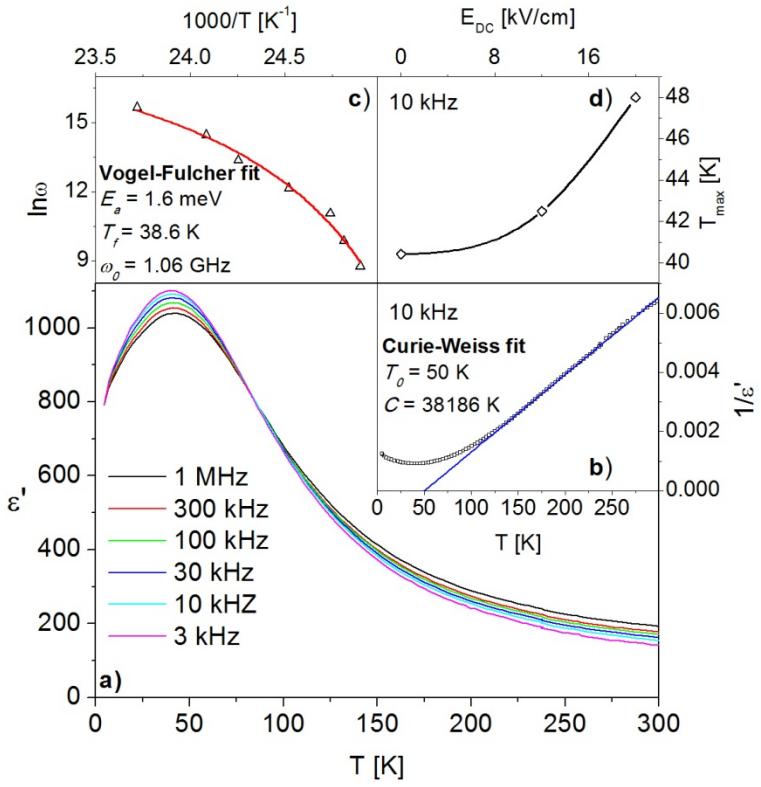

Figure 4.32: a) Temperature dependence of the dielectric permittivity ε' of the 4C $KTaO_3$ film on the alumina substrate measured in the 3 kHz to 1 MHz frequency range. b) Curie-Weiss fit of the 10 kHz experimental data. c) Vogel-Fulcher fit of the experimental data. d) DC electric field E_{DC} dependence of the temperature of the permittivity maximum T_{max} at 10 kHz. In d) the line between the experimental points is a guide to the eye. Amplitude of the probing AC field was 4 kV/cm.

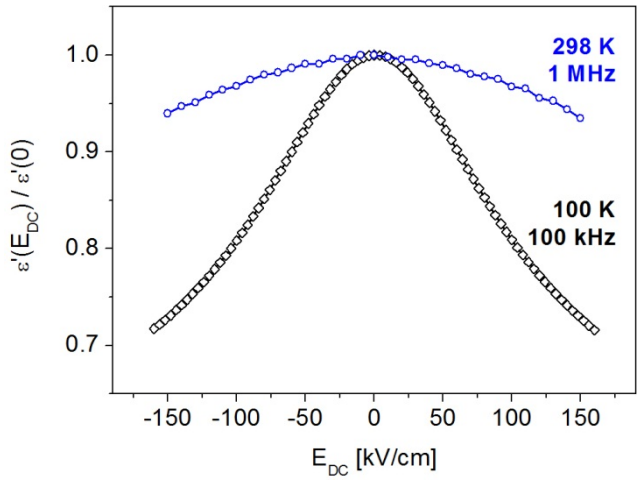

Figure 4.33: DC electric field E_{DC} dependence of the normalized dielectric permittivity $\varepsilon'(E_{DC})/\varepsilon'(0)$ of the 4C $KTaO_3$ thin film on alumina substrate. The measurement was performed at 298 K and 100 K, while the frequencies were 1 MHz and 100 kHz, respectively. The voltage cycle was: $-E_{DCmax} \rightarrow 0$ V $\rightarrow E_{DCmax}$.

To further analyze the nature of the low-temperature state of the $KTaO_3$ films, the quasi-static polarization was measured on heating after zero-field (ZFC) or field (FC) cooling at E_{DC} of 400 kV/cm (Figure 4.34). At ~15 K the ZFC polarization has the value of ~0.48 C/m^2 and this continuously decreases with increasing temperature above this temperature, indicating a sluggish transition from the ferroelectric to the paraelectric phase. On the other hand, the FC polarization vanishes in a much narrower temperature interval at ~45 K. Similar hysteretic behavior around the ferroelectric phase transition, which depends on the history of the of the sample, was also observed in 0.71 PMN – 0.29 PT single crystals and 9/65/35 PLZT ceramics[i] [201,202].

The temperature dependence of the quasi-static permittivity ε'_s measured in the ZFC regime by applying E_{DC} of 40 kV/cm at each measured temperature is in qualitative agreement with the behavior of the RF permittivity (inset of Figure 4.34). It increases on cooling from room temperature until it exhibits a maximum in the temperature interval between 20 K and 40 K, with the approximate value of 330. The behavior is similar to the one observed for the RF-permittivity ε', though the absolute peak-value is significantly smaller. The difference arises from the rather large DC field in the case of the ε'_s measurement; in addition it is also indicating a strongly non-linear *P-E* dependence (see Chapter 3.2.10.2)

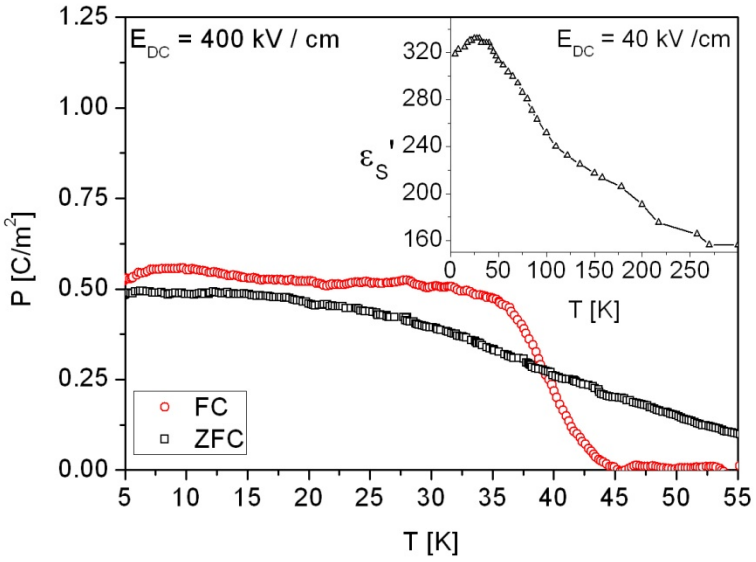

Figure 4.34: Temperature dependence of the quasi-static polarization *P* of the 4C $KTaO_3$ thin film on alumina substrate measured on heating at DC electric field E_{DC} = 400 kV/cm after field cooling (FC) or zero-field cooling (ZFC). Quasi-static permittivity ε'_s measured in ZFC regime by applying 40 kV/cm at each temperature is shown in the inset.

The low-temperature value of the quasi-static polarization *P* increases with increasing DC field from 0.2 C/m^2 to 1.15 C/m^2 at 84 kV/cm and 800 kV/cm, respectively (Figure 4.35). The 84 kV/cm FC value drops to zero at ~50 K. An interesting result arises from the electric field dependence of the polarization at 15 K plotted in the inset of Figure 4.35. It can be divided into two parts: high-field part, where the polarization increases with the field almost linearly; and low-field part (marked with arrow), where the polarization

[i]Measured above the critical field at which the ferroelectric state is induced.

significantly deviates from the linear behavior. Even though the measurements are very sensitive, the behavior most probably arises from the domain dynamics in the vicinity of the coercive field E_c, or some polarization depinning threshold electric field E value. The latter can exist due to the presence of structural and/or diffusive point defects, or due to the stress field arising from the substrate [203].

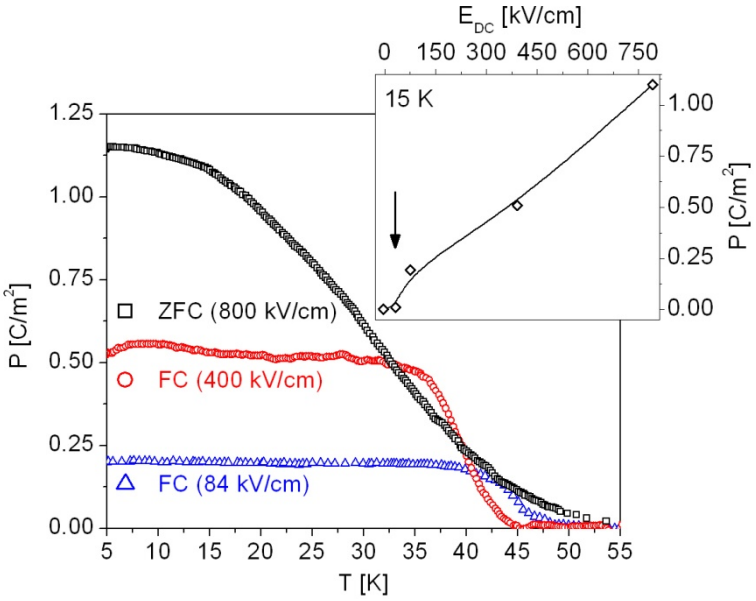

Figure 4.35: Temperature dependence of the quasi-static polarization P of the 4C $KTaO_3$ thin film on alumina substrate measured on heating at different DC electric fields E_{DC}, i.e., 84 kV/cm, 400 kV/cm and 800 kV/cm, after zero-field cooling (ZFC) or field cooling (FC). Electric field dependence of the polarization P measured at 15 K is shown in the inset. The first point is taken from the low-field RF measurements (Figure 4.32). Line between the experimental points is a guide to the eye.

4.2.2.2 Microwave, Terahertz and Infrared Properties

A similar temperature dependence of the MW permittivity ε' and losses $\tan\delta$ of the $KTaO_3$ thin films on alumina and c-sapphire substrates, measured at 15.5 GHz and 16.2 GHz, respectively, can be observed in Figure 4.36. The permittivity ε' increases with decreasing temperature from the room-temperature value of ~200, until it exhibits a broad maximum, present in the temperature range from 30 K to 45 K and from 40 K to 60 K, in the case of the alumina and c-sapphire, respectively. Maxima are also present in the respective losses $\tan\delta$, which increase from the room-temperature values of 0.011 and 0.019, respectively. However, they are rather noisy around the maximum because of the small quality factor Q of the resonating structure.

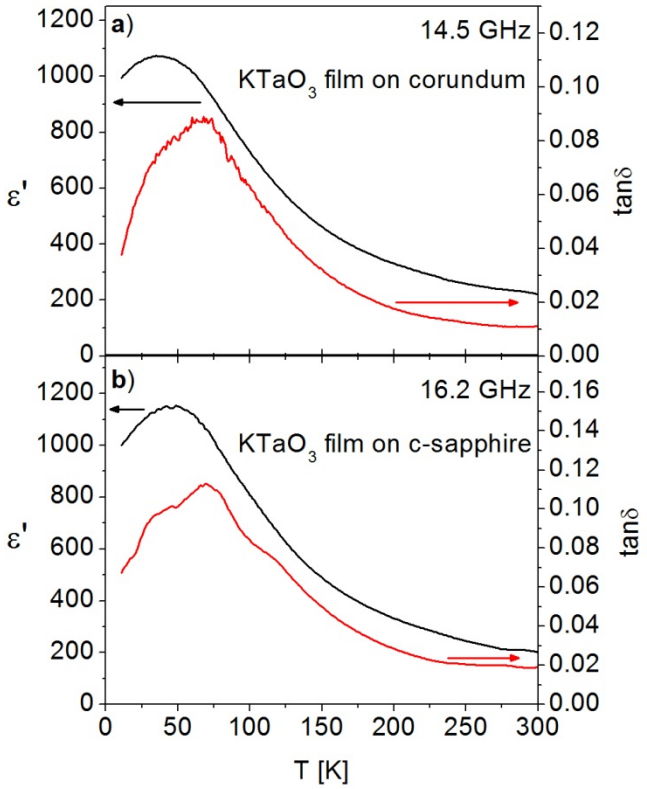

Figure 4.36: Temperature dependence of the MW permittivity ε' and dielectric losses $\tan\delta$ of the 4C $KTaO_3$ thin films on a) corundum and b) c-sapphire substrate, measured at 14.5 and 16.2 GHz, respectively.

THz time-domain spectroscopy in the frequency range between 0.2 THz and 2.3 THz was employed to probe the soft-mode behavior in the film on a c-sapphire substrate (Figure 4.37). At room temperature the real permittivity ε' value of ~200 does not show significant frequency dependence until ~2.0 THz when it starts to decrease, while the imaginary permittivity ε'' monotonously increases with the increasing frequency, indicating the presence of the soft-mode (SM) resonance above the observable frequency range. At lower temperatures the SM is characterized in the spectra by the temperature-dependent ε'' peak. The ε' does not saturate in the low-frequency range, instead it starts to strongly increase at lower frequencies as the temperature decreases. This is evidence of the onset of some additional relaxation, i.e., the central mode (CM), with its relaxation frequency Γ_{CM} lying below the obtainable frequency range.

We have simultaneously fitted all the experimental data using the model of a linearly coupled oscillator and Debye relaxation, describing the SM and CM, respectively:

$$\varepsilon^*(\omega) = \frac{f\left(1 - i\frac{\omega}{\Gamma_{CM}}\right) + g(\omega_{SM}^2 - \omega^2 - i\omega\gamma) + 2\delta\sqrt{fg}}{(\omega_{SM}^2 - \omega^2 - i\omega\gamma)\left(1 - i\frac{\omega}{\Gamma_{CM}}\right) - \delta^2} + \varepsilon_\infty. \qquad (4.8)$$

In the above equation the SM is characterized with the temperature-dependent frequency ω_{SM}, damping γ, and temperature-independent oscillator strength $f \approx 1.3 \times 10^6$ cm^{-2}. The temperature-independent relaxation frequency $\Gamma_{CM} \approx 6$ cm^{-1} and temperature-dependent strength g characterize the CM. The obtained coupling constant $\delta \approx 27$ cm^{-1} was taken as

a constant at all temperatures. The ε_∞ describes the contribution of the higher-frequency hard modes (TO2 and TO4) and of the electronic polarization. The agreement between the fits and the experimental data are presented in Figure 4.37. The same procedure was previously used to analyze the dielectric behavior around the paraelectric-ferroelectric phase transition of epitaxial PLD-derived $SrTiO_3$ thin films on (110) $DyScO_3$ substrates [155,204].

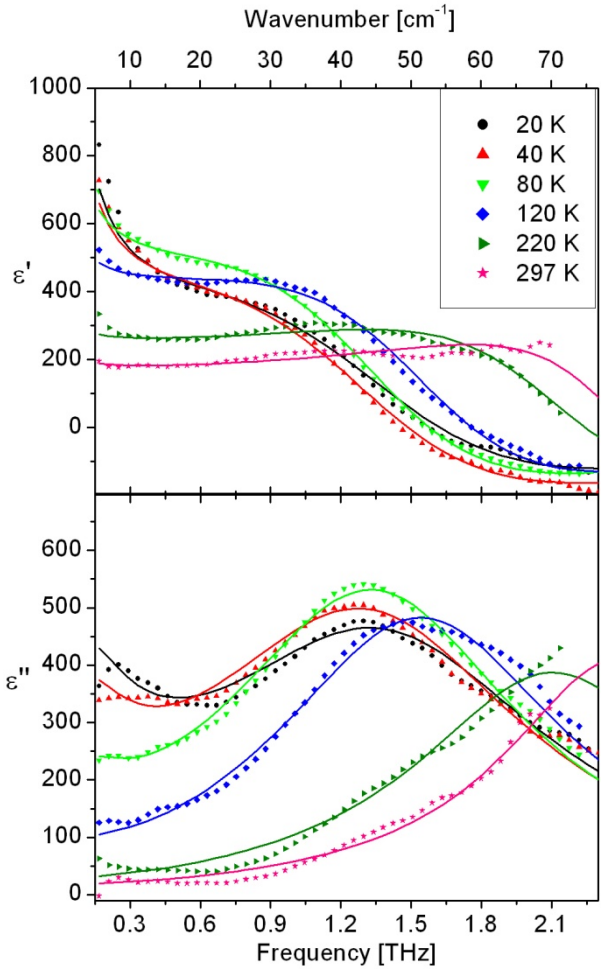

Figure 4.37: Real $\varepsilon'(\omega)$ and imaginary $\varepsilon''(\omega)$ parts of the complex dielectric permittivity $\varepsilon^*(\omega)$ of the 4C $KTaO_3$ thin film on the c-sapphire substrate. The experimental data (symbols) at different temperatures were obtained by transmission THz time-domain spectroscopy. Lines – fits to the Equation (3.7).

To expand the frequency range to higher wavenumber values, the IR reflectance spectra of the $KTaO_3$ thin film, as well as of the bare c-sapphire substrate, were recorded at room temperature (Figure 4.38). Oscillations present in the low-frequency region of both spectra are the consequence of the interference phenomena in the substrates. In addition, some higher-wavelength oscillations can also be observed. These are most probably arising from the non-ideal (0001) cut of the substrate. Reflection bands, corresponding to the TO1 (SM), TO2 and TO4 polar modes, at approximately 82 cm^{-1}, 197 cm^{-1} and 548 cm^{-1}, respectively, are nicely expressed in the spectrum of the film. The ω_{TOj} values are in agreement with the single-crystal [176] and ceramics data (Chapter 4.1.4)

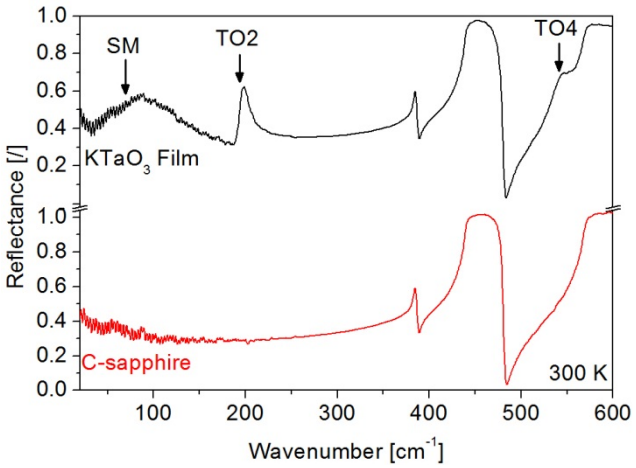

Figure 4.38: IR reflectivity spectra of the bare c-sapphire substrate and of the 4C $KTaO_3$ thin film measured at 300 K. Approximate positions of the TO1 (SM), TO2 and TO4 polar modes are marked with arrows. Spectra are displaced vertically for reason of clarity.

Oscillations associated with the interference phenomena in the substrates can also be observed in the IR transmission spectra measured in the 300 K to 5 K temperature range (Figure 4.39). The transmission is smaller at higher temperatures due to increased phonon damping in the substrate. Broad minima in the spectra of the films correspond to the SM and TO2 polar modes. At higher frequencies the substrate is too opaque to observe the TO4 mode, while the CM frequency Γ_{CM}, detected in the THz measurements, lies below the obtainable frequency range.

The transmission spectra of the substrate were fitted by a sum of the harmonic oscillators using Fresnel formulas for the coherent transmission of a plane-parallel sample, taking into account the interference effects. The thus obtained parameters of the substrate were used for the fit of the $KTaO_3$/c-sapphire two-layer system. Its complex transmittance was computed by the transfer-matrix formalism method [205]. The fitting was performed simultaneously with the THz transmission and MW data, using the model of a coupled oscillator and Debye relaxation (Equation (4.8)) for the SM and CM, respectively. The TO2 mode was treated as an independent damped harmonic oscillator (Equation (10.2)). With the exception of the coupling δ between the SM and CM, and ε_∞, which in this case takes into account only the contribution of the TO4 mode and the electronic polarization (~6), all the common parameters were kept the same as in the fitting procedure of the bare THz data only. An example of the agreement between the fit and the IR experimental data obtained at 120 K is shown in Figure 4.40.

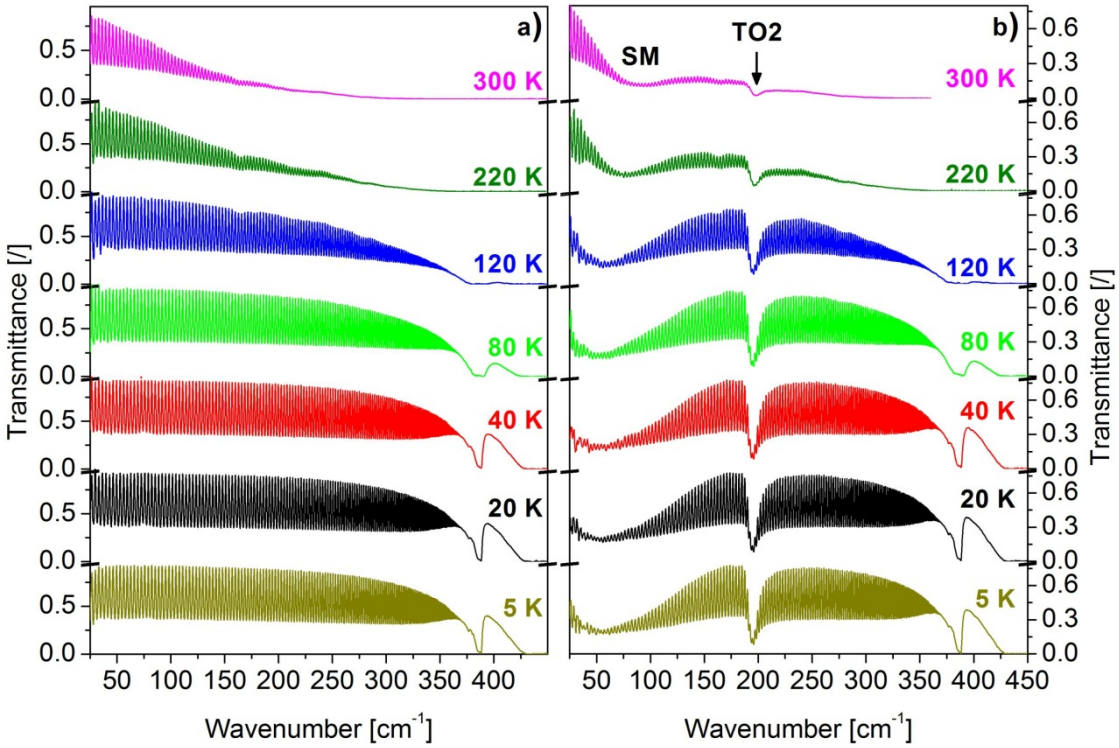

Figure 4.39: IR transmission spectra of the a) bare c-sapphire substrate and b) the $KTaO_3$ thin film at selected temperatures in the 300 K to 5 K range. Approximate positions of the SM and TO2 polar modes of the film are marked. Spectra are displaced vertically for reasons of clarity.

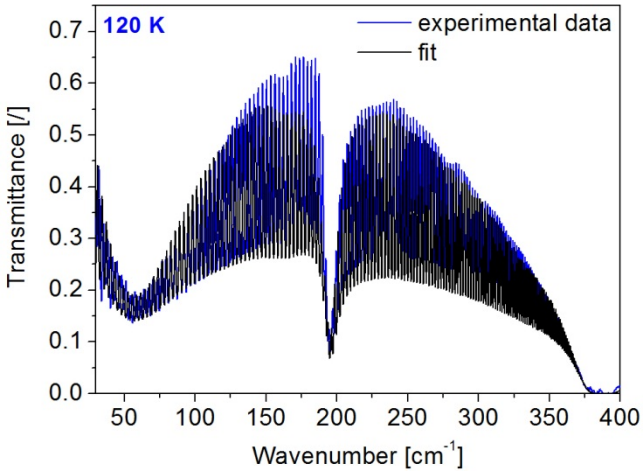

Figure 4.40: Comparison of the experimental IR transmission spectrum of the $KTaO_3$ thin film on c-sapphire at 120 K with the fit.

Thus obtained ε' and ε'' are plotted and compared to the MW data in Figure 4.41. The resonances corresponding to the TO2 and SM modes, as well as the relaxation corresponding to the CM, can be easily observed.

Temperature dependences of the selected fitting parameters, i.e., polar phonon frequencies ω_{TOj}, relaxation strength of the CM g and the coupling between the CM and SM δ, are plotted in Figure 4.42. The soft-mode frequency ω_{SM} decreases on cooling from 85 cm^{-1} to 51 cm^{-1} in the temperature range from 300 K to ~60 K and increases afterwards to the value of 56 cm^{-1} at 5 K. Around ~60 K the CM strength g also becomes non-zero and starts to increase with the decreasing temperature. This indicates that above this

temperature the CM is "silent" and it linearly couples to the polarization below. This is also the range where it significantly contributes to the permittivity ε' value (Figure 4.41). The phenomenological coupling constant δ [206] decreases from the room-temperature value of 24 cm^{-1} to 22 cm^{-1} at 5 K with the maximum value of 35 cm^{-1} at 120 K.

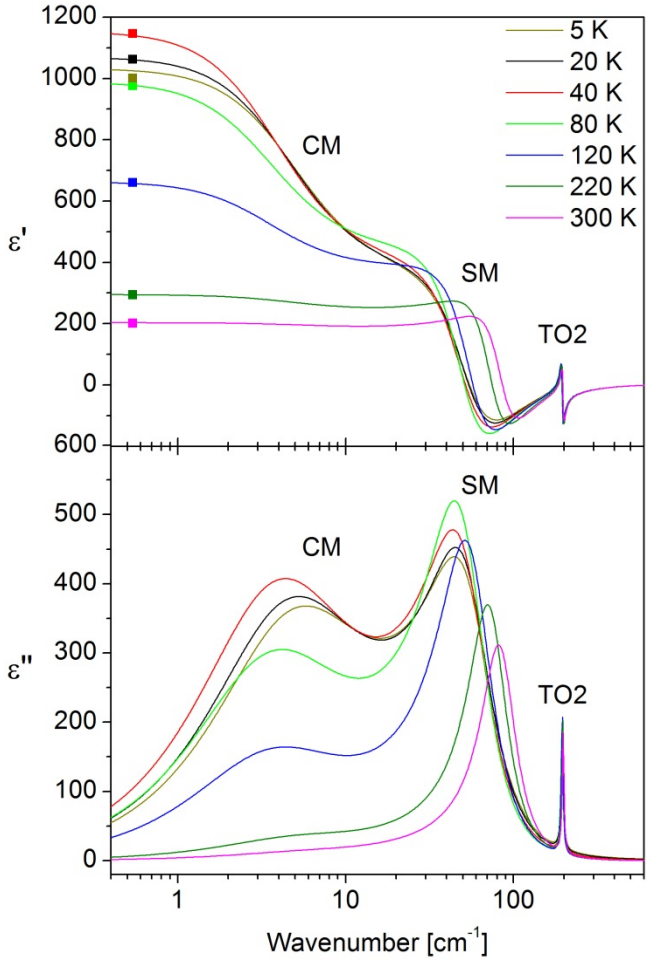

Figure 4.41: a) Real $\varepsilon'(\omega)$ and b) imaginary $\varepsilon''(\omega)$ parts of the complex dielectric permittivity $\varepsilon^*(\omega)$ of the $KTaO_3$ thin films on c-sapphire calculated from the simultaneous fits of the IR, THz and MW data. Approximate positions of the CM, SM and TO2 modes are marked. MW experimental data are shown as symbols.

The above analysis shows the crossover between the displacive- and order-disorder-type ferroelectric phase transitions in $KTaO_3$ thin films on a c-sapphire substrate, as observed in many perovskite ferroelectrics, including $BaTiO_3$ (see Appendix). Even though the CM might arise from the defects, recent models predicts its intrinsic origin in the highly anharmonic form of the soft-mode potential [207].

In fact, very similar dynamics were observed in epitaxial (100) $SrTiO_3$ thin films deposited by PLD on (110) $DyScO_3$ substrates. The films were under tensile epitaxial strain, arising from the mismatch of the lattice parameters between the film and the substrate (Chapter 1.1.3.3). The paraelectric-ferroelectric phase transition at ~270 K was characterized by the simultaneous increase of the soft-mode frequency ω_{SM} and central mode relaxation strength g, with its frequency $\Gamma_{CM} \approx 10$ cm^{-1} [155,204].

Using the IR spectroscopy, Železny et al. [119] evaluated the soft-mode behavior in

1.2-μm-thick polycrystalline $KTaO_3$ films on (100) Si substrates. They did not observe the ferroelectric phase transition, instead the soft mode was found to be strongly stiffened at low temperatures, with the ω_{SM} value at 10 K ~55 cm^{-1}. For comparison, in the single crystals the soft mode softens to ~20 cm^{-1} [122]. The possible origin of the induced ferroelectricity in polycrystalline $KTaO_3$ thin films will be discussed in the following chapter.

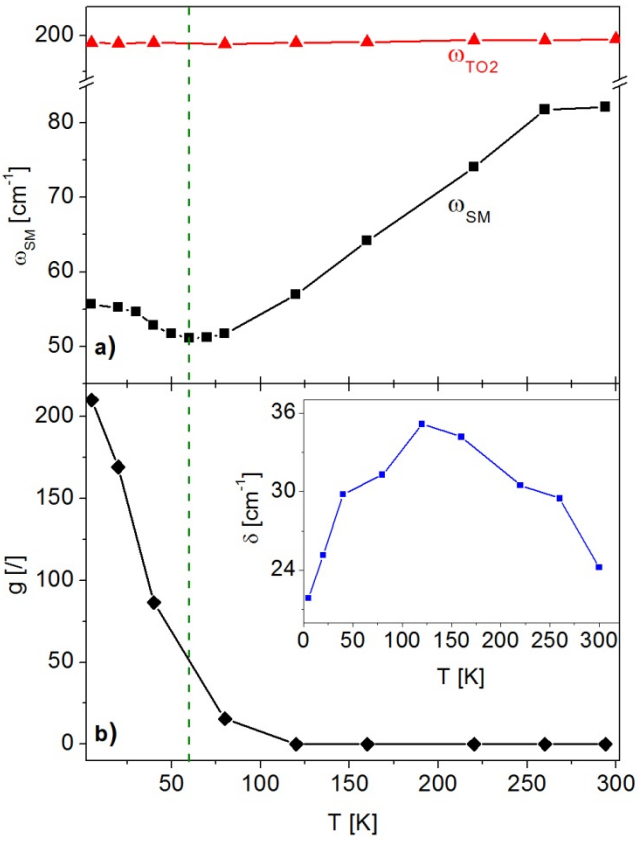

Figure 4.42: Temperature dependences of a) ω_{SM} and ω_{TO2} polar phonon frequencies, b) relaxation strength g and coupling constant δ between SM and CM, obtained from the simultaneous fits of the IR, THz transmission and MW data of the $KTaO_3$ thin film on the c-sapphire substrate. Lines between the points are guides to the eye.

4.2.3 Summary

Perovskite $KTaO_3$ thin films were successfully prepared from the 24-h-refluxed sols based on potassium acetate and transition metals in 2-methoxyethanol, containing 30 % excess of potassium acetate. The 200-nm-thick films on alumina and c-sapphire substrates were prepared by four deposition steps, each of them followed by heating at 900°C. The slightly (100) preferentially oriented perovskite phase was attributed to the anisotropy of the surface energies of different crystal faces. The TEM-EDXS analysis confirmed the perovskite chemical composition through the thickness of the film on the alumina substrate. The films have an in-plane grain size of ~160 nm.

A maximum was observed in the RF and MW dielectric permittivity at low temperatures, which contradicts the incipient ferroelectricity of the polycrystalline $KTaO_3$ thin films on the alumina substrate. Instead, the low-temperature ferroelectric phase was

fingerprinted by the quasi-static polarization measurements. This ferroelectric phase transition is rather diffuse and depends on the history of the sample.

The $KTaO_3$ thin film on the c-sapphire substrate shows qualitatively the same MW dielectric behavior. At room temperature, the TO1, TO2 and TO4 polar phonon frequencies were revealed by the THz and IR spectroscopies, as expected for the $Pm\bar{3}m$ cubic structure of $KTaO_3$. However, by decreasing the temperature, the evidence for the soft-mode-driven paraelectric-ferroelectric phase transition was revealed at ~60 K. In addition, the partial order-disorder character of the transition was confirmed by the onset of the central mode. It is silent in the paraelectric phase, while below the ferroelectric transition temperature it becomes directly coupled to the polarization with a progressively increasing bare strength.

In contrast to $KTaO_3$ single crystals and ceramics, where long-range ferroelectric order is not established, the low-temperature ferroelectric state was detected by several spectroscopic methods in polycrystalline $KTaO_3$ thin films. Discussion on its origin and a comparison of the behavior of all three forms of $KTaO_3$ are the topics of the next chapter.

4.3 Single Crystals – Ceramics – Polycrystalline Thin Films Relations in $KTaO_3$

As shown in Chapters 4.1 and 4.2 the $KTaO_3$ ceramics and polycrystalline thin films have fundamentally different dielectric properties, the first exhibiting a low-temperature quantum paraelectric state, while the long-range ferroelectric order was evidenced in the films. A comparison of these properties with the literature data on single crystals and a discussion on the origin of the observed behavior are the topics of this chapter.

The dielectric permittivity ε' and soft-mode frequency ω_{SM} of the single crystal, ceramic and the polycrystalline film on a c-sapphire substrate are compared in Figure 4.43. The single crystals and ceramics show classic incipient ferroelectric behavior: the permittivity ε' increase and SM frequency ω_{SM} decrease, both leveling off at low temperatures due to quantum fluctuations. The ε' of the ceramics reaches the plateau value of ~4000, which is not significantly lower than the single-crystal value of ~4500. Also, the ω_{SM} values are comparable, having the 20 K value of 23 cm^{-1}.

On the other hand, the dielectric behavior of the polycrystalline film is remarkably different. The broad permittivity ε' maximum, with the value of 1150, appears in the 40–60 K temperature range, the same range where the soft-mode frequency ω_{SM} experiences its minimum value of 51 cm^{-1}, indicating an SM-driven paraelectric-ferroelectric phase transition.

In general, the differences in dielectric behavior of the ceramics and polycrystalline thin films, as compared to single crystals, can arise from:

- Different stoichiometry and homogeneity state, as well as increased concentration of the defects inside the crystal structure, associated with the completely different experimental conditions during processing.
- Presence of grain boundaries and pores between (or within) the grains.
- Appearance of the layers with changed dielectric properties between both surfaces of the film [14]:
    - due to suppressed softness of the crystal lattice near both surfaces,
    - due to the electrode-film interaction.

  No matter of their origin, these layers behave as additional low-permittivity capacitors connected in-series or in-parallel with the film in the case of the out-of-plane or in-plane measurement, respectively. According to Tagantsev et al. [14] the expected influence of these layers on the permittivity ε' value in the 200-nm-thick film measured in the in-plane geometry is of the order of 1 %.
- Non-zero strain-state of thin films due to the presence of the substrates.

In the following discussion the two main influences will be considered in detail: the presence of grain boundaries (and pores) and in the case of thin films the stress arising from the presence of the substrate. However, since the processing issues can never be completely avoided, the influence of the homogeneity and defects will be simultaneously considered.

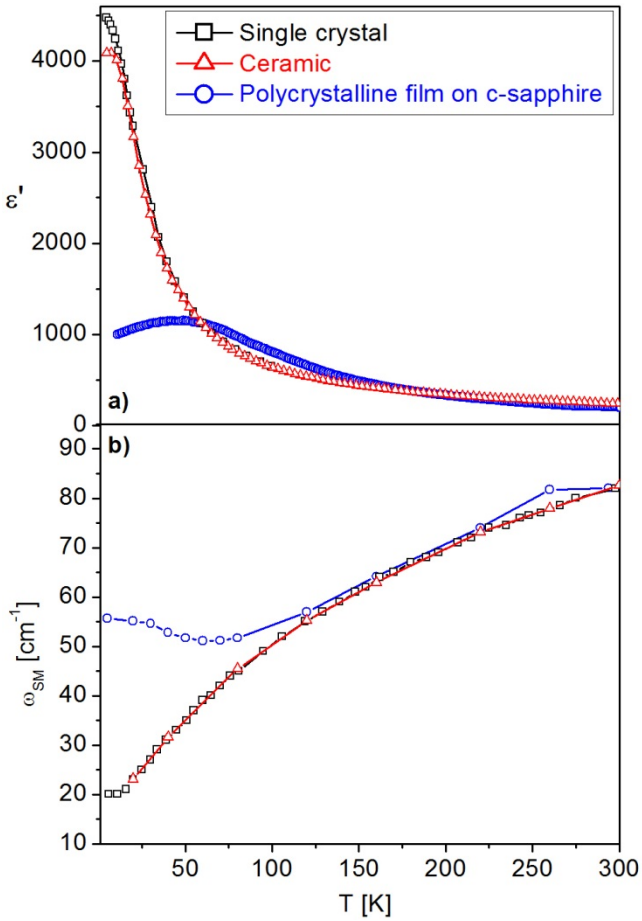

Figure 4.43: Comparison of a) permittivity ε' and b) soft-mode frequency ω_{SM} of the $KTaO_3$ single crystal, ceramic and polycrystalline thin film on a c-sapphire substrate. The respective permittivities were measured at 100 Hz [20], 1 kHz (Figure 4.13a) and 16.2 GHz (Figure 4.36b) The soft-mode frequencies were obtained from the fits of the IR and THz data, while the single-crystal data were obtained from the hyper-Raman measurements in the *x(yy)z* scattering configuration [122].[i]

4.3.1 Grain Boundaries and Pores

To account for the porosity, ceramics can be considered as a composite of single-crystal grains and air, with the respective permittivities ε'_{sc} and ε'_{air}. The measured ε'_{eff} can be expressed by the combination of both, using different models depending on the shape of the grains and the spatial distribution of the pores. Assuming spherical shapes and the small porosity p, the famous Maxwell-Garnett formula can be employed [208]:

$$\varepsilon'_{eff} = \left(1 - \frac{3p}{2+p}\right)\varepsilon'_{sc} + \frac{3p}{2+p}\frac{3\varepsilon'_{air}\varepsilon'_{sc}}{(2+p)\varepsilon'_{air} + (1-p)\varepsilon'_{sc}}. \qquad (4.9)$$

The above equation was employed to estimate the influence of the 2 % and 5 % porosity on the permittivity value of $KTaO_3$ ceramics, using the single-crystal permittivity values from Ref. [20] The result is compared to the experimental data in Figure 4.44.

[i]The x, y, and z stand for cubic axes. The light polarized in y direction is send to the (100) cut sample in the x axis direction. Response of the sample is measured in the z direction.

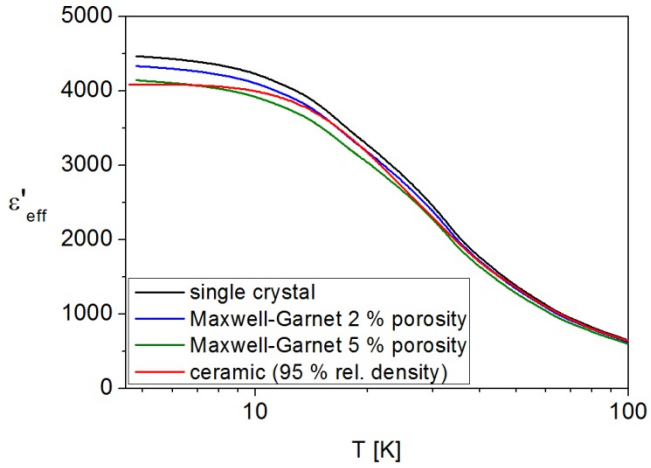

Figure 4.44: Temperature dependence of the permittivity ε' of the $KTaO_3$ single crystal (from Salce et al. [20], 100 Hz) and ceramic (2C-HP, 1 kHz) compared to the effective permittivity of the single-crystal–air composite calculated from Equation (4.9), assuming 2 % and 5 % porosity.

A profound influence of the porosity can be observed as a decrease of the effective permittivity, which is most prominent at low temperatures. When the 5 % porosity is taken into account, the low-temperature effective permittivity value is comparable to the 2C-HP ceramics, with the 95 % relative density. The temperature dependence of the permittivity and soft-mode frequency and their values indicate a rather small influence of grain boundaries on the macroscopic dielectric response of the $KTaO_3$ ceramics (grain size in the approximate range from 0.1 μm to 5 μm).

However, for the MW losses of the ceramics (Figure 4.15), which are partially of extrinsic origin, frequency dispersions observed in the RF range (Figure 4.14), as well as the first-order Raman scattering observed at low temperatures (Figure 4.22), indicate the presence of symmetry-breaking defects inside the ceramics. They most probably arise from Co and W determined by chemical analysis (Table 4.2), and from a rather large off-stoichiometry within the grains was observed by the TEM-EDXS analysis. Further investigations of smaller grain size ceramics by means of high-resolution transmission electron microscopy and broadband dielectric spectroscopy are needed in order to estimate the possible dielectric grain size effect in $KTaO_3$ ceramics, i.e., identify the type of the majority of defects, their spatial position and the structure of grain boundaries.

The in-plane grain size of dense $KTaO_3$ thin films is ~160 nm and their soft mode becomes strongly stiffened compared to the single crystals below ~120 K. Strong stiffening was also observed in the CSD-derived $SrTiO_3$ thin films, and was attributed to the presence of grain boundaries and nano-crack type porosity (Chapter 1.1.3.3) [63]. Even if both effects were also to be present in our films, their contribution alone cannot induce ferroelectricity.

4.3.2 Biaxial Stress

As discussed in Chapter 1.1.3.3 the incipient ferroelectrics are structurally rather unstable and the ferroelectric phase can be induced in several ways, for instance doping. However, the amount of the impurities in the powders prepared from the sols is below 60 ppm

(Table 4.6), which is substantially below the amount that could induce the ferroelectricity [22]. In addition, only K and Ta atoms were determined in $KTaO_3$ films on alumina by the TEM-EDXS analysis, therefore unintentional Al-doping can be excluded as well.

Several theoretical investigations predict the ferroelectricity in the nano-sized incipient ferroelectrics (Chapter 1.1.3.3) [43,44]. The characteristic dimensions of our films, i.e., thickness of 200 nm and in-plane grain size of 160 nm, are greater than the ones discussed in the afore-mentioned predictions (up to 20 nm).

There is no epitaxial relationship between the $KTaO_3$ film and the alumina (or c-sapphire) substrate. Possible strain existing in the films must therefore preferentially arise on cooling from the crystallization temperature of 900°C, due to the difference between both thermal expansion coefficients (Equation (1.13)). For the $KTaO_3$ and alumina the thermal expansion coefficients α values are 6.3 x 10^{-6} K^{-1}[209][i] and 8.2 x 10^{-6} K^{-1}[139][ii], respectively. The Young's modulus E = 395 GPa and Poisson's ratio ν = 0.194 were calculated from the single-crystal elastic constants [210]. The obtained u_{therm} and σ_{therm} values at 60 K are -0.21 % and ~-1.0 GPa, respectively. Since the Al_2O_3 shows only small anisotropy of the thermal expansion coefficients [211], a very similar situation is also valid for the film on the c-sapphire substrate. In the case of the RF- and quasi-static-measurements an additional stress contribution may arise from the presence of 120-nm-thick-Au electrodes, which have a room-temperature α = 14.2 x 10^{-6} K^{-1} [212]. During the measurement (on cooling), this can result in a gradient stress field with increasing compressive value towards the upper surface of the film.

Even though the above analysis is only a rough approximation, it reveals that at low temperatures the polycrystalline $KTaO_3$ films on alumina and c-sapphire are under a non-negligible compressive strain. However, its magnitude is below the theoretically predicted value of -1 %, which is expected to induce the out-of-plane ferroelectricity in coherently strained (100)-oriented $KTaO_3$ thin films [42].

Nevertheless, the nature of the strain-induced ferroelectricity in thin films of incipient ferroelectrics is rather complicated. As was discussed in recent reports, in the case of $SrTiO_3$ films, the strain has a role of stabilizing the long-range order of the pre-existing polar nano-regions, arising from the A-site off-stoichiometry (intentional or unintentional). As shown in Chapter 4.1.1.2, potassium excess is needed to prepare phase-pure perovskite $KTaO_3$, indicating significant losses of potassium species upon high-temperature heating. Even though the TEM-EDXS analysis revealed the stoichiometric composition of the film on a corundum substrate after heating at 900°C (Figure 4.30), some small amounts of the A-site deficiency, which are within the error of the method, can be expected. These could form short-range polar entities within the film. Similar to the $SrTiO_3$ thin films, a delicate interplay between these polar regions and strain might also exist in the polycrystalline $KTaO_3$ films. However, further investigations by means of high-resolution XRD, TEM and Raman investigations are needed to confirm this speculation.

[i] Obtained at room temperature.
[ii] Obtained in 25–1000°C temperature range.

4.4 $KTa_{0.6}Nb_{0.4}O_3$ Thin Films

We have shown in the preceding chapters that $KTaO_3$ ceramics and thin films possess a rich range of exciting phenomena. Still, their applicability in microwave devices operating at room temperature is limited. Therefore, we have also studied CSD-derived $KTa_{0.6}Nb_{0.4}O_3$ thin films, which should possess a high-enough permittivity to be efficiently tuned at room temperature.

The present chapter begins with an investigation of the structural changes inside the sols upon refluxing by the extended X-ray-absorption fine-structure spectroscopy (EXAFS) in the neighborhood of both B-site transition metals, complemented by the IR spectroscopy of the distillates.

The influence of the reflux time on the microstructure, phase composition and dielectric properties of the films is presented in the second part. Analysis of the RF and MW dielectric properties of the phase-pure $KTa_{0.6}Nb_{0.4}O_3$ thin films is described in the last part. A possible origin of the dielectric behavior is discussed. A comparison of the $KTaO_3$ and $KTa_{0.6}Nb_{0.4}O_3$ thin films brings the chapter to the end.

4.4.1 Preparation of the Films

4.4.1.1 Synthesis of the Sols

Stoichiometric $KTa_{0.6}Nb_{0.4}O_3$ sols were prepared from the potassium acetate and transition-metal ethoxides in 2-methoxyethanol (Chapter 3.1.2.1). After dissolution of the starting compounds the sols were refluxed for different times, i.e., 1 h, 4 h, 24 h and 48h, followed by a distillation to remove the by-products, and are further denoted as the KTN1, KTN4, KTN24 and KTN48 sols, respectively.

4.4.1.1.1 EXAFS Spectra of the $KTa_{0.6}Nb_{0.4}O_3$ Sols

We performed the EXAFS analysis of the KTN sols to determine structural differences in the transition metals local environments after different reflux times. The Ta L_3-edge and Nb K-edge EXAFS spectra (Figure 4.45) were analyzed with the IFEFFIT program package [213]. Distinctive peaks in the Fourier transforms of the EXAFS spectra (Figure 4.46) are the contributions of the photoelectron backscattering on the near-neighbor shells around the central atom, and represent the approximate radial distribution of the atoms surrounding the transition-metal atom. A strong compound peak in the *R* range between 1 Å and 2.4 Å can be attributed to the nearest oxygen neighbors of the Ta or Nb atoms. Due to a high signal-to-noise ratio, the contributions of the more distant Ta and Nb coordination shells up to ~4 Å can be clearly resolved in all the spectra. A qualitative comparison of the spectra shows that there are no structural changes around the Ta atoms in the sols after different reflux times (Figure 4.46a). On the other hand, significant structural changes are indicated in the Nb environment in the nearest and more distant coordination shells (Figure 4.46b).

The quantitative structural information of the local Ta and Nb neighborhood (type and average number of neighbors, radii and Debye-Waller factors of neighboring shells) was obtained by an EXAFS analysis in which the model EXAFS function was fitted to the

measured EXAFS spectra. For this purpose, we constructed model EXAFS functions *ab initio*, from a set of scattering paths of the photoelectron obtained in a tentative spatial distribution of the neighbor atoms with the FEFF6 program code [214]. The atomic species of the neighbors were identified in the fit by their specific scattering factors and phase shifts. The model for Ta EXAFS comprised oxygen atoms in the first coordination shell, and carbon and potassium atoms in more distant shells. An additional shell of Nb neighbors had to be introduced for the Nb EXAFS spectra.

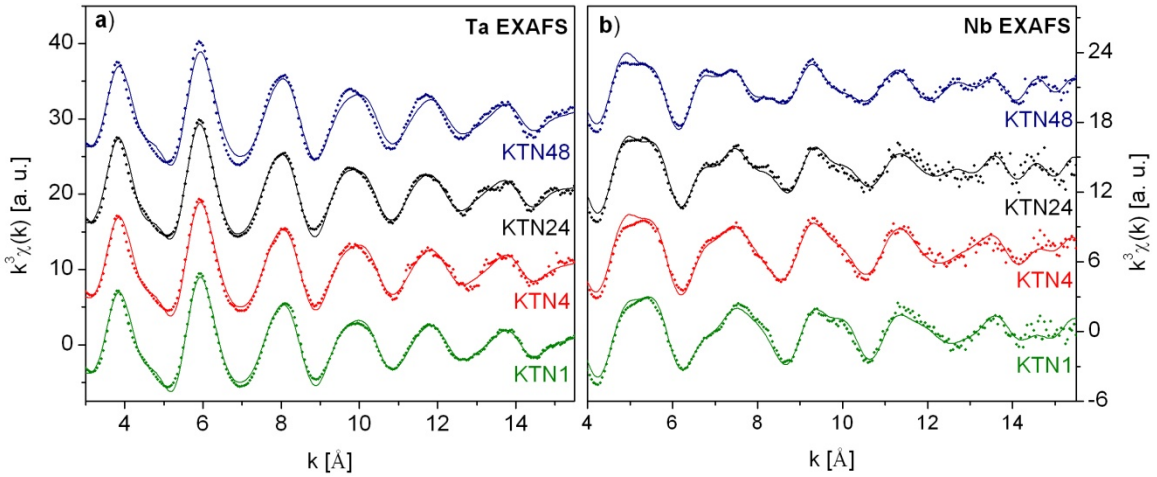

Figure 4.45: The k^3-weighted a) Ta and b) Nb EXAFS spectra of the KTN1, KTN4, KTN24 and KTN48 sols (dots) in comparison with the best-fit EXAFS model (solid lines).

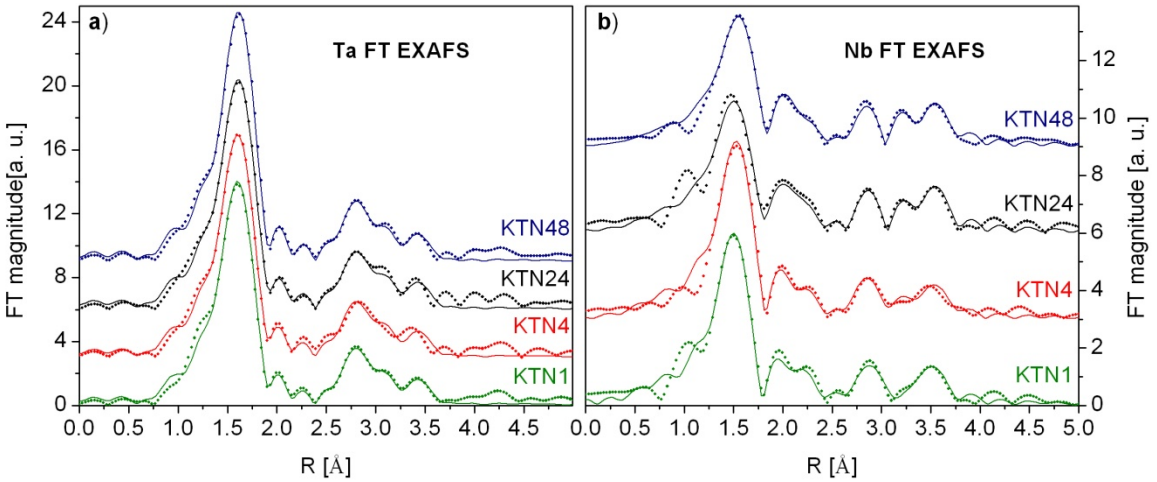

Figure 4.46: Fourier transforms of the k^3-weighted a) Ta and b) Nb EXAFS spectra of KTN1, KTN4, KTN24 and KTN48 sols from Fig. 1, calculated in the k-range from 3 Å^{-1} to 15 Å^{-1} for Ta, and from 4 Å^{-1} to 15 Å^{-1} for Nb EXAFS spectra. Dots – experiment; solid lines – best-fit EXAFS model.

We introduced three variable parameters for each shell of neighbors: the shell coordination number (N), the distance (R) and the Debye-Waller factor (σ^2). In addition, the common shift of the energy origin, ΔE_0, was allowed to vary. The amplitude reduction factor S_o^2 was fixed to 0.99 for the Ta and to 0.80[215] for the Nb EXAFS spectra. For the Ta spectra, the fitting was performed in the k range from 3.0 Å^{-1} to 15 Å^{-1}, and the R

range from 1.1 Å to 3.8 Å and for the Nb spectra in the *k* range of 4.0 $Å^{-1}$ to 15 $Å^{-1}$, and the *R* range from 1.2 Å to 3.9 Å.

To minimize the relatively large uncertainties of the coordination numbers and the Debye-Waller factor, due to high correlations between these parameters in the fit of each individual spectrum, a simultaneous fit of all Ta spectra, and separately a simultaneous fit of all Nb EXAFS spectra were performed. In the simultaneous relaxation, some of the parameters within the group of the spectra were constrained to common values, in particular, for Ta spectra, the common energy shift ΔE_0, the interatomic distances of the corresponding shells of neighbors and the corresponding Debye-Waller factors, except for the parameters of the nearest oxygen shell. In the fit of the Nb EXAFS spectra, constraining all these common parameters to the same value for all of the spectra would represent a too rigid model, which could not adequately describe all of the structural differences that appeared for the Nb neighborhood after different reflux times. In this manner 26 active parameters of the model against 80 independent points were obtained for the fit of the Ta spectra and 41 active parameters against 74 independent points for the Nb spectra.

A complete list of the best-fit parameters for all of the samples is given in Table 4.7 and Table 4.8. The quality of the fits is illustrated in Figure 4.45 and Figure 4.46.

Table 4.7: Parameters of the nearest coordination shells around the Ta in $KTa_{0.6}Nb_{0.4}O_3$ sols after different reflux times: atomic species, average number of the atomic species *N*, distance *r* and Debye-Waller factor σ^2. The uncertainty of the last digit is given in parentheses.

Sol	Neighbor atom	*N*	*r* [Å]	σ^2[Å^2]
KTN1	O	5.1(1)	1.956(2)	0.0044(2)
	O	1	2.36(2)	0.011(2)
	C	5.2(7)	3.117(5)	0.006(1)
	K	1	3.59(1)	0.0041(7)
	C	17(2)	3.722(7)	0.014(2)
KTN4	O	5.1(3)	1.956(2)	0.0044(2)
	O	1	2.36(2)	0.011(2)
	C	5(1)	3.117(5)	0.006(1)
	K	1	3.59(1)	0.0041(7)
	C	17(4)	3.722(7)	0.014(2)
KTN24	O	5.4(2)	1.964(2)	0.0045(3)
	O	1	2.36(2)	0.011(2)
	C	5(1)	3.117(5)	0.006(1)
	K	1	3.59(1)	0.0041(7)
	C	18(3)	3.722(7)	0.014(2)
KTN48	O	5.4(2)	1.964(2)	0.0036(2)
	O	1	2.36(2)	0.011(2)
	C	5(1)	3.117(5)	0.006(1)
	K	1	3.59(1)	0.0041(7)
	C	18(3)	3.722(7)	0.014(2)

Table 4.8: Parameters of the nearest coordination shells around the Nb in $KTa_{0.6}Nb_{0.4}O_3$ sols after different reflux times: atomic species, average number of the atomic species *N*, distance *r* and Debye-Waller factor σ^2. The uncertainty of the last digit is given in parentheses.

Sol	Neighbor atom	N	r [Å]	σ^2[Å^2]
KTN1	O	2.4(3)	1.897(4)	0.0032(6)
	O	1.0	2.26(2)	0.008(2)
	O	2.5(3)	2.51(1)	0.011(2)
	C	4(1)	3.101(6)	0.006
	C	8(2)	3.37(1)	0.008
	K	0.5	3.60(1)	0.0018(5)
	Nb	1.2(2)	3.83(1)	0.006
	C	7(3)	4.12(2)	0.01
KTN4	O	2.7(2)	1.922(4)	0.0034(4)
	O	1.0	2.26(2)	0.008(2)
	O	2.3(2)	2.51(1)	0.011(2)
	C	4(1)	3.101(6)	0.006
	C	8(1)	3.37(1)	0.008
	K	0.75	3.60(1)	0.0018(5)
	Nb	1.1(2)	3.83(1)	0.006
	C	6(2)	4.12(2)	0.01
KTN24	O	2.4(4)	1.913(6)	0.005(1)
	O	1.0	2.26(2)	0.008(2)
	O	2.6(4)	2.51(1)	0.009(1)
	C	4(1)	3.101(6)	0.006
	C	8(2)	3.35(1)	0.007
	K	1.0	3.60(1)	0.0018(5)
	Nb	1.6(3)	3.83(1)	0.006
	C	7(2)	4.12(2)	0.01
KTN48	O	2.4(2)	1.946(4)	0.0046(5)
	O	1.0	2.26(2)	0.008(2)
	O	2.6(2)	2.51(1)	0.009(1)
	C	4.0(7)	3.101(6)	0.006
	C	8(1)	3.35(1)	0.007
	K	1.0	3.60(1)	0.0018(5)
	Nb	1.4(2)	3.83(1)	0.006
	C	8(1)	4.12(2)	0.01

4.4.1.1.2 Ta and Nb Local Environments

In all KTN sols the Ta atom is octahedrally coordinated by O atoms, as also found in other studies of Ta-alkoxides [100,102]. Five O atoms are located at 1.956 Å in the KTN1 and KTN4 sols and at a slightly larger distance, i.e., 1.964 Å, after long reflux times. There is an additional contribution of O atoms at 2.36 Å in all cases. Despite the simultaneous fit, the correlation between average occupation number *N* and Debye-Waller factor σ^2 of this neighbor shell remained high; therefore *N* was set to one to obtain the coordination number of six. In more distant shells, one K atom is detected at a distance of

3.59 Å in all the sols. Ta-O-K bonds are clearly established by the results of the analysis.

Two shells of carbon atoms, one at 3.12 Å and one broad shell at 3.72 Å are ascribed to the different organic groups bonded to the Ta. The relatively large uncertainty in the number of C atoms is a consequence of the highly correlated N and σ^2 in the fit. The unrealistically large number of carbon atoms at 3.72 Å is a consequence of the approximation in the EXAFS model, which described the signal at these distances with a single broad shell of carbon atoms. The models including Ta and/or Nb atoms in the second shell were also tested, but the existence of Ta-O-Ta or Ta-O-Nb correlations was excluded by the fit.

In the Nb local environment, the first coordination shell is populated with approximately six O atoms at three different distances. In the KTN1 sol, approximately three O atoms are present at 1.897 Å. Their distance from the central atom varies with the reflux time and reaches 1.946 Å in the KTN48 sol. One O atom is located at 2.26 Å in all cases. The number was not allowed to vary because of the high correlation with the Debye-Waller factor. Approximately two O atoms are present in all the sols at 2.51 Å. Their value was tied to the number of O atoms at closer distances to keep the total coordination number of six, as typical for niobium alkoxides [100,102].

Potassium was identified in all the sols at about 3.60 Å. The average number of K atoms could be determined only with a rather large uncertainty, but a gradual increase of the number of K neighbors with increasing the reflux time to 24 h was detected unambiguously. Approximately one Nb atom has been determined at 3.83 Å. The average number of Nb neighbors increases slightly with the reflux time. Again, the Nb-O-Ta correlations were excluded by the fit. Several C atoms were also identified in the Nb neighborhood at three significantly different distances in the range from 3.10 Å to 4.12 Å. They can be ascribed to different organic groups bonded to Nb.

4.4.1.1.3 Local Structure and Reactions in the Sols upon Refluxing

The nearest neighborhood of both Ta and Nb consists of six O atoms. The closest O atoms belong to the terminal alkoxide groups, which can be either ethoxide and/or 2-methoxyethoxide, as a product of the transalcoholysis reaction (Equation (1.19)), which takes place already at room temperature [101]. However, according to Sedlar and Sayer [216] the transalcoholysis reaction of Nb-ethoxide is not completed at room temperature; therefore, the reaction could proceed also during refluxing, which is in agreement with the observed change of the Nb-O distance from 1.897 Å to 1.946 Å with increasing reflux time. The Ta-O distances did not change significantly at longer reflux times. The solvent could coordinatively bond to Nb via its hydroxy or ether groups (Figure 1.13) [101].

The Nb neighborhood is populated with at least one Nb atom at 3.83 Å, which indicates the dimeric structure of the Nb species (Figure 1.12) [102]. A slight increase of the number of Nb-neighbors with increasing reflux time could be explained by thermally activated segregation, resulting in the formation of polynuclear oxoalkoxides [101]. In contrast, Ta alkoxide keeps its monomeric structure in all the sols.

The K atoms were identified in the more distant shells of both TMs in all the sols. In the case of Ta, the number of K neighbors does not change with the reflux time and can be set to 1. In contrast, in the Nb environment, the number of K atoms gradually increases

from 0.5 to 1.0 in the KTN1 and KTN24 sols. So, a longer reflux time favors the formation of Nb-O-K bonds.

Potassium can bond to the TM via oxo or acetate bridges, formed by the ester-elimination reaction (Equation (4.10)) or by the addition reaction (Equation (4.11)), respectively [101]:

$$KOOCH_3 + TM(OR)_5 \rightarrow K - O - TM(OR)_4 + ROOCH_3 \quad (4.10)$$

$$KOOCH_3 + TM(OR)_5 \rightarrow KOOCH_3\text{-}TM(OR)_5, \quad (4.11)$$

where R can be either the ethoxide (OCH_2CH_3) or 2-mehoxyethoxide ($OCH_2CH_2OCH_3$) group. Both equations are simplified and shown for monomeric species.

The infrared (IR) spectra of the distillates and 2-methoxyethanol were recorded and in the majority of the wavelength range they are identical. However, an absorption band at 1740 cm^{-1}, which is not present in the spectrum of the solvent, appears in the spectra of the distillates (Figure 4.47). Its intensity gradually increases from the KTN1 to the KTN24 and KTN 48 spectra. It is characteristic for the stretching vibration of the C=O bond in esters. Additional bands, characteristic for the stretching vibrations of the C–O–C ester bonds, should also be present, but the response of the 2-methoxyethanol, which is the main component in the distillates, prevails in the 1300-1000 cm^{-1} range. The result confirms the esterification reaction (Equation (4.10)); however, the simultaneous onset of the addition reaction cannot be omitted also. In the 2-methoxyethanol route of the PZT system both reactions have been confirmed, resulting in a precursor consisting of oxo, alkoxo and acetate groups [217].

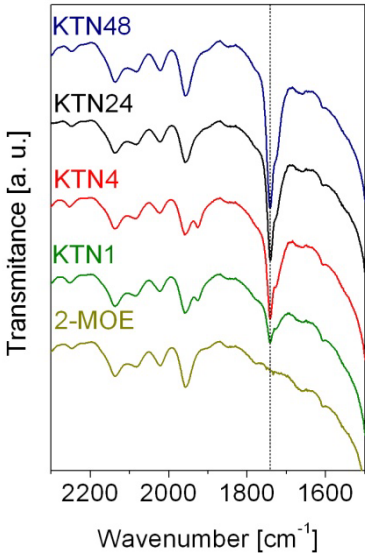

Figure 4.47: IR spectra of the KTN1, KTN4, KTN24 and KTN48 distillates. For comparison, a spectrum of the 2-methoxyethanol (2-MOE) is also shown. The dashed line stresses the presence of the absorption band at 1740 cm^{-1} in all distillates' spectra. Spectra are displaced vertically for reasons of clarity.

As a summary, the local environment of Ta atoms is almost independent of the reflux time; it is coordinated by six oxygen atoms in the first shell and a potassium atom in the

second shell of neighbors. There are no Ta-O-Ta or Ta-O-Nb correlations present in the sols. In contrast, the Nb local environment changes with reflux time. After 1 h of reflux, Nb is present in the form of dimers and the number of Nb neighbors slightly increases with the reflux time. The Nb-O-K correlations were confirmed already after 1 h; however, a steady state was established only after 24 h of reflux.

4.4.1.2 Thermal Decomposition of the Dried Sols

The 1-h- and 24-h-refluxed sols (KTN1 and KTN24) were selected for further investigations. Prior to the thermal analysis the sols were dried at 60°C for at least 12 h. The analyses were performed in a flowing air atmosphere (Chapter 3.2.1).

The TG curves of both powders are compared in Figure 4.48. From 25°C to 755°C the KTN1 and KTN24 dried sols lose 22.4 % and 20.8 % of the starting mass, respectively. The mass loss of both powders can be divided into three approximate intervals: 25–200°C, 200–570°C and 570–755°C. The main differences between the two arise in the first two intervals, in which the KTN1 powder loses 4.8 % and 15.2 %, respectively. The respective relative mass losses of the KTN24 powder are 6.9 % and 11.2 %. Both powders lose approximately 2.5 % of the starting mass in the last interval. The process of mass loss is not completely finished even at 755°C.

Differences can also be observed in the DTG curves, shown in the inset of Figure 4.48. Several minima are distinguished in the KTN24 curve (see Figure 4.49 for details) at 105°C, 262°C (the strongest), 353°C, 530°C, 609°C and 655°C. In the case of the KTN1 sol the strongest minimum is present at a slightly higher temperature, i.e., 270°C and is also much broader.

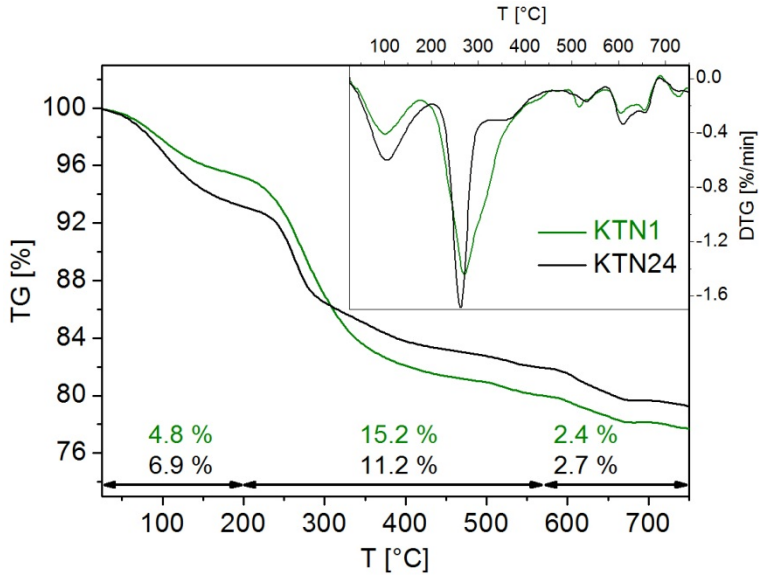

Figure 4.48: Comparison of the TG curves of the KTN1 and KTN24 stoichiometric $KTa_{0.6}Nb_{0.4}O_3$ sols after drying at 60°C. The DTG curves of both sols are compared in the inset.

In Figure 4.49 the detailed TG and DTG, as well as the DTA and EGA, curves of the KTN24 sols after drying are presented. The first interval is characterized by a broad endo-peak in the DTA curve at ~117°C, accompanied by a maximum in the EGA curve corresponding to the H_2O (mass fragment 18). In the second interval a strong exothermic

peak at 270°C and a shoulder at 360°C are present in the DTA curve. In the same temperature range the H_2O and CO_2 (mass fragment 44) are evolving. In the last mass loss interval two small exo-DTA peaks are present at 604°C and 667°C. Both are accompanied by the evolving CO_2 and, to minor extent, also H_2O. The XRD pattern of the powder after the analysis revealed the presence of the perovskite, as the main, and pyrochlore, as the secondary phase in both the KTN1 and KTN24 powders (Figure 4.50).

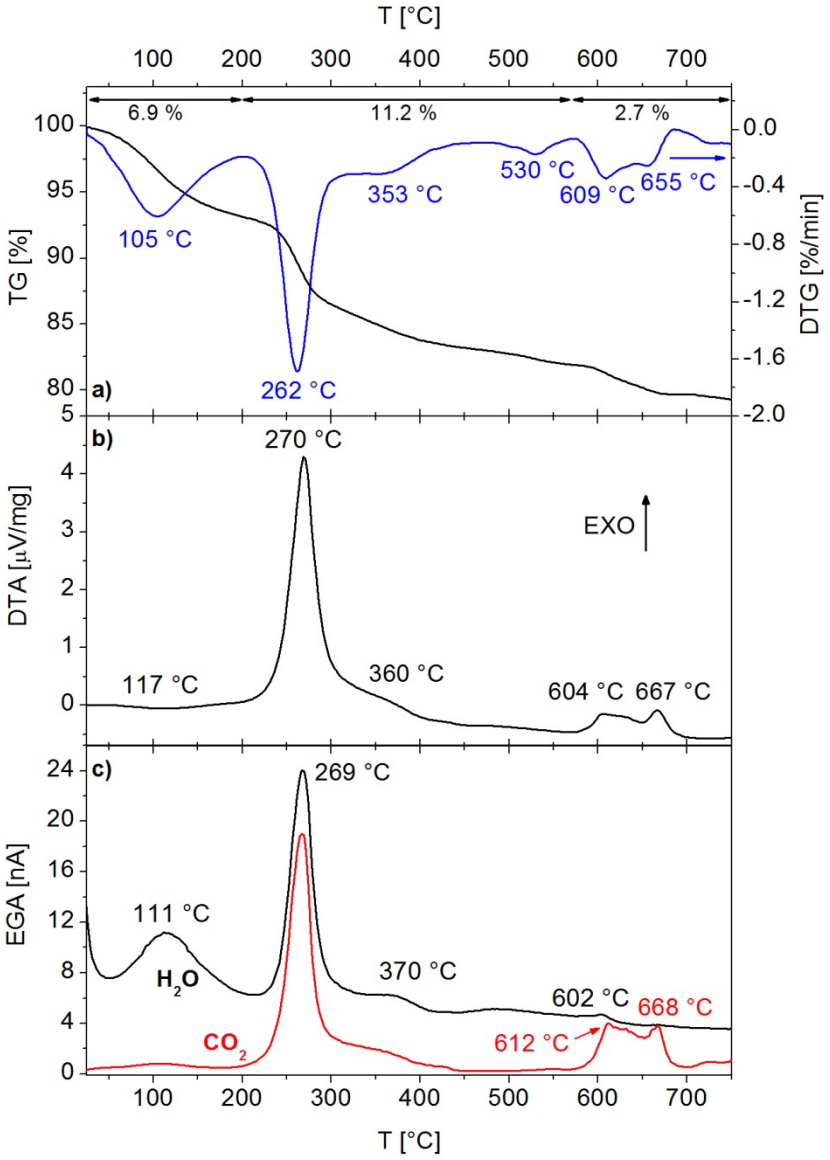

Figure 4.49: a) TG and DTG, b) DTA and c) EGA curves of the 24-h-refluxed stoichiometric $KTa_{0.6}Nb_{0.4}O_3$ sol after drying at 60°C. Positions of the strongest maxima and minima in the curves are denoted.

In the first temperature interval the main mechanism of the mass loss is the evaporation of the adsorbed H_2O and probably also residues of the 2-methoxyethanol, both being endothermic events. Between 200°C and 570°C, where the mass loss is the largest, the thermal decomposition of the organic, predominantly alkoxide (Equations (4.1) and (4.2)), groups occur, which is in the presence of O_2 a strongly exothermic process. The process is mainly accomplished at ~350°C; however, the proceeding evolution of H_2O and CO_2 are indicating further decomposition of the organic and carbon

residues [187]. If the acetate groups are still present in the sols, their decomposition through a carbonate phase could also take place in the second temperature interval (Equation (4.3)). The main difference between the thermal decompositions of the KTN1 and KTN24 sols was observed in this range (Figure 4.48), indicating the different structure of the organic species in both sols.

The overlapping exothermic peaks between 570°C and 755°C are associated with the crystallization process. According to the literature, the first one most probably corresponds to the pyrochlore, and the second one to the perovskite phase. [103] Both are overlapping with the decomposition of the organic and carbon residues.

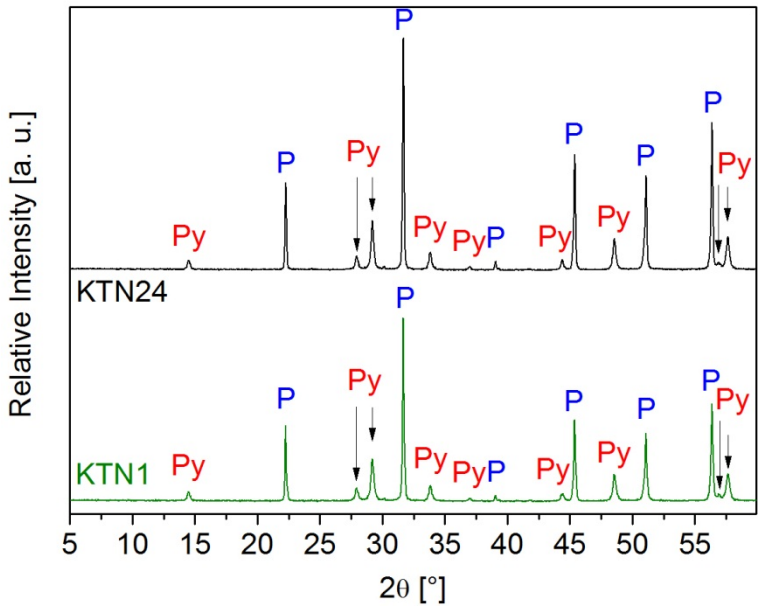

Figure 4.50: XRD patterns of the KTN1 and KTN24 $KTa_{0.6}Nb_{0.4}O_3$ powders after the thermal analysis. P-perovskite phase [142]; Py-pyrochlore phase [164].

4.4.1.3 Phase Composition and Microstructure of the Films

The 1-h- and 24-h-refluxed sols were chosen for the preparation of the films on alumina substrates. After spin-coating the films were pyrolyzed at 350°C and the procedure was repeated four times to increase the thickness. Final annealing was performed for 15 min in the RTA furnace (Chapter 3.1.2.3).

XRD patterns of the films prepared from the 1-h-refluxed stoichiometric sols are shown in Figure 4.51a. Peaks corresponding to the perovskite, pyrochlore and some unidentified phase can be observed after heating at 700°C. The relative intensity of the perovskite peaks gradually increases with increasing heating temperature; however, even after 900°C traces of pyrochlore and unidentified phase are still present in the films. The films were also prepared from the sols with added 10 % excess of potassium acetate (Figure 4.52b). The phase composition of the KTN1-10 films after heating at 700°C, 800°C and 900°C is qualitatively the same as in KTN1 films, consisting of the perovskite, pyrochlore, and at least one unidentified phase.

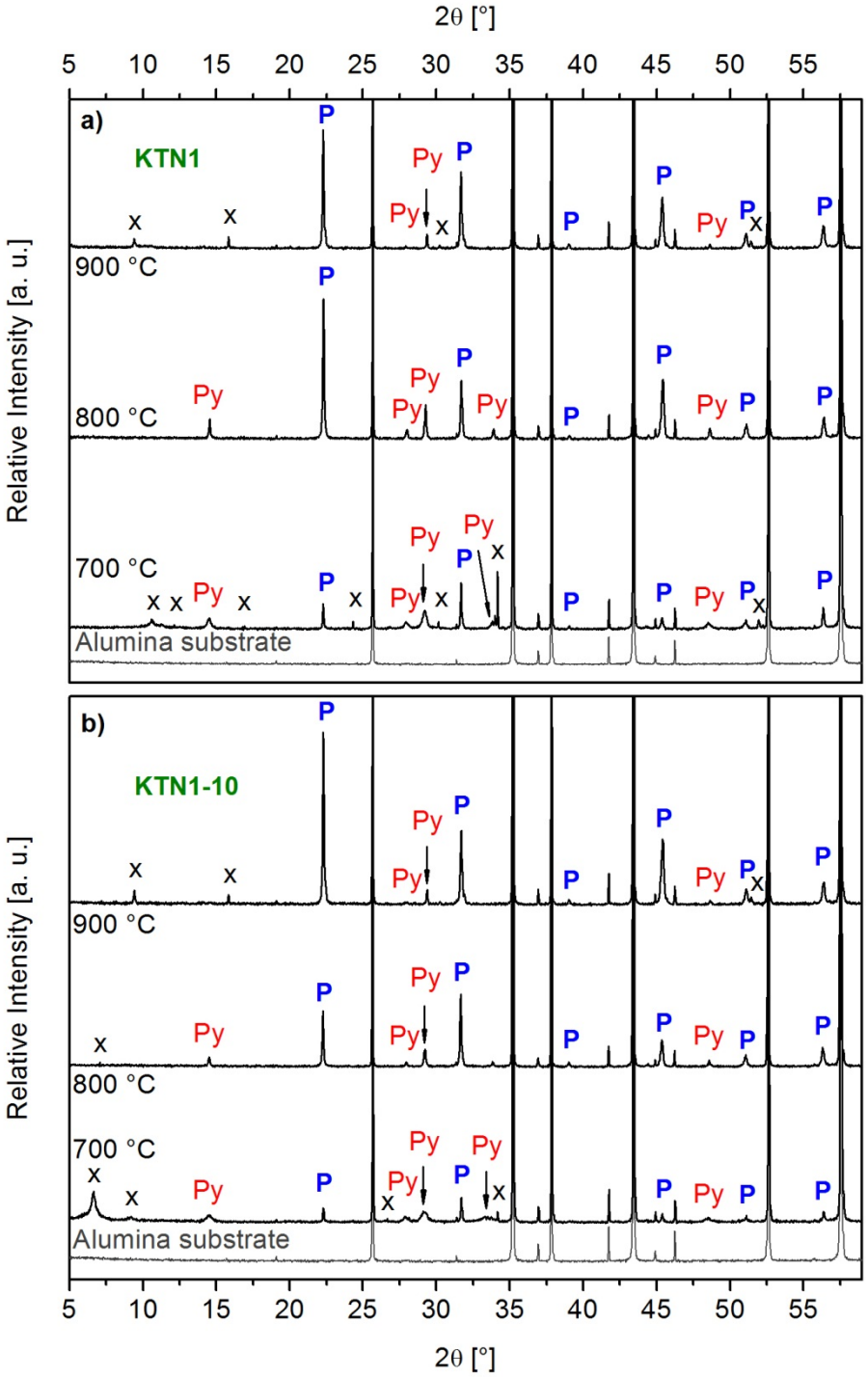

Figure 4.51: XRD patterns of the $KTa_{0.6}Nb_{0.4}O_3$ thin films on alumina substrates prepared from the 1-h-refluxed a) stoichiometric sols and b) from the sols with 10 % excess of the potassium excess (b). After four depositions final annealing was performed for 15 min at 700°C, 800°C, or 900°C. Pattern of the alumina substrate is also shown. P – perovskite phase [142]; Py – pyrochlore phase [164]; X – unidentified peaks.

The films were also prepared from the 24-h-refluxed sols and the XRD patterns after heating at 700°C, 800°C and 900°C are shown in Figure 4.52. Again, the films prepared from the stoichiometric sols are composed of perovskite, pyrochlore and at least one secondary phase after heating at 700°C, 800°C, or 900°C. The KTN24-10 films, prepared from the sols with 10 % excess of potassium acetate, show a multi-phased composition

after heating at 700°C and 800°C as well; however, they are single-phase cubic perovskites according the XRD analysis after heating at 900°C (Figure 4.52b).

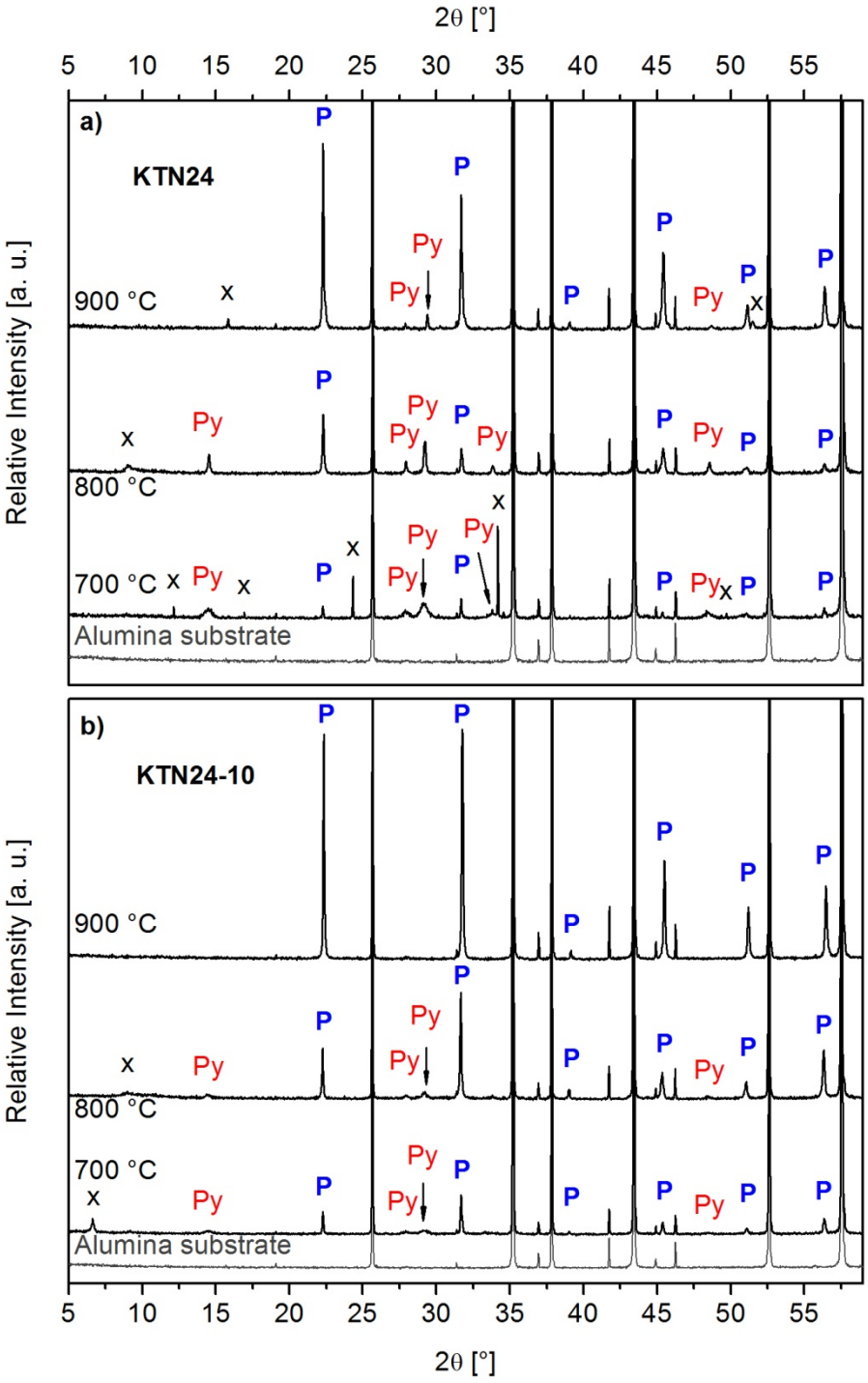

Figure 4.52: XRD patterns of the $KTa_{0.6}Nb_{0.4}O_3$ thin films on alumina substrates prepared from the a) 24-h-refluxed stoichiometric sols and b) from the sols with 10 % excess of the potassium excess. After four depositions final annealing was performed for 15 min at 700°C, 800°C, or 900°C. Pattern of the alumina substrate is also shown. P – perovskite phase [142]; Py – pyrochlore phase [164]; X – unidentified peaks.

Similar to the $KTaO_3$, also the $KTa_{0.6}Nb_{0.4}O_3$ films have the tendency to crystallize in the (100) preferentially oriented perovskite phase. The Lotgering factor $f_{(100)}$ (Equation

(4.4)), calculated in the 5–60° 2θ range of the KTN24-10 film after heating at 900°C, is ranging from 0 to 0.3 (evaluated in 5 different samples). The tendency for the (100)-oriented perovskite phase can be explained by the lowest surface energy of the (100) crystal face (Chapter 4.2.1.2).

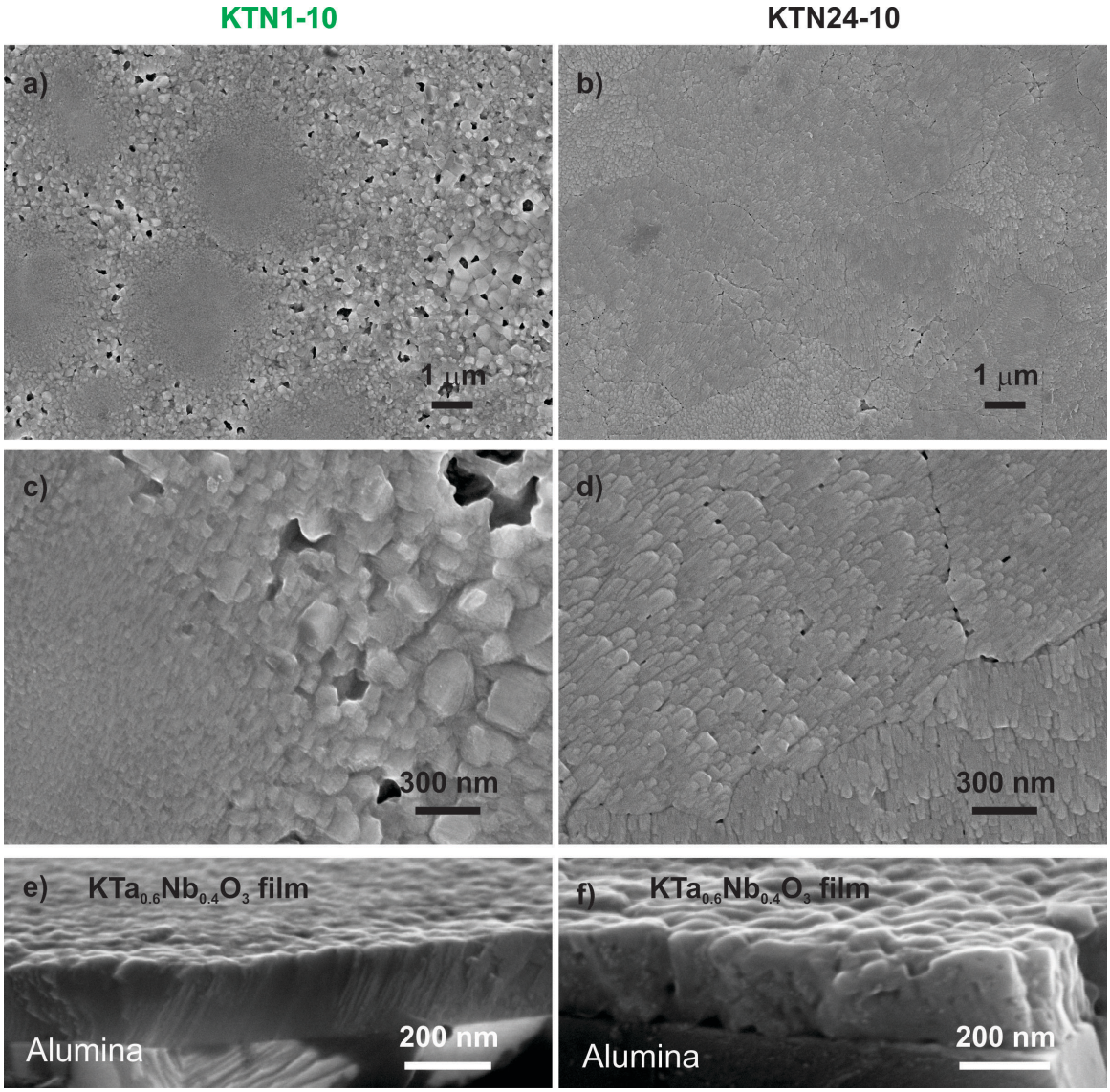

Figure 4.53: a), b), c) and d) plane-view and e), f) cross-section view FE-SEM micrographs of the KTN1-10 (a), c), e)) and KTN24-10 (b), d), f)) $KTa_{0.6}Nb_{0.4}O_3$ thin films on the alumina substrates after heating at 900°C. The films were prepared from the 1-h- and 24-h-refluxed sols, respectively, containing 10 % of the potassium acetate excess.

Microstructures of the KTN1-10 and KTN24-10 thin films after heating at 900°C, prepared from the 1-h- and 24-h-refluxed sols, respectively, are compared in Figure 4.53. The plane-view microstructure of the KTN1-10 thin films is heterogeneous, consisting of the fine-grained (~10 nm) dense regions and porous coarse-grained (above 100 nm) regions. The surface of the KTN-24 thin film is much more homogeneous, consisting of the regions with different grain orientations, having a size of approximately 70 nm, as obtained from the lineal analysis. The cross-section micrographs reveal 220-nm- and 240-nm-thick KTN1-10 and KTN-24, respectively, but in the first case the thickness can be

quite non-uniform due to the heterogeneous microstructure.

The coexistence of perovskite and pyrochlore phases in the $KTa_{0.6}Nb_{0.4}O_3$ thin films, prepared from the 1-h-refluxed sols, and their heterogeneous microstructure is in agreement with the literature reports on the CSD-processing of the $K(Ta,Nb)O_3$ films on substrates that exhibit no structural matching (Chapter 1.2.3.2) [106,111,113,114]. Even though the RTA process was used, the pyrochlore phase is always present in the films. However, by prolonging the reflux time to 24 h, the phase-pure $KTa_{0.6}Nb_{0.4}O_3$ films homogeneous microstructures were successfully prepared after heating at 900°C. From the results of the EXAFS analysis of the sols it follows that the formation of the bimetallic species between potassium and both transition metals is directly related to the enhanced crystallization on the alumina substrates.

4.4.2 Radio-Frequency and Microwave Dielectric Properties

The room-temperature dielectric properties of the KTN1-10 and KTN24-10 $KTa_{0.6}Nb_{0.4}O_3$ thin films, prepared from the 1-h- and 24-h-refluxed sols, respectively, after heating at 900°C, were analyzed. RF-range measurements were performed in the planar capacitor structure (Figure 3.4), while the electrode-less split-post dielectric resonator method was used for the MW characterization. The KTN1-10 thin film has the room-temperature permittivity ε' at 1-MHz value of 860, which decreases with increasing frequency to 360 at 14.5 GHz. The respective dielectric losses $\tan\delta$ values are 0.01 and 0.34 (Table 4.9). A similar frequency dependence of the dielectric properties can be observed also for the KTN24-10 films, with significantly higher permittivity values, decreasing from 2200 at 1 MHz to 610 at 14.5 GHz.

Table 4.9: Room-temperature dielectric permittivity ε' and losses $\tan\delta$ of the KTN1-10 and KTN24-10 $KTa_{0.6}Nb_{0.4}O_3$ thin films after heating at 900°C, measured in the RF and MW frequency range.

		Frequency			
Film		*1 MHz*	*7.3 GHz*	*9.9 GHz*	*14.5 GHz*
KTN1-10	**ε'**	860	440	*380*	*360*
	$\tan\delta$	0.01	0.25	0.31	0.34
KTN24-10	**ε'**	2200	730	670	610
	$\tan\delta$	0.08	0.28	0.34	0.37

The response of the normalized permittivity $\varepsilon'(E_{DC})/\varepsilon'(0)$ on the applied bias field E_{DC} of the KTN1-10 and KTN24-10 films is shown in Figure 4.54. In the case of the KTN1-10 films the permittivity decreases to 41 % of the starting value, at the applied filed of 100 kV/cm. A much steeper decrease of the permittivity with increasing E_{DC} is observed for the KTN24-10 film. The tunability n (Equation (1.4)) of the KTN1-10 film is 2.5 (92 kV/cm), and of the KTN24-10 film is 3.8 (100 kV/cm). For comparison, taking the 1 MHz room-temperature permittivity value of $KTa_{0.6}Nb_{0.4}O_3$ ceramics 2880 and its non-linear coefficient $\beta = 3 \times 10^9$ J C^{-4} m^5, by using the Equation (1.7) one gets the tunability n value of 5.1 at the applied field 100 kV /cm. However, to apply such fields in the ceramics, extremely high voltages, of the order of several kV, are needed, while only 30

V were applied in the case of $KTa_{0.6}Nb_{0.4}O_3$ film.

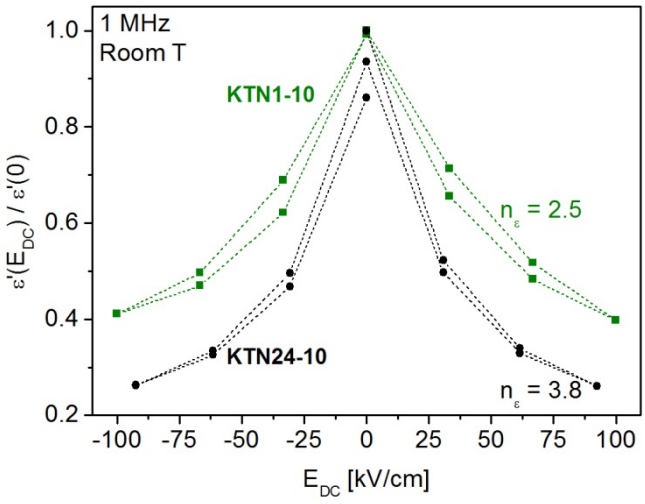

Figure 4.54: DC electric field E_{DC} dependence of the normalized dielectric permittivity $\varepsilon'(E_{DC})/\varepsilon'(0)$ of the KTN1-10 and KTN24-10 $KTa_{0.6}Nb_{0.4}O_3$ thin films after heating at 900°C (voltage cycle: 0 V → +30 V → 0 V → -30 V → 0 V). The measurements were performed at room temperature and 1 MHz. Lines between the experimental points are guides to the eye. The probing AC field was 1 kV/cm.

The dielectric properties of the phase-pure KTN24-10 $KTa_{0.6}Nb_{0.4}O_3$ thin films were analyzed in detail. The temperature dependence of the real ε' and imaginary ε'' parts of the complex permittivity in the frequency range from 3 kHz to 1 MHz are shown in Figure 4.55. A relaxor-like broad dispersive dielectric maximum can be observed, consistent with the measurements performed on the KTN ceramics (Chapter 1.2.2) [90,91]. The maximum of the permittivity ε' at 10 kHz, equal to 2600, is at 270 K, which is lower than the value of ~300 K, which is expected from the single-crystal studies [66]. The maximum of the permittivity ε' is due to a dynamic process, typical for relaxor materials (Chapter 1.1.1), while the paraelectric-ferroelectric phase transition could be expected as low as ~170 K, where a shoulder of the ε'' can be observed. The origin of the third broad maximum of the ε'' below 100 K, denoted by an arrow in Figure 1, cannot be explained at present.

The permittivity ε', measured at 14.5 GHz, reaches the maximum at 340 K, as shown in Figure 4.56. The dielectric losses $\tan\delta$ are approximately constant from 235 K to 298 K with a value of 0.52, then they start to decrease, reaching 0.29 at 358 K.

The temperature dependence of the characteristic relaxation frequency, obtained from the peaks of the permittivity ε' was further analyzed in order to confirm the relaxor-like behavior of the $KTa_{0.6}Nb_{0.4}O_3$ thin films (Figure 4.57). The experimental data follow the Vogel-Fulcher law (Equation (1.1)), and the obtained attempt frequency f_0, activation energy E_a and the freezing temperature T_f are 116 x 10^{12} Hz, 86 meV and 227 K, respectively. The respective Vogel-Fulcher parameters reported for the 0.9 PMN – 0.1PT relaxor ceramics are 1.03 x 10^{12} Hz, 40 meV and 291.5 K [8].

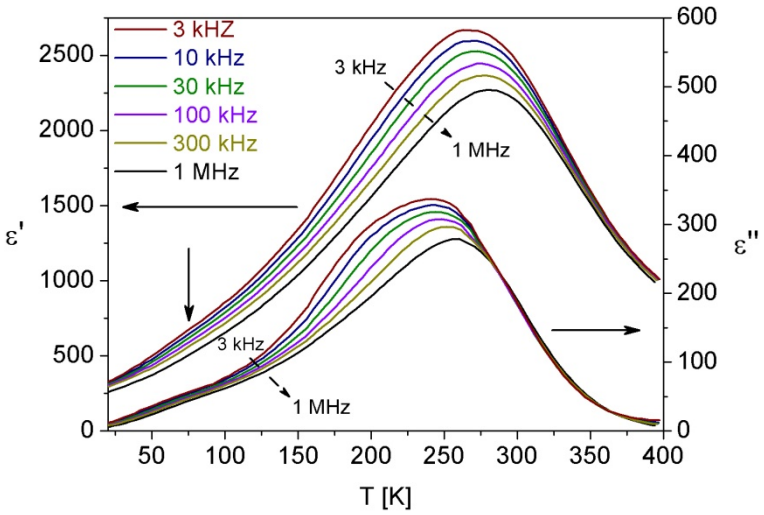

Figure 4.55: Temperature dependence of the real ε' and imaginary ε'' parts of the complex dielectric permittivity ε^* of the KTN24-10 $KTa_{0.6}Nb_{0.4}O_3$ thin film after heating at 900°C, measured in the 3 kHz to 1 MHz frequency range. The probing AC field was 3.3 kV/cm.

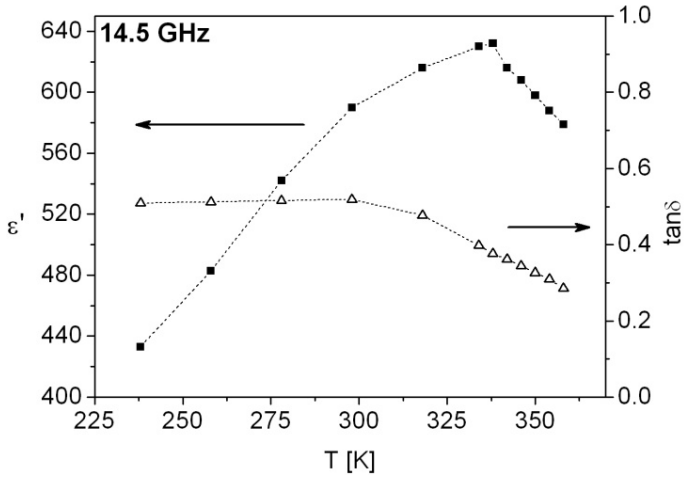

Figure 4.56: Temperature dependence of the permittivity ε' and dielectric losses tanδ of the KTN24-10 $KTa_{0.6}Nb_{0.4}O_3$ thin film after heating at 900°C, measured at 14.5 GHz. Lines through the experimental points are guides to the eye only.

The room-temperature values of the permittivity ε' and dielectric losses tanδ, measured at 7.3 GHz are 730 and 0.33, respectively. The frequency dependence of dielectric properties is shown in Figure 4.58. As expected from the relaxor-like dielectric properties behavior in Figure 4.56, the permittivity is decreasing with increasing frequency from 2430 to 590, measured at 10 kHz and 14.5 GHz, respectively. An increase in the dielectric losses value from 0.09 to 0.52, measured at 1 MHz and 14.5 GHz, respectively, can be attributed to the polydispersive nature of the relaxation, which is typical for relaxors. A very similar broadband frequency dependence of the permittivity and losses, which depends also on the temperature, was observed in the PMN single crystals [3].

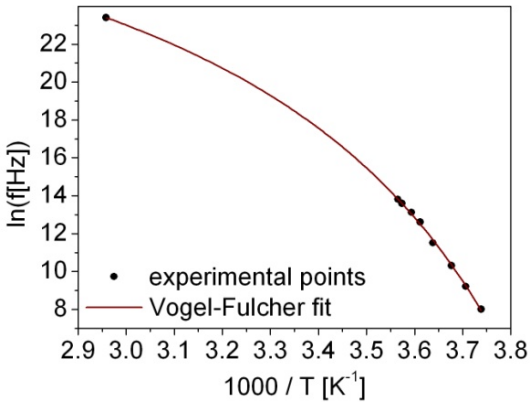

Figure 4.57: Vogel-Fulcher fit of the real permittivity ε' of the KTN24-10 $KTa_{0.6}Nb_{0.4}O_3$ thin films after heating at 900°C.

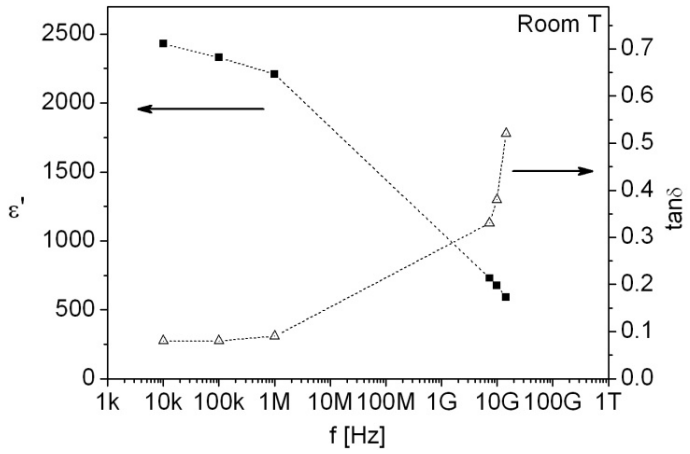

Figure 4.58: Frequency dependence of the permittivity ε' and dielectric losses tanδ of the KTN24-10 $KTa_{0.6}Nb_{0.4}O_3$ thin films after heating at 900°C measured at room temperature. Lines between the experimental points are guides to the eye.

4.4.2.1 Discussion on Processing – Dielectric Properties Relations in $KTa_{0.6}Nb_{0.4}O_3$ Films

The KTN24-10 films, prepared from the 24-h-refluxed sols, show increased permittivity and tunability values, as compared to the KTN1-10 films (Table 4.9). We attribute the enhancement to the single-phase composition and the dense, as well as more homogeneous, microstructure.

A similar relation between the reflux time of the sols and the permittivity ε' value was observed in PMN thin films prepared from the 2-methoxyethanol-based sols using lead and magnesium acetate, and niobium ethoxide as the metal sources [218]. The authors observed the promoted formation of Mg-O-Nb bonds in the sols upon refluxing and correlated it to the increased permittivity value of the films prepared from the sols refluxed for 48 h. In our case, the permittivity increase in the films prepared from the 24-h-refluxed sols is directly related to the formation of the bimetallic species between potassium and both transition metals, as evidenced by EXAFS (Chapter 4.4.1.1.1).

However, the RF and MW studies of the dielectric properties revealed relaxor-like behavior of polycrystalline $KTa_{0.6}Nb_{0.4}O_3$ thin films. Even though an RF-dispersion was observed in the KTN single crystals with small concentration of Nb (i.e., $KTa_{0.97}Nb_{0.03}O_3$)

[219], in more Nb-rich single-crystal compositions, such as $KTa_{0.7}Nb_{0.3}O_3$ and $KTa_{0.5}Nb_{0.5}O_3$ [220], the RF-permittivity does not exhibit relaxor-like behavior [27]. On the other hand, similar behavior was observed in the $K(Ta,Nb)O_3$ ceramics [90,91] and was attributed to the presence of a thermally fluctuating local polarization, possibly due to the presence of charged defects arising from potassium or oxygen vacancies and to the inhomogeneous distribution of the Ta and Nb. Recent results on strained and strain-free PLD- and MBE-derived $SrTiO_3$ thin films with thicknesses up to 1 μm have shown that even minute amounts of the A-site off-stoichiometry may result in relaxor thin-film behavior [57,135]. Since the necessity of the addition of 10 % excess of potassium acetate in the sols to prepare single-phase $KTa_{0.6}Nb_{0.4}O_3$ films indicates some losses of potassium species upon heating, small deviations from the stoichiometry cannot be overruled.

Generally BST thin films do not show relaxor-like frequency dependence of dielectric properties.[13,14] However, Tyunina and co-workers [221,222] reported on strongly frequency dependent dielectric behavior of PLD-derived BST films, deduced from the RF-range studies. The films of various compositions, thicknesses and microstructures were studied and the relaxor-like state was always confirmed. The exact origin of this behavior is not clear.

Note that the PLD-derived $KTa_{0.6}Nb_{0.4}O_3$ thin films on several substrates did not exhibit relaxor-like properties in the 6–40 GHz frequency range (Chapter 1.2.3.3)[133]. However, the existence of some local polar fluctuations above the Curie point were later determined in the 300-nm-thick epitaxial $KTa_{0.65}Nb_{0.35}O_3$ and $KTa_{0.50}Nb_{0.50}O_3$ thin films on (100) $LaAlO_3$ and (100) MgO substrates using Raman spectroscopy [135].

According to the EXAFS investigation of the $KTa_{0.6}Nb_{0.4}O_3$ sols, the Ta- and Nb-species are stable as monomers and dimers, respectively. On prolonged refluxing, the number of Nb neighbors around the Nb slightly increases, which can be explained by thermally activated segregation. As consequence the $KTa_{0.6}Nb_{0.4}O_3$ sol, after 24 h of reflux, is heterogeneous on the molecular level and according to the study of Xu et al. [85] these heterogeneities remain in the material also after high-temperature heating. Therefore, we believe that the main contribution to the relaxor-like properties of our films arises from the compositional deviations, i.e., heterogeneous distribution of the Ta and Nb atoms.

4.4.3 Summary

EXAFS analyses of the stoichiometric $KTa_{0.6}Nb_{0.4}O_3$ sols revealed that the local environment of Ta atoms is almost independent of the reflux time; it is coordinated by six oxygen atoms in the first shell and a potassium atom in the second shell of neighbors. There are no Ta-O-Ta or Ta-O-Nb correlations present in the sols.

In contrast, the Nb local environment changes with reflux time. After 1 h of reflux, Nb is present in the form of dimers and the number of Nb neighbors slightly increases with the reflux time. The Nb-O-K correlations were confirmed already after 1 h; however, a steady state was established only after 24 h of reflux.

The phase composition, microstructure and dielectric properties of the films on the alumina substrates are strongly dependent on the reflux time of the solutions. The single

phase perovskite thin films were obtained only from the 24-h-refluxed solutions and upon heating at 900°C, while the films prepared from the 1-h-refluxed solutions had multi-phase composition and heterogeneous microstructures. Enhancement of the crystallization behavior is directly related to the formation of bimetallic species between potassium and both transition metals inside the sols. The preferred (100) orientation of the perovskite phase was attributed to the anisotropy of the surface energies of different crystallographic faces.

The improved microstructural and compositional homogeneity is also attributed to the enhanced dielectric properties. The 1-MHz room-temperature values of the dielectric permittivity ε' and tunability n of the films increase from 860 and 2.5, respectively, for the films prepared from the 1-h-refluxed solutions, to 2200 and 3.8, for the films, prepared from the 24-h-refluxed solutions.

Dielectric properties of the phase-pure $KTa_{0.6}Nb_{0.4}O_3$ thin films from 24-h-refluxed sols were analyzed in detail. The relaxor-like dielectric properties were confirmed by fitting the experimental data to the Vogel-Fulcher law. The room-temperature value of the permittivity decreases from 2430 to 590 and the dielectric losses increase from 0.08 to 0.52 in the frequency range from 10 kHz to 14.5 GHz. The observed behavior was correlated to the thermally activated segregation of the Nb-species inside the sol during the reflux, resulting in the heterogeneous distribution of Ta and Nb atoms.

5 Summary, Conclusions and Future Prospects

An archetypal incipient ferroelectric $KTaO_3$ was studied in the form of ceramics and polycrystalline thin films. The ceramics were prepared by the solid-state synthesis and the thin films were processed by the chemical solution deposition on polycrystalline alumina and c-sapphire substrates. Their broadband dielectric properties were measured and the lattice dynamics were evaluated. They showed fundamentally different dielectric behavior. $KTaO_3$ ceramics are typical incipient ferroelectrics with a negligible influence of the grain boundaries on the dielectric response. On the other hand, the low-temperature ferroelectric state is induced in thin films. Both behaviors have been observed for the first time.

In addition, the $KTa_{0.6}Nb_{0.4}O_3$ thin films on polycrystalline alumina substrates were prepared by chemical solution deposition and their dielectric properties were investigated. Differently from the single crystals, the films show relaxor-like dielectric behavior in the radio- and microwave-frequency ranges.

The main conclusions are summarized in the chapters below. In addition, future activates are proposed.

5.1 $KTaO_3$ Ceramics and Thin Films

$KTaO_3$ powders were obtained after calcination of the partially amorphous mechanochemically activated K_2CO_3-Ta_2O_5 powder mixtures at 800°C. According to XRD the powders were single-phase perovskites; however, analytical TEM analysis revealed the existence of K- and Ta-rich nanoparticles attached to the micron-sized particles. An additional calcination at 800°C was implemented to enhance the homogeneity of the powders.

Sintering of the single-calcined powder compacts at 1325°C in an oxygen atmosphere resulted in ceramics with an 85 % relative density, which is among the highest values reported for stoichiometric $KTaO_3$ ceramics; however, the sublimation of potassium oxide led to the formation of a $K_6Ta_{10.8}O_{30}$ secondary phase. Phase-pure ceramics with relative densities above 95 % were obtained by hot pressing the powder compacts at 1250°C. The hot pressing at by 75 K lower temperature, as compared to the atmosphere sintering, effectively contributed to the enhanced densification of the $KTaO_3$ ceramic and simultaneously also to the reduced sublimation of potassium oxide. All the ceramics showed bimodal grain size distributions though the size of the grains and their distribution varied. In the case of the hot pressed ceramic, prepared from double-calcined powders, the larger grains could exceed the size of ~3 μm, while the smaller grains, which were located inside the porous regions, had the sizes below ~500 nm.

Ceramics prepared from the single-calcined powders were found to be structurally and compositionally heterogeneous. Amorphous triple pockets with sizes between 10 nm and 30 nm were observed. Their composition is strongly potassium deficient, with a K/Ta ratio of 0.55. The composition of the majority of large grains has a K/Ta ratio between 0.76 and 0.84. Additionally, a small amount of K-rich large grains with the K/Ta ratio of 1.30 was detected. The composition of the small grains revealed a slight excess of Ta relative to the nominal composition.

Compositional deviations were also observed in the hot pressed ceramics, prepared from the double-calcined powders. Smaller grains are either stoichiometric or have a K-rich composition, with a K/Ta ratio even up to 1.6. In addition to the stoichiometric and K-rich compositions, some larger grains are also Ta-rich and have a K/Ta down to 0.8. Even though rather large scattering of the composition within some of the grains was observed, the amorphous phase was not detected and the structural homogeneity of these ceramics is improved.

Double-calcination of the $KTaO_3$ contributed to a higher dielectric permittivity ε' and lower dielectric losses $\tan\delta$ of the ceramics. The respective values of the hot pressed $KTaO_3$ ceramics are 4090 and 0.0048, measured at 5 K and 1 kHz. The former value is almost doubled as compared to the value of the ceramics prepared from the single-calcined powders. The enhancement is attributed to the different microstructure and improved structural homogeneity of the ceramics prepared from the double-calcined powders. The permittivity value is also only slightly lower than the one in single crystals, i.e., 4500. The result points out the efficiency of the mechanochemical activation for the preparation of the $KTaO_3$ ceramics by the solid-state synthesis.

The $KTaO_3$ ceramics prepared from the double-calcined powders were characterized by a number of spectroscopic techniques in a broad spectral range. The three polar optic phonons, TO1 (Slater mode), TO2 (Last mode) and TO4 (Axe mode), were observed by the THz and infrared spectroscopies, and a weak coupling of the Slater and Last modes was revealed by the mode-plasma frequencies analysis. The increase of the radio and microwave frequency permittivity with decreasing temperature is directly related to the strong softening of the TO1 mode (soft mode), which primarily corresponds to the vibration of the Ta^{5+} ions against the rigid O_6 octahedra. Its eigen-frequency values are comparable to the ones in single crystals. These results indicate the pure displacive behavior of $KTaO_3$ ceramics, which is typical for incipient ferroelectrics, and the negligible influence of grain boundaries on their macroscopic dielectric response.

On the other hand, the microwave losses of the $KTaO_3$ ceramics at room temperature and ~6 GHz are 0.0095, which is higher than the value reported for the single crystals, i.e., 1.4×10^{-4} at 3 GHz, indicating extrinsic contributions. In addition, the first-order Raman scattering peaks, which are forbidden in the cubic $Pm\bar{3}m$ structure, were observed below ~150 K. Their appearances are associated with the presence of defects inside the crystal lattice of the ceramics. In our case the most plausible origin of these defects is the traces of Co (and W), arising from the wear of the milling vial and balls during the high-energy milling, and non-stoichiometry (A-site deficiency) detected in some of the grains.

Further processing optimization of the $KTaO_3$ ceramics, with the scope of the

homogeneity enhancement, are needed. In addition, investigations of smaller grain size ceramics by means of high-resolution transmission electron microscopy and broadband dielectric spectroscopy are needed in order to estimate the possible dielectric grain size effect in $KTaO_3$ ceramics: identify the type of the majority of defects, their spatial position and the structure of the grain boundaries.

We have also prepared polycrystalline $KTaO_3$ thin films on polycrystalline alumina and (0001) sapphire substrates from the alkoxide-based sols. If stoichiometric sols were used and the crystallization was performed after four deposition-pyrolysis steps, the films had a multi-phase composition after heating at 900°C in a rapid thermal annealing furnace. The phase composition was improved by adding 30 % excess of potassium acetate in the sols and crystallization at 900°C after each deposition. The single-phase perovskite films were slightly (100) preferentially oriented, which was explained by the anisotropy of the surface energies of different crystallographic phases. The 200-nm-thick films had the in-plane grain size of ~160 nm.

The dielectric properties of the films on alumina substrates were measured in the radio- and microwave-frequency ranges. In contrast to the classical incipient ferroelectric behavior, the maximum of the permittivity ε' was observed in the 30–45 K temperature range. The low-temperature ferroelectric state was finger-printed by the quasi-static polarization measurements. The quasi-static polarization, measured on heating after field-cooling at E_{DC} = 400 kV/cm, has a low-temperature value of ~0.5 C/m^2 and vanishes to zero at ~45 K; however, the exact temperature of the polarization zero-value depends on the measurement conditions (field-cooling or zero-field-cooling).

The films on c-sapphire substrates, which show qualitatively the same microwave dielectric behavior as the films on alumina, were also investigated in the terahertz and infrared frequency ranges. Similar to the single crystals and ceramics, the bands corresponding to the TO1, TO2 and TO4 polar optic modes were observed in the infrared reflectivity spectra. The soft mode (TO1) softens on cooling, having the minimum frequency at ~60 K, which roughly equals the temperature where the microwave permittivity maximum was observed. Below this temperature it hardens. The soft mode was found to be coupled to the central mode, which is silent in the paraelectric phase and becomes coupled to the polarization below the ferroelectric transition temperature with a progressively increasing bare strength. The data are a strong indication of the soft-mode-driven ferroelectric phase transition with a mixed, displacive and order-disorder character. Induced ferroelectricity in the chemical solution derived thin films of incipient ferroelectrics has been observed for the first time.

Based on the extensive research on epitaxially-strained $SrTiO_3$ thin films, we have attributed the phenomenon to the thermal strain, arising from the mismatch between the thermal expansion coefficients of the films and the substrate, and its delicate interplay between the small amounts of possible polar defects arising from the unintentional A-site deficiency. However, further investigations are needed to determine its exact origin.

5.2 $KTa_{0.6}Nb_{0.4}O_3$ Thin Films

Stoichiometric $KTa_{0.6}Nb_{0.4}O_3$ sols were prepared from the potassium acetate and transition-metal ethoxides by 1 h, 4 h, 24 h and 48 h reflux in 2-methoxyethanol. Extended X-ray absorption spectroscopy was employed to obtain information about the correlations between the constituent atoms, depending on the time of reflux.

The local environment of the Ta atoms is almost independent of the reflux time; it is coordinated by six oxygen atoms in the first shell and the potassium atom in the second shell of neighbors. There are no Ta-O-Ta or Ta-O-Nb correlations present in the sols.

In contrast, the Nb local environment changes with reflux time. After 1 h of reflux, Nb is present in the form of dimers and the number of the Nb neighbors slightly increases with the reflux time. The Nb-O-K correlations were confirmed after 1 h; however, a steady state was established only after 24 h of reflux.

The 1-h- and 24-h-refluxed sols were used for the preparation of the $KTa_{0.6}Nb_{0.4}O_3$ films on the polycrystalline alumina substrate. After four deposition-pyrolysis steps, final heating was performed in a rapid thermal annealing furnace. The addition of the 10 % excess of potassium acetate in the sols and heating at 900°C were found to be obligatory for the preparation of perovskite films. In addition, the phase composition and microstructure of the films was strongly dependent on the reflux time of the sols. We obtained single-phase films only from the 24-h-refluxed sols, while the films prepared from the 1-h-refluxed sols had a multi-phase composition and heterogeneous microstructures. Enhancement of the crystallization behavior is directly related to the formation of bimetallic species between potassium and both transition metals upon refluxing. The preferred (100) orientation of the perovskite phase was attributed to the anisotropy of the surface energies of the different crystallographic faces.

The improved microstructural and compositional homogeneity are also attributed to the enhanced dielectric properties. The 1-MHz room-temperature values of dielectric permittivity and tunability (at ~100 kV / cm) of the films, prepared from the 1-h-refluxed solutions, are 860 and 2.5, respectively. The respective values for the films, prepared from the 24-h-refluxed solutions, are 2200 and 3.8.

The dielectric properties of the $KTa_{0.6}Nb_{0.4}O_3$ thin films were studied in the radio-frequency and microwave-frequency ranges, and were found to be strongly frequency dependent. The relaxor-like dielectric properties of the films prepared from the 24-h-refluxed solutions were confirmed by fitting the experimental data to the Vogel-Fulcher law. The room-temperature value of the permittivity decreases from 2430 to 590 and the dielectric losses increase from 0.08 to 0.52 in the frequency range from 10 kHz to 14.5 GHz. The observed behavior was correlated to the thermally activated segregation of Nb-species inside the sol during the reflux, resulting in the heterogeneous distribution of Ta and Nb atoms.

Frequency dispersion of the dielectric properties as well as rather high dielectric losses present a challenge for possible applications of the chemical-solution-derived $K(Ta,Nb)O_3$ thin films in tunable microwave devices. Still, studies on the chemical modification of the Nb-precursor and its influence on the films are of great interest for the improvement of the functional properties of $KTa_{0.6}Nb_{0.4}O_3$ thin films.

6 Acknowledgements

The first acknowledgement goes to Prof. Marija Kosec and Prof. Barbara Malič who accepted me for the Electronic Ceramics Department (K5) at the Jožef Stefan Institute already as an undergraduate student and introduced me to the astonishing world of ferroelectric materials. I am grateful for their guidance, numerous motivating and knowledge-broadening discussions and their positivism. I am also very thankful for enabling me to visit various labs and many conferences around the world, during which time I was able to work with the leading experts of the field and confront my ideas with them, as well as fulfilling my love for travel.

Prof. Zdravko Kutnjak is acknowledged for the support with the advanced dielectric spectroscopy and discussions of all the physics-related problems. His ability to explain the complicated physical issues in a chemist-understandable language is amazing.

I would like also to thank to all my co-workers from the K5 department, especially Brigita Kužnik, Jena Cilenšek and Silvo Drnovšek for their invaluable help with the technicalities in the lab. Luka Golob, Ana Lazar and Veronika Mojskerc are acknowledged for their laboratory work. I am thankful also to Dr. Marko Hrovat and Dr. Tadej Rojac for their guidance during my student-work period at the department.

A special acknowledgement goes to my "roommates" through all these years, Dr. Hana Uršič and Dr. Gregor Trefalt. Our every-day discussions on science and life in general meant a lot to me.

I would also like to show appreciation to Dr. Stanislav Kamba, Dr. Jan Petzelt and all the co-workers of the Department of Dielectrics at Institute of Physics ASCR. My stay in Prague and the high-frequency dielectric measurements were really the icing on the cake of my thesis.

In addition I would like to thank to Prof. Iztok Arčon and Prof. Alojz Kodre for EXAFS measurements, Dr. Elena Tchernychova for the TEM analyses, Dr. Cene Filipič for low-temperature dielectric measurements, Edi Kranjc and Dr. Bojan Budič from the National Institute of Chemistry Slovenia for the XRD and ICP measurements, respectively, Assist. Prof. Bojan Kozlevčar from the University of Ljubljana for the mid-infrared measurements, Prof. Hong Wang from Xi'an Jiaotong University and Prof. Jerzy Krupka from Warsaw University of Technology for the microwave measurements of the $K(Ta,Nb)O_3$ thin films.

The most important acknowledgment goes to my family, my future wife Karin, parents and sister, who gave me full support during my studies, shared the good moments with me and encouraged me during the moments of crisis. Without you I would never make it this far.

7 References

[1] Jaffe, B.; Cook, W. R.; Jaffe, H. *Piezoelectric Ceramics* (Academic Press, London, 1971).

[2] Damjanović, D. Ferroelectric, Dielectric and Piezoelectric Properties of Ferroelectric Thin Films and Ceramics. *Reports on Progress in Physics* **61**, 1267 (1998).

[3] Bovtun, V.; Veljko, S.; Kamba, S.; Petzelt, J.; Vakhrushev, S.; Yakymenko, Y.; Brinkman, K.; Setter, N. Broad-Band Dielectric Response of $PbMg_{1/3}Nb_{2/3}O_3$ Relaxor Ferroelectrics: Single Crystals, Ceramics and Thin Films. *Journal of the European Ceramic Society* **26**, 2867 (2006).

[4] Levstik, A.; Kutnjak, Z.; Filipič, C.; Pirc, R. Glassy Freezing in Relaxor Ferroelectric Lead Magnesium Niobate. *Physical Review B* **57**, 11204 (1998).

[5] Kutnjak, Z.; Filipič, C.; Pirc, R.; Levstik, A.; Farhi, R.; El Marssi, M. Slow Dynamics and Ergodicity Breaking in a Lanthanum-Modified Lead Zirconate Titanate Relaxor System. *Physical Review B* **59**, 294 (1999).

[6] Bokov, A. A.; Ye, Z. G. Recent Progress in Relaxor Ferroelectrics with Perovskite Structure. *Journal of Materials Science* **41**, 31 (2006).

[7] Kutnjak, Z.; Petzelt, J.; Blinc, R. The Giant Electromechanical Response in Ferroelectric Relaxors as a Critical Phenomenon. *Nature* **441**, 956 (2006).

[8] Viehland, D.; Jang, S. J.; Cross, L. E.; Wuttig, M. Freezing of the Polarization Fluctuations in Lead Magnesium Niobate Relaxors. *Journal of Applied Physics* **68**, 2916 (1990).

[9] Setter, N. (ed.) *Piezoelectric Materials in Devices* (Ceramics Laboratory, EPFL Swiss Federal Institute of Technology, Lausanne, 2002).

[10] Scott, J. F. Applications of Modern Ferroelectrics. *Science* **315**, 954 (2007).

[11] Setter, N.; Damjanović, D.; Eng, L.; Fox, G.; Gevorgian, S.; Hong, S.; Kingon, A.; Kohlstedt, H.; Park, N. Y.; Stephenson, G. B.; Stolitchnov, I.; Taganstev, A. K.; Taylor, D. V.; Yamada, T.; Streiffer, S. Ferroelectric Thin Films: Review of Materials, Properties, and Applications. *Journal of Applied Physics* **100**, 051606 (2006).

[12] Gevorgian, S. *Ferroelectrics in Microwave Devices, Circuits and Systems: Physics, Modeling, Fabrication and Measurements* (Springer-Verlag, London, 2009).

[13] Bao, P.; Jackson, T. J.; Wang, X.; Lancaster, M. J. Barium Strontium Titanate Thin Film Varactors for Room-Temperature Microwave Device Applications. *Journal of*

Physics D: Applied Physics **41**, 063001 (2008).

[14] Tagantsev, A. K.; Sherman, V. O.; Astafiev, K. F.; Venkatesh, J.; Setter, N. Ferroelectric Materials for Microwave Tunable Applications. *Journal of Electroceramics* **11**, 5 (2003).

[15] Geyer, R. G.; Riddle, B.; Krupka, J.; Boatner, L. A. Microwave Dielectric Properties of Single-Crystal Quantum Paraelectrics $KTaO_3$ and $SrTiO_3$ at Cryogenic Temperatures. *Journal of Applied Physics* **97**, 104111 (2005).

[16] Vendik, O. G.; Hollmann, E. K.; Kozyrev, A. B.; Prudan, A. M. Ferroelectric Tuning of Planar and Bulk Microwave Devices. *Journal of Superconductivity* **12**, 325 (1999).

[17] Mitsui, T.; Nomura, S.; Adachi, M.; Harada, J.; Ikeda, T.; Nakamura, E.; Sawaguchi, E.; Shigenari, T.; Shiozoaki, Y.; Tatsuzaki, I.; Toyoda, K.; Yamada, T.; Gesi, K.; Makita, Y.; Marutake, M.; Shisoaki, T.; Wakino, K. *Landolt-Börnstein. Numerical Data and Functional Relationships in Science and Technology. Group III: Crystal and Solid State Physics. Ferroelectrics and Related Substances: Oxides*. Hellwege, K. H., Helwege, A. M. (ed.) (Springer-Verlag, Berlin, 1981).

[18] Müller, K. A.; Burkard, H. $SrTiO_3$: An Intrinsic Qantum Paraelectric Below 4 K. *Physical Review B* **19**, 3593 (1979).

[19] Barrett, J. H. Dielectric Constant in Perovskite Type Crystals. *Physical Review* **86**, 118 (1952).

[20] Salce, B.; Gravil, J. L.; Boatner, L. A. Disorder and Thermal Transport in Undoped $KTaO_3$. *Journal of Physics: Condensed Matter* **6**, 4077 (1994).

[21] Samara, G. A.; Morosin, B. Anharmonic Effects in $KTaO_3$: Ferroelectric Mode, Thermal Expansion, and Compressibility. *Physical Review B* **8**, 1256 (1973).

[22] Samara, G. A. The Relaxational Properties of Compositionally Disordered ABO_3 Perovskites. *Journal of Physics: Condensed Matter* **15**, R367 (2003).

[23] Laguta, V. V.; Glinchuk, M. D.; Bykov, I. P.; Rosa, J.; Jastrabík, L.; Savinov, M.; Trybuła, Z. Paramagnetic Dipole Centers in $KTaO_3$: Electron-Spin-Resonance and Dielectric Spectroscopy Study. *Physical Review B* **61**, 3897 (2000).

[24] Trepakov, V.; Smutny, F.; Vikhnin, V.; Bursian, V.; Sochava, L.; Jastrabik, L.; Syrnikov, P. The Effects of Defect System Ordering in a Weakly Doped Incipient Ferroelectric ($KTaO_3$): Dielectric Manifestation. *Journal of Physics: Condensed Matter* **7**, 3765 (1995).

[25] Savinov, M. *Low Frequency Dielectric Spectroscopy of Nominally Pure and Diluted $KTaO_3$, $KTaO_3$: Li and $KTaO_3$: Li+Nb*. PhD Thesis (Czech Technical University in Prague, Prague, 2001).

[26] Nowick, A. S.; Fu, S. Q.; Lee, W. K.; Lim, B. S.; Scherban, T. Dielectric Relaxation of Paired Defects in Perovskite-Type Oxides. *Materials Science and Engineering: B* **23**, 19 (1994).

[27] Samara, G. A. From Ferroelectric to Quantum Paraelectric: $KTa_{1-x}Nb_xO_3$ (KTN), a

Model System. *MRS Proceedings* **718**, 10 (2002).

[28] Petzelt, J. Dielectric Grain-Size Effect in High-Permittivity Ceramics. *Ferroelectrics* **400**, 117 (2010).

[29] Petzelt, J.; Ostapchuk, T.; Gregora, I.; Nuzhnyy, D.; Rychetsky, I.; Maca, K.; Shen, Z. Grain Boundary and Size Effect on the Dielectric, Infrared and Raman Response of $SrTiO_3$ Nanograin Ceramics. *Ferroelectrics* **363**, 227 (2008).

[30] Petzelt, J.; Ostapchuk, T.; Gregora, I.; Rychetský, I.; Hoffmann-Eifert, S.; Pronin, A. V.; Yuzyuk, Y.; Gorshunov, B. P.; Kamba, S.; Bovtun, V.; Pokorný, J.; Savinov, M.; Porokhonskyy, V.; Rafaja, D.; Vaněk, P.; Almeida, A.; Chaves, M. R.; Volkov, A. A.; Dressel, M.; Waser, R. Dielectric, Infrared, and Raman response of Undoped $SrTiO_3$ Ceramics: Evidence of Polar Grain Boundaries. *Physical Review B* **64**, 184111 (2001).

[31] Sakudo, T.; Unoki, H. Dielectric Properties of $SrTiO_3$ at Low Temperatures. *Physical Review Letters* **26**, 851 (1971).

[32] Petzelt, J.; Ostapchuk, T.; Gregora, I.; Kužel, P.; Liu, J.; Shen, Z. Infrared and Raman Studies of the Dead Grain-Boundary Layers in $SrTiO_3$ Fine-Grain Ceramics. *Journal of Physics: Condensed Matter* **19**, 196222 (2007).

[33] Ernst, F.; Kienzle, O.; Ruhle, M. Structure and Composition of Grain Boundaries in Ceramics. *Journal of the European Ceramic Society* **19**, 665 (1999).

[34] Carrasco, J.; Illas, F.; Lopez, N.; Kotomin, E. A.; Zhukovskii, Y. F.; Evarestov, R. A.; Mastrikov, Y. A.; Piskunov, S.; Maier, J. First-Principles Calculations of the Atomic and Electronic Structure of F Centers in the Bulk and on the (001) Surface of $SrTiO_3$. *Physical Review B* **73**, 064106 (2006).

[35] Shao, R.; Chisholm, M. F.; Duscher, G.; Bonnell, D. A. Low-Temperature Resistance Anomaly at $SrTiO_3$ Grain Boundaries: Evidence for an Interface-Induced Phase Transition. *Physical Review Letters* **95**, 197601 (2005).

[36] Bednorz, J. G.; Muller, K. A. $Sr_{1-x}Ca_xTiO_3$ - An XY Quantum Ferroelectric with Transition to Randomness. *Physical Review Letters* **52**, 2289 (1984).

[37] Hemberger, J.; Lunkenheimer, P.; Viana, R.; Böhmer, R.; Loidl, A. Electric-Field-Dependent Dielectric Constant and Nonlinear Susceptibility in $SrTiO_3$. *Physical Review B* **52**, 13159 (1995).

[38] Itoh, M.; Wang, R.; Inaguma, Y.; Yamaguchi, T.; Shan, Y. J.; Nakamura, T. Ferroelectricity Induced by Oxygen Isotope Exchange in Strontium Titanate Perovskite. *Physical Review Letters* **82**, 3540 (1999).

[39] Uwe, H.; Sakudo, T. Stress-Induced Ferroelectricity and Soft Phonon Modes in $SrTiO_3$. *Physical Review B* **13**, 271 (1976).

[40] Uwe, H.; Sakudo, T. Raman-Scattering Study of Stress-Induced Ferroelectricity in $KTaO_3$. *Physical Review B* **15**, 337 (1977).

[41] Schlom, D. G.; Chen, L. Q.; Eom, C. B.; Rabe, K. M.; Streiffer, S. K.; Triscone, J. M. Strain Tuning of Ferroelectric Thin Films. *Annual Review of Materials Research*

37, 589 (2007).

[42] Tyunina, M.; Narkilahti, J.; Plekh, M.; Oja, R.; Nieminen, R. M.; Dejneka, A.; Trepakov, V. Evidence for Strain-Induced Ferroelectric Order in Epitaxial Thin Film $KTaO_3$. *Physical Review Letters* **104**, 227601 (2010).

[43] Akbarzadeh, A. R.; Bellaiche, L.; Iniguez, J.; Vanderbilt, D. Theoretical Phase Diagram of Ultrathin Films of Incipient Ferroelectrics. *Applied Physics Letters* **90**, 242918 (2007).

[44] Morozovska, A. N.; Glinchuk, M. D.; Eliseev, E. A. Phase Transitions Induced by Confinement of Ferroic Nanoparticles. *Physical Review B* **76**, 014102 (2007).

[45] Freund, I. B.; Suresh, S. *Thin Film Materials: Stress, Defect Formation and Surface Evolution* (Cambridge University Press, Cambridge, 2003).

[46] Ohring, M. *The Material Science of Thin Films* (Academic Press, Boston, 1992).

[47] Simon, W. K.; Akdogan, E. K.; Safari, A. Misfit Strain Relaxation in $Ba_{0.6}Sr_{0.4}TiO_3$ Epitaxial Thin Films on Orthorhombic $NdGaO_3$ Substrates. *Applied Physics Letters* **89**, 022902 (2006).

[48] Pertsev, N. A.; Tagantsev, A. K.; Setter, N. Phase Transitions and Strain-Induced Ferroelectricity in $SrTiO_3$ Epitaxial Thin Films. *Physical Review B* **61**, R825 (2000).

[49] Pertsev, N. A.; Tagantsev, A. K.; Setter, N. Erratum: Phase Transitions and Strain-Induced Ferroelectricity in $SrTiO_3$ Epitaxial Thin Films [Phys. Rev. B 61, R825 (2000)]. *Physical Review B* **65**, 219901 (2002).

[50] Dieguez, O.; Rabe, K. M.; Vanderbilt, D. First-Principles Study of Epitaxial Strain in Perovskites. *Physical Review B* **72**, 144101 (2005).

[51] Haeni, J. H.; Irvin, P.; Chang, W.; Uecker, R.; Reiche, P.; Li, Y. L.; Choudhury, S.; Tian, W.; Hawley, M. E.; Craigo, B.; Tagantsev, A. K.; Pan, X. Q.; Streiffer, S. K.; Chen, L. Q.; Kirchoefer, S. W.; Levy, J.; Schlom, D. G. Room-Temperature Ferroelectricity in Strained $SrTiO_3$. *Nature* **430**, 758 (2004).

[52] Wördenweber, R.; Hollmann, E.; Kutzner, R.; Schubert, J. Induced Ferroelectricity in Strained Epitaxial $SrTiO_3$ Films on Various Substrates. *Journal of Applied Physics* **102**, 044119 (2007).

[53] Nuzhnyy, D.; Petzelt, J.; Kamba, S.; Kužel, P.; Kadlec, C.; Bovtun, V.; Kempa, M.; Schubert, J.; Brooks, C. M.; Schlom, D. G. Soft Mode Behavior in $SrTiO_3/DyScO_3$ Thin Films: Evidence of Ferroelectric and Antiferrodistortive Phase Transitions. *Applied Physics Letters* **95**, 232902 (2009).

[54] Biegalski, M. D.; Jia, Y.; Schlom, D. G.; Trolier-McKinstry, S.; Streiffer, S. K.; Sherman, V.; Uecker, R.; Reiche, P. Relaxor Ferroelectricity in Strained Epitaxial $SrTiO_3$ Thin Films on $DyScO_3$ Substrates. *Applied Physics Letters* **88**, 192907 (2006).

[55] Warusawithana, M. P.; Cen, C.; Sleasman, C. R.; Woicik, J. C.; Li, Y. L.; Kourkoutis, L. F.; Klug, J. A.; Li, H.; Ryan, P.; Wang, L. P.; Bedzyk, M.; Muller,

D. A.; Chen, L. Q.; Levy, J.; Schlom, D. G. A Ferroelectric Oxide Made Directly on Silicon. *Science* **324**, 367 (2009).

[56] Nuzhnyy, D.; Petzelt, J.; Kamba, S.; Marti, X.; Cechal, T.; Brooks, C. M.; Schlom, D. G. Infrared Phonon Spectroscopy of a Compressively Strained (001) $SrTiO_3$ Film Grown on a (110) $NdGaO_3$ Substrate. *Journal of Physics: Condensed Matter* **23**, 045901 (2011).

[57] Jang, H. W.; Kumar, A.; Denev, S.; Biegalski, M. D.; Maksymovych, P.; Bark, C. W.; Nelson, C. T.; Folkman, C. M.; Baek, S. H.; Balke, N.; Brooks, C. M.; Tenne, D. A.; Schlom, D. G.; Chen, L. Q.; Pan, X. Q.; Kalinin, S. V.; Gopalan, V.; Eom, C. B. Ferroelectricity in Strain-Free $SrTiO_3$ Thin Films. *Physical Review Letters* **104**, 197601 (2010).

[58] Nuzhnyy, D.; Petzelt, J.; Kamba, S.; Yamada, T.; Tyunina, M.; Tagantsev, A. K.; Levoska, J.; Setter, N. Polar Phonons in Some Compressively Stressed Epitaxial and Polycrystalline $SrTiO_3$ Thin Films. *Journal of Electroceramics* **22**, 297 (2009).

[59] Kim, Y. S.; Kim, D. J.; Kim, T. H.; Noh, T. W.; Choi, J. S.; Park, B. H.; Yoon, J. G. Observation of Room-Temperature Ferroelectricity in Tetragonal Strontium Titanate Thin Films on $SrTiO_3$ (001) Substrates. *Applied Physics Letters* **91**, 042908 (2007).

[60] Kim, Y. S.; Choi, J. S.; Kim, J.; Moon, S. J.; Park, B. H.; Yu, J.; Kwon, J. H.; Kim, M.; Chung, J. S.; Noh, T. W.; Yoon, J. G. Defect-Related Room-Temperature Ferroelectricity in Tensile-Strained $SrTiO_3$ Thin Films on $GdScO_3$ (110) Substrates. *Applied Physics Letters* **97**, 242907 (2010).

[61] Tenne, D. A.; Farrar, A. K.; Brooks, C. M.; Heeg, T.; Schubert, J.; Jang, H. W.; Bark, C. W.; Folkman, C. M.; Eom, C. B.; Schlom, D. G. Ferroelectricity in Nonstoichiometric $SrTiO_3$ Films Studied by Ultraviolet Raman Spectroscopy. *Applied Physics Letters* **97**, 142901 (2010).

[62] Galt, D.; Price, J. C.; Beall, J. A.; Ono, R. H. Characterization of a Tunable Thin-Film Microwave $YBa_2Cu_3O_{7-x}/SrTiO_3$ Coplanar Capacitor. *Applied Physics Letters* **63**, 3078 (1993).

[63] Ostapchuk, T.; Petzelt, J.; Železny, V.; Pashkin, A.; Pokorny, J.; Drbohlav, I.; Kužel, R.; Rafaja, D.; Gorshunov, B. P.; Dressel, M.; Ohly, C.; Hoffmann-Eifert, S.; Waser, R. Origin of Soft-Mode Stiffening and Reduced Dielectric Response in $SrTiO_3$ Thin Films. *Physical Review B* **66**, 235406 (2002).

[64] Reisman, A.; Triebwasser, S.; Holtzberg, F. Phase Diagram of the System $KNbO_3$-$KTaO_3$ by the Methods of Differential Thermal and Resistance Analysis. *Journal of the American Chemical Society* **77**, 4228 (1955).

[65] Reisman, A.; Banks, E. Reactions of the Group VB Pentoxides. VIII. Thermal, Density and X-Ray Studies of the Systems $KNbO_3$-$NaNbO_3$ and $KTaO_3$-$KNbO_3$. *Journal of the American Chemical Society* **80**, 1877 (1958).

[66] Triebwasser, S. Study of Ferroelectric Transitions of Solid-Solution Single Crystals of $KNbO_3$-$KTaO_3$. *Physical Review* **114**, 63 (1959).

[67] Hanske-Petitpierre, O.; Yacoby, Y.; Mustre de Leon, J.; Stern, E. A.; Rehr, J. J. Off-Center Displacement of the Nb Ions below and above the Ferroelectric Phase Transition of $KTa_{0.91}Nb_{0.09}O_3$. *Physical Review B* **44**, 6700 (1991).

[68] Rankel, S.; Zalar, B.; Laguta, V. V.; Blinc, R.; Toulouse, J. ^{93}Nb NMR Study of Disorder in $KTa_{1-x}Nb_xO_3$. *Physical Review B* **71**, 144110 (2005).

[69] Reisman, A.; Holtzberg, F.; Berkenblit, M.; Berry, M. Reactions of the Group VB Pentoxides with Alkali Oxides and Carbonates. III. Thermal and X-Ray Phase Diagrams of the System K_2O or K_2CO_3 with Ta_2O_5. *Journal of the American Chemical Society* **78**, 4514 (1956).

[70] Roth, R. S.; Parker, H. S.; Brower, W. S.; Waring, J. L. Phase Equilibriums, Crystal Chemistry, and Crystal Growth of Alkali Oxide-Metal Oxide Systems. In: Van Gool, W. (ed.) *Proceedings of NATO Advanced Study Institute*. 217 (Belgirate, 1972).

[71] Axelsson, A. K.; Pan, Y.; Valant, M.; Alford, N. Synthesis, Sintering, and Microwave Dielectric Properties of $KTaO_3$ Ceramics. *Journal of the American Ceramic Society* **92**, 1773 (2009).

[72] Villesuzanne, A.; Elissalde, C.; Pouchard, M.; Ravez, J. New Considerations on the Role of Covalency in Ferroelectric Niobates and Tantalates. *European Physical Journal B* **6**, 307 (1998).

[73] Elissalde, C.; Villesuzanne, A.; Hornebecq, V.; Ravez, J. Prediction of Ferroelectric Properties in Niobates and Tantalates Based on Covalency Considerations. *Ferroelectrics* **229**, 1 (1999).

[74] Chen, Z. X.; Zhang, X. L.; Cross, L. E. Low-Temperature Dielectric Properties of Ceramic Potassium Tantalate ($KTaO_3$). *Journal of the American Ceramic Society* **66**, 511 (1983).

[75] Tkach, A.; Vilarinho, P. M.; Almeida, A. Role of Initial Potassium Excess on the Properties of Potassium Tantalate Ceramics. *Journal of the European Ceramic Society* **31**, 2303 (2011).

[76] Shimada, S.; Kodaira, K.; Matsushita, T. Sintering $LiTaO_3$ and $KTaO_3$ with the Aid of Manganese Oxide. *Journal of Materials Science* **19**, 1385 (1984).

[77] Axelsson, A. K.; Pan, Y. Y.; Valant, M.; Alford, N. M. Chemistry, Processing, and Microwave Dielectric Properties of Mn-Substituted $KTaO_3$ Ceramics. *Journal of the American Ceramic Society* **93**, 800 (2010).

[78] Axelsson, A. K.; Valant, M.; Alford, N. M. Influence of Point Defects in $KTaO_3$ on Low-Temperature Dielectric Relaxation. *Journal of the European Ceramic Society* **30**, 941 (2010).

[79] Axelsson, A. K.; Pan, Y. Y.; Valant, M.; Vilarinho, P. M.; Alford, N. M. Polar Fluctuations in Mn Substituted $KTaO_3$ Ceramics. *Journal of Applied Physics* **108**, 064109 (2010).

[80] Hill, V. G.; Chang, L. L. Y.; Harker, R. I. Subsolidus Stability Relations in the System $KTaO_3$-$KNbO_3$. *Journal of the American Ceramic Society* **51**, 723 (1968).

[81] Soules, T. F.; Busbey, R. F. Sodium Diffusion in Alkali Silicate Glass by Molecular Dynamics. *Journal of Chemical Physics* **75**, 969 (1981).

[82] Heintz, J. M.; Besson, J. J. M.; Rabardel, L.; Bonnet, J. P. Grain-Growth and Densification Study of β-Ta_2O_5. *Ceramics International* **18**, 263 (1992).

[83] Milanese, C.; Buscaglia, V.; Maglia, F.; Anselmi-Tamburini, U. Reactive Growth of Niobium Silicides in Bulk Diffusion Couples. *Acta Materialia* **51**, 4837 (2003).

[84] Slinkina, M. V.; Doncov, G. I. "Difuzija sovstvenih komponentov v keramike cirkonata-titanata svinca" (Self-Diffusion of Components in Lead Zirconate Titanate Ceramics). *Neorganičeskie materiali* **28**, 567 (1992).

[85] Xu, J.; Wilkinson, A. P.; Pattanaik, S. Manipulating and Quantifying the Compositional Heterogeneity in Sol-Gel Processed $K(Ta_{1-x}Nb_x)O_3$. *Chemistry of Materials* **13**, 1185 (2001).

[86] Stojanovič, B. D. Mechanochemical Synthesis of Ceramic Powders with Perovskite Structure. *Journal of Materials Processing Technology* **143**, 78 (2003).

[87] Rojac, T.; Benčan, A.; Kosec, M. Mechanism and Role of Mechanochemical Activation in the Synthesis of $(K,Na,Li)(Nb,Ta)O_3$ Ceramics. *Journal of the American Ceramic Society* **93**, 1619 (2010).

[88] Rojac, T.; Benčan, A.; Uršič, H.; Malič, B.; Kosec, M. Synthesis of a Li- and Ta-Modified $(K,Na)NbO_3$ Solid Solution by Mechanochemical Activation. *Journal of the American Ceramic Society* **91**, 3789 (2008).

[89] Wu, E. T.; Kuang, A. X.; MacKenzie, J. D. Hot-Pressed KTN Prepared from Ultrahomogeneous Oxide Powders Derived by Sol-Gel Technique, II. Ceramics. In: Wood, V. E. (ed.) *Sixth IEEE International Symposium on Applications of Ferroelectrics*. 391 (Bethlehem, 1986).

[90] Venkatesh, J.; Sherman, V.; Setter, N. Synthesis and Dielectric Characterization of Potassium Niobate Tantalate Ceramics. *Journal of the American Ceramic Society* **88**, 3397 (2005).

[91] DiAntonio, C. B.; Pilgrim, S. M. Processing, Characterization, and Dielectric Studies on $K(Ta_{1-x}Nb_x)O_3$ for Use at Cryogenic Temperatures. *Journal of the American Ceramic Society* **84**, 2547 (2001).

[92] Khemakhem, H.; Ravez, J.; Daoud, A. Dielectric Properties of KTN Ferroelectric Ceramics Sintered with LiF. *Ferroelectrics* **188**, 41 (1996).

[93] Khemakhem, H.; Ravez, J.; Daoud, A. Effect of DC and AC Bias Fields on the Dielectric and Ferroelectric Properties of a KTN Ceramic. *Physica Status Solidi (a)* **161**, 557 (1997).

[94] Yoshikawa, K.; Asaka, T.; Higuchi, M.; Azuma, Y.; Katayama, K. Effects of Excess K_2O and Processing Conditions on the Preparation of Dense $K(Ta_{1-x}Nb_x)O_3$ Ceramics. *Ceramics International* **34**, 609 (2008).

[95] Debely, P.; Gunter, P.; Arend, H. Preparation and Electrooptic Properties of Hot-Pressed Potassium Niobate-Tantalate Ceramic. *American Ceramic Society Bulletin*

58, 606 (1979).

[96] Kingon, A. I.; Muralt, P.; Setter, N.; Waser, R. Electroceramic Thin Films for Microelectronics and Microsystems. In: Buchanan, R. C. (ed.) *Ceramic Materials for Electronics: Third Edition, Revised and Expanded*. 465 (Marcel Dekker, Basel, 2004).

[97] Schwartz, R. W.; Schneller, T.; Waser, R. Chemical Solution Deposition of Electronic Oxide Films. *Comptes Rendus Chimie* **7**, 433 (2004).

[98] Brennecka, G. L.; Ihlefeld, J. F.; Maria, J. P.; Tuttle, B. A.; Clem, P. G. Processing Technologies for High-Permittivity Thin Films in Capacitor Applications. *Journal of the American Ceramic Society* **93**, 3935 (2010).

[99] Hubert-Pfalzgraf, L. G.; Riess, J. G. Isolation of a Mixed Niobium Tantalum Alkoxide. *Inorganic Chemistry* **14**, 2854 (1975).

[100] Bradley, D. C.; Mehrotra, R. C.; Gaur, D. P. *Metal Alkoxides* (Academic Press, London, 1978).

[101] Brinker, C. J.; Scherer, G. W. *Sol-Gel Science: The Physics and Chemistry of Sol-Gel Processing* (Academic Press, Boston, 1990).

[102] Turova, N. Y.; Turevskaya, E. P.; Kessler, V. G.; Yanovskaya, M. I. *The Chemistry of Metal Alkoxides* (Kluwer Academic Publishers, Boston, 2002).

[103] Hirano, S.; Yogo, T.; Kikuta, K.; Morishita, T.; Ito, Y. Preparation of Potassium Tantalate Niobate by Sol-Gel Method. *Journal of the American Ceramic Society* **75**, 1701 (1992).

[104] Yogo, T.; Kikuta, K.; Ito, Y.; Hirano, S. Synthesis of Highly Oriented $K(Ta,Nb)O_3$ (Ta:Nb = 65:35) Film Using Metal Alkoxides. *Journal of the American Ceramic Society* **78**, 2175 (1995).

[105] Suzuki, K.; Sakamoto, W.; Yogo, T.; Hirano, S. Processing of Oriented $K(Ta,Nb)O_3$ Films Using Chemical Solution Deposition. *Journal of the American Ceramic Society* **82**, 1463 (1999).

[106] Nazeri, A.; Kahn, M. Preparation of $KTaO_3$ and $KNbO_3$ Solid Solutions Through Sol-Gel Processing. *Journal of the American Ceramic Society* **75**, 2125 (1992).

[107] Nazeri, A.; Kahn, H.; Bender, B.; Allen, C. Microstructure of $KTa_xNb_{1-X}O_3$ Thin Films on MgO (100) Single Crystals. *Journal of the American Ceramic Society* **77**, 2450 (1994).

[108] Hirano, S. I.; Kato, K. Synthesis of $LiNbO_3$ by Hydrolysis of Metal Alkoxides. *Advanced Ceramic Materials* **2**, 142 (1987).

[109] Hirano, S.; Kato, K. Formation of $LiNbO_3$ Films by Hydrolysis of Metal Alkoxides. *Journal of Non-Crystalline Solids* **100**, 538 (1988).

[110] Eichorst, D. J.; Payne, D. A.; Wilson, S. R.; Howard, K. E. Crystal Structure of $LiNb(OCH_2CH_3)_6$: a Precursor for Lithium Niobate Ceramics. *Inorganic Chemistry* **29**, 1458 (1990).

[111] Kuang, A. X.; Lu, C. J.; Huang, G. Y.; Wang, S. M. Preparation of $KTa_{0.65}Nb_{0.35}O_3$

Thin Films by a Sol-Gel Process. *Journal of Crystal Growth* **149**, 80 (1995).

[112] Wang, S. M.; Zhon, T. S.; Wang, L. H.; Kuang, A. X. Preparation of Highly Oriented KTN/$SrTiO_3$ (111), KTN/$SrTiO_3$ (100) Thin Films by Sol-Gel Method. *Ferroelectrics* **195**, 259 (1997).

[113] Bao, D. H.; Kuang, A. X.; Gu, H. S. Effects of Sol-Gel Processing Parameters and Substrates on Crystallization of Potassium Tantalate-Niobate Thin Films. *Physica Status Solidi (a)* **163**, 67 (1997).

[114] Lu, C. J.; Kuang, A. X. Preparation of Potassium Tantalate Niobate Through Sol-Gel Processing. *Journal of Materials Science* **32**, 4421 (1997).

[115] Buršik, J.; Drbohlav, I.; Vanek, P.; Železny, V. Preparation of Potassium Tantalate Thin Films Through Chemical Solution Deposition. *Journal of the European Ceramic Society* **24**, 455 (2004).

[116] Buršik, J.; Železny, V.; Vanek, P. Preparation of Potassium Tantalate Niobate Thin Films by Chemical Solution Deposition and Their Characterization. *Journal of the European Ceramic Society* **25**, 2151 (2005).

[117] Weber, I. T.; Audebrand, N.; Bouquet, V.; Guilloux-Viry, M.; Perrin, A. $KTaO_3$ Powders and Thin Films Prepared by Polymeric Precursor Method. *Solid State Sciences* **8**, 606 (2006).

[118] Nazeri, A. Crystallization of Sol-Gel Deposited Potassium-Tantalate-Niobate Thin Films on Platinum. *Applied Physics Letters* **65**, 295 (1994).

[119] Železny, V.; Buršik, J.; Vanek, P. Preparation and Infrared Characterization of Potassium Tantalate Thin Films. *Journal of the European Ceramic Society* **25**, 2155 (2005).

[120] Železny, V.; Buršik, J.; Vanek, P. CSD Ceramic $K(Ta,Nb)O_3$ Thin Films and Their Characterization by Infrared Spectroscopy. *Journal De Physique Iv* **128**, 71 (2005).

[121] Vogt, H.; Uwe, H. Hyper-Raman Scattering from the Incipient Ferroelectric $KTaO_3$. *Physical Review B* **29**, 1030 (1984).

[122] Vogt, H. Refined Treatment of the Model of Linearly Coupled Anharmonic-Oscillators and its Application to the Temperature-Dependence of the Zone-Center Soft-Mode Frequencies of $KTaO_3$ and $SrTiO_3$. *Physical Review B* **51**, 8046 (1995).

[123] Sashital, S. R.; Krishnakumar, S.; Esener, S. Synthesis and Characterization of RF-Planar Magnetron Sputtered $KTa_xNb_{1-x}O_3$ Thin Films. *Applied Physics Letters* **62**, 2917 (1993).

[124] Gutmann, R.; Hulliger, J.; Hauert, R.; Moser, E. M. Auger Electron and X-Ray Photoelectron Spectroscopy of Monocrystalline Layers of $KTa_{1-x}Nb_xO_3$ Grown by Liquid-Phase Epitaxy. *Journal of Applied Physics* **70**, 2648 (1991).

[125] Onoe, A.; Yoshida, A.; Chikuma, K. Epitaxial Growth of Orientation-Controlled $KNbO_3$ Crystal Films on MgO Using $KTa_xNb_{1-x}O_3$ Intermediate Layer by Metalorganic Chemical Vapor Deposition. *Applied Physics Letters* **79**, 1217 (2001).

[126] Nichols, B. M.; Hoerman, B. H.; Hwang, J. H.; Mason, T. O.; Wessels, B. W. Phase

Stability of Epitaxial $KTa_xNb_{1-x}O_3$ Thin Films Deposited by Metalorganic Chemical Vapor Deposition. *Journal of Materials Research* **18**, 106 (2003).

[127] Yilmaz, S.; Venkatesan, T.; Gerhardmulthaupt, R. Pulsed Laser Deposition of Stoichiometric Potassium-Tantalate-Niobate Films from Segmented Evaporation Targets. *Applied Physics Letters* **58**, 2479 (1991).

[128] Yilmaz, S.; Gerhardmulthaupt, R.; Bonner, W. A.; Hwang, D. M.; Inam, A.; Martinez, J. A.; Ravi, T. S.; Sands, T.; Wilkens, B. J.; Wu, X. D.; Venkatesan, T. Electro-Optic Potassium-Tantalate-Niobate Films Prepared by Pulsed Laser Deposition from Segmented Pellets. *Journal of Materials Research* **9**, 1272 (1994).

[129] Christen, H. M.; Norton, D. P.; Gea, L. A.; Boatner, L. A. Pulsed Laser Deposition of Solid-Solution Films Using Segmented Targets. *Thin Solid Films* **312**, 156 (1998).

[130] Knauss, L. A.; Harshavardhan, K. S.; Christen, H. M.; Zhang, H. Y.; He, X. H.; Shih, Y. H.; Grabowski, K. S.; Knies, D. L. Growth of Nonlinear Optical Thin Films of $KTa_{1-x}Nb_xO_3$ on GaAs by Pulsed Laser Deposition for Integrated Optics. *Applied Physics Letters* **73**, 3806 (1998).

[131] Bae, H. J.; Sigman, J.; Norton, D. P.; Boatner, L. Dielectric Properties of Ti-Doped $K(Ta,Nb)O_3$ Thin Films Grown by Pulsed Laser Deposition. *Materials Science and Engineering B* **117**, 87 (2005).

[132] Chang, W.; Carter, A. C.; Horwitz, S. W.; Kirchoefer, S. W.; Pond, M. J.; Grabowski, K. S.; Chrisey, D. B. Dielectric and Structural Properties of (100) $KTa_{1-x}Nb_xO_3$ Films Grown on MgO, $LaAlO_3$, and $SrTiO_3$ Substrates by Pulsed Laser Deposition. *MRS Proceedings* **493**, 353 (1998).

[133] Laur, V.; Tanne, G.; Laurent, P.; Rousseau, A.; Bouquet, V.; Guilloux-Viry, M.; Huret, F. Dielectric Properties at Microwave Frequencies: Substrate Influence. *Ferroelectrics* **353**, 455 (2007).

[134] Rousseau, A.; Laur, V.; Deputier, S.; Bouquet, V.; Guilloux-Viry, M.; Tanne, G.; Laurent, P.; Huret, F.; Perrin, A. Influence of Substrate on the Pulsed Laser Deposition Growth and Microwave Behaviour of $KTa_{0.6}Nb_{0.4}O_3$ Potassium Tantalate Niobate Ferroelectric Thin Films. *Thin Solid Films* **516**, 4882 (2008).

[135] Bartasyte, A.; Kreisel, J.; Peng, W.; Guilloux-Viry, M. Temperature-Dependent Raman Scattering of $KTa_{1-x}Nb_xO_3$ Thin Films. *Applied Physics Letters* **96**, 262903 (2010).

[136] Burgio, N.; Iasonna, A.; Magini, M.; Martelli, S.; Padella, F. Mechanical Alloying of the Fe−Zr System. Correlation Between Input Energy and End Products. *Il Nuovo Cimento D* **13**, 459 (1991).

[137] Shriver, D. F.; Drezdzon, M. A. *The Manipulation of Air-Sensitive Compounds* (John Wiley & Sons, New York, 1986).

[138] Malič, B. *"Alkoksidna sol-gel sinteza materialov v sistemu PbO-ZrO_2-TiO_2" (Alkoxide Sol-Gel Synthesis of Materials in the PbO-ZrO_2-TiO_2 System)* PhD Thesis (University of Ljubljana, Ljubljana, 1995).

[139] Polished Substrates For Thin Film Applications. http://www.coorstek.com/resources/8510-1083_Polished_Substrates.pdf (accessed November, 2011)

[140] X'Pert HighScore, Version 2.1b(2.1.2), Release 2005, PANalytical B. V., Almelo, Netherlands.

[141] PDF-ICDD, PCPDFWin Version 2.2, June 2001, International Center for Diffraction Data (2002).

[142] PDF-ICDD 38-1470.

[143] Egerton, R. F. *Electron Energy-Loss Spectroscopy in the Electron Microscope* (Plenum Press, New York, 1996).

[144] Horita, Z.; Sano, T.; Nemoto, M. An Extrapolation Method for the Determination of Cliff-Lorimer k_{AB} Factors at Zero Foil Thickness. *Journal of Microscopy* **143**, 215 (1986).

[145] Tchernychova, E.; Glinšek, S.; Malič, B.; Kosec, M. Combined Analytical Transmission Electron Microscopy Approach to Reliable Composition Evaluation of $KTaO_3$. *Journal of the American Ceramic Society* **94**, 1611 (2011).

[146] Vendik, O. G.; Zubko, S. P.; Nikol'ski, M. A. Modeling and Calculation of the Capacitance of a Planar Capacitor Containing a Ferroelectric Thin Film. *Technical Physics* **44**, 349 (1999).

[147] Vukadinović, M.; Malič, B.; Kosec, M.; Križaj, D. Modelling and Characterization of Thin Film Planar Capacitors: Inherent Errors and Limits of Applicability of Partial Capacitance Methods. *Measurement Science and Technology* **20**, 115106 (2009).

[148] Levstik, A.; Filipic, C.; Kutnjak, Z.; Levstik, I.; Pirc, R.; Tadic, B.; Blinc, R. Field-Cooled and Zero-Field-Cooled Dielectric Susceptibility in Deuteron Glasses. *Physical Review Letters* **66**, 2368 (1991).

[149] Brinkman, K. *Positional Order in Lead Scandium Tantalate (PST) as a <<Tool>> for the Investigation of Relaxor Ferroelectric Behavior in Thin Films*. PhD Thesis (EPFL Swiss Federal Institute of Technology, Lausanne, 2004).

[150] Krupka, J. Frequency Domain Complex Permittivity Measurements at Microwave Frequencies. *Measurement Science and Technology* **17**, R55 (2006).

[151] Bovtun, V.; Pashkov, V.; Kempa, M.; Kamba, S.; Eremenko, A.; Molchanov, V.; Poplavko, Y.; Yakymenko, Y.; Lee, J. H.; Schlom, D. G. An Electrode-Free Method of Characterizing the Microwave Dielectric Properties of High-Permittivity Thin Films. *Journal of Applied Physics* **109**, 024106 (2011).

[152] Krupka, J.; Gregory, A. P.; Rochard, O. C.; Clarke, R. N.; Riddle, B.; Baker-Jarvis, J. Uncertainty of Complex Permittivity Measurements by Split-Post Dielectric Resonator Technique. *Journal of the European Ceramic Society* **21**, 2673 (2001).

[153] Easton, C. D.; Jacob, M. V.; Krupka, J. Non-Destructive Complex Permittivity Measurement of Low Permittivity Thin Film Materials. *Measurement Science and*

Technology **18**, 2869 (2007).

[154] Kužel, P.; Nemec, H.; Kadlec, F.; Kadlec, C. Gouy Shift Correction for Highly Accurate Refractive Index Retrieval in Time-Domain Terahertz Spectroscopy. *Optics Express* **18**, 15338 (2010).

[155] Kadlec, C.; Kadlec, F.; Němec, H.; Kužel, P.; Schubert, J.; Panaitov, G. High Tunability of the Soft Mode in Strained $SrTiO_3$/$DyScO_3$ Multilayers. *Journal of Physics: Condensed Matter* **21**, 115902 (2009).

[156] Skoromets, V.; Glinšek, S.; Bovtun, V.; Kempa, M.; Petzelt, J.; Kamba, S.; Malič, B.; Kosec, M.; Kužel, P. Ferroelectric Phase Transition in Polycrystalline $KTaO_3$ Thin Film Revealed by Terahertz Spectroscopy. *Applied Physics Letters* **99**, 052908 (2011).

[157] Kužel, P.; Petzelt, J. Time-Resolved Terahertz Transmission Spectroscopy of Dielectrics. *Ferroelectrics* **239**, 949 (2000).

[158] Rojac, T.; Kosec, M.; Šegedin, P.; Malič, B.; Holc, J. The Formation of a Carbonato Complex During the Mechanochemical Treatment of a Na_2CO_3-Nb_2O_5 Mixture. *Solid State Ionics* **177**, 2987 (2006).

[159] Gatehouse, B. M.; Livingstone, S. E.; Nyholm, R. S. The Infrared Spectra of Some Simple and Complex Carbonates. *Journal of the Chemical Society (Resumed)*, 3137 (1958).

[160] Schutte, C. J. H.; Buijs, K. The Infra-Red Spectra of K_2CO_3 and Its Hydrates. *Spectrochimica Acta* **17**, 921 (1961).

[161] PDF-ICDD 25-0922.

[162] PDF-ICDD 11-0655.

[163] PDF-ICDD 20-0886.

[164] PDF-ICDD 35-1464.

[165] Busca, G.; Lorenzelli, V. Infrared Spectroscopic Identification of Species Arising from Reactive Adsorption of Carbon Oxides on Metal-Oxide Surfaces. *Materials Chemistry* **7**, 89 (1982).

[166] Watters, R. L. NIST Standard Reference Database N° 69, United States, June 2005 Release (robert.watters@nist.gov).

[167] Rojac, T.; Kosec, M.; Połomska, M.; Hilczer, B.; Šegedin, P.; Benčan, A. Mechanochemical Reaction in the K_2CO_3–Nb_2O_5 System. *Journal of the European Ceramic Society* **29**, 2999 (2009).

[168] PDF-ICDD 70-1800.

[169] Popovič, A.; Bencze, L.; Koruza, J.; Malič, B.; Kosec, M. Knudsen Effusion Mass Spectrometric Approach to the Thermodynamics of Na_2O–Nb_2O_5 System. *International Journal of Mass Spectrometry* **309**, 70 (2011).

[170] Coble, R. L. Sintering Alumina: Effect of Atmospheres. *Journal of the American Ceramic Society* **45**, 123 (1962).

[171] Kang, S. J. L. *Sintering: Densification, Grain Growth, and Microstructure* (Elsevier, Amsterdam, 2005).

[172] Greskovich, C.; Rosolowski, J. H. Sintering of Covalent Solids. *Journal of the American Ceramic Society* **59**, 336 (1976).

[173] Breeze, J. D.; Perkins, J. M.; McComb, D. W.; Alford, N. M. Do Grain Boundaries Affect Microwave Dielectric Loss in Oxides? *Journal of the American Ceramic Society* **92**, 671 (2009).

[174] Buzin, I. M.; Ivanov, I. V.; Chistyakov, V. A. "Vzaimodeistvie mod i dielektricheskie poteri v tantalate kaliya" (Interaction of Modes and Dielectric Losses in Potassium Tantalate). *Fizika Tverdogo Tela* **9**, 2 (1980).

[175] Belokopytov, V.; Ivanov, I. V.; Katanov, S. I.; Moiseev, N. N.; Syrnikov, P. P. "Dielektricheskie poteri kristallov tantalata kaliya na chastotah 0.5-15 GGc" (Dielectric Losses of Potassium Tantalate Crystals in 0.5–15 GHz Frequency Range). *Fizika Tverdogo Tela* **24**, 3 (1982).

[176] Miller, R. C.; Spitzer, W. G. Far Infrared Dielectric Dispersion in $KTaO_3$. *Physical Review* **129**, 94 (1963).

[177] Perry, C. H.; McNelly, T. F. Ferroelectric "Soft" Mode in $KTaO_3$. *Physical Review* **154**, 456 (1967).

[178] Ichikawa, Y.; Nagai, M.; Tanaka, K. Direct Observation of the Soft-Mode Dispersion in the Incipient Ferroelectric $KTaO_3$. *Physical Review B* **71**, 092106 (2005).

[179] Hlinka, J.; Petzelt, J.; Kamba, S.; Nuzhnyy, D.; Ostapchuk, T. Infrared Dielectric Response of Relaxor Ferroelectrics. *Phase Transitions* **79**, 41 (2006).

[180] Singh, D. J. Stability and Phonons of $KTaO_3$. *Physical Review B* **53**, 176 (1996).

[181] Wemple, S. H. Some Transport Properties of Oxygen-Deficient Single-Crystal Potassium Tantalate ($KTaO_3$). *Physical Review* **137**, A1575 (1965).

[182] Nilsen, W. G.; Skinner, J. G. Raman Spectrum of Potassium Tantalate. *The Journal of Chemical Physics* **47**, 1413 (1967).

[183] Uwe, H.; Lyons, K. B.; Carter, H. L.; Fleury, P. A. Ferroelectric Microregions and Raman-Scattering in $KTaO_3$. *Physical Review B* **33**, 6436 (1986).

[184] Vogt, H. Evidence of Defect-Induced Polarization Clusters in Nominally Pure $KTaO_3$ from Low-Temperature Raman and Hyper-Raman Spectra. *Journal of Physics: Condensed Matter* **3**, 3697 (1991).

[185] Judd, M. D.; Plunkett, B. A.; Pope, M. I. The Thermal Decomposition of Calcium, Sodium, Silver and Copper(II) Acetates. *Journal of Thermal Analysis* **6**, 555 (1974).

[186] Coffman, P. R.; Barlingay, C. K.; Gupta, A.; Dey, S. K. Structure Evolution in the PbO-ZrO_2-TiO_2 Sol-Gel system: Part II - Pyrolysis of Acid and Base-Catalyzed Bulk and Thin Film Gels. *Journal of Sol-Gel Science and Technology* **6**, 83 (1996).

[187] Merkle, R.; Bertagnolli, H. Investigation of the Pyrolysis of Lead Zirconate Titanate Gels with Coupled Differential Thermal Analysis, Thermogravimetry and Infrared

Spectroscopy. *Journal of Materials Science* **33**, 4341 (1998).

[188] Subramanian, M. A.; Aravamudan, G.; Rao, G. V. S. Oxide Pyrochlores - a Review. *Progress in Solid State Chemistry* **15**, 55 (1983).

[189] Goh, G. K. L.; Haile, S. M.; Levi, C. G.; Lange, F. F. Hydrothermal Synthesis of Perovskite and Pyrochlore Powders of Potassium Tantalate. *Journal of Materials Research* **17**, 3168 (2002).

[190] Lotgering, F. K. Topotactical Reactions with Ferrimagnetic Oxides Having Hexagonal Crystal Structures - I. *Journal of Inorganic and Nuclear Chemistry* **9**, 113 (1959).

[191] Kupec, A.; Malič, B.; Tellier, J.; Tchernychova, E.; Glinšek, S.; Kosec, M. Lead-Free Ferroelectric Potassium Sodium Niobate Thin Films from Solution: Composition and Structure. *Journal of the American Ceramic Society* DOI: 10.1111/j.1551-2916.2011.04892.x, (2012).

[192] Tanaka, K.; Hayashi, H.; Kakimoto, K.; Ohsato, H.; Iijima, T. Effect of (Na,K)-Excess Precursor Solutions on Alkoxy-Derived (Na,K)NbO_3 Powders and Thin Films. *Japanese Journal of Applied Physics* **46**, 6964 (2007).

[193] Čakare-Samarđija, L.; Malič, B.; Kosec, M. $K_{0.5}Na_{0.5}NbO_3$ Thin Films Prepared by Chemical Solution Deposition. *Ferroelectrics* **370**, 113 (2008).

[194] Ahn, C. W.; Lee, S. Y.; Lee, H. J.; Ullah, A.; Bae, J. S.; Jeong, E. D.; Choi, J. S.; Park, B. H.; Kim, I. W. The Effect of K and Na Excess on the Ferroelectric and Piezoelectric Properties of $K_{0.5}Na_{0.5}NbO_3$ Thin Films. *Journal of Physics D: Applied Physics* **42**, 215304 (2009).

[195] Cho, C. R.; Grishin, A. Background Oxygen Effects on Pulsed Laser Deposited $Na_{0.5}K_{0.5}NbO_3$ Films: From Superparaelectric State to Ferroelectricity. *Journal of Applied Physics* **87**, 4439 (2000).

[196] Scherer, G. W. Sintering of Sol-Gel Films. *Journal of Sol-Gel Science and Technology* **8**, 353 (1997).

[197] Thompson, C. V. Structure Evolution During Processing of Polycrystalline Films. *Annual Review of Materials Science* **30**, 159 (2000).

[198] Maki, K.; Soyama, N.; Nagamine, K.; Mori, S.; Ogi, K. Low-Temperature Crystallization of Sol-Gel Derived Pb($Zr_{0.4}Ti_{0.6}$)O_3 Thin Films. *Japanese Journal of Applied Physics* **40**, 5533 (2001).

[199] Hoffmann, S.; Hasenkox, U.; Waser, R.; Jia, C. L.; Urban, K. Chemical Solution Deposited $BaTiO_3$ and $SrTiO_3$ Thin Films with Columnar Microstructure. *MRS Proceedings* **474**, 9 (1997).

[200] Hoffmann, S.; Waser, R. Control of the Morphology of CSD-Prepared (Ba,Sr)TiO_3 Thin Films. *Journal of the European Ceramic Society* **19**, 1339 (1999).

[201] Kutnjak, Z.; Filipič, C.; Levstik, A. Linear and Nonlinear Dielectric Constant as Function of Bias Electric Field in Relaxor Materials. *Journal of the European Ceramic Society* **21**, 1313 (2001).

[202] Kutnjak, Z. Thermal and Electric Field Hysteresis Effects in Structuraly Disordered Ferroelectric Materials. *Ferroelectrics* **400**, 214 (2010).

[203] Kutnjak, Z.; Filipič, C.; Bobnar, V.; Levstik, A. Aging of the Linear and Nonlinear Dielectric Susceptibility in a PLZT Relaxor System. *Ferroelectrics* **240**, 1539 (2000).

[204] Kadlec, C.; Skoromets, V.; Kadlec, F.; Němec, H.; Hlinka, J.; Schubert, J.; Panaitov, G.; Kužel, P. Temperature and Electric Field Tuning of the Ferroelectric Soft Mode in a Strained $SrTiO_3/DyScO_3$ Heterostructure. *Physical Review B* **80**, (2009).

[205] Heavens, O. S. Optical Properties of Thin Films. *Reports on Progress in Physics* **23**, 1 (1960).

[206] Petzelt, J. Far Infrared and Near-Millimetre Spectroscopy of Partially Disordered Crystals. *Ferroelectrics* **104**, 121 (1990).

[207] Hlinka, J.; Ostapchuk, T.; Nuzhnyy, D.; Petzelt, J.; Kužel, P.; Kadlec, C.; Vanek, P.; Ponomareva, I.; Bellaiche, L. Coexistence of the Phonon and Relaxation Soft Modes in the Terahertz Dielectric Response of Tetragonal $BaTiO_3$. *Physical Review Letters* **101**, (2008).

[208] Rychetsky, I.; Petzelt, J.; Ostapchuk, T. Grain-Boundary and Crack Effects on the Dielectric Response of High-Permittivity Films and Ceramics. *Applied Physics Letters* **81**, 4224 (2002).

[209] White, G. K. Thermal Expansion of $KTaO_3$ at Low Temperatures. *Journal of Physics C: Solid State Physics* **14**, L297 (1981).

[210] Goh, G. K. L.; Chan, K. Y. S.; Tan, B. S. K.; Zhang, Y. W.; Kim, J. H.; Osipowicz, T. Low Temperature Epitaxy of $KTaO_3$ and $KNbO_3$ Films. *Journal of the Electrochemical Society* **155**, D52 (2008).

[211] Wachtman, J. B.; Scuderi, T. G.; Cleek, G. W. Linear Thermal Expansion of Aluminum Oxide and Thorium Oxide from 100 K to 1100 K. *Journal of the American Ceramic Society* **45**, 319 (1962).

[212] Lide, D. R. (ed.) *CRC Handbook of Chemistry and Physics*, 79th Ed. (CRC Press, Boston, 1999).

[213] Ravel, B.; Newville, M. ATHENA, ARTEMIS, HEPHAESTUS: Data Analysis for X-Ray Absorption Spectroscopy Using IFEFFIT. *Journal of Synchrotron Radiation* **12**, 537 (2005).

[214] Rehr, J. J.; Albers, R. C.; Zabinsky, S. I. High-Order Multiple-Scattering Calculations of X-Ray-Absorption Fine-Structure. *Physical Review Letters* **69**, 3397 (1992).

[215] Kodre, A.; Tellier, J.; Arčon, I.; Malič, B.; Kosec, M. Extended X-Ray Absorption Fine Structure Study of Phase Transitions in the Piezoelectric Perovskite $K_{0.5}Na_{0.5}NbO_3$. *Journal of Applied Physics* **105**, 113528 (2009).

[216] Sedlar, M.; Sayer, M. Reactivity of Titanium Isopropoxide, Zirconium Propoxide

and Niobium Ethoxide in the System of 2-methoxyethanol, 2,4-pentanedione and Water. *Journal of Sol-Gel Science and Technology* **5**, 27 (1995).

[217] Malič, B.; Arčon, I.; Kodre, A.; Kosec, M. Homogeneity of $Pb(Zr,Ti)O_3$ Thin Films by Chemical Solution Deposition: Extended X-Ray Absorption Fine Structure Spectroscopy Study of Zirconium Local Environment. *Journal of Applied Physics* **100**, 051612 (2006).

[218] Nagakari, S.; Kamigaki, K.; Nambu, S. Dielectric Properties of Sol-Gel Derived $Pb(Mg_{1/3}Nb_{2/3})O_3$-$PbTiO_3$ Thin Films. *Japanese Journal of Applied Physics* **35**, 4933 (1996).

[219] Toulouse, J.; Pattnaik, R. Relaxor and Superparaelectric Behavior in the Disordered Ferroelectrics KLT and KTN. *Ferroelectrics* **199**, 287 (1997).

[220] Toulouse, J.; Pattnaik, R. K. Nonlinear Electrostriction in the Mixed Ferroelectric $KTa_{1-x}Nb_xO_3$. *Physical Review B* **65**, (2002).

[221] Tyunina, M.; Levoska, J. Coexistence of Ferroelectric and Relaxor Properties in Epitaxial Films of $Ba_{1-x}Sr_xTiO_3$. *Physical Review B* **70**, 132105 (2004).

[222] Tyunina, M.; Levoska, J. The Paraelectric State in Thin-Film $(Ba,Sr)TiO_3$. *Journal of Applied Physics* **101**, 084119 (2007).

[223] Schönhals, A.; Kremer, F. Theory of Dielectric Relaxation In: Kremer, F., Schönhals, A. (ed.) *Broadband Dielectric Spectroscopy*. 1 (Springer, Berlin, 2003).

[224] Gervais, F. High-Temperature Infrared Reflectivity Spectroscopy by Scanning Interferometry. In: Button, K. J. (ed.) *Infrared and Millimeter Waves*. 279 (Academic Press, New York, 1983).

[225] Petzelt, J.; Kamba, S. Spectroscopic Properties and Lattice Dynamics of Ferroelectric and Related Functional Oxide Ceramics. In: Yarwood, J., Douthwaite, R., Dusckett, S. (ed.) *Spectroscopic Properties of Inorganic and Organometallic Compounds*. 71 (The Royal Society of Chemistry, 2009).

[226] Fontana, M. D.; Metrat, G.; Servoin, J. L.; Gervais, F. Infrared Spectroscopy in $KNbO_3$ Through the Successive Ferroelectric Phase Transitions. *Journal of Physics C: Solid State Physics* **17**, 483 (1984).

[227] Fedorov, I.; Železny, V.; Petzelt, J.; Trepakov, V.; Jelínek, M.; Trtík, V.; Čerňansk, M.; Studnička, V. Far-Infrared Spectroscopy of a $SrTiO_3$ Thin Film. *Ferroelectrics* **208-209**, 413 (1998).

[228] Ostapchuk, T.; Petzelt, J.; Železny, V.; Kamba, S.; Bovtun, V.; Porokhonskyy, V.; Pashkin, A.; Kužel, P.; Glinchuk, M. D.; Bykov, I. P.; Gorshunov, B.; Dressel, M. Polar Phonons and Central Mode in Antiferroelectric $PbZrO_3$ Ceramics. *Journal of Physics: Condensed Matter* **13**, 2677 (2001).

[229] Cochran, W. Crystal Stability and the Theory of Ferroelectricity. *Physical Review Letters* **3**, 412 (1959).

[230] Kamba, S.; Nuzhnyy, D.; Denisov, S.; Veljko, S.; Bovtun, V.; Savinov, M.; Petzelt, J.; Kalnberga, M.; Sternberg, A. Quantum Paraelectric Behavior of Pyrochlore

$Pb_{1.83}Mg_{0.29}Nb_{1.71}O_{6.39}$. *Physical Review B* **76**, 054125 (2007).

[231] Comes, R.; Lambert, M.; Guinier, A. The Chain Structure of $BaTiO_3$ and $KNbO_3$. *Solid State Communications* **6**, 715 (1968).

[232] Petzelt, J.; Kozlov, G. V.; Volkov, A. A. Dielectric Spectroscopy of Paraelectric Soft Modes. *Ferroelectrics* **73**, 101 (1987).

8 Index of Figures

Figure 1.1: a) Typical ferroelectric (*P-E*) hysteresis loop. Remanent polarization P_r and coercive field E_c are marked. b) Schematic temperature dependence of the dielectric permittivity ε', inverse permittivity $1/\varepsilon'$ and spontaneous polarization P_s of a first-order ferroelectric. The T_0 and T_C are the Curie-Weiss temperature and Curie point, respectively. 17

Figure 1.2: a) Schematic temperature dependence of the permittivity ε', inverse permittivity $1/\varepsilon'$ and spontaneous polarization P_s of the relaxor. An arrow is indicating the increase of the frequency. b) Slim relaxor *P-E* hysteresis loop. 19

Figure 1.3: Schematic temperature dependence of the permittivity ε' and inverse permittivity $1/\varepsilon'$ of the incipient ferroelectrics. 22

Figure 1.4: Frequency dependence of the dielectric losses $\tan\delta$ of the $KTaO_3$ single crystal measured at different temperatures. After Geyer et al. [15]. 23

Figure 1.5: Schematic presentation of the temperature – in-plane biaxial strain u phase diagram of the epitaxial single-domain (100) $SrTiO_3$ thin films obtained from the thermodynamic analysis. The arrows indicate the expected direction of the polarization: in-plane and out-of-plane for the tensile and compressive strains, respectively. The ranges of the ferroelectric transitions are due to the spread of the reported coefficients used in the calculation [48,51]. 26

Figure 1.6: $KNbO_3$-$KTaO_3$ phase diagram. Dashed lines indicate transitions between the cubic, tetragonal, orthorhombic and rhomobohedral phases. After Reisman et al. [65] and Triebwasser et al. [64,66]. 29

Figure 1.7: Temperature dependence of the dielectric permittivity ε' for the $KTa_xNb_{1-x}O_3$ solid solution for different compositions measured at 10 kHz. After Triebwasser [66]. 29

Figure 1.8: Ta_2O_5-K_2O (K_2CO_3) phase diagram. After Reisman et al. [69]. 31

Figure 1.9: Ta_2O_5-$KTaO_3$ phase diagram. GTB – Gatehouse tungsten bronze at 89 % of Ta_2O_5; TTBs – tetragonal tungsten bronze with superstructure between 83.3 % and 80 % of Ta_2O_5; HTB – hexagonal tungsten bronze at 77.3 % of Ta_2O_5; H_1 – hexagonal phase at 73.85 % of Ta_2O_5; H_2 – hexagonal phase at 73.5 % of Ta_2O_5. TTB – tetragonal tungsten bronze near 66 % of Ta_2O_5 ($K_6Ta_{10.8}O_{30}$). After Roth et al. [70]. 32

Figure 1.10: Subsolidus phase relations in the $KNbO_3$-$KTaO_3$ phase diagram. After Hill et al. [80]. 34

Figure 1.11: Schematic presentation of the chemical solution deposition process. 37

Figure 1.12: Scheme of the dimeric structure of the $[M(OR)_5]_2$ (M - Ta, Nb; R - CH_3, CH_2–CH_3). Adopted from Bradley et al. [100]. 37

Figure 1.13: Structure of the chelate cycle formed by 2-methoxyethanol. M – metal. From Turova et al. [102]. 39

Figure 3.1: Schematic presentation of the $KTaO_3$ ceramics' processing. 45

Figure 3.2: Schematic presentation of the synthesis of the $KTaO_3$ and $KTa_{0.6}Nb_{0.4}O_3$ sols. 47

Figure 3.3: Schematic presentation of the $KTaO_3$ and $KTa_{0.6}Nb_{0.4}O_3$ thin films' preparation route. 48

Figure 3.4: Schematic presentation of the planar thin film capacitor. h_f and h_s – thickness of the film and the substrate, respectively; s – gap between the electrodes (2-3 μm); l – length of the electrodes (1.5 mm); w – width of the electrodes (750 μm). 52

Figure 3.5: Schematic diagram of the experimental setup for the quasistatic measurements. 53

Figure 3.6: THz time-domain waveforms of the bare c-sapphire substrate and substrate with the 200-nm-thick $KTaO_3$ thin film, both measured at 20 K. 0 - direct pass; 1 – first internal Fabry-Pérot reflection. 56

Figure 4.1: XRD patterns of the K_2CO_3-Ta_2O_5 powder mixtures after the homogenization (0 h) and after 5 h and 10 h of the mechanochemical treatment. Note the change of the scale for different patterns. T – Ta_2O_5[161]; K – $K_2CO_3 \cdot 1.5\,H_2O$ [162]; KH – $K_4H_2(CO_3)_3 \cdot 1.5\,H_2O$ [163]; Py – pyrochlore $K_2Ta_2O_6$ [164]. 58

Figure 4.2: IR spectra of the K_2CO_3-Ta_2O_5 powder mixtures after the homogenization (0 h), and after 5 h and 10 h of the mechanochemical treatment. 59

Figure 4.3: Structure of the carbonate CO_3^{2-} ion and its common coordination types. M – metal. 59

Figure 4.4: XRD patterns of the $KTaO_3$ powders after the first (1C) and the second (2C) heating at 800°C for 4 h. All peaks correspond to the perovskite $KTaO_3$ phase [142]. 60

Figure 4.5: Particle size distribution with the median particle size d_{50} of the $KTaO_3$ powders after a) the first (1C) and b) the second (2C) heating at 800°C for 4 h. 60

Figure 4.6: a) and b) FE-SEM, c) and d) TEM micrographs of the single (1C) and double (2C) heated $KTaO_3$ powders. Both heatings were performed at 800°C for 4 h. In a) the arrows indicate nanoparticles attached to the larger particles. 61

Figure 4.7: a) TEM micrograph of the 1C $KTaO_3$ powder, single heated at 800°C for 4h. Numbers denote the areas from which the composition shown in b) was obtained by the EDXS analysis. The area 1 represents well-crystallized cubic-shaped particles; the area 2 represents the particles with disturbed edges; while the area 3 represents poorly crystalline or amorphous nanoparticles attached to larger ones. In b) the dotted horizontal line denotes the nominal compositions, while grey areas correspond to the standard deviation ± 2δ (± 2.6 at.%). For the concentration of O obtained by EELS see Ref. [145]. 61

Figure 4.8: XRD patterns of the 1C-Air, 1C-O_2, 1C-HP and 2C-HP $KTaO_3$ ceramics. In b) detailed view of the square rooted XRD patterns in the 20–40° 2θ range is shown. Peaks denoted with the Miller indices correspond to the perovskite $KTaO_3$ phase [142]. X – $K_6Ta_{10.8}O_{30}$ phase [168]. 62

Figure 4.9: FE-SEM micrographs of the fractured (a, c, e) and polished (b, d, f) surfaces of the $KTaO_3$ ceramics prepared by sintering in air at 1325°C (1C-Air) and by hot pressing at 1250°C (1C-HP, 2C-HP). The images of the fractured and polished surfaces were obtained by the secondary- and back-scattered-electron imaging modes, respectively..... 63

Figure 4.10: a) TEM micrograph of the 1C-HP $KTaO_3$ ceramic prepared from the single-heated powders by hot pressing at 1250°C. Numbers denote the areas from which the composition shown in b) was obtained by the EDXS analysis. The area 1 represents small grains with the perovskite composition and a slightly Ta-rich tendency. The area 2 represents large grains and small grains in their vicinity, both with a similar Ta-rich composition. The number 3 correspond to either small or large grains with a K-rich composition. In b) the dotted horizontal line denotes the nominal compositions, while grey areas correspond to the standard deviation ± 2δ (± 2.6 at.%). For the concentration of O obtained by EELS see Ref. [145]. 65

Figure 4.11: TEM micrograph of the 1C-HP $KTaO_3$ ceramic. The amorphous triple pocket (1) between the two grains (2) is shown in the inset. Numbers represent the areas where the combined EDXS/EELS analyses were performed. 65

Figure 4.12: a) TEM micrograph of the 2C-HP $KTaO_3$ ceramic prepared from the double-heated powders by hot pressing at 1250°C. The areas from which the compositions shown in b) and c) were obtained by the EDXS analyses are marked. In b) area 1 represents small grains with the perovskite composition, while area 2 represents small grains with the K-rich compositions. In c) area 1 represents large grains with a perovskite composition, area 2 represents large grains with Ta-rich compositions and area 3 represents the grains with K-rich compositions. Some of the grains showed large compositional variations. Examples are shown in the insets of b) and c). The dotted horizontal line denotes the nominal compositions, while the grey areas correspond to the standard deviation ± 2δ (± 2.6 at.%) for each element. 66

Figure 4.13: a) Temperature dependence of dielectric permittivity ε' and b) dielectric losses $\tan\delta$ of the 1C-HP and 2C-HP $KTaO_3$ ceramics measured at 1 kHz. Note the logarithmic scale in both cases. Lines between the experimental points are guides to the eye. 67

Figure 4.14: a) Temperature dependence of dielectric losses $\tan\delta$ of the 2C-HP ceramic measured at 1 kHz, 10 kHz and 100 kHz. Different frequency-dispersion regions are marked. b) Arrhenius plots of the three dispersion regions in the frequency range from 100 Hz to 100 kHz. Calculated activation energies E_a are also given. 68

Figure 4.15: Temperature dependence of the permittivity ε' and dielectric losses $\tan\delta$ of the 2C-HP ceramic measured in the 2–6 GHz frequency range. 69

Figure 4.16: IR reflectivity spectra (lines), together with the reflectivity calculated from THz transmission data (symbols), of 2C-HP $KTaO_3$ ceramics measured at a) 300 K and b) at selected temperatures in the 300–20 K range. In b) note the logarithmic wavenumber scale. Approximate positions of the TO1, TO2 and TO4 polar modes are marked. In b) the experimental data are compared to the fits (dashed lines).* – two-phonon combination band. 70

Figure 4.17: a) Real $\varepsilon'(\omega)$ and b) imaginary $\varepsilon''(\omega)$ parts of the complex dielectric permittivity $\varepsilon^*(\omega)$ of the 2C-HP $KTaO_3$ ceramics calculated from the simultaneous fits of the IR and THz data (the latter shown as the symbols) measured at different temperatures. 71

Figure 4.18: Temperature dependences of the ω_{TO1}, ω_{TO2} and ω_{TO4} polar phonon frequencies. The lines are guides to the eye. Inset: Temperature dependence of the TO1 mode damping constant γ_{TO1} 72

Figure 4.19: Temperature dependences of the Ω_{TO1} Ω_{TO2} and Ω_{TO4} mode-plasma frequencies, together with the overall plasma frequency Ω_{TOT}. Lines between the points are guides to the eye. 73

Figure 4.20: Temperature dependence of the 1-kHz permittivity ε' and soft-mode frequency ω_{SM}. Blue line: Curie-Weiss fit from 300 K to 30 K. Red line: Barret fit from 300 K to 5 K; Black line: Cochran fit from 300 K to 20 K. 74

Figure 4.21: Temperature dependence of the RF (1 kHz) and MW (26 GHz) dielectric permittivity ε' compared to the phonon contribution calculated from the IR and THz data fits. Lines between the experimental points are guides to the eye. 74

Figure 4.22: Raman spectra of the 2C-HP $KTaO_3$ ceramics measured at selected temperatures. The spectra are displaced vertically for clarity. The positions of the Raman-forbidden one-phonon features are marked. 75

Figure 4.23: Fit of the Raman spectrum measured at 50 K. Positions of the one-phonon peaks are marked. 76

Figure 4.24 a) TG and DTG, b) DTA and c) EGA curves of the stoichiometric $KTaO_3$ sol after drying at 60°C. Positions of the strongest maxima and minima of the curves are denoted. 80

Figure 4.25: XRD pattern of the $KTaO_3$ powder after the thermal analysis. All the peaks denoted with Miller indices correspond to the pyrochlore $K_2Ta_2O_6$ [164]. 81

Figure 4.26: XRD patterns of the 1C $KTaO_3$ films on alumina substrates prepared from the stoichiometric sol (0 %) and sols with 10 %, 20 % and 30 % excess of potassium acetate. The films were pyrolyzed at 350°C. After 4 depositions the final annealing was performed at 900°C for 15 min. The pattern of the alumina substrate is also shown. P – perovskite phase [142]; Py – pyrochlore phase [164]; X – unidentified peaks..... 82

Figure 4.27: XRD patterns of the 4C $KTaO_3$ thin films on alumina substrates prepared from the sols with 30 % excess of potassium acetate. Films were dried at 180°C and annealed after each deposition at 700°C, 800°C and 900°C, respectively. The procedure was repeated 4 times. The pattern of the alumina substrate is also shown. P – perovskite phase [142]; Py – pyrochlore phase [164]; X – unidentified peak. 82

Figure 4.28: XRD patterns of the 4C $KTaO_3$ thin films prepared on a) alumina and b) c-sapphire substrates. The films were dried at 180°C and annealed after each deposition at 900°C. The procedure was repeated 4 times. Patterns of the substrates are also shown. Peaks corresponding to the perovskite phase [142] are denoted with the Miller indices. In the inset of (b), unknown peak, which occasionally appeared in the patterns of the films on the c-sapphire, is shown. Note the logarithmic intensity scale in both patterns. 83

Figure 4.29: a), b), c), d) plane-view and e), f) cross-section view FE-SEM micrographs of the 4C $KTaO_3$ thin films on corundum (a), c), e)) and on c-sapphire (b), d), f)) substrates. In a) surface of the polycrystalline alumina is shown. 85

Figure 4.30: Cross-section STEM bright-field micrograph (above) and compositional STEM-EDXS line scan over the cross-section of the 4C $KTaO_3$ thin film on the alumina substrate. The position of the line scan is denoted with the arrow. The error bars represent $\pm 2\delta$ standard deviation. The dotted horizontal line denotes the nominal compositions, while the grey areas correspond to the standard deviation $\pm 2\delta$ ($\pm$ 2.6 at.%) for each element..... 86

Figure 4.31: Schematic presentation of the crystallization process in the solution-derived thin films. a) Thick crystallizing layer, where both, heterogeneous and homogeneous, nucleation mechanisms compete. b) Thin crystallizing layer where mainly the crystallites with the lowest-energy faces, oriented in-plane, nucleate and grow. c) Thin crystallizing layer, where mainly heterogeneous nucleation of the randomly oriented nuclei takes place. The in-plane grain growth is governed by the criterion of the lowest surface energy. Crystallization of only one phase, i.e., perovskite, is assumed. 87

Figure 4.32: a) Temperature dependence of the dielectric permittivity ε' of the 4C $KTaO_3$ film on the alumina substrate measured in the 3 kHz to 1 MHz frequency range. b) Curie-Weiss fit of the 10 kHz experimental data. c) Vogel-Fulcher fit of the experimental data. d) DC electric field E_{DC} dependence of the temperature of the permittivity maximum T_{max} at 10 kHz. In d) the line between the experimental points is a guide to the eye. Amplitude of the probing AC field was 4 kV/cm. 88

Figure 4.33: DC electric field E_{DC} dependence of the normalized dielectric permittivity $\varepsilon'(E_{DC})/\varepsilon'(0)$ of the 4C $KTaO_3$ thin film on alumina substrate. The measurement was performed at 298 K and 100 K, while the frequencies were 1 MHz and 100 kHz, respectively. The voltage cycle was: $-E_{DCmax} \rightarrow 0$ V $\rightarrow E_{DCmax}$. 88

Figure 4.34: Temperature dependence of the quasi-static polarization P of the 4C $KTaO_3$ thin film on alumina substrate measured on heating at DC electric field E_{DC} = 400 kV/cm after field cooling (FC) or zero-field cooling (ZFC). Quasi-static permittivity ε'_s measured in ZFC regime by applying 40 kV/cm at each temperature is shown in the inset. 89

Figure 4.35: Temperature dependence of the quasi-static polarization P of the 4C $KTaO_3$ thin film on alumina substrate measured on heating at different DC electric fields E_{DC}, i.e., 84 kV/cm, 400 kV/cm and 800 kV/cm, after zero-field cooling (ZFC) or field cooling (FC). Electric field dependence of the polarization P measured at 15 K is shown in the inset. The first point is taken from the low-field RF measurements (Figure 4.32). Line between the experimental points is a guide to the eye. 90

Figure 4.36: Temperature dependence of the MW permittivity ε' and dielectric losses $\tan\delta$ of the 4C $KTaO_3$ thin films on a) corundum and b) c-sapphire substrate, measured at 14.5 and 16.2 GHz, respectively. 91

Figure 4.37: Real $\varepsilon'(\omega)$ and imaginary $\varepsilon''(\omega)$ parts of the complex dielectric permittivity $\varepsilon^*(\omega)$ of the 4C $KTaO_3$ thin film on the c-sapphire substrate. The experimental data (symbols) at different temperatures were obtained by transmission THz time-domain spectroscopy. Lines – fits to the Equation (3.7). 92

Figure 4.38: IR reflectivity spectra of the bare c-sapphire substrate and of the 4C $KTaO_3$ thin film measured at 300 K. Approximate positions of the TO1 (SM), TO2 and TO4 polar modes are marked with arrows. Spectra are displaced vertically for reason of clarity. 93

Figure 4.39: IR transmission spectra of the a) bare c-sapphire substrate and b) the $KTaO_3$ thin film at selected temperatures in the 300 K to 5 K range. Approximate positions of the SM and TO2 polar modes of the film are marked. Spectra are displaced vertically for reasons of clarity. 94

Figure 4.40: Comparison of the experimental IR transmission spectrum of the $KTaO_3$ thin film on c-sapphire at 120 K with the fit. 94

Figure 4.41: a) Real $\varepsilon'(\omega)$ and b) imaginary $\varepsilon''(\omega)$ parts of the complex dielectric permittivity $\varepsilon^*(\omega)$ of the $KTaO_3$ thin films on c-sapphire calculated from the simultaneous fits of the IR, THz and MW data. Approximate positions of the CM, SM and TO2 modes are marked. MW experimental data are shown as symbols. 95

Figure 4.42: Temperature dependences of a) ω_{SM} and ω_{TO2} polar phonon frequencies, b) relaxation strength g and coupling constant δ between SM and CM, obtained from the simultaneous fits of the IR, THz transmission and MW data of the $KTaO_3$ thin film on the c-sapphire substrate. Lines between the points are guides to the eye. 96

Figure 4.43: Comparison of a) permittivity ε' and b) soft-mode frequency ω_{SM} of the $KTaO_3$ single crystal, ceramic and polycrystalline thin film on a c-sapphire substrate. The respective permittivities were measured at 100 Hz [20], 1 kHz (Figure 4.13a) and 16.2 GHz (Figure 4.36b) The soft-mode frequencies were obtained from the fits of the IR and THz data, while the single-crystal data were obtained from the hyper-Raman measurements in the *x(yy)z* scattering configuration [122]. 100

Figure 4.44: Temperature dependence of the permittivity ε' of the $KTaO_3$ single crystal (from Salce et al. [20], 100 Hz) and ceramic (2C-HP, 1 kHz) compared to the effective permittivity of the single-crystal–air composite calculated from Equation (4.9), assuming 2 % and 5 % porosity. 101

Figure 4.45: The k^3-weighted a) Ta and b) Nb EXAFS spectra of the KTN1, KTN4, KTN24 and KTN48 sols (dots) in comparison with the best-fit EXAFS model (solid lines). 104

Figure 4.46: Fourier transforms of the k^3-weighted a) Ta and b) Nb EXAFS spectra of KTN1, KTN4, KTN24 and KTN48 sols from Fig. 1, calculated in the k-range from 3 $Å^{-1}$ to 15 $Å^{-1}$ for Ta, and from 4 $Å^{-1}$ to 15 $Å^{-1}$ for Nb EXAFS spectra. Dots – experiment; solid lines – best-fit EXAFS model. 104

Figure 4.47: IR spectra of the KTN1, KTN4, KTN24 and KTN48 distillates. For comparison, a spectrum of the 2-methoxyethanol (2-MOE) is also shown. The dashed line stresses the presence of the absorption band at 1740 cm^{-1} in all distillates' spectra. Spectra are displaced vertically for reasons of clarity..... 108

Figure 4.48: Comparison of the TG curves of the KTN1 and KTN24 stoichiometric $KTa_{0.6}Nb_{0.4}O_3$ sols after drying at 60°C. The DTG curves of both sols are compared in the inset. 109

Figure 4.49: a) TG and DTG, b) DTA and c) EGA curves of the 24-h-refluxed stoichiometric $KTa_{0.6}Nb_{0.4}O_3$ sol after drying at 60°C. Positions of the strongest maxima and minima in the curves are denoted. 110

Figure 4.50: XRD patterns of the KTN1 and KTN24 $KTa_{0.6}Nb_{0.4}O_3$ powders after the thermal analysis. P-perovskite phase [142]; Py-pyrochlore phase [164]. 111

Figure 4.51: XRD patterns of the $KTa_{0.6}Nb_{0.4}O_3$ thin films on alumina substrates prepared from the 1-h-refluxed a) stoichiometric sols and b) from the sols with 10 % excess of the potassium excess (b). After four depositions final annealing was performed for 15 min at 700°C, 800°C, or 900°C. Pattern of the alumina substrate is also shown. P – perovskite phase [142]; Py – pyrochlore phase [164]; X – unidentified peaks. 112

Figure 4.52: XRD patterns of the $KTa_{0.6}Nb_{0.4}O_3$ thin films on alumina substrates prepared from the a) 24-h-refluxed stoichiometric sols and b) from the sols with 10 % excess of the potassium excess. After four depositions final annealing was performed for 15 min at 700°C, 800°C, or 900°C. Pattern of the alumina substrate is also shown. P – perovskite phase [142]; Py – pyrochlore phase [164]; X – unidentified peaks. 113

Figure 4.53: a), b), c) and d) plane-view and e), f) cross-section view FE-SEM micrographs of the KTN1-10 (a), c), e)) and KTN24-10 (b), d), f)) $KTa_{0.6}Nb_{0.4}O_3$ thin films on the alumina substrates after heating at 900°C. The films were prepared from the 1-h- and 24-h-refluxed sols, respectively, containing 10 % of the potassium acetate excess. 114

Figure 4.54: DC electric field E_{DC} dependence of the normalized dielectric permittivity $\varepsilon' (E_{DC})/ \varepsilon'(0)$ of the KTN1-10 and KTN24-10 $KTa_{0.6}Nb_{0.4}O_3$ thin films after heating at 900°C (voltage cycle: 0 V → +30 V → 0 V → -30 V → 0 V). The measurements were performed at room temperature and 1 MHz. Lines between the experimental points are guides to the eye. The probing AC field was 1 kV/cm. 116

Figure 4.55: Temperature dependence of the real ε' and imaginary ε'' parts of the complex dielectric permittivity ε^* of the KTN24-10 $KTa_{0.6}Nb_{0.4}O_3$ thin film after heating at 900°C, measured in the 3 kHz to 1 MHz frequency range. The probing AC field was 3.3 kV/cm. 117

Figure 4.56: Temperature dependence of the permittivity ε' and dielectric losses $\tan\delta$ of the KTN24-10 $KTa_{0.6}Nb_{0.4}O_3$ thin film after heating at 900°C, measured at 14.5 GHz. Lines through the experimental points are guides to the eye only. 117

Figure 4.57: Vogel-Fulcher fit of the real permittivity ε' of the KTN24-10 $KTa_{0.6}Nb_{0.4}O_3$ thin films after heating at 900°C. 118

Figure 4.58: Frequency dependence of the permittivity ε' and dielectric losses $\tan\delta$ of the KTN24-10 $KTa_{0.6}Nb_{0.4}O_3$ thin films after heating at 900°C measured at room temperature. Lines between the experimental points are guides to the eye. 118

Figure 10.1: Ion displacements along one of the Cartesian coordinates of the IR active zone-center modes in cubic ABO_3 perovskites: a) Slater, b) Last and c) Axe mode. Figure is taken from Hlinka et al. [179]. 160

Figure 10.2: a) IR reflectivity spectrum of the $KTaO_3$ ceramic measured at room temperature. The experimental data (black solid line) were fitted using the generalized 4-parameter oscillators model (Equation (10.3)) (blue dashed line). The calculated $\varepsilon'(\omega)$ and $\varepsilon''(\omega)$ are shown in b) and c), respectively. Distinctive frequency regions with contributions of the TO1, TO2 and TO4 polar modes are marked. Band marked with * is a combinational band which does not correspond to the fundamental vibrational mode. 161

Figure 10.3: Real $\varepsilon'(\omega)$ and imaginary $\varepsilon''(\omega)$ parts of the complex permittivity of the $BaTiO_3$ single crystal measured from 298 K to 398 K. The probed electric field $E(\omega)$ was polarized parallel to the spontaneous polarization P_S (modes are of the A_1 symmetry). Central (Debye relaxation), Last, Slater and Axe modes are marked with letters D, L, S and A, respectively. THz data are shown as symbols. Figure is taken from Hlinka et al[207]. 163

Figure 10.4: Eight possible off-center sites of the Ti ion in the tetragonal phase of $BaTiO_3$ [231]. The Ti ions mainly fluctuate among the 4 “ground” states (full circles, black arrows). Occasionally they can also hop towards the excited states (dotted circles, red arrows). These hops are responsible for the appearance of the central mode. The direction of the spontaneous polarization P_S is presented with blue arrow. 164

9 Index of Tables

Table 1.1: Permittivity ε', dielectric losses tanδ, and non-linear coefficient β of typical microwave ferroelectrics in their single-crystal form. 21

Table 1.2: Room-temperature dielectric properties of the substrates typically used in thin films for microwave devices [12,13]. 22

Table 1.3: Parameters of the Barrett equation for the $KTaO_3$ single crystal ((100) direction) [21]..... 23

Table 1.4: Temperature of the tanδ maximum measured at 1 kHz, Arrhenius activation energy E_a and attempt frequency ω_0, of the $KTaO_3$ single crystals doped with various ions. The concentration of all the dopants is between 0.01 at.% and 0.1 at.%..... 24

Table 1.5: Low-temperature permittivity ε', dielectric losses tanδ, and measured frequency f of the $KTaO_3$ ceramics taken from the literature. Reported relative density ρ_{rel} and grain size are also given..... 33

Table 1.6: Maximum diffusion coefficient D_0, activation energy E_a *and* the value of the diffusion coefficient extrapolated to 800°C $D_{800°C}$ of the K, Ta, Nb and O species [81-84]. 34

Table 1.7: Overview of the literature reports on $KTa_xNb_{1-x}O_3$ ceramics. T_{calc} – calcination temperature; T_{sint} – sintering temperature; SM – sintering method: CS – conventional sintering, HP – hot pressing, UHP – uniaxial hot pressing; ρ_{rel} – relative density; T_{max} – temperature of the permittivity ε' maximum; f – measurement frequency; Room-temperature permittivity ε' and dielectric losses tanδ values are given. 35

Table 1.8: Overview of the important literature reports on the CSD-processing of the $KTa_xNb_{1-x}O_3$ thin films. T_{cry} – crystallization temperature; P – perovskite phase; Py – pyrochlore phase. 41

Table 3.1: Chemicals used during the synthesis of the $KTaO_3$ ceramics. 46

Table 3.2: High-energy milling parameters. 46

Table 3.3: Chemicals used during the processing of thin films..... 47

Table 4.1: Composition of the amorphous triple pocket and the adjacent grain observed in the 1C-HP ceramic obtained by the combined EDXS and EELS analysis. The nominal values in the perovskite $KTaO_3$ phase are also given. 65

Table 4.2: Chemical composition of the 1C-HP and 2C-HP $KTaO_3$ ceramics determined by the ICP spectrometry. The nominal values for K and Ta in the perovskite phase are also given. 67

Table 4.3: Arrhenius activation energy E_a and attempt frequency ω_0 of the three frequency-dispersion regions observed in the loss spectra of the 2C-HP ceramic (Figure 4.14).....68

Table 4.4: Curie-Weiss, Barret and Cochran fit parameters of the 2C-HP $KTaO_3$ ceramics (Figure 4.20). 74

Table 4.5: Phonon mode frequencies (in cm^{-1}) of the $KTaO_3$ ceramics obtained by the Raman and combined THz and IR spectroscopies at selected temperatures. For comparison, the room-temperature single-crystal values (SC) obtained from the hyper-Raman measurements are added [121]. 76

Table 4.6: Typical amounts of the impurities present in the powders prepared by heating the sol with 30 % excess of potassium acetate to 900°C. The analysis was performed with ICP spectrometry. 81

Table 4.7: Parameters of the nearest coordination shells around the Ta in $KTa_{0.6}Nb_{0.4}O_3$ sols after different reflux times: atomic species, average number of the atomic species N, distance r and Debye-Waller factor σ^2. The uncertainty of the last digit is given in parentheses. 105

Table 4.8: Parameters of the nearest coordination shells around the Nb in $KTa_{0.6}Nb_{0.4}O_3$ sols after different reflux times: atomic species, average number of the atomic species N, distance r and Debye-Waller factor σ^2. The uncertainty of the last digit is given in parentheses. 106

Table 4.9: Room-temperature dielectric permittivity ε' and losses $\tan\delta$ of the KTN1-10 and KTN24-10 $KTa_{0.6}Nb_{0.4}O_3$ thin films after heating at 900°C, measured in the RF and MW frequency range. 115

Table 10.1: Polar mode frequencies ω_{TOj} and mode-plasma frequencies Ω_{TOj} of typical ABO_3 perovskites, i.e., $KNbO_3$[226], $SrTiO_3$[227] and $PbZrO_3$[228] in the cubic phase [179]. The room-temperature data for the $KTaO_3$ ceramics obtained in the Thesis (Chapter 4.1.4.1) are also shown. 161

10 Appendix

10.1 High-Frequency Spectroscopic Properties and Lattice Dynamics of Perovskite Ferroelectrics and Related Materials

The complex dielectric permittivity $\varepsilon^*(\omega) = \varepsilon'(\omega) - i\varepsilon''(\omega)$ describes the response of the substance to an applied electric field $E(\omega)$. It is a second-rank tensor; however, in the scope of the thesis mainly ceramics and polycrystalline thin films are considered, therefore the permittivity is treated as macroscopically isotropic and is written in the form of scalar.

In general, the dielectric response of the materials arises from different polarization mechanisms, such as electronic polarization, atomic polarization, dipolar polarization, etc. Each of these contributions appears in the dielectric spectrum as a dispersion of the permittivity $\varepsilon^*(\omega)$ in a distinguishing frequency range. The dispersions are characterized by the peaks of the imaginary part $\varepsilon''(\omega)$ and the corresponding dispersion regions of the real part $\varepsilon'(\omega)$ of the permittivity, which can be either of the relaxation or resonance type. Both parts are connected through Kramers-Kronig relations. The complete dielectric response of the material is described as the sum of all the individual contributions [223].

In crystals, the atomic contribution is typically caused by coherent vibrational motions of the atoms around their equilibrium positions, called fundamental vibrational modes (normal modes, phonon modes). The normal modes have characteristic frequencies ω_j that depend on the lattice force constants and the masses of the atoms, while the total number of the normal modes is defined by the structure of the crystal lattice. Two types of phonon modes exist: transverse optic (TO) modes, with atoms vibrating perpendicularly to the propagation of the phonon wave (direction of the wave vector), and longitudinal optic (LO) modes with atoms vibrating along the direction of the wave vector. The TO modes can be either non-polar or polar, depending on whether their dipole moment is zero or non-zero, respectively. The polar modes consist of the motions of positive ions against negative ions and directly interact with the infrared electromagnetic wave, typically in the THz and IR frequency range. IR spectra of the ionic crystalline materials are usually dominated by the bands corresponding to the first-order absorption of the photon by the phonon, which can take place only if both have the same wave vector (the same direction and wavelength). If the vibration mode were be completely harmonic it would appear in the IR spectrum as a delta function. In reality, the modes have an at least partially anharmonic character, which is characterized by damping γ_j [224].

The IR dielectric response of materials is often measured in the reflection mode, employing normal specular reflectance from the mirror-flat planar surface of a thick (opaque) sample. This kind of measurement is sensitive not only to the TO modes features, observed in the spectra as the maxima of reflectivity (in the case of not very

strong and weakly damped polar modes), but also to the LO modes features, observed in the spectra as the minima. The measured normal reflectivity $R(\omega)$ is related to the dielectric permittivity $\varepsilon^*(\omega)$ by

$$R(\omega) = \left| \frac{\sqrt{\varepsilon^*(\omega)} - 1}{\sqrt{\varepsilon^*(\omega)} + 1} \right|^2. \tag{10.1}$$

Since the information about the phase of the reflected radiation is missing in the standard Fourier transform IR measurement, the real $\varepsilon'(\omega)$ and imaginary $\varepsilon''(\omega)$ parts of the permittivity must be obtained by fitting the experimental data. A Kramer-Kronig analysis might be inaccurate because of the limited measurable frequency range; therefore, different models for fitting the data exist. The simplest model for the description of the IR measured dielectric permittivity of ferroelectrics and similar materials is the sum of the independent damped harmonic oscillators

$$\varepsilon^*(\omega) = \varepsilon_\infty + \sum_j^n \frac{\Delta\varepsilon_j \omega_{TOj}^2}{\omega_{TOj}^2 - \omega^2 + i\omega\gamma_{TOj}}. \tag{10.2}$$

In the above equation, each oscillator is described with three parameters, ω_{TOj}, γ_{TOj} and $\Delta\varepsilon_j$, which are the frequency, damping and dielectric strength of the j-th TO mode, respectively. The dielectric strength characterizes the contribution of the j-th mode to the static permittivity $\varepsilon(0)$[i] (Equation (10.6)). An additional parameter ε_∞ characterizes the high-frequency electronic contribution. In the case of ferroelectrics it is rather small ($\varepsilon_\infty < 10$) and is usually taken as a temperature-independent constant [225].

In reality, the strong polar modes (high $\Delta\varepsilon_j$) often become coupled between each other. This can be observed in the spectra as e.g. a non-additive overlapping of the imaginary functions $\varepsilon''(\omega)$ belonging to the two bare polar modes. In these cases it is not possible to fit the reflectivity data using Equation (1.21), instead, the spectra can be fitted by the so-called generalized oscillators model with a factorized form of the permittivity $\varepsilon^*(\omega)$

$$\varepsilon^*(\omega) = \varepsilon_\infty \prod_j^n \frac{\omega_{LOj}^2 - \omega^2 + i\omega\gamma_{LOj}}{\omega_{TOj}^2 - \omega^2 + i\omega\gamma_{TOj}}. \tag{10.3}$$

In addition to the j-th TO mode parameters, this model also allows independent adjustment of the j-th LO mode parameters, i.e., the frequency ω_{LOj} and damping γ_{LOj}. The model partially accounts for mode-coupling phenomena with four free fitting parameters for each oscillator. The dielectric strength of the m-th mode $\Delta\varepsilon_m$ is defined as:

$$\Delta\varepsilon_m = \varepsilon_\infty \frac{\prod_j^n \omega_{LOj}^2 - \omega_{TOm}^2}{\prod_{j\neq m}^n \omega_{TOj}^2 - \omega_{TOm}^2} \frac{1}{\omega_{TOm}^2}. \tag{10.4}$$

In the static limit the generalized 4-parameter model yields to the famous Lyddane-Sachs-Teller relation:

[i] Value of the permittivity obtained by the extrapolation of the fit to zero frequency.

$$\frac{\varepsilon(0)}{\varepsilon_\infty} = \prod_j^n \frac{\omega_{LOj}^2}{\omega_{TOj}^2}. \tag{10.5}$$

This relation is usually used to compare the crystal lattice (phonon) contribution to the permittivity with the permittivity measured in the lower (radio-frequency (RF), microwave (MW)) frequency range [224].

In both, 3- and 4-parameter models, the phonon contribution to the static permittivity $\varepsilon(0)$ can also be expressed as a sum of the separate dielectric strengths $\Delta\varepsilon_m$.

$$\varepsilon(0) = \varepsilon_\infty + \sum_m \Delta\varepsilon_m \tag{10.6}$$

Another important quantity that can be evaluated directly from the IR spectra is the mode-plasma frequency Ω_m of the m-th polar mode, defined as:

$$\Omega_m = \sqrt{\Delta\varepsilon_m \cdot \omega_{TOm}^2} \tag{10.7}$$

The mode-plasma frequency is related to the mode eigen-vector by a set of Born effective charge[i] tensors for all in-equivalent ions in the unit cell and can be used for the assignment of the polar modes [179].

The cubic ABO_3 type perovskites ($Pm\bar{3}m$ space group) have 3 triply degenerate zone-center[ii] IR active modes of the $3F_{1u}$ symmetry, which are usually denoted as TO1, TO2 and TO4. There is an additional F_{2u} mode (TO3 mode), however, it is not IR active in the cubic phase and its dipolar strength $\Delta\varepsilon_m$ in the ferroelectric phase is rather small, therefore it will be omitted from this discussion. Considering the movement of the ions along one of the Cartesian coordinates only the eigen-displacements of the 3 polar modes are presented in Figure 10.1. In the Slater mode, the B cations are oscillating against the rigid O_6 octahedra. In the Last mode, the A cations are oscillating against the rigid BO_6 structure. The third mode, Axe mode, corresponds to the bending of the O_6 octahedra.

On cooling through the ferroelectric phase-transition temperature, spontaneous polarization P_s appears. In the case of $PbTiO_3$, $BaTiO_3$, $KNbO_3$, etc., which are tetragonal just below the transition temperature, P_s appears along one of the cubic axes and the three F_{1u} triplet modes split into A_1-E pairs. Modes of the A_1 and E symmetry contribute to the dielectric permittivity tensor parallel and perpendicular to the spontaneous polarization, respectively. The eigen-displacements of these modes can be also described with the Slater, Last and Axe nomenclature.

[i] Born effective charge is approximately a measure of a local dipole moment which develops as the atoms are moved.

[ii] Wave vectors of the IR photons are very small in comparison with the wave vectors of phonons, apart from those that belong to the "center" of the Brillouin zone (wave vectors $k \approx 0$). These are the ones that the IR photons interact with and are observable in the IR spectra.

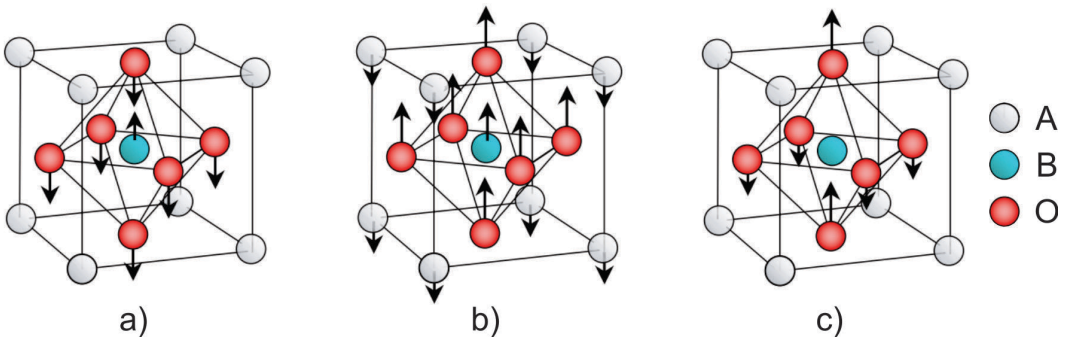

Figure 10.1: Ion displacements along one of the Cartesian coordinates of the IR active zone-center modes in cubic ABO_3 perovskites: a) Slater, b) Last and c) Axe mode. Figure is taken from Hlinka et al. [179].

As an example, the room-temperature IR reflectivity spectrum of the $KTaO_3$ ceramic obtained in the Thesis is shown in Figure 10.2a. The reflection bands, corresponding to the TO1, TO2 and TO4 polar modes, are present at 83 cm^{-1}, 201 cm^{-1} and 543 cm^{-1}, respectively. An additional band at 761 cm^{-1} is a combinational band of the TO2 and TO4 modes and does not correspond to any fundamental vibration. The experimental data were fitted by the generalized 4-parameter oscillators model (Equation (10.3)) and the calculated $\varepsilon'(\omega)$ and $\varepsilon''(\omega)$ are plotted in Figure 10.2b and c, respectively. As discussed above, the dispersion regions corresponding to each polar mode appear as a distinctive resonance in the $\varepsilon'(\omega)$ spectrum and as a peak in the $\varepsilon''(\omega)$ spectrum. The positions of the $\varepsilon''(\omega)$ maxima approximately correspond to the modes frequencies ω_{TOj}. Note that the lowest frequency TO1 mode has the largest dielectric strength.

To assign the polar modes observed in Figure 10.2, the mode-plasma frequencies Ω_{TOj} (Equation (10.7)) of the TO1, TO2 and TO4 modes were calculated. The values are shown in Table 10.1, together with the literature values for the typical ABO_3 perovskites in their cubic phase. According to Hlinka et al. [179], the mode with the largest mode-plasma frequency Ω_{TOj} always corresponds to the Slater-type due to the large Born effective charge of the B cation. The Last mode is always the one with the smallest Ω_{TOj}. Thus, in the case of the $KTaO_3$ the TO1, TO2 and TO4 modes are of the Slater, Last and Axe types, respectively. Note that the lowest-frequency ω_{TOj} mode in the case of $KNbO_3$, $SrTiO_3$ and $KTaO_3$ is of the Slater-type, while in the case of $PbZrO_3$ it is of the Last type. This can be generalized to other lead-based systems [179].

The general sum rule of the squared mode-plasma frequencies requires that that the total plasma frequency Ω_{TOT} has to be temperature independent:

$$\Omega_{TOT} = \sqrt{\Omega_{TO1}^2 + \Omega_{TO2}^2 + \Omega_{TO4}^2} \qquad (10.8)$$

Even more, if the phonon modes are not coupled, e.g., well separated in the frequency, even each Ω_{TOj} should be temperature independent as well. As it follows from Equation (10.7), if the phonon frequency ω_{TOj} changes with temperature it should be accompanied by a change of dielectric strength $\Delta\varepsilon_{TOj}$, and according to Equation (10.6) also the static permittivity $\varepsilon(0)$ must change.

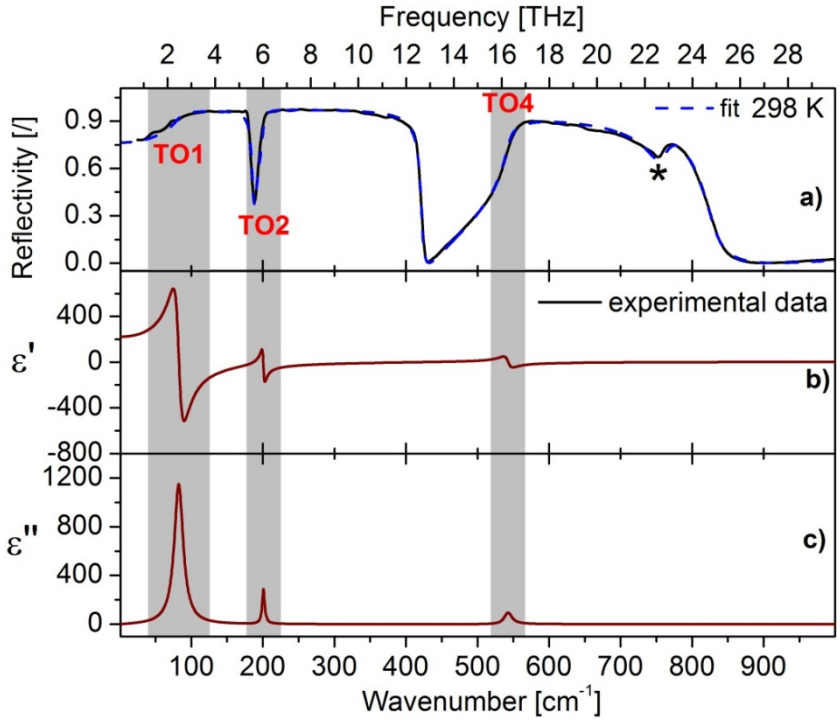

Figure 10.2: a) IR reflectivity spectrum of the $KTaO_3$ ceramic measured at room temperature. The experimental data (black solid line) were fitted using the generalized 4-parameter oscillators model (Equation (10.3)) (blue dashed line). The calculated $\varepsilon'(\omega)$ and $\varepsilon''(\omega)$ are shown in b) and c), respectively. Distinctive frequency regions with contributions of the TO1, TO2 and TO4 polar modes are marked. Band marked with * is a combinational band which does not correspond to the fundamental vibrational mode.

Table 10.1: Polar mode frequencies ω_{TOj} and mode-plasma frequencies Ω_{TOj} of typical ABO_3 perovskites, i.e., $KNbO_3$[226], $SrTiO_3$[227] and $PbZrO_3$[228] in the cubic phase [179]. The room-temperature data for the $KTaO_3$ ceramics obtained in the Thesis (Chapter 4.1.4.1) are also shown.

Material	ε_∞	[cm^{-1}]		**Type**	[cm^{-1}]		**Type**	[cm^{-1}]		**Type**
		ω_{TO1}	Ω_{TO1}		ω_{TO2}	Ω_{TO2}		ω_{TO4}	Ω_{TO4}	
$KNbO_3$ (710 K)	5.53	96	**1455**	Slater	198	**465**	Last	521	**918**	Axe
$SrTiO_3$ (300 K)	5.6	91	**1575**	Slater	176	**335**	Last	546	**680**	Axe
$PbZrO_3$ (510 K)	5.86	36	**645**	Last	200	**898**	Slater	519	**686**	Axe
$KTaO_3$ (300 K)	4.3	83	**1197**	Slater	201	**492**	Last	543	**823**	Axe

When the ferroelectric material in its cubic phase is cooled towards the ferroelectric phase transition, interesting phenomena occur. In the case of a displacive phase transition, when the anharmonicity of phonons is small, the frequency of the TO1 polar mode ω_{TO1} strongly decreases with decreasing temperature – it becomes "soft"; therefore it is called the soft mode (SM). At the phase transition point the crystal loses its stability against the soft mode vibration and a lower symmetry polar phase appears. Above the transition, the temperature of the soft mode is described by the Cochran law [229] (Equation (10.9)):

$$\omega_{SM}^2 = A(T - T_C), \tag{10.9}$$

where A is a constant and T_c is the Curie temperature. If the phonons are not coupled, the parameters of the TO2 and TO4 phonons do not change anomalously with temperature (hard phonons). In this case, the Cochran law for the static permittivity $\varepsilon(0)$ results in the Curie-Weiss law (Equation (1.1)). The Curie-Weiss constant is defined as $C = \Omega^2_{SM}/A = \Delta\varepsilon_{SM}\,\omega^2_{TO1}/A$ [225].

In the case of incipient ferroelectrics at low temperatures the soft mode levels off due to quantum fluctuations according to the modified Barrett formula [230]:

$$\omega^2_{SM} = A\left[\left(\frac{T_1}{2}\right)coth\left(\frac{T_1}{2T}\right) - T_0\right], \tag{10.10}$$

where the temperature T_1 denotes the temperature where the quantum fluctuations start to play a role. The crossover between the Curie-Weiss and Barrett-type behavior is in our case observed near 30 K.

The above described dynamics of the soft mode holds for the displacive ferroelectric phase transitions. In the case of order-disorder transitions, in which the lattice has a strongly anharmonic character, the picture is quite different. Softening of any polar phonon is not observed and all the polar modes remain hard; instead, a new dispersion of the relaxation type appears below the polar modes' frequencies (usually in the MW range) and is related to the hopping of the disordered atoms among the available sites. This dispersion can be described with the model of Debye relaxation:

$$\varepsilon^*(\omega) = \varepsilon_{LST} + \frac{\Delta\varepsilon_R\omega_R}{\omega_R + i\omega}, \tag{10.11}$$

where ε_{LST} is the high-frequency dielectric contribution of the electrons and polar modes, while $\Delta\varepsilon_R$ is the dielectric strength of the relaxation. The ω_R is the relaxation frequency, which decreases on cooling to the transition temperature according to:

$$\omega_R = A_R(T - T_C). \tag{10.12}$$

Again, for the static permittivity $\varepsilon(0)$ the Curie-Weiss law (Equation(1.1)) is obtained.

In reality, pure displacive and order-disorder type dynamics are only limiting situations. The anomalies around the ferroelectric phase transition often show features of both. In the case of $BaTiO_3$, softening of the soft mode above the transition temperature has been experimentally confirmed, indicating displacive phase transition. However, an additional relaxation dispersion, which substantially contributes to the static permittivity $\varepsilon(0)$ value, appears near the transition point. The dispersion can be modeled with the Debye relaxation (Equation (10.11)) and is called the central mode (CM). It is indicating that the ferroelectric phase transition is at least partially of the order-disorder type. As an example, the combined THz and IR reflectivity spectra of the $BaTiO_3$ single crystal measured along *Ps* in the tetragonal ferroelectric phase (298–398 K) are shown in Figure 10.3. [207] The calculated $\varepsilon''(\omega)$ and $\varepsilon'(\omega)$ are also shown. Dispersion regions arising from the Last, Slater and Axe polar modes of A_1 symmetry, can be nicely observed. The contribution of the central mode is present in the lower frequency range (marked with D), and is especially strong in the vicinity of the phase transition ($T_C \approx 395$°C).

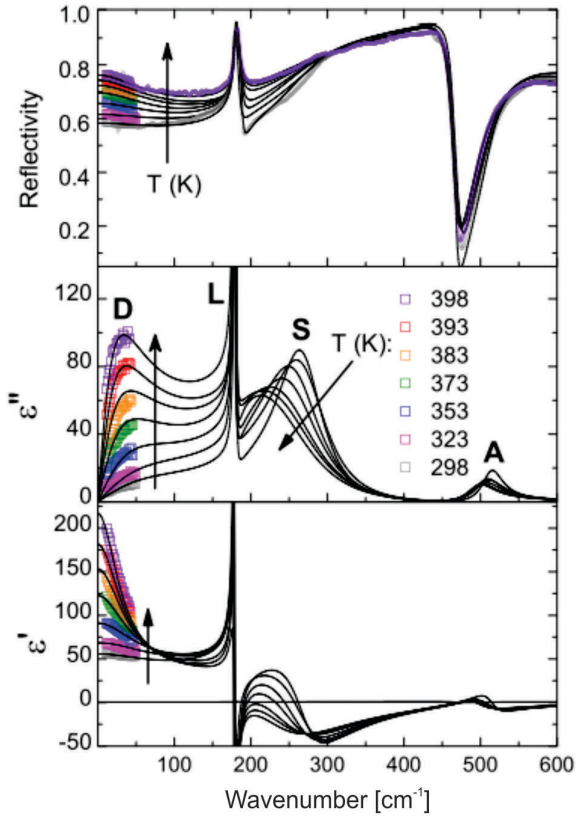

Figure 10.3: Real $\varepsilon'(\omega)$ and imaginary $\varepsilon''(\omega)$ parts of the complex permittivity of the $BaTiO_3$ single crystal measured from 298 K to 398 K. The probed electric field $E(\omega)$ was polarized parallel to the spontaneous polarization P_S (modes are of the A_1 symmetry). Central (Debye relaxation), Last, Slater and Axe modes are marked with letters D, L, S and A, respectively. THz data are shown as symbols. Figure is taken from Hlinka et al[207].

The authors made an attempt to determine the origin of the central mode by molecular dynamics (MD) simulations based on the order-disorder Comes-Guinier-Lambert model [231]. Within this model, the tetragonal phase of the $BaTiO_3$ with the spontaneous polarization P_s along (001) direction, corresponds to the preferential fluctuation of the Ti ions among (111), (1-11), (-111) and (-1-11) quadruplet (Figure 10.4). These "ground" states are stabilized by the (001) molecular field. On the other side, there are also "excited" (11-1), (1-1-1), (-11-1) and (-1-1-1) states (Figure 10.4). As confirmed by matching of the MD simulations with the experimental spectroscopic data, occasional hops of the Ti ions towards the "excited" states are responsible for the appearance of the central mode [207].

In addition to $BaTiO_3$, the crossover between the displacive and order-disorder type ferroelectric phase transition has been observed in a large number ferroelectric materials [232].

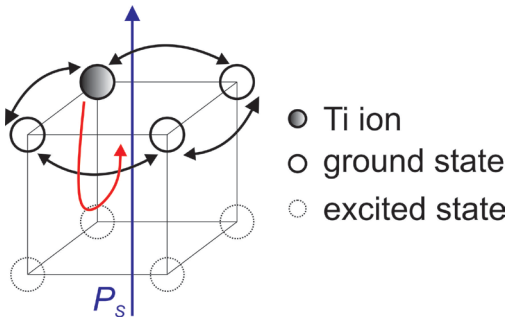

Figure 10.4: Eight possible off-center sites of the Ti ion in the tetragonal phase of $BaTiO_3$ [231]. The Ti ions mainly fluctuate among the 4 “ground” states (full circles, black arrows). Occasionally they can also hop towards the excited states (dotted circles, red arrows). These hops are responsible for the appearance of the central mode. The direction of the spontaneous polarization P_S is presented with blue arrow.

11 Personal Bibliography

11.1 Scientific Articles from the Thesis

[1] Glinšek S.; Malič B.; Vukadinović M.; Kužnik B.; Kosec M. Processing and Electric Field Dependent Dielectric Properties of $KTa_{0.6}Nb_{0.4}O_3$ Thin Films on Alumina. *Ferroelectrics* **387**, 112 (2009).

[2] Glinšek S.; Malič B.; Kutnjak Z.; Krupka J.; Kosec M.; Wang H. Dielectric Properties of $KTa_{0.6}Nb_{0.4}O_3$ Thin Films on Alumina Substrates Prepared by Chemical Solution Deposition. *Applied Physics Letters* **94**, 172905 (2009).

[3] Tchernychova E.; Glinšek S.; Malič B.; Kosec M. Combined Analytical Transmission Electron Microscopy Approach to Reliable Composition Evaluation of $KTaO_3$. *Journal of the American Ceramic Society* **94**, 1611 (2011).

[4] Glinšek S.; Malič B.; Rojac T.; Filipič C.; Budič B.; Kosec M. $KTaO_3$ Ceramics Prepared by the Mechanochemically Activated Solid-state Synthesis. *Journal of the American Ceramic Society* **94**, 1368 (2011).

[5] Skoromets V.; Glinšek S.; Bovtun V.; Kempa M.; Petzelt J.; Kamba S.; Malič B.; Kosec M.; Kužel P. Ferroelectric Phase Transition in Polycrystalline $KTaO_3$ Thin Film Revealed by Terahertz Spectroscopy. *Applied Physics Letters* **99**, 052908 (2011).

[6] Glinšek S.; Arčon I.; Malič B.; Kodre A.; Kosec M. Structural Evolution of the $KTa_{0.6}Nb_{0.4}O_3$ Alkoxide-Based Solutions: Probing the Transition Metals Local Environment by X-Ray Absorption Spectroscopy. *Journal of Sol-Gel Science and Technology,* DOI: 10.1007/s10971-011-2669-3 (2012).

[7] Glinšek S.; Nuzhnyy D.; Petzelt J.; Malič B.; Kamba S.; Bovtun V.; Skoromets V.; Kužel P.; Gregora I.; Kosec M. Lattice Dynamics and Broadband Dielectric Properties of the $KTaO_3$ Ceramics. *Journal of Applied Physics*, submitted (2012).

11.2 Other Scientific Articles

[1] Hrovat M.; Holc J.; Glinšek S.; Subsolidus Phase Equilibria in the RuO_2-ZnO-SiO_2 System. *Journal of Materials Science* **42**, 5883 (2007).

[2] Kupec A.; Malič B.; Tellier J.; Tchernychova E.; Glinšek S.; Kosec M. Lead-Free Ferroelectric Potassium Sodium Niobate Thin Films from Solution: Composition and Structure. *Journal of the American Ceramic Society*, DOI: 10.1111/j.1551-2916.2011.04892.x (2012).

[3] Bobnar V.; Li X.; Casar G.; Eršte A.; Glinšek S.; Qian X.; Zhang Q.M. Tailoring Electrically-Induced Properties by Stretching Relaxor Polymer Films. *Journal of Applied Physics*, accepted (2012).

11.3 Chapters in Monographs

[1] Malič B.; Glinšek S.; Kosec M. Low-Temperature Processing of Functional-Oxide Thin Films. In: Schneller T.; Waser R.; Kosec M.; Payne D. (ed.) *Chemical Solution Deposition of Functional Oxide Thin Films*. (Springer, October 2012).

11.4 Conference Contributions

11.4.1 Published Scientific Conference Contributions

[1] Glinšek S.; Malič B.; Kutnjak Z.; Wang H.; Krupka J.; Kosec M. Radio and Microwave Frequency Range Dielectric Properties of $K(Ta,Nb)O_3$ Thin Films. In: Topič M.; Krč J.; Šorli I. (ed.) *Proceedings of* the *45th International Conference on Microelectronics, Devices, and Materials and the Workshop on Advanced Photovoltaic Devices and Technologies.* 203 (Postojna, 2009).

[2] Glinšek S. Preparation and Dielectric Properties of $K(Ta,Nb)O_3$ Thin Films Prepared by Chemical Solution Deposition. In: Blinc R. (ed.) *Proceedings of the 2nd Slovenian-Japanese Symposium.* (Ljubljana, 2009).

[3] Glinšek S.; Malič B.; Rojac T.; Filipič C.; Budič B.; Kosec M. Influence of the Alkali Excess on Dielectric Properties of $KTaO_3$ Ceramics. In: Đonlagić D.; Šorli I.; Šorli P. (ed.) *Proceedings of* the *46th International Conference on Microelectronics, Devices and Materials and the Workshop on Optical Sensors.* 71 (Radenci, 2010).

[4] Glinšek S.; Malič B.; Tchernychova E.; Filipič C.; Kosec M. Processing of High-Quality $KTaO_3$ Ceramics. In: Petelin D.; Tavčar A.; Rožič B.; Pogorelc B. (ed.) *Proceedings of the 3rd Jožef Stefan International Postgraduate School Students Conference*. 162 (Ljubljana, 2011).

11.4.2 Published Scientific Conference Contributions – Invited Talks

[1] Kosec M.; Malič B.; Vukadinović M.; Glinšek S. Processing Issues of CSD Ferroelectric Thin Films. In: *The 6th Asian Meeting on Ferroelectrics.* (Taipei, 2008).

[2] Kosec M.; Malič B.; Mandeljc M.; Vukadinović M.; Glinšek S. Towards High Performing Ferroelectric Thin Films. In: *The 17th IEEE International Symposium on Applications of Ferroelectrics, and Meeting of the Electronics Division of the American Ceramic Society.* (Santa Fe, 2008).

[3] Malič B.; Glinšek S.; Kužnik B.; Cilenšek J.; Tchernychova E.; Vukadinović M.; Kosec M. Lead-Free Perovskite Thin Films with High Permittivity by Chemical Solution Deposition Routes. In: *The International Union of Materials Research Societies International Conference in Asia.* (Nagoya, Japan).

[4] Malič B.; Benčan A.; Koruza J.; Glinšek S.; Rojac T.; Kosec M. Understanding and Controlling Microstructure Evolution in Lead-Free Piezoelectric Sodium Potassium Niobate Ceramics. In: *Electroceramics XII.* (Trondheim, 2010).

[5] Kosec M.; Rojac T.; Malič B.; Trefalt G.; Glinšek S. Towards Extreme Properties of Functional Ceramics by Novel Powder Processing Routes. In: *12th Conference of the European Ceramic Society*. (Stockholm, 2011).

[6] Malič B.; Glinšek S.; Kupec A.; Tchernychova E.; Kosec M. Optimized Functional Properties of Solution-Derived Ferroelectric Thin Films by Microstructure Design. In: *12th European Meeting on Ferroelectricity.* (Bordeaux, 2011).

[7] Kosec M.; Rojac T.; Malič B.; Glinšek S. Novel Dielectric Materials Through Novel Powder Processing. In: *Materials Science & Technology Conference & Exhibition.* (Columbus, 2011).

[8] Malič B.; Glinšek S.; Kupec A.; Tchernychova E.; Kosec M. Solution Processing of Perovskite Thin Films for Optimized Functional Properties. In: *Materials Science & Technology Conference & Exhibition.* (Columbus, 2011).

[9] Rojac T.; Malič B.; Benčan A.; Holc J.; Glinšek S.; Šegedin P.; Kosec M. Mechanochemical Synthesis of Alkaline Niobates and Tantalates: Understanding Reaction Mechanisms. In: Uskoković D. (ed.) *VIIth International Conference on Mechanochemistry and Mechanical Alloying.* (Herceg Novi, 2011).

[10] Malič B.; Glinšek S.; Kupec A.; Tchernychova E.; Kosec M. Solution-Derived Functional Oxide Thin Films: Crystallization, Microstructure, Functional Properties. In: Srdić V.; Mitoseriu L. (ed). *The Ninth Students' Meeting. Processing and Application of Ceramics and The Second Early Stage Researchers Workshop of the COST MP0904 Action* (Novi Sad, 2011).

11.4.3 Published Scientific Conference Contributions – Abstracts

[1] Glinšek S.; Malič B.; Vukadinović M.; Kužnik B.; Kosec M. Processing and Electric Field Dependent Dielectric Properties of $KTa_{0.6}Nb_{0.4}O_3$ Thin Films on Alumina. In: *The 5th International Conference on Microwave Materials and Their Applications.* (Hangzhou, 2008).

[2] Glinšek S.; Malič B.; Kosec M. Processing and Dielectric Properties of $KTa_{0.6}Nb_{0.4}O_3$ Thin Films on Alumina. In: Mihailović D.; Kobe S.; Remškar M.; Jamnik J.; Čopič M.; Drobne D. (ed.) *Hot nano topics 2008, Incorporating SLONANO 2008.* (Portorož, 2008).

[3] Glinšek S.; Malič B.; Kosec M. "Priprava in lastnosti tankih plasti $KTa_{0.6}Nb_{0.4}O_3$ na podlagah Al_2O_3." In: Ponikvar Svet M. (ed.) "*Dan mladih raziskovalcev 2008."* (Ljubljana, 2008).

[4] Glinšek S.; Malič B.; Vukadinović M.; Kužnik B.; Kosec M. Processing and Dielectric Properties of $KTa_{0.6}Nb_{0.4}O_3$ Thin Films on Alumina. In: Jenko M. (ed.) *1st International Conference on Materials and Technology sponsored by FEMS and IUVSTA.* (Portorož, 2008).

[5] Glinšek S.; Malič B.; Kosec M. Functional Properties of $K(Ta,Nb)O_3$ Thin Films for Applications in Electronically Tunable Microwave Devices. In: Mihailović D.; Dominko R.; Vilfan M. (ed.) *SLONANO 2009.* (Ljubljana, 2009).

[6] Glinšek S.; Malič B.; Kosec M. "Vpliv pogojev sinteze sola na lastnosti tankih plasti $KTa_{0.6}Nb_{0.4}O_3$." In: Iskra J.; Milošev I. (ed.) "*Dan mladih raziskovalcev 2009."* (Ljubljana, 2009).

[7] Glinšek S.; Kosec M.; Malič B.; Kutnjak Z. Processing and Dielectric Properties of Chemical Solution Deposition Derived $KTa_{0.6}Nb_{0.4}O_3$. In: *European Materials Research Society 2009 Spring Meeting.* (Strasbourg, 2009).

[8] Malič B.; Glinšek S.; Kužnik B.; Kosec M. Processing and Dielectric Properties of CSD-Derived Tunable Ferroelectric Thin Films. In: Stojanović B.; Nanni P. (ed.) *Final Workshop* of the *COST 539 Action.* (Novi Sad, 2009).

[9] Glinšek S. "Feroelektrične tanke plasti, uporabne v moderni elektroniki." In: Torkar M. (ed.) "*Promocija študija in raziskav materialov."* (Ljubljana, 2009).

[10] Malič B.; Glinšek S.; Kužnik B.; Cilenšek J.; Tchernychova E.; Vukadinović M.; Kosec M. Chemical Solution Deposition of Perovskite Thin Films with High Permittivity. In: *3rd Slovenia-Korea Workshop on Advanced Materials.* (Ljubljana, 2009).

[11] Malič B.; Kužnik B.; Glinšek S.; Benčan A.; Kosec M.; Eršte A.; Bobnar V. Influence of Microstructure on Dielectric Properties of Solution-Derived $CaCu_3Ti_4O_{12}$ Thin Films. In: *Electroceramics XII.* (Trondheim, 2010).

[12] Glinšek S.; Malič B.; Rojac T.; Filipič C.; Kosec M. Synthesis of $KTaO_3$ Ceramics from Mechanochemically Activated Powders. In: *Electroceramics XII.* (Trondheim, 2010).

[13] Tchernychova E.; Glinšek S.; Malič B.; Kosec M. $KTaO_3$ Ceramic: Nanoscale Compositional Analysis as an Assisting Tool in Improving the Dielectric Properties. In: Mihailović D.; Hočevar S.; Arčon D.; Kunej Š.; Umek P.; Knavs M. (ed.) *SLONANO 2010.* (Ljubljana, 2010).

[14] Glinšek S.; Malič B.; Kosec M. Dielectric Properties of Solution Derived $KTaO_3$ and $K(Ta,Nb)O_3$. In: *16th Workshop on Dielectrics in Microelectronics.* (Bratislava, 2010).

[15] Malič B.; Kužnik B.; Glinšek S.; Benčan A.; Tchernychova E.; Kosec M.; Eršte A.; Bobnar V. Tailoring of Dielectric Properties of Solution-Derived $CaCu_3Ti_4O_{12}$ Thin Films by Processing. In: *6th International Conference on Microwave Materials and their Applications.* (Warsaw, 2010).

[16] Glinšek S.; Malič B.; Filipič C.; Tchernychova E.; Kosec M. $KTaO_3$ Ceramics and Solution Derived Thin Films. In: *6th International Conference on Microwave Materials and their Applications.* (Warsaw, 2010).

[17] Glinšek S.; Malič B.; Filipič C.; Tchernychova E.; Kosec M. $KTaO_3$ Ceramics – Optimization of Dielectric Properties by Processing. In: Jenko M. (ed.) *18th Conference on Materials and Technology.* (Portorož, 2010).

[18] Glinšek S.; Malič B.; Kosec M. "Funkcijske lastnosti tankih plasti $K(Ta,Nb)O_3$, uporabnih v napetostno prilagodljivih elektronskih komponentah." In: Kuščer D.; Perc B. (ed.) "*4. dan mladih raziskovalcev."* (Ljubljana, 2010).

[19] Tchernychova E.; Glinšek S.; Kužnik B. Transmission Electron Microscopy Specimens Preparation. In: Benčan A.; Kuščer D.; Malič B.; Kosec M. (ed.) *Workshop on Structural Characterization* (Ljubljana, 2010).

[20] Tchernychova E.; Glinšek S.; Malič B.; Kosec M. Quantitative Compositional Analysis of Lead Free $KTaO_3$ Ceramic Using Spectroscopic Techniques of Transmission Electron Microscopy. In: Glavič P.; Brodnjak Bončina D. (ed.) "*Slovenski kemijski dnevi 2010."* (Maribor, 2010).

[21] Glinšek S.; Malič B.; Kosec M. Ferroelectric Thin Films for Tunable Microwave Applications. In: Kaluža B.; Eleršič K.; Pogorelc B.; Šetina B.; Vahčič M. (ed.) *2nd Jožef Stefan International Postgraduate School Students Conference.* (Ljubljana, 2010).

[22] Glinšek S.; Nuzhnyy D.; Bovtun V.; Skoromets V.; Kempa M.; Kužel P.; Petzelt J.; Kamba S.; Malič B.; Kutnjak Z.; Kosec M. Broadband Dielectric Properties of $KTaO_3$ Ceramics and Solution Derived Thin Films. In: *First Dedicated Early Stage Researchers Meeting of the COST MP0904 Action*. (Hasselt, 2011).

[23] Glinšek S.; Malič B.; Filipič C.; Tchernychova E.; Kutnjak Z.; Kosec M. Processing-Dependent Dielectric Properties of $KTaO_3$ Ceramics and Solution-Derived Thin Films. In: *12th Conference of the European Ceramic Society*. (Stockholm, 2011).

[24] Glinšek S.; Skoromets V.; Nuzhnyy D.; Bovtun V.; Kužel P.; Kamba S.; Petzelt J.; Kutnjak Z.; Filipič C.; Malič B.; Kosec M. Induced Ferroelectricity in Polycrystalline $KTaO_3$ Thin Films. In: *The 20th IEEE International Symposium on Applications of Ferroelectrics and International Symposium on Piezoresponse Force Microscopy & Nanoscale Phenomena in Polar Materials.* (Vancouver, 2011).

[25] Frunza R.; Canu G.; Kužnik B.; Glinšek S.; Malič B.; Kosec M. Low-temperature Processing and Properties of Solution Derived Tantalum Oxide-Based Thin Films. In: *European Materials Research Society Fall Meeting*. (Warsaw, 2011).

11.4.4 Unpublished Scientific Conference Contributions

[1] Malič B.; Glinšek S.; Kosec M. "Feroelektrični tankoplastni varaktorji z uporabo v mikrovalovnem območju." In: *"Posvet o naprednih materialih."* (Ljubljana, 2009).